

SOL-GEL SYNTHESIS OF HIGHLY ORIENTED LEAD BARIUM TITANATE AND  
LANTHANUM NICKELATE THIN FILMS FOR HIGH STRAIN SENSOR AND  
ACTUATOR APPLICATIONS

Thesis by

Stacey Walker Boland

In Partial Fulfillment of the Requirements

for the Degree of

Doctor of Philosophy

California Institute of Technology

Pasadena, CA

2005

(Defended March 14, 2005)

© 2005

Stacey W. Boland

All Rights Reserved

## **Acknowledgements**

This thesis would not have been possible without the tremendous support I have received from family and friends. Words cannot express the gratitude I feel for my husband Justin Boland and my parents, Benn and April Walker, who have been my anchors to reality throughout this graduate school experience. I'd also like to thank those in my research group who have made life here so much richer. Special thanks to Lisa Cowan, Mary Thundathil, Martin Smith-Martinez, and Kenji Sasaki for the friendship in addition to the intellectual support. I'd also like to thank Melody Grubbs for her hard work and enthusiasm in the lab through the Caltech FSI and SURF programs, and again for continuing to work even after that! Thanks to my colleagues Victor Shih, P.J. Chen, and Scott Miserendino, who went out of their way to help me explore some of the integration strategies mentioned in Chapter IV, and to Justin, who also helped with these efforts! To my thesis supervisory and examination committee, Sossina Haile, Kaushik Bhattacharya, Dave Goodwin, and George Rossman, I'd like to thank you for your guidance throughout my research endeavors, and again for reading my thesis.

Also thanks to...

Caltech for letting me plant a garden full of daisies, Omar Knedlik for inventing the ICEE, and Brett Favre for being a great quarterback.

## Abstract

Piezoelectric materials, capable of 0.1% strains, have been extensively used in sensor and actuator applications. Ferroelectric materials, a subset of the piezoelectric class, are capable of strains an order of magnitude larger. For a ferroelectric material with tetragonal crystal structure, large strains can be achieved through 90° domain switching between  $a$  and  $c$  domains. Bulk barium titanate has been shown to produce strains of 0.9% through such domain switching under combined electromechanical loading. Lead titanate has a larger  $c/a$  ratio and would be expected to produce 6% strains, though it is prone to brittle fracture. By examining the solid solution lead barium titanate, larger strains can be achieved while maintaining mechanical integrity. The work presented here covers the development of multiple sol-gel processes for producing powder and highly oriented thin film lead barium titanate, and a detailed discussion of their parametric optimization towards low temperature crystallization. Finally, results of early efforts toward integrating these films into useful structures and devices are discussed, including sol-gel synthesis of highly oriented conductive oxide electrodes. Thin film barium lead oxide and lanthanum nickelate electrodes were produced using sol-gel processing. (100)-oriented lanthanum nickelate electrodes were produced on a wide variety of amorphous and crystalline substrates, and subsequently deposited PBT showed excellent (100/001)-orientation regardless of substrate. The ability to produce highly oriented ferroelectric films on oxide electrodes deposited directly on Si promises to improve fatigue characteristics and greatly facilitate efforts to integrate ferroelectric thin films into MEMS process.

# Table of Contents

<b>I. Introduction</b> .....	<b>1</b>
I.1. Ferroelectrics .....	4
I.1.1. Ferroelectric vs. Piezoelectric.....	6
I.1.2. Domain Switching .....	6
I.1.3. PBT vs. PZT .....	8
I.2. Experimental Method .....	10
I.2.1. Introduction to Sol-gel.....	10
I.2.2. Advantages of Sol-gel over Other Techniques.....	12
I.2.3. Sol-gel Processing of BT, PT, and PBT: Literature Survey .....	13
I.2.4. Parameters Involved in Sol-gel.....	16
I.2.5. Selection of Precursors .....	17
I.2.5.1. Chelating Agent Selection .....	19
I.2.5.2. Solvent Selection .....	21
I.2.5.3. Substrate Selection .....	22
I.2.5.4. Deposition Method .....	23
I.2.6. Analytical Techniques .....	24
<b>II. Sol-gel Synthesis of <math>\text{Pb}_{1-x}\text{Ba}_x\text{TiO}_3</math></b> .....	<b>26</b>
II.1. Precursor Selection.....	26
II.2. Choosing the Best Sol Candidates .....	29
II.2.1. Stability of Selected Systems .....	30

II.3. Parametric Optimization of Sols and Powders.....	32
II.4. Parametric Optimization of Thin Film Deposition Process .....	36
II.5. Detailed Results for TIpDEA System.....	37
II.5.1. Optimizing the TIpDEA Sol .....	37
II.5.2. Effect of Calcination Atmosphere on TIpDEA System.....	43
II.5.3. PBT Thin Films.....	54
II.6. Summary .....	66
<b>III. Electrodes.....</b>	<b>67</b>
III.1. Pt Electrode.....	67
III.2. Conductive Oxide Electrodes .....	70
III.2.1. BaPbO <sub>3</sub> : Literature Survey .....	74
III.2.2. Sol-gel Synthesis of BaPbO <sub>3</sub> .....	76
III.2.3. Lanthanum Nickelate Literature Survey.....	83
III.2.4. Sol-gel Synthesis of LaNiO <sub>3</sub> .....	84
III.2.5. PBT on LaNiO <sub>3</sub> .....	99
III.2.6. Other Ferroelectrics on LaNiO <sub>3</sub> .....	105
<b>IV. Integration.....</b>	<b>107</b>
IV.1. Introduction to Integration Issues .....	107
IV.1.1. Thermal Constraints.....	107
IV.1.2. Contamination.....	108
IV.1.3. Integration Strategy .....	109

IV.2. Patterning.....	110
IV.2.1. Photolithography.....	110
IV.2.2. UV Patterning.....	111
IV.2.3. Selective Deposition.....	115
IV.3. Orientation: IBAD MgO.....	121
IV.3.1. Membrane Process Flow.....	123
IV.3.2. TEM Windows.....	125
IV.4. Orientation: Lanthanum Nickelate .....	125
IV.4.1. LaNiO <sub>3</sub> /PBT/LaNiO <sub>3</sub> /Si Stacks .....	126
IV.4.2. Commercial Arrays.....	127
IV.4.3. Membrane Process Flow.....	130
IV.4.4. Mask Design .....	132
IV.4.5. XeF <sub>2</sub> Dry Etch.....	133
IV.5. Soluble Substrates.....	136
IV.5.1. PBT on LiF .....	139
IV.5.2. PBT on NaCl.....	141
<b>V. Conclusions.....</b>	<b>144</b>
V.1. Suggestions for Future Research .....	145
V.1.1. Electrical and mechanical testing.....	145
V.1.2. Solvent selection for LaNiO <sub>3</sub> .....	145
V.1.3. Application of electric field during calcination .....	146
V.1.4. Patterning using broad spectrum UV source.....	146

V.1.5. Orientation of $\text{LaNiO}_3$ .....	147
V.1.6. Porosity of $\text{LaNiO}_3$ .....	147
V.1.7. Solid solution range of $\text{Pb}_{1-x}\text{Ba}_x\text{TiO}_3$ .....	148
V.1.8. Effect of calcination atmosphere.....	148
V.2. Final Remarks & Outlook.....	149
<b>References.....</b>	<b>151</b>
<b>A. Appendix.....</b>	<b>173</b>
A.1. TIpAc System: Standard Procedure.....	173
A.2. TBuAc System: Standard Procedure .....	175
A.3. TBuDEA System: Standard Procedure.....	177
A.4. TBuDEA System: Rotary Evaporator Procedure .....	179
A.5. TIpDEA System: Standard Procedure .....	180
A.6. BPO System: Standard Procedure .....	182
A.7. LNO System: Standard Procedure.....	183
A.8. Solubility Test Results .....	184
A.9. Sol-gel Systems Investigated .....	188
A.10. AAC System: Additional Results .....	191
A.11. EG2NO3 System: Additional Results.....	193
A.12. F3AC System: Additional Results .....	200
A.13. TIpAc System: Additional Results .....	203
A.14. TIpDEA System: Additional Results.....	207

A.15. LaNiO <sub>3</sub> : Effect of Pyrolysis Temperature on Surface Morphology .....	220
A.16. LaNiO <sub>3</sub> : Effect of Number of Layers on Surface Morphology .....	223
A.17. LaNiO <sub>3</sub> : Effect of Calcination Temperature and Heating Rate on Surface Morphology .....	226

## Figures

Figure 1. The six variants of a ferroelectric tetragonal unit cell. The arrows represent the polarization direction. ....	5
Figure 2. Ferroelectric thin film micropump schematic. Polarization direction indicated by arrows. [Image courtesy Kaushik Bhattacharya] .....	8
Figure 3. Scheme for typical sol-gel process. ....	27
Figure 4. Stability against rapid hydrolysis of titanium isopropoxide and titanium butoxide with varied chelating agent:titanium ratio. [Data collected by Arvind Subramaniam] .....	33
Figure 5. Schematic of the TIpDEA sol-gel process for producing powder and thin film PBT. ....	38
Figure 6. XRD of TIpDEA sols prepared with the stated water:titanium (R <sub>w</sub> ) ratio and calcined at 500°C (* indicates BaCO <sub>3</sub> impurity phase). ....	39
Figure 7. FTIR of TIpDEA sol, xerogel, and calcined powders. ....	41
Figure 8. FTIR of modified TIpDEA sol, xerogel, and calcined powders made with lead acetate. ....	42
Figure 9. XRD of TIpDEA powders calcined at the given temperatures. ....	43
Figure 10. TGA of TIpDEA xerogels in the %O <sub>2</sub> atmosphere indicated. ....	46
Figure 11. DTGA of TIpDEA xerogels in the %O <sub>2</sub> atmosphere indicated. ....	46
Figure 12. DSC of TIpDEA xerogels in the %O <sub>2</sub> atmosphere indicated. ....	47
Figure 13. Percent weight loss occurring within various temperature ranges as a function of % oxygen atmosphere. ....	52

Figure 14. Micro-Raman analysis of TIpDEA samples after STA treatment to 700°C. ..	53
Figure 15. XRD of single layer TIpDEA films produced with the spin speeds indicated (Tc = 600°C). .....	55
Figure 16. Cross-sectional SEM of 3 layer TIpDEA film deposited on MgO showing thickness is approximately 60nm/layer.....	56
Figure 17. XRD of two layer TIpDEA films produced with a five minute pyrolysis at the temperature indicated and full calcination between layers (Tc = 600°C). .....	58
Figure 18. XRD of two layer TIpDEA films produced with a five minute pyrolysis at the temperature indicated before calcination (Tc = 600°C). .....	59
Figure 19. XRD of three layer TIpDEA films pyrolyzed at the temperature indicated between layers (Tc = 600°C). .....	60
Figure 20. SEM images of TIpDEA films pyrolyzed at the given temperatures and then calcined to 600°C. Note the increased surface roughness of the film pyrolyzed at 300°C.....	61
Figure 21. XRD of 6 and 8 layer films prepared with Tp = 200°C between layers and a full calcination after the 3rd or 4th layer, respectively (Tc = 600°C). .....	62
Figure 22. XRD of three layer TIpDEA films (Tp = 200°C) calcined with the indicated heating rates (Tc = 600°C). .....	63
Figure 23. SEM image of three layer TIpDEA film prepared with Tp = 200°C between layers and a heating rate of 5°C/min (Tc = 600°C). .....	64
Figure 24. SEM image of three layer TIpDEA film prepared with Tp = 200°C between layers and a heating rate of 40°C/min. ....	64

Figure 25. XRD of three layer $Pb_{1-x}Ba_xTiO_3$ films with the compositions indicated (TIpDEA system, $T_p = 200^\circ C$ , $T_c = 600^\circ C$ ).....	65
Figure 26. Local piezoresponse-electric field hysteresis curve obtained from out-of-plane polarization via PFM for three layer PBT film deposited on Pt/Si <sub>3</sub> N <sub>4</sub> /Si (TIpDEA system, 3 layers, $T_p = 200^\circ C$ , $T_c = 600^\circ C$ ). [Data collected by Y.B. Park].....	68
Figure 27. PFM results showing actuation strain for PBT film deposited on Pt/Si <sub>3</sub> N <sub>4</sub> /Si (TIpDEA system, 3 layers, $T_p = 200^\circ C$ , $T_c = 600^\circ C$ ). [Data collected by Y.B. Park] .....	69
Figure 28. Atomic force microscopy of PBT thin film showing surface topography (left) and demonstration of 180° domain patterning using piezoresponse force microscopy (right). Light regions in the PFM image indicate polarization directed into the page, and dark areas show polarization directed out of the page. (TIpDEA system, 3 layers, $T_p = 200^\circ C$ , $T_c = 600^\circ C$ ) [Data collected by Y.B. Park] .....	70
Figure 29. XRD of initial attempts to produce BPO powders. (Ba-ac = barium acetate, Pb-ac = lead acetate, Pb-N = lead nitrate, AA = acetic acid, EG = ethylene glycol, $T_c = 600^\circ C$ ).....	76
Figure 30. Influence of added water on BPO formation. XRD of xerogels with $R_w = 0$ and 4, as indicated.....	78
Figure 31. TGA/DSC of dried BaPbO <sub>3</sub> xerogel.....	79
Figure 32. XRD of powders calcined in air at the temperatures indicated. The powder calcined at 550°C shows BaCO <sub>3</sub> (ICSD 05-0378) and PbO (05-0570). All others show BaPbO <sub>3</sub> . .....	80

Figure 33. XRD of single layer and three layer BaPbO <sub>3</sub> thin films deposited on MgO and calcined to 600°C in air.....	81
Figure 34. XRD of (a) BaPbO <sub>3</sub> thin film on MgO and (b) single layer Pb <sub>0.5</sub> Ba <sub>0.5</sub> TiO <sub>3</sub> film on BaPbO <sub>3</sub> /MgO showing preferred (001/100) orientation.....	83
Figure 35. Sol-gel system for producing LaNiO <sub>3</sub> thin films.....	85
Figure 36. Simultaneous thermal analysis (DSC/TGA) of LaNiO <sub>3</sub> xerogel and mass spectrometry data of volatiles released during heating (heating rate = 5°C/min, 20%O <sub>2</sub> /80%Ar).....	86
Figure 37. XRD of four layer LaNiO <sub>3</sub> deposited on Si <sub>3</sub> N <sub>4</sub> /Si with five minute pyrolysis at 400°C between layers and final calcination at 700°C for 2 hours with heating rate of 5°C/min.....	87
Figure 38. XRD of LaNiO <sub>3</sub> deposited on fused silica and calcined at the temperatures indicated. (4 layers, T <sub>p</sub> = 300°C) The amorphous hump seen at low 2-theta is due to the amorphous silica substrate.....	88
Figure 39. XRD of LaNiO <sub>3</sub> thin films deposited on a variety of substrates. (4 layers, T <sub>p</sub> = 400°C, T <sub>c</sub> = 700°C).....	91
Figure 40. Illustration of the orientation mechanism of LaNiO <sub>3</sub> . (top) Heterogeneous random nucleation occurs at the film-substrate interface. Light nuclei are those with the (100) plane parallel to the substrate and dark nuclei are those with (100) plane at an angle to the substrate. (middle) During growth, the (100) surfaces grow slower than planes with higher surface energy, resulting in unfavorably oriented dark nuclei growing faster vertically and taking on a triangular shape while favorably oriented	

light nuclei grow outward. (bottom) Outward growth of favorably oriented nuclei overtakes unfavorably oriented grains, leaving a (100)-oriented film.....	92
Figure 41. XRD of $\text{LaNiO}_3$ thin films deposited on Si(100) with the number of layers indicated ( $T_p = 400$ , $T_c = 700^\circ\text{C}$ ).....	94
Figure 42. Graphical representation of the previous table showing rapid decline in $\text{LaNiO}_3$ sheet resistance with increasing number of layers.....	95
Figure 43. Atomic force microscopy (AFM) of 4 layer $\text{LaNiO}_3$ films deposited on the substrates indicated. [Data courtesy Melanie Cole, Army Research Laboratory] ....	96
Figure 44. SEM image of 4 layer $\text{LaNiO}_3$ film deposited on Si (sol concentration 0.32M, $T_p = 400^\circ\text{C}$ , $T_c = 700^\circ\text{C}$ ).....	97
Figure 45. SEM image of 4 layer $\text{LaNiO}_3$ film deposited on MgO using sol with 0.22M concentration ( $T_p = 400^\circ\text{C}$ , $T_c = 700^\circ\text{C}$ ).....	98
Figure 46. SEM image of 4 layer $\text{LaNiO}_3$ film deposited on MgO using sol with 0.42M concentration ( $T_p = 400^\circ\text{C}$ , $T_c = 700^\circ\text{C}$ ).....	98
Figure 47. SEM images at 8 and 150k magnification of cracking in 4 layer $\text{LaNiO}_3$ film deposited on MgO using sol with 0.42M concentration ( $T_p = 400^\circ\text{C}$ , $T_c = 700^\circ\text{C}$ ).....	99
Figure 48. PBT on LNO on various substrates (4 layers LNO, $T_p = 400^\circ\text{C}$ , $T_c = 700^\circ\text{C}$ ; 3 layers PBT, $T_p = 200^\circ\text{C}$ , $T_c = 600^\circ\text{C}$ ).....	100
Figure 49. Effect of humidity on the crystallization of PBT produced using the TBuDEA system. (3 layer, $T_p = 200^\circ\text{C}$ , $T_c = 600^\circ\text{C}$ ). [Data collected by G. Sukul].....	102
Figure 50. XRD of 'best case' PBT thin film deposited on MgO (35% humidity) versus typical PBT film deposited on LNO/MgO using TBuDEA system (PBT: 3 layer, $T_p = 200^\circ\text{C}$ , $T_c = 600^\circ\text{C}$ ; LNO: 4 layer, $T_p = 400^\circ\text{C}$ , $T_c = 700^\circ\text{C}$ ).....	103

Figure 51. XRD of PBT thin films deposited on MgO and LNO/MgO as indicated under the same atmospheric conditions (PBT: TIpDEA system, 3 layer, $T_p = 200^\circ\text{C}$ , $T_c = 600^\circ\text{C}$ ; LNO: 6 layer, $T_p = 400^\circ\text{C}$ , $T_c = 700^\circ\text{C}$ ).....	104
Figure 52. XRD of 3 layer PBT films deposited on the substrates indicated and calcined at the stated temperatures. (PBT: TIpDEA system, $T_p = 200^\circ\text{C}$ , LNO: 4 layers, $T_p = 400$ , $T_c = 700^\circ\text{C}$ ).....	105
Figure 53. XRD of 3 layer PZT thin film deposited on MgO and LNO/Si, as indicated. XRD of the LNO/Si film before PZT deposition is also shown. (PZT: 3 layers, $T_p = 200^\circ\text{C}$ , $T_c = 600^\circ\text{C}$ ; LNO: 4 layers, $T_p = 400^\circ\text{C}$ , $T_c = 700^\circ\text{C}$ ).....	106
Figure 54. UV transmission spectrum for TIpDEA sol. ....	113
Figure 55. UV transmission spectrum for TBuDEA sol. ....	113
Figure 56. XRD of PBT thin films with and without UV treatment, as indicated.....	114
Figure 57. PBT sol injected into PDMS mold on glass slide showing ability to fill connecting channels from single injection point. The main channel is $50\mu\text{m}$ wide, and the two smaller branches are $40\mu\text{m}$ wide. ....	118
Figure 58. Channel filled with xerogel after drying showing cracking as function of channel width. (Dried $100^\circ\text{C}$ , 20 hours) Widest part is $50\mu\text{m}$ . ....	118
Figure 59. PBT deposited using capillary technique on 10mm square MgO substrate showing variety of line widths. Line widths from left to right: 10, 50, 100, and $500\mu\text{m}$ . ....	120
Figure 60. Thickest ( $500\mu\text{m}$ ) line in previous figure, close-up after calcination.....	120
Figure 61. XRD of PBT thin film on single crystal MgO and IBAD MgO/Si <sub>3</sub> N <sub>4</sub> /Si. (PBT: 3 layer, TIpDEA, $T_p = 200^\circ\text{C}$ , $T_c = 600^\circ\text{C}$ ).....	122

Figure 62. Process flow for producing partially released PBT/MgO/Si <sub>3</sub> N <sub>4</sub> membranes.	123
Figure 63. Process flow for final release of PBT/MgO/Si <sub>3</sub> N <sub>4</sub> membranes.....	124
Figure 64. PBT-coated TEM window (left) and schematic showing side view of structure (right). .....	125
Figure 65. XRD of stack structure LNO/PBT/LNO/Si(111). .....	127
Figure 66. LaNiO <sub>3</sub> film (2 layers) deposited on commercially purchased 6 x 6 Si <sub>3</sub> N <sub>4</sub> membrane array. ....	128
Figure 67. XRD of LaNiO <sub>3</sub> film (2 layers) deposited on 6x6 Si <sub>3</sub> N <sub>4</sub> membrane array....	128
Figure 68. XRD of 3 layer PBT films deposited on 2 layer LNO on commercially obtained Si <sub>3</sub> N <sub>4</sub> /Si arrays.....	129
Figure 69. Photograph of array after PBT deposition showing which membranes remained intact.....	130
Figure 70. Process flow for producing released PBT/LNO membranes on Si. ....	131
Figure 71. Die mask designed for producing released PBT/LNO membranes for electrical and mechanical testing.....	133
Figure 72. Partially released Si membranes produced using DRIE.....	134
Figure 73. Small (0.5mm) square membrane showing partial release from the Si substrate after 11 etch loops (20x magnification). .....	135
Figure 74. Cracking and rupture of partially released membrane in large square (1.5mm) membrane after 11 etch loops (20x magnification). .....	136
Figure 75. PBT thin films on LiF with the heating rates and number of layers indicated (T <sub>c</sub> = 600°C). .....	140

Figure 76. PBT thin films on LiF with the calcination temperatures indicated (HR = 5°C/min).....	140
Figure 77. PBT thin films deposited on NaCl(111) with the number of layers indicated (Tc = 600°C for 120 minutes in air, HR = 5°C/min).....	141
Figure 78. PBT thin films deposited on NaCl(100) and calcined at the temperatures indicated (HR = 1°C/min). ....	142
Figure 79. Optical microscope image of fresh cleaved NaCl(100) surface, 50x magnification. ....	143
Figure 80. Picture at 10x magnification showing micro interferometry of a released membrane of PBT(180nm)/LaNiO <sub>3</sub> (96nm)/Si <sub>3</sub> N <sub>4</sub> (100nm) showing vertical deflection of the film. The substrate is tilted with respect to the camera. Fringe spacing is 0.273µm. [Image courtesy Rongjing Zhang] .....	150
Figure 81. Schematic of TIpAc system procedure for producing PBT powders or thin films. ....	174
Figure 82. Schematic of TBuAc system procedure for producing PBT powders or thin films. ....	176
Figure 83. Schematic of TBuAc system procedure for producing PBT powders or thin films. ....	178
Figure 84. Schematic of TIpDEA system procedure for producing PBT powders or thin films. ....	181
Figure 85. Schematic of BPO system procedure for producing BaPbO <sub>3</sub> sol.....	182
Figure 86. Schematic of LNO system procedure for producing LaNiO <sub>3</sub> sol.....	183
Figure 87. AAC System: Powder XRD, R <sub>w</sub> = 4, varied Tc. ....	192

Figure 88. EG2NO <sub>3</sub> System: Powder XRD, $R_w = 0$ , varied $T_c$ .	194
Figure 89. EG2NO <sub>3</sub> System: Powder XRD, $T_c = 400^\circ\text{C}$ , varied $R_w$ .	195
Figure 90. EG2NO <sub>3</sub> System: TGA, $R_w = 0$ .	196
Figure 91. EG2NO <sub>3</sub> System: Powder XRD, $R_w = 0$ .	197
Figure 92. XRD of EG2NO <sub>3</sub> thin film ( $R_w = 0$ , $T_p = 150^\circ\text{C}$ , $T_c = 600^\circ\text{C}$ ).	198
Figure 93. Optical microscope image of EG2NO <sub>3</sub> film surface.	198
Figure 94. F3AC System procedure.	201
Figure 95. F3AC System: Powder XRD, $R_w = 4$ , varied $T_c$ .	202
Figure 96. TIpAc powder XRD, $R_w = 8$ , $RA = 4$ calcined at the temperatures indicated.	205
Figure 97. TIpAc system powder XRD, $T_c = 600^\circ\text{C}$ , $T_p = 450^\circ\text{C}$ , with heating rate indicated.	206
Figure 98. TIpDEA System: Powder XRD, $T_c = 500^\circ\text{C}$ , varied $R_w$ .	208
Figure 99. TIpDEA system: Powder XRD, $R_w = 4$ , varied $T_c$ .	209
Figure 100. STA with mass spectrometry data for TIpDEA (pure Ar atmosphere).	210
Figure 101. DTG of TIpDEA in pure Ar has peaks at $264^\circ\text{C}$ ( $-2.427\text{ J/g}$ ), $359^\circ\text{C}$ , and $576^\circ\text{C}$ ( $-0.3482\text{ J/g}$ ). The peak at $359^\circ\text{C}$ is not accompanied by a discernible DSC peak.	210
Figure 102. STA of TIpDEA in 5%O <sub>2</sub> atmosphere.	211
Figure 103. DTGA of TIpDEA (5%O <sub>2</sub> ) showing peaks at $258^\circ\text{C}$ ( $-4.174\text{ J/g}$ ), $358^\circ\text{C}$ ( $-0.1601\text{ J/g}$ ), and $576^\circ\text{C}$ ( $-1.057\text{ J/g}$ ).	211
Figure 104. STA with mass spectrometry data for TIpDEA in 10%O <sub>2</sub> atmosphere.	212

Figure 105. DTGA of TIpDEA in 10%O <sub>2</sub> showing peaks at 260, 474 (-93.14 J/g), and 579°C (+0.2053 J/g). There is also a slight shoulder at 435° and a broader peak at 346° that do not correspond to DSC events. ....	213
Figure 106. STA with mass spectrometry data for TIpDEA in 20%O <sub>2</sub> atmosphere. ....	214
Figure 107. DTG of TIpDEA in 20%O <sub>2</sub> shows clear peaks at 261°C (-17.59J/g), 423°C, 458°C (-98.68J/g), and 579°C (0.1431 J/g), which agrees well with DSC. The spike at 501°C is not accounted for. ....	214
Figure 108. STA with mass spectrometry data for TIpDEA in 50%O <sub>2</sub> atmosphere showing masses 2-42. ....	215
Figure 109. STA with mass spectrometry data for TIpDEA in 20%O <sub>2</sub> atmosphere showing masses 44-59. ....	216
Figure 110. DTG of TIpDEA in 50%O <sub>2</sub> atmosphere showing clear peaks at 251 (-9.489 J/g), 352, 434 (-99.07 J/g), and 581°C, as well as a spike at 228. The peaks 251 and 434 correspond well with DSC. The peak at 352 is unaccounted for, as is the small peak at 581°C. ....	217
Figure 111. STA of TIpDEA with 50%O <sub>2</sub> atmosphere using high flow rate of 120mL/min. ....	218
Figure 112. DTG shows clear peaks at 258 (-12.57 J/g), 351, 433 (-130.5 J/g), and 582°C. This corresponds well with DSC. ....	219
Figure 113. SEM image of 6 layer LaNiO <sub>3</sub> film deposited on fused silica with T <sub>p</sub> = 200°C. ....	220
Figure 114. SEM image of 6 layer LaNiO <sub>3</sub> film deposited on fused silica with T <sub>p</sub> = 300°C. ....	221

Figure 115. SEM image at lower magnification, showing extensive cracking on surface of 6 layer $\text{LaNiO}_3$ film deposited on fused silica with $T_p = 300^\circ\text{C}$ . .....	221
Figure 116. SEM image of 6 layer $\text{LaNiO}_3$ film deposited on fused silica with $T_p =$ $400^\circ\text{C}$ .....	222
Figure 117. SEM image of 6 layer $\text{LaNiO}_3$ film deposited on fused silica with $T_p =$ $500^\circ\text{C}$ .....	222
Figure 118. SEM image of 1 layer $\text{LaNiO}_3$ film deposited on Si ( $T_p = 400^\circ\text{C}$ ).....	223
Figure 119. SEM image of 2 layer $\text{LaNiO}_3$ film deposited on Si ( $T_p = 400^\circ\text{C}$ ).....	224
Figure 120. SEM image of 3 layer $\text{LaNiO}_3$ film deposited on Si ( $T_p = 400^\circ\text{C}$ ).....	224
Figure 121. SEM image of 4 layer $\text{LaNiO}_3$ film deposited on Si ( $T_p = 400^\circ\text{C}$ ).....	225
Figure 122. SEM image of 4 layer $\text{LaNiO}_3$ film deposited on Si without pyrolysis step ( $T_c = 700$ ). .....	226
Figure 123. SEM image of 4 layer $\text{LaNiO}_3$ film deposited on Si with $T_p = 400$ , $T_c = 800$ . .....	227
Figure 124. SEM image of 4 layer $\text{LaNiO}_3$ film deposited on $\text{Si}_3\text{N}_4/\text{Si}$ with only $T_p = 400$ between layers, and final calcination at $T_c = 700$ with $\text{HR} = 5^\circ\text{C}/\text{min}$ . .....	228

## Tables

Table 1. Hydration enthalpies of commonly used titanium alkoxides, as reported in [61]. .....	18
Table 2. Chelating agents studied for PBT sol-gel synthesis.....	20
Table 3. Lattice parameter and thermal coefficient of expansion for selected substrates.	23
Table 4. Metallic sources, solvents, and chelating agents investigated for sol-gel PBT.	26
Table 5. Summary of sol-gel systems investigated. Shading highlights differences between systems.....	28
Table 6. Four sol-gel systems suitable for depositing thin film PBT. ....	30
Table 7. Composition of annealing atmosphere and flow rates.....	44
Table 8. Weight loss and endo-/exotherms observed between 100-600°C for the TIpDEA system, with %O <sub>2</sub> atmosphere indicated (exotherms in italics are questionable).....	45
Table 9. Percent weight loss in Region I (100-285°C) for the indicated %O <sub>2</sub> atmosphere. .....	48
Table 10. Percent weight loss in Region II (285-380°C) for the indicated %O <sub>2</sub> atmosphere. ....	49
Table 11. Percent weight loss in Region III (380-550°C) for the indicated %O <sub>2</sub> atmosphere. ....	50
Table 12. Percent weight loss in Region IV (550-600°C) for the indicated %O <sub>2</sub> atmosphere. ....	51
Table 13. Summary of lattice parameters and resistivities of several conductive oxide materials. Lattice parameters of PBT are included for comparison.....	71

Table 14. Surface resistance of BaPbO <sub>3</sub> thin films calcined at 600°C.....	82
Table 15. Summary of LaNiO <sub>3</sub> sol-gel systems investigated. ....	85
Table 16. Orientation factors (the sum of the intensities of (100) and (200) LaNiO <sub>3</sub> peaks divided by the intensity of all peaks) and sheet resistances of LaNiO <sub>3</sub> films deposited on fused silica prepared using the pyrolysis temperatures (Tp) indicated. (6 layers, Tc = 700°C).....	89
Table 17. Orientation and conductivity of the LaNiO <sub>3</sub> films deposited on various substrates. ....	93
Table 18. Orientation and sheet resistance of LaNiO <sub>3</sub> thin films with the indicated number of layers (on Si, Tp = 400°C, Tc = 700°C). ....	94
Table 19. Orientation of LNO and PBT on various substrates. ....	101
Table 20. Properties of LiF, NaCl, and Pb <sub>0.5</sub> Ba <sub>0.5</sub> TiO <sub>3</sub> . ....	138
Table A-1. Solubility of Barium Precursors .....	184
Table A-2. Solubility of Lead Precursors .....	186
Table A-3. Solubility of Lead and Barium Precursors Together .....	187
Table A-4. PBT Sol-gel Systems Investigated .....	188
Table A-5. Pros and Cons of Various PBT Sol-gel Systems .....	189
Table A-6. Further Details of Selected PBT Sol-gel Systems .....	190

## I. Introduction

Ferroelectric materials, which are characterized by permanent macroscopic reversible polarization, are of considerable interest for use in a wide range of dielectric and electromechanical applications. The polarization of a ferroelectric material can be altered through the application of a mechanical stress or electric field. Valued for their dielectric, pyroelectric, and piezoelectric properties, ferroelectric materials have been integrated into a wide range of products, from pressure sensors to non-volatile FERAM and tunable microwave devices [1-5]. Such applications generally capitalize on the significant change in dielectric constant associated with the ferroelectric-paraelectric transition near the Curie temperature. The work reported here represents part of a larger effort to exploit the *mechanical* properties of ferroelectrics, namely the large strains induced via domain switching.

For tetragonal ferroelectrics, switching domains between  $a$  and  $c$ -axis orientation produces a mechanical strain directly related to the  $c/a$  ratio. It is thus valuable to consider systems with large  $c/a$  ratios for potential use as large strain sensors and actuators. Lead titanate ( $\text{PbTiO}_3$ ), or PT, is known to have a very high  $c/a$  ratio (1.063). If it were possible to harness all of the strain of an  $a$ -to- $c$  domain switch, a 6% strain would be obtained, remarkably higher than the 0.1% strain typical of piezoelectric actuators in common use. However, PT requires a large coercive field to induce domain wall motion and is prone to brittle fracture. Bulk barium titanate, with  $c/a = 1.01$  ( $\text{BaTiO}_3$ , BT), in contrast, has been shown to exhibit usable strains of 0.9% on domain

switching [6, 7]. It is hoped that a solid solution of lead barium titanate ( $\text{Pb}_{1-x}\text{Ba}_x\text{TiO}_3$ , PBT) will provide intermediate strains while retaining mechanical integrity.

In order for PBT to be successfully utilized in microactuation applications and also be integrated into silicon device technology, it is necessary to synthesize high-quality epitaxial thin films at moderate temperatures. Moderate crystallization temperatures are desired to facilitate easy integration into current semiconductor microelectromechanical (MEMS) processing, where high temperatures can cause layers to melt together and doping levels to be redistributed. While there are several widely used techniques for fabricating oxide thin films, including physical/chemical vapor deposition, ion beam sputtering, electron beam evaporation, and pulsed laser ablation, the sol-gel method has been selected here because of its potential for low temperature crystallization and the possibility of low cost fabrication. In the sol-gel process, controlled hydrolysis of dissolved metalorganic precursors (forming M-OH bonds) followed by a condensation reaction (forming M-O-M or M-OH-M bonds), resulting in the formation of a three dimensional network of particles [8]. Key challenges in the sol-gel synthesis of PBT are the identification of a solvent system in which multiple metalorganic precursors are mutually compatible and the preparation of a sol stable against uncontrolled hydrolysis. Moreover, while sol-gel and other solution techniques have been widely used for the fabrication of ferroelectric films of  $\text{PbTiO}_3$  and  $\text{BaTiO}_3$  [9-14], few studies of solution deposition techniques to prepare PBT thin films have been reported [15, 16]. Here, a parametrically optimized sol-gel route for the low temperature crystallization of powder

and thin film PBT is detailed, and the impact of various process parameters on crystallization behavior is examined.

The goal is to crystallize phase pure, highly oriented thin film PBT at low temperatures, and then to integrate the film into a variety of test structures. This can be broken down into three development phases: (1) producing a stable sol, (2) using the sol to produce oriented thin films, and (3) integrating the films into useful structures.

### **Scope of the Thesis**

While sol-gel and other solution techniques have been widely used for the fabrication of ferroelectric films of  $\text{PbTiO}_3$  and  $\text{BaTiO}_3$ , few studies of solution deposition techniques to prepare PBT thin films have been reported. Here, a series of parametrically optimized sol-gel routes for the low temperature crystallization of powder and thin film PBT is described. A systematic approach to materials engineering via sol-gel processing is followed in order to maximize the usability of results as they apply to other related materials systems. By comparing results between systems, the relevance of various processing parameters, particularly solution chemistry, was determined. The particular chelating agent used was found to have a large effect on sol stability and phase purity, and an understanding of the roles played by chelating agents is discussed in detail.

Suitable precursors were identified, and a low cost and highly reliable process for producing PBT is described in detail. A detailed and optimized procedure for depositing oriented PBT thin films on MgO via spin coating is also given.

Efforts towards integrating PBT into useful devices and structures are also detailed, including a summary of efforts to use ion beam assisted deposition of MgO thin films on Si<sub>3</sub>N<sub>4</sub>/Si to provide orientation on a Si-based substrate. Additional work towards the integration of this material into semiconductor processing techniques is also presented, including the investigation of conductive oxide electrodes including barium metaplumbate (BaPbO<sub>3</sub>) and, particularly, lanthanum nickelate (LaNiO<sub>3</sub>). A method to deposit highly oriented LaNiO<sub>3</sub> on a variety of amorphous and crystalline substrates is detailed, which enables the production of highly oriented PBT thin films on a wide variety of substrates without additional buffer layers. This breakthrough allows for highly crystalline, highly oriented ferroelectrics to be deposited on a conducting oxide electrode directly on Si, which will greatly improve fatigue characteristics of the ferroelectric, and speed integration of ferroelectric thin films into MEMS process.

## **I.1. Ferroelectrics**

Ferroelectric materials are crystalline solids that have a spontaneous polarization direction below a certain temperature, known as the Curie temperature. At the Curie temperature ferroelectric materials undergo a phase transition. Above the Curie temperature, a ferroelectric material is cubic, while below the Curie temperature a non-cubic polar crystal structure forms. This polar structure is generally further subdivided into domains, each having a particular polarization direction. For a tetragonal unit cell in the absence of external fields, this polarization can exist in six energetically equivalent

states [Figure 1]. Because these states remain stable until an external force or electric field is applied, ferroelectrics have been used in a wide range of applications. One of the most prominent applications is ferroelectric non-volatile random access memory (NVRAM or FERAM). Polarization states are read as 1's and 0's, which provide a long-lasting record of information without requiring the constant application of an electric field. NVRAM has been used to reduce power requirements in many portable devices. The large change in the pyroelectric coefficient near the Curie temperature phase transition is also exploited in a host of applications, including infrared detectors and tunable microwave filters [17-19]. Ferroelectrics have also been used in capacitors, acoustic transducers, waveguides, optical memory, cameras, and chemical detectors [20-26].

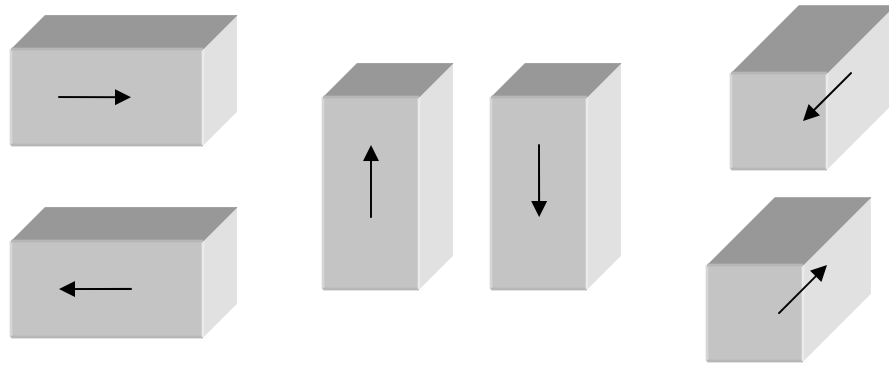


**Figure 1.** The six variants of a ferroelectric tetragonal unit cell. The arrows represent the polarization direction.

### **I.1.1. Ferroelectric vs. Piezoelectric**

Ferroelectric materials are a subset of the piezoelectric class of materials. Piezoelectric materials develop a polarization in response to an applied stress and produce strains when exposed to electric fields. They are commonly used as transducers and have found wide application in a variety of sensor and actuator applications. Though all ferroelectrics are also piezoelectrics, not all piezoelectrics are ferroelectric. The most common example of a piezoelectric that is not ferroelectric is quartz. While ferroelectrics maintain their domain structure once a coercive electric field or stress is removed, piezoelectrics that lack the ferroelectric property return to a randomly polarized state.

### **I.1.2. Domain Switching**

The domains in ferroelectrics with a tetragonal unit cell can consist of any of the six polarization variants shown in Figure 1. The polarization directions of the variants differ from each other by either  $90^\circ$  or  $180^\circ$ , and thus the boundaries between domains of different variants are referred to as  $90^\circ$  or  $180^\circ$  domain walls, respectively. Through application of a stress, coercive electric field, or combination of the two, the polarization direction of ferroelectric domains can be aligned along a preferred direction through a process known as poling. Once the field and/or stress is removed, the domains will remain aligned until an outside force or field acts upon the material.

Once a ferroelectric material has its domains aligned, large strains can be obtained through the ferroelastic switching of domains from one orientation to another non- $180^\circ$  variant. For a tetragonal unit cell, for example, the strain obtained from switching an  $a$

domain to a  $c$  domain is given by:  $c/a - 1$  (strain = elongation / unit length =  $(c-a)/a = c/a - 1$ ). The larger the difference between  $a$  and  $c$ , the larger the strain. Barium titanate, a well-known ferroelectric with a tetragonal unit cell and  $c/a = 1.01$ , has been shown to produce strains of 0.9% under combined electromechanical loading [6]. Lead titanate has a  $c/a$  ratio of 1.06 and would presumably produce larger strain; however, it is prone to brittle fracture and requires a larger electric field to induce switching. By using solid solution lead barium titanate, the  $c/a$  ratio presumably can be varied between 1.01 and 1.06. Studying this solid solution, we can determine the maximum strains attainable without mechanical failure. If these materials can then be integrated into useful devices and structures, such large strain capability would enable a host of new sensor and actuator applications and have an enormous impact on the future of microelectromechanical systems (MEMS).

A ferroelectric thin film micropump has been suggested as a preliminary device concept that takes advantage of the large strains associated with domain switching [Figure 2]. The device consists of a uniformly (100) or (001)-oriented ferroelectric thin film, which is fully released in a square region. Upon application of an electric field, the film undergoes  $90^\circ$  domain switching, forming domain walls as shown in Figure 2, thus deforming out of plane in a tent-like structure. The in-plane stress of the film provides a restoring force to return the pump to its rest position once the field is removed. When used with appropriate check valves, this reversible deformation can be used as a microfluidic pump.

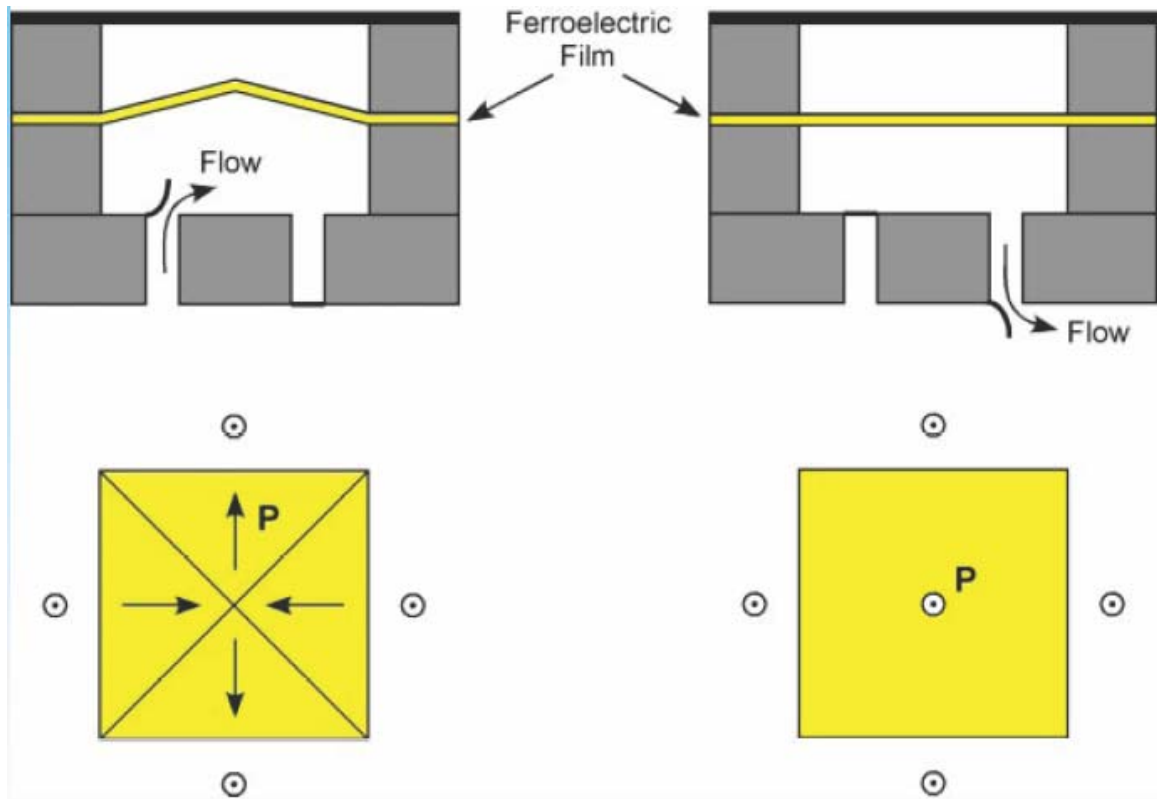


**Figure 2.** Ferroelectric thin film micropump schematic. Polarization direction indicated by arrows. [Image courtesy Kaushik Bhattacharya]

### I.1.3. PBT vs. PZT

Much ferroelectric research has focused on lead zirconate titanate ( $\text{PbZr}_x\text{Ti}_{1-x}\text{O}_3$ , PZT), which consists of a mixture of tetragonal  $\text{PbTiO}_3$  and rhombohedral  $\text{PbZrO}_3$ . PZT has been widely used as an active material layer in MEMS, and deposition methods involving sol-gel, pulsed laser deposition (PLD), sputtering, metal organic chemical vapor deposition (MOCVD), and others have been widely investigated, though crystallization temperatures are generally high and integration of the material into standard semiconductor processes is extremely limited [22, 27-32]. The advantage of PBT over

PZT is most apparent through comparing their strains. Strains of 0.1% are typically achieved with PZT, whereas PBT is expected to produce strains an order of magnitude larger.

The PBT system has another, more subtle advantage over the more commonly studied PZT. In the PZT system, large piezoelectric strains are attainable only near a compositional morphotropic phase boundary, where the tetragonal and rhombohedral phases are both present. Off-stoichiometric PZT suffers from greatly diminished piezoelectric strains. Even small lead loss can be detrimental to such a delicately balanced system. In the case of PBT, however, the strains achievable are expected to be linearly tied to composition. The large strains are derived from switching the tetragonal crystal structure between variants and are not dependant on finding a compositional “sweet spot.” Thus, small compositional fluctuations are considerably less important in the PBT system, as films are expected to be actively switchable throughout the entire solid solution range.

Our computational collaborators also benefit from the relative simplicity of the PBT system compared to multi-phase ferroelectrics like PZT. In terms of modeling, the advantage of a single phase material is obvious. Thus, PBT provides an excellent opportunity for concurrent theoretical study with experimental validation.

## I.2. Experimental Method

In order for PBT to be successfully utilized in microactuation applications and also be integrated into silicon device technology, it is necessary to synthesize high-quality oriented thin films at moderate temperatures. Moderate crystallization temperatures are desired to facilitate integration with standard semiconductor processing techniques. While there are a variety of techniques for fabricating oxide thin films, including physical vapor deposition, ion beam sputtering, electron beam evaporation, and pulsed laser ablation, the sol-gel method has been selected here because of the potential for meeting the objectives of low temperature crystallization and low cost fabrication.

### I.2.1. Introduction to Sol-gel

Historically, sol-gel synthesis was synonymous with silica. First widely developed in the 1960s and expanded to study perovskite films in the mid 1980s, the sol-gel field has since expanded to include almost any wet chemical route to produce powders and thin films through drying and subsequent heat treatment [33, 34]. Indeed, there are a number of competing definitions of a sol-gel process. By the most general definition, the sol-gel process involves the controlled hydrolysis of dissolved metalorganic precursors ( $M(OR)_n + x H_2O \rightarrow M(OH)_x(OR)_{n-x} + x ROH$ ) followed by a condensation reaction ( $M-OR + M-OH \rightarrow M-O-M + R-OH$  or  $M-OH + M-OH \rightarrow M-O-M + H-OH$ ), resulting in the formation of a three dimensional network of particles [8, 35]. Depending on the type of precursors, the temperatures and pressures used, and the extent that gelation is or is not involved, the technique can be variously termed sol-gel, metalorganic solution deposition

(MOSD), chemical solution deposition (CSD), chelate method, or metalorganic decomposition (MOD). The difference between these techniques is largely semantic. Most involve the dissolution of precursors into a common solvent (forming a sol), followed by hydrolysis and polycondensation reactions, which form a gel network. A broader term, ‘soft solution processing,’ has been suggested to encompass all of the above and more, but has yet to gain a significant following [36, 37]. Schwartz [34] distinguishes between *sol-gel* methods that are 2-methoxyethanol-based systems, and *hybrid sol-gel* or *chelate* methods that involve chelating agents to modify the metal alkoxide. Following these conventions, the techniques in this thesis are most appropriately referred to as *hybrid sol-gel* or *chelate* methods, in the case of lead barium titanate. The methods used for lanthanum nickelate conductive oxide electrodes, which are 2-methoxyethanol-based, represent a more conventional sol-gel approach.

After deposition, thermal treatments are used to crystallize the sol-gel film. During heat treatment, crystal nuclei can form either within the bulk of the film or at the film-substrate interface. These two types of nucleation are referred to as *homogeneous* (or *bulk*) and *heterogeneous* nucleation, respectively. Bulk nucleation is generally associated with randomly oriented films as crystalline growth in regions far from the surface and substrate is energetically equivalent in all directions. For grains nucleating near a substrate, however, growth of the crystalline orientation associated with the lowest interface energy is favored [38]. Thus, preferentially oriented thin films can be produced via sol-gel with heterogeneous nucleation at a lattice-matched substrate. Some authors suggest heterogeneous nucleation is aided by the use of very thin films (thickness <

average grain size), which ensures nucleation occurs ‘near’ the substrate, or faster heating rates that can provide a higher temperature near the substrate to encourage heterogeneous nucleation (and provide less energy to surmount the nucleation barriers in the bulk) [38-40]. The use of seed layers to encourage nucleation at the substrate is also widely reported [41-44]. It is important to note that these two nucleation mechanisms are not mutually exclusive, and oriented films can sometimes be obtained even without pure heterogeneous nucleation. In some cases with mixed homo- and heterogeneous nucleation, heterogeneously nucleated crystal grains grow to consume the bulk-nucleated, randomly oriented grains to eventually produce oriented films [43, 45].

### **I.2.2. Advantages of Sol-gel over Other Techniques**

Sol-gel is a widely used technique for a variety of reasons. First, the use of a sol-gel process provides enhanced homogeneity. Since all of the precursors are mixed in the liquid state, homogeneity is expected on a molecular scale [46]. Sol-gel is also desirable for its versatility. Once a stable sol is produced, conformal coatings can be produced for a wide range of substrate geometries through spin, dip, or spray coating. For some exceptionally stable sols, thin films can be prepared from stock solution days, weeks, or even months later without degradation [23]. Further, producing doped materials via sol-gel is generally straightforward, as dopants can be dissolved in the sol to produce a homogeneous dopant distribution.

Compositional control is also facilitated by sol-gel, as precursor stoichiometry is directly reflected in the resulting materials [47]. In contrast, chemical vapor deposition (CVD) stoichiometry is controlled through indirect mechanisms, chiefly through controlling precursor gas flow rates in a control loop, and sputtering stoichiometry is determined by target composition, which is not, however, the same as film composition. In both cases, experimental determination of ideal flow rates or target composition and O<sub>2</sub> partial pressures is required to get desired stoichiometry. Other physical methods, such as rf magnetron sputtering, also tend to suffer poor stoichiometric control and low deposition rates [48]. Unlike sputtering, sol-gel is not limited to line-of-sight deposition. Recently, the adaptation of ink jet printers for use in direct sol-gel patterning has been reported, and sols might also be of use in the emerging field of AFM dip-pen nanolithography [49, 50].

Sol-gel processing is often a low cost technique involving minimal equipment, especially when compared with more capital-intensive high vacuum techniques such as CVD and molecular beam epitaxy (MBE). It is also considered more environmentally friendly than vapor techniques, which require more energy to vaporize the precursors as well as more sophisticated containment mechanisms for toxic byproducts [37, 46].

### **I.2.3. Sol-gel Processing of BT, PT, and PBT: Literature Survey**

Two approaches have been recently pursued in the literature as a means of crystallizing the end-member barium titanate from sol-gel methods at temperatures close to ambient. The first, demonstrated by Frey and Payne [51], involves the use of barium and titanium

alkoxides that are relatively stable against rapid hydrolysis and, therefore, can be prepared with a high water to metal cation ratio ( $R_w$ ) for the gelation step. The high water content apparently ensures that all metal alcohol ligands are completely replaced with metal oxygen bonds during gel formation, and all alcohol byproducts are evaporated during a drying step carried out under mild heating (50-125°C). By eliminating organic components during drying, barium carbonate, an intermediate product that otherwise requires high temperature calcination for conversion to the perovskite phase, is avoided. Crystallization, using barium and titanium methoxyethoxides dissolved in 2-methoxyethanol, has been reported to occur at temperatures as low as 120°C. The second approach, developed by Kuwabara and co-workers [13], relies on the preparation of highly concentrated alkoxide solutions, without concern for the particular ligand group used. Such solutions yield very dense gel-structures, which, for reasons that are not entirely obvious, readily crystallize at low temperatures. Crystallization at temperatures as low as 50°C has been obtained when gels (prepared as thin films) were aged under water/alcohol saturated atmospheres, although no preferential orientation resulted [52].

Low temperature crystallization of the second end member in the PBT system, lead titanate, via sol-gel methods has been explored to a much lesser extent. The most important demonstration has been that of Selvaraj et al. [10], who obtained oriented thin-film  $\text{PbTiO}_3$  from solutions of lead acetylacetonate and titanium isopropoxide in 2-methoxyethanol at temperatures as low as 425°C. The use of lead acetylacetonate as opposed to the more typical lead acetate trihydrate apparently ensured the absence of any water from the solution prior to the hydrolysis step and led to more stable gels. It is

likely that the acetylacetonate ligand also served as a chelating agent for the titanium in the system, further stabilizing the system. It is not entirely obvious why stable gels should result in lower temperature crystallization.

Synthesis of PBT through sol-gel methods has been studied to an even lesser extent. Meng et al. [53] examined grain size effects on Curie temperature for sol-gel prepared powders over the entire range of  $\text{Pb}_{1-x}\text{Ba}_x\text{TiO}_3$ . Few synthetic details were provided, and crystallization was carried out at unspecified temperatures in the range of 500-900°C. More recently, Giridharan and Jayavel [15] reported the synthesis of  $\text{Pb}_{0.8}\text{Ba}_{0.2}\text{TiO}_3$  thin films via a sol-gel route. The starting materials were barium acetate, lead acetate trihydrate, and titanium butoxide as cation sources, acetic acid as the solvent, and 2-methoxyethanol as the chelating agent. Complete crystallization of films required calcination temperatures of  $\sim 650^\circ\text{C}$  (with the onset of crystallization at  $400^\circ\text{C}$ ), and films showed a random orientation on the Pt-coated Si and fused quartz substrates utilized. Little rationale for the particular chemical system or substrates selected was provided.

The studies of the end-member compounds suggest competing approaches to sol-gel systems that yield crystalline products at low temperatures, which cannot be simultaneously implemented: incorporation of high water content to avoid carbonate formation; preparation of highly concentrated solutions; and use of an anhydrous lead precursor. Furthermore, the precursors and solvent implied by those earlier investigations, barium methoxyethoxide, titanium methoxyethoxide, lead acetylacetonate, and methoxyethanol, were found here to be incompatible. That is, a transparent sol based

on these compounds could not be prepared. In light of this initial result, an extensive survey was carried out to determine a tenable combination of metal sources, chelating agents, and solvents, and is documented in Chapter II.

#### **I.2.4. Parameters Involved in Sol-gel**

The number of parameters affecting the sol-gel process presents both a strength and weakness of the technique. Such parameters include choice of starting materials, solvent selection, concentration of reagents, order of mixing, mixing times and temperatures, and particular thermal treatment used, to name only a very few [27]. Indeed, references abound regarding the affect of processing parameters on sol-gel processes [33, 45, 54-58]. The number of parameters involved reflects the versatility of the sol-gel method, as it can be adapted as necessary for each material. However, it is difficult to determine exactly how each of the parameters interacts, and generally optimization is done through rote experiment. A carefully controlled study, as is presented here, allows for a deeper understanding of these interactions, and the gained insight allows a more predictive accounting of processing parameters capable of shortening development time for new sol-gel systems.

The sheer number of processing parameters also presents difficulty when sol-gel results are published in literature. In most articles, few synthetic details are given. Thus, it is frequently difficult to ascertain whether the published conclusions apply universally or only within the controlled setting of the authors' lab. It is often impossible to distill an

entire procedure from published literature, and occasionally the only description given is a listing of starting reagents. Thus, reproducing published experiments is akin to trying to craft a complicated recipe given only a list of ingredients. Only in rare instances can one find a full accounting of synthetic details. Thus, much effort was taken to provide for a full accounting of synthetic details in this work, and a strict systematic approach was taken towards parametric optimization.

### **I.2.5. Selection of Precursors**

The most commonly used metallic precursors in sol-gel are metal alkoxides with the chemical structure  $M(OR)_n$  where M is a metal cation (in this case, Ti). Alkoxides are favored for use in sol-gel processes due to their high reactivity and capability of forming desired phases at low processing temperatures. During hydrolysis, alkoxides favor the formation of M-O-M bonds, helping to preserve homogeneity throughout the gelation process. There has been some progress in the development of multiple metal alkoxides, and there is strong indication that a multiple metal alkoxide would provide very low processing temperatures and excellent homogeneity as M'-O-M bonds would form during condensation [59]. However, mixed metal alkoxides are expensive and difficult to handle. They are generally very sensitive to even trace amounts of moisture and tend to decompose rapidly. Furthermore, for the PBT system, there is no known single Pb-Ba-Ti alkoxide precursor, and the individual alkoxides are not mutually compatible. Titanium

alkoxides, however, are readily available [60].<sup>1</sup> Thus, a hybrid alkoxide route is taken here, involving titanium alkoxides with lead and barium salts.

Titanium alkoxides, though easy to obtain, are generally not stable when exposed to atmospheric moisture. The hydration enthalpies of the most common titanium alkoxides are given in Table 1 below, as originally reported by Golubko et al. [61]. The value for titanium isopropoxide is notably the largest, and this is attributed to its being a monomeric species (i.e., there is no oligomeric bonding between the alkoxide molecules). Since titanium isopropoxide lacks oligomeric bonds, the monomers can be attacked from all sides by water without first undergoing depolymerization. Titanium butoxide and titanium ethoxide are trimeric (i.e., the fundamental unit consists of three identical oligomerically bonded monomers). Thus, for these two alkoxides, significant energy is expended breaking the oligomeric bonds before hydrolysis can proceed, leading to a lower hydration enthalpy [61].

**Table 1.** Hydration enthalpies of commonly used titanium alkoxides, as reported in [61].

	<b>Hydration Enthalpy (kJ/mol)</b>
<b>Titanium Butoxide (TBu)</b>	-19.3
<b>Titanium Ethoxide (TEt)</b>	-14.2
<b>Titanium Isopropoxide (TIp)</b>	-64.9

In order to stabilize titanium precursors against rapid decomposition, chelating agents are often used to modify the titanium. Chelating agents achieve this by either physically

<sup>1</sup> The first metal alkoxide, titanium tetraethoxide, was reported in 1875.

surrounding the Ti cation in solution (steric hindrance), or bonding directly with it to lower its chemical reactivity (inductive effect).

### **I.2.5.1. Chelating Agent Selection**

The most widely reported chelating agent used for titanium in the preparation of widely studied PZT is acetylacetonone (also known as 2,2-pentanedione). Acetylacetonone (acac) substitutes for some or all of the alkoxide ligands, and since acac-ligands are not readily hydrolysable, the overall hydrolysis rate of the chelated sol is lowered. The ratio of acac:Ti has been shown to have a profound effect on hydrolysis rate, particle size, and the condensation pathway [59, 62-64]. It is important to note, however, that complete removal of the alkoxy ligands is generally not possible under neutral conditions, even in the presence of excess water [64]. Further, it has been shown that acac-ligands remain tightly bound to the metal cation after hydrolysis and condensation, and can necessitate high temperatures for complete removal [34]. Indeed, the presence of acac-ligands after hydrolysis and condensation has been linked to a dependence on condensed particle size with chelating agent:titanium molar ratio.

Acetic acid has also been widely used to reduce the reactivity of titanium alkoxides [27, 33, 65-67]. Gelation and precipitation in sols containing titanium alkoxides can be suppressed with the addition of moderate amounts of acetic acid; however, when the acetic acid:titanium ratio is large, insoluble acetate species can be formed [67-69]. Hasenkox suggests  $\text{TiO}_2$  particles form as acetate precipitates decompose, preventing

direct crystallization into the perovskite phase, and increasing inhomogeneity in the film [68]. Thus, the proper acetic acid:titanium ratio is crucial to production of homogeneous films when acetic acid is used as a chelating agent.

Another chelating agent, diethanolamine (DEA), has been found to be useful in the production of  $\text{TiO}_2$  via sol-gel processes [70-74]. Use of diethanolamine in ferroelectric sol-gel synthesis, however, has been reported to a lesser extent [9, 23, 75-77]. DEA is a low-melting solid and has a basic pH. DEA was found to provide TIP and TBU with extreme stability against hydrolysis.

The chemical formulas and boiling points for these three chelating agents are given in Table 2.

**Table 2.** Chelating agents studied for PBT sol-gel synthesis.

	<b>Chemical Formula</b>	<b>Boiling Point</b>
<b>Acetylacetone</b>	$\text{CH}_3\text{COCH}_2\text{COCH}_3$	140°C
<b>Diethanolamine</b>	$\text{NH}(\text{CH}_3\text{CH}_2\text{O})_2$	217°C
<b>Acetic Acid</b>	$\text{HOOCCH}_3$	118°C

### **I.2.5.2. Solvent Selection**

The choice of a solvent is primarily driven by the need to identify a medium in which Ba, Pb, and Ti species are mutually compatible. Secondary considerations include viscosity, availability, stability, and toxicity. A number of different solvents suitable for sol-gel processing have been reported in literature, including acids, alcohols, glycols, diols, and alkanolamines.

The most widely reported sol-gel systems involve 2-methoxyethanol (2-MOE) as a solvent. However, 2-methoxyethanol is very toxic to humans [14]. It further requires multiple time-consuming distillation steps that necessitate a rotary evaporation system. (Where possible, methods were adapted to use hotplate/stirrer techniques rather than rotary evaporation.) Alternate solvents were thus considered to reduce the cost, complexity, and toxicity of synthesis.

Simple alcohols were generally found to be incapable of co-dissolving lead and barium species. Their use in sol-gel ferroelectric literature is often relegated to dilution of sols, rather than as a primary solvent.

Diols, glycols, and alkanolamines were found to be particularly attractive as solvents. In addition to being able to co-dissolve the precursors, glycols and diols generally have a higher viscosity than alcohols, enabling the production of thicker films through spin coating [14]. They have also been shown to aid in the preparation of denser, crack-free films [27]. Ethylene glycol, in particular, has been used variously as a solvent and

additive. Yi, for example, uses it to “prevent cracking and improve surface smoothness” of PZT films prepared using acetic acid as a solvent [27]. Diols are known to form complexes with titanium leading to highly polymeric species [78]. They have the further benefit of being less moisture-sensitive (than 2-MOE, for example) and relatively stable in air.

Additional detailed discussions of precursor selection are available in the literature [43, 59]. In this work, many solvents were investigated empirically, and ultimately ethylene glycol was chosen as the ideal solvent for PBT systems, acetic acid was used for BaPbO<sub>3</sub>, and 2-methoxyethanol was used for LaNiO<sub>3</sub>.

### **I.2.5.3. Substrate Selection**

In order to produce oriented thin film PBT, heterogeneous nucleation at a lattice-matched substrate is desired. Cubic magnesium oxide (MgO) single crystals ( $a = 4.21\text{\AA}$ ) are readily attainable commercially and provide good lattice matching with PBT. Further, MgO has been widely used to produce oriented ferroelectric films, including BaTiO<sub>3</sub> and PbTiO<sub>3</sub> [26, 79, 80]. The thermal coefficients of expansion (TCE) of MgO and PBT also compare favorably and place the film under compressive stress on cooling, favoring c-axis orientation [26, 54, 81]. Prior to use, MgO substrates were cleaned by annealing at high temperatures in a tube furnace to provide the best growth surface, as demonstrated in [82, 83].

The lattice parameters and TCEs of several commonly used substrates are given below (Table 3).

**Table 3.** Lattice parameter and thermal coefficient of expansion for selected substrates.

	<b>a</b> <b>(cubic phase)</b>	<b>TCE</b> <b>(<math>\times 10^{-6}</math>)</b>	<b>Reference</b>
<b>MgO</b>	4.21	14.8	[84], [26, 79, 80, 85]
<b>SrTiO<sub>3</sub></b>	3.95	11.7	[56, 86]
<b>Pt</b>	3.91	9.6	[86], [87, 88]
<b>Si</b>	5.43	2.6	[84, 89]
<b>Fused Silica</b>	N/A	0.5	[90], [2, 23]

#### **I.2.5.4. Deposition Method**

There are many methods available to produce thin films from stable sols. Spin coating and dip coating are perhaps the most common methods used to produce sol-gel films [91]. Spin coating involves dispensing sol onto a substrate mounted on a rotating chuck, and held in place by a vacuum. Film thickness is determined by spin speed, with faster rotation producing thinner films as excess sol is cast off due to higher centripetal force. Film thickness uniformity is excellent; however, some edge effects can result if substrates are not round. Efforts to reduce such edge effects are well-documented in literature [92, 93].

Dip coating involves immersing the substrate into a sol and withdrawing it at a constant rate, fully coating all sides of the substrate [77]. Films are somewhat less uniform than those produced via spin coating due to gravitational gradients during withdrawal, although substrate shape is not a large factor in uniformity.

Since single-sided films are desired for eventual integration into actuator applications, spin coating was chosen as the deposition mechanism. Spin coating is already widely used in the semi-conductor industry, especially for production of photoresist films [94].

### **I.2.6. Analytical Techniques**

Chemical features of the sols were probed by FTIR spectroscopy (Nicolet Magna 860 spectrometer) over the wave number range 4000 to 400  $\text{cm}^{-1}$ . Thermal decomposition characteristics of oven-dried gels were studied by simultaneous differential scanning calorimetry (DSC) and thermogravimetric analysis (TGA, Netzsch, STA-449) at a constant heating rate of 5-10°C/min under an argon atmosphere. In some cases, the gaseous byproducts evolved during thermal analysis were examined using mass spectrometry (Balzers AMU200). Calcined powders were examined by X-ray diffraction (XRD, Bruker D8 Discover, or Philips X'Pert), FTIR, and micro-Raman spectroscopy (Renishaw M1000 Micro-Raman Spectrometer with Ar ion laser at 514.5 nm excitation through optical microscope). Thin films were produced via spin coating (Chemat, KW4-A or Laurell WS-400B-6NPP-LITE) and were calcined either in a conventional tube furnace or rapid thermal annealer (ULVAC MILA-3000-P-F). Thin films were examined

by XRD, micro-Raman spectroscopy, and field emission scanning electron microscopy (FESEM, LEO 1550VP) with energy dispersive spectrometer (EDS, Oxford INCA Energy 300).

## II. Sol-gel Synthesis of $\text{Pb}_{1-x}\text{Ba}_x\text{TiO}_3$

### II.1. Precursor Selection

Key challenges in the sol-gel synthesis of PBT are the preparation of a sol stable against uncontrolled hydrolysis and the identification of a solvent system in which multiple metal-organic precursors are compatible. A group of readily available barium, lead, and titanium precursors and solvents (Table 4) was chosen for investigation. Extensive solubility studies were performed to determine a set of mutually-compatible lead and barium precursors (see Appendix). Once a stable pair of lead and barium precursors was identified, they were tested for compatibility with various titanium alkoxides. Acetylacetonone (2,4-pentanedione, AcAc), acetic acid (AA), and diethanolamine (DEA) were used in select systems as chelating agents for titanium.

**Table 4.** Metallic sources, solvents, and chelating agents investigated for sol-gel PBT.

	<b>Successfully Demonstrated</b>	<b>Not Successfully Demonstrated</b>
<b>Barium Source</b>	Barium Acetate, Barium 2-Ethylhexanoate	Barium Hydroxide, Barium Nitrate, Barium Oxalate, Barium Chloride, Barium Isopropoxide
<b>Lead Source</b>	Lead Acetate Trihydrate, Lead Citrate, Lead Nitrate	Lead Acetylacetonate
<b>Titanium Source</b>	Titanium Isopropoxide, Titanium Butoxide	Titanium Ethoxide
<b>Solvent</b>	Ethylene Glycol, Acetic Acid, Trifluoroacetic Acid	Methanol, Ethanol, Isopropanol, 1,3-propanediol, Acetone, Butanol, Acetylacetonone, Ethylenediamine, Propylene Glycol, Tetrahydrofuran, 2-Methoxyethanol, N,N-Dimethylacetamide
<b>Chelating Agent</b>	Acetic Acid, Acetylacetonone, Diethanolamine	Ethanolamine, Triethanolamine

These metal precursors and solvents were then incorporated into a series of sol-gel processes, schematically shown in Figure 3, to produce  $\text{Pb}_{0.5}\text{Ba}_{0.5}\text{TiO}_3$  powders. A listing of compatible precursor/solvent/chelating agent combinations is given in Table 5.

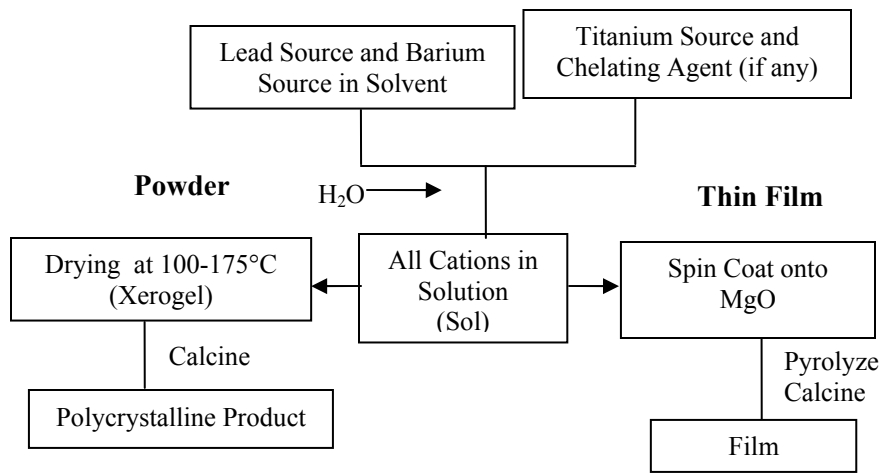


**Figure 3.** Scheme for typical sol-gel process.

**Table 5.** Summary of sol-gel systems investigated. Shading highlights differences between systems.

System Name	Barium Source	Lead Source	Titanium Source	Solvent	Chelating Agent <sup>2</sup>	Outcome
<i>TIpAc</i>	Acetate	Acetate	Isopropoxide	Ethylene Glycol	AcAc	✓
<i>AAS</i>	Acetate	Acetate	Isopropoxide	Ethylene Glycol & Acetic Acid		Too acidic
<i>AAC</i> <sup>3</sup>	Acetate	Nitrate	Isopropoxide	Ethylene Glycol	AA	Too acidic
<i>TIpDEA</i>	Acetate	Nitrate	Isopropoxide	Ethylene Glycol	DEA	✓
<i>TBuDEA</i>	Acetate	Nitrate	Butoxide	Ethylene Glycol	DEA	✓
<i>TBuAc</i>	Acetate	Nitrate	Butoxide	Ethylene Glycol	AcAc	✓
<i>EG2NO3</i>	Acetate	Nitrate	Isopropoxide	Ethylene Glycol		Fast gelation
<i>F3</i>	Acetate	Citrate	Isopropoxide	Trifluoroacetic Acid		Unstable & too acidic
<i>BEtF3</i>	Ethylhexanoate	Acetate	Isopropoxide	Trifluoroacetic Acid		Unstable & too acidic
<i>PCBeF3</i>	Ethylhexanoate	Citrate	Isopropoxide	Trifluoroacetic Acid		Unstable & too acidic

<sup>2</sup> AcAc = acetylacetone (2,4-pentanedione); AA = acetic acid; DEA = diethanolamine

<sup>3</sup> AAC differs from AAS in the lead precursor used, and amount of acetic acid present. Acetic acid is used in large quantities as a solvent for the AAS system, but only in limited quantities as a chelating agent in the AAC system.

## II.2. Choosing the Best Sol Candidates

Sols were prepared for each of the various systems given in Table 5. Excluding the TIpAc system, all systems could be easily reproducibly prepared using either a rotary evaporator or hotplate/stirrer. The TIpAc system could only be prepared using a hotplate/stirrer, as discussed below.

Parameters considered likely to affect material properties, such as water:titanium molar ratios ( $R_w$ ) and chelating agent:Ti molar ratios ( $R_a$ ), were then varied individually for each system, and a series of powders was produced. XRD was used to determine phase purity. Systems capable of producing phase pure PBT powders at moderate temperatures ( $<800^\circ\text{C}$ ) were then used to produce thin films.

Systems involving trifluoroacetic acid were found to be unstable. Though the sols were initially transparent, within hours or days they precipitated heavily. Further, strongly acidic systems are not suitable for thin film deposition since they have a tendency to attack substrates [70]. The AAS, AAC, F3, BEtF3, and PCBeF3 systems were strongly acidic, and thus were not considered further (see Appendix).

The EG2NO3 system is the only system without a chelating agent having a reasonable pH. As would be expected, however, since it lacks a chelating agent, it is relatively unstable and undergoes rapid hydrolysis when exposed to even trace amounts of water.

$R_w$  values greater than 2 resulted in immediate gelation. Fast gelation upon exposure to air is undesired, as it makes production of films with uniform thickness and composition difficult under atmospheric conditions. Rapid hydrolysis is also undesirable because it is associated with bulk nucleation, while heterogeneous nucleation at the substrate is desired to produce textured films [95]. Lacking suitable glove box facilities to perform the entire synthesis and deposition in a dry environment, this system was not considered further (see Appendix).

Thus, four systems were selected for further consideration (Table 6). Each is described in more detail below.

**Table 6.** Four sol-gel systems suitable for depositing thin film PBT.

<b>System Name</b>	<b>Barium Source</b>	<b>Lead Source</b>	<b>Titanium Source</b>	<b>Solvent</b>	<b>Chelating Agent</b>
<i>TIpAc</i>	Acetate	Acetate	Isopropoxide	Ethylene Glycol	AcAc
<i>TBuAc</i>	Acetate	Nitrate	Butoxide	Ethylene Glycol	AcAc
<i>TIpDEA</i>	Acetate	Nitrate	Isopropoxide	Ethylene Glycol	DEA
<i>TBuDEA</i>	Acetate	Nitrate	Butoxide	Ethylene Glycol	DEA

### II.2.1. Stability of Selected Systems

The TIpAc system (chemical precursors: barium acetate, lead acetate, titanium isopropoxide, ethylene glycol, and acetylacetone) was prepared exclusively using a

hotplate/stirrer and condenser. Heavy precipitation occurred when using a rotary evaporator to mix the lead and barium sources. Thus, this system was not able to be reproduced in a rotary evaporator. As suggested by Hasenkox, success using the hotplate/stirrer is likely due to the increased turbulence during mixing, which can influence the degree of coordination between solutes [68]. Further, the TIpAc system was extremely sensitive to any procedural variation and often resulted in precipitates rather than stable sol, likely due to unequal rates of hydrolysis of the various metal-organic components [69, 96]. Once a sol was successfully produced, however, it was remarkably stable against hydrolysis. Sols remained stable in sealed vials for over two years without any noticeable changes. It is noteworthy that attempts to replace lead acetate with lead nitrate in this system caused heavy precipitation.

The TBuAc system (chemical precursors: barium acetate, lead nitrate, titanium butoxide, ethylene glycol, and acetylacetonone) was easily reproducible using hotplate/stirrer techniques. It involves different lead and titanium precursors than the TIpAc system and does not suffer the same degree of atmospheric and procedural sensitivity. Sols with chelating agent:titanium molar ratio ( $R_w$ )  $\leq 4$  remained stable in sealed vials for several months.

TIpDEA system (chemical precursors: barium acetate, lead nitrate, titanium isopropoxide, ethylene glycol, and diethanolamine) samples were prepared using conventional rotary evaporator techniques with  $R_w$  values between 2 and 32. Sols with  $R_w \leq 8$  remained stable for longer than 6 months. Similarly, TBuDEA sols (chemical

precursors: barium acetate, lead nitrate, titanium butoxide, ethylene glycol, and diethanolamine) with  $R_w \leq 4$  remained stable for several months. Both systems were readily adapted to hotplate/stirrer techniques. The use of lead acetate trihydrate in the hotplate technique for TIpDEA was also investigated for completeness.

### II.3. Parametric Optimization of Sols and Powders

Parameters considered likely to affect crystallization behavior and ultimately material properties were examined for each system. These include chelating agent:Ti molar ratio ( $R_a$ ), water:Ti molar ratio ( $R_w$ ), mixing times and temperatures, drying times, and aging conditions [33, 52, 56, 97].

First, the chelating agent:titanium ratio was considered for each of the titanium sources and chelating agents. Since all organics introduced to the system must be fully removed during calcination in order to obtain phase pure powders, we chose to use the minimum chelating agent content that was capable of stabilizing the titanium to withstand the moderate hydrolysis condition  $R_w = 8$ . The stability of each titanium precursor against rapid hydrolysis for varied chelating agent:Ti is shown in Figure 4. A detailed procedure for the stability testing, based on [9, 70] is given in the Appendix. At low values of  $R_a$ , titanium butoxide appears more hydrolytically stable than titanium isopropoxide. This is easily explained by the difference in their enthalpies of hydrolysis (Chapter I, Table 1), since titanium isopropoxide has a much more negative enthalpy of

hydrolysis, it is not surprising that TIP tends to decompose in the presence of even small amounts of water. At higher values of  $R_a$ , however, TIP becomes more stable than titanium butoxide, probably because of more complete ligand exchange. Using the data in Figure 4, the optimal values of  $R_a$  for titanium butoxide, as defined above, were found to be 4 and 2 for acetylacetonate and diethanolamine, respectively.<sup>4</sup> For titanium isopropoxide,  $R_a = 4$  was selected for both chelating agents.

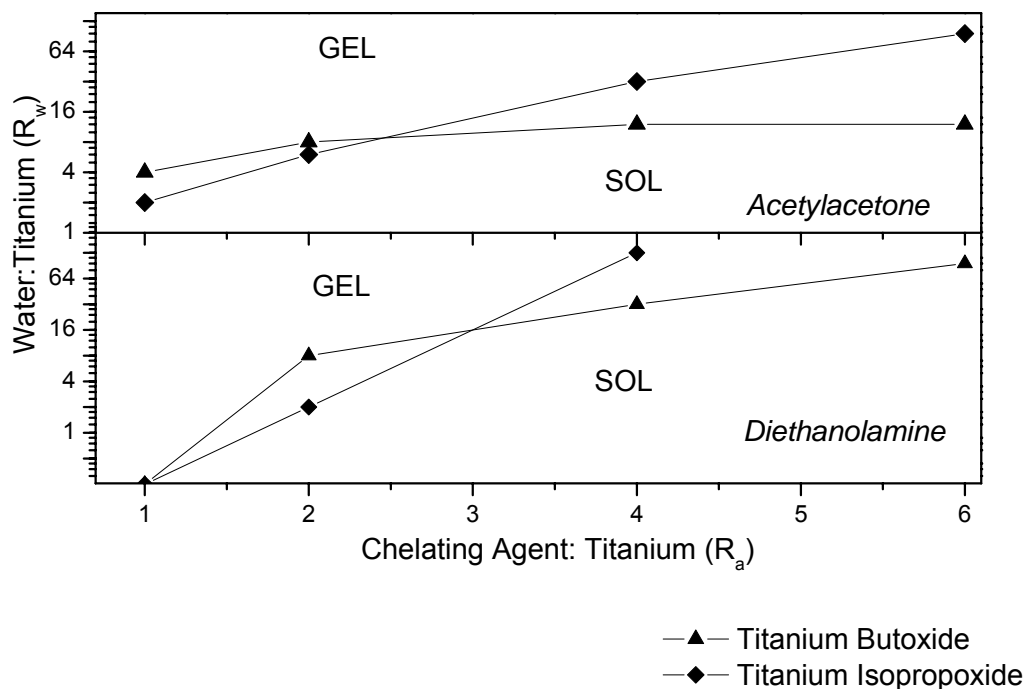


**Figure 4.** Stability against rapid hydrolysis of titanium isopropoxide and titanium butoxide with varied chelating agent:titanium ratio. [Data collected by Arvind Subramaniam]

<sup>4</sup> It was later found that using  $R_a = 4$  for the titanium butoxide and diethanolamine system produced more oriented films. This is possibly explained by unseen precipitates in sols prepared with  $R_a = 2$ , which would provide additional nucleation points within the films leading to less oriented films.

With an optimal value of  $R_a$  in hand, a series of powders was produced with water:Ti molar ratio ( $R_w$ ) varied between 2-32 and calcination temperatures ( $T_c$ ) between 400-600°C. The resulting effect on powders was determined using XRD and FTIR. The parameters were optimized with the goal of obtaining low-temperature, phase-pure perovskite crystallization.

As expected, not all parameters initially investigated were important, and several additional important parameters were identified along the way. Drying time and aging conditions were found to have no effect on resulting powders. Interestingly, however, pH was found to have a prominent effect.

Occasionally the addition of water would cause a DEA-based sol to precipitate, especially for sols with varied Ba:Pb stoichiometries. This was attributed to the difference in nitrate:acetate ligands, and specifically to the varying pH associated with such variations. Since the nitrate ligand is strongly acidic, whereas the acetate ligand is a weak acid, lead rich (and thus nitrate-rich) sols had lower pH than barium (acetate) rich sols. Sols with very low or very high pH were found to be less favorable for thin film deposition, as they were associated with either weak crystallinity or impurity phases. The effect of varying stoichiometry can be somewhat compensated for by pH adjustment of the resulting sols before water addition. pH was lowered using acetic acid (nitric acid additions resulted in rapid precipitation) or raised through the addition of diethanolamine. FTIR showed that the addition of acetic acid did not introduce new bonds, rather it

simply increased the amplitude of  $\text{COO}^-$  symmetric and asymmetric stretching. FTIR of sols prepared with varying amounts of DEA were also found to be similar. Thus, we have reason to believe that the role of the additives was only to modify the pH of the sol.

The pH of an aqueous solution has long been known to affect the specific hydrolytic route taken by metal cations [33, 59]. Brinker gives a detailed discussion of the effect of pH on the coordination number of water molecules surrounding metal ions [59]. Each of these coordination schemes promotes a distinct mechanism for hydrolysis and condensation. Titanium, for example, tends to be surrounded by  $\text{H}_2\text{O}$  molecules at low pH values (known as the “aquo” regime), by  $\text{OH}^-$  ions at moderate pH values (“hydroxo”), and by  $\text{O}^{2-}$  ions at higher pH values (“oxo”). Barium and lead ions, having an oxidation number of +2, are capable of only the  $\text{H}_2\text{O}$  and  $\text{OH}^-$  schemes. Though Brinker’s discussion is limited to metal ions dissolved in noncomplexing aqueous solutions, the results seem to apply here as well. Based on experimental observations, it found that the narrow pH range where  $\text{Ti}^{4+}$ ,  $\text{Ba}^{2+}$ , and  $\text{Pb}^{2+}$  all exist within the same hydrolytic regime leads to the best films. For the DEA system, this is the  $\text{OH}^-$  regime, corresponding to the hydroxo state. As the upper pH boundary is approached, the titanium becomes more oxo-hydroxo, whereas the Ba and Pb become aquo-hydroxo. At low pH values, the Ba and Pb are thoroughly aquo, whereas the titanium becomes aquo-hydroxo. Since each of these hydrolytic processes has its own rate constant, at pH values where Ti, Ba, and Pb are in different ionic states, we would expect to have differing hydrolysis rates amongst the various metals, and thus a propensity for phase separation. In the ideal case, Pb, Ba, and Ti would hydrolyze at the same rate, thus tending to form a

perfectly random (and hence uniform) network of particles. This suggests the DEA-based systems, in which all species exist in the same regime, are preferred for producing homogeneous PBT. Through adjusting the pH of a sol before adding water, we can alter the hydrolysis-condensation pathway, in hopes of achieving this balance. Indeed, such pH adjustment proved necessary for producing sols for the full solid solution range of  $\text{Ba}_x\text{Pb}_{1-x}\text{TiO}_3$ .

#### **II.4. Parametric Optimization of Thin Film Deposition Process**

Thin films were prepared from optimized sols using a spin coating process. A substrate is held in place on a vacuum chuck, and the substrate surface is covered with sol. The spin coater (Chemat KW-4A or Laurell WS-400B-6NPP-LITE) is then programmed to rotate the substrate at a given speed to produce a uniform thin film. By controlling spin speed, the film thickness can be varied. Faster spin speeds lead to thinner films, whereas slow speeds lead to thick films. The thickness of films is generally limited by the achievable uniformity at low speeds. Further, to obtain oriented PBT thin films on single crystal MgO, the layers must be thin enough to encourage heterogeneous nucleation at the film/substrate interface rather than homogeneously in the bulk. Typically, thicker oriented films are produced via a multi-step spin coating process involving alternating spinning and pyrolysis (drying) steps. Spin speed was varied to determine the slowest speed for which oriented films could be produced, thereby maximizing individual layer thickness.

## II.5. Detailed Results for TIpDEA System

The basic optimization procedure was the same for each of the four chosen systems. Ultimately, the preferred method of synthesis was determined to be the TIpDEA route, as it proved to be the most robust to small variations in process parameters. Thus, the optimization procedure for TIpDEA will be presented in the most detail. Results for the optimization process for TIpAc are detailed in [98] and the Appendix. Switching the titanium precursor to butoxide from isopropoxide had limited effects beyond changing the ideal  $R_a$  and  $R_w$ , as discussed in [99]. Unless otherwise specified, all PBT results presented hereafter specifically apply to the TIpDEA system.

### II.5.1. Optimizing the TIpDEA Sol

A schematic of the TIpDEA sol-gel synthesis procedure is given in Figure 5. The general procedure is to dissolve lead nitrate and barium acetate in ethylene glycol at 60°C in a rotary evaporator, while separately mixing titanium isopropoxide and diethanolamine (in a prescribed ratio  $R_a$ ) at room temperature (stirred at 600rpm with a magnetic stirrer). After allowing the Pb/Ba solution to cool to room temperature, the chelated titanium sol is added to the Pb/Ba, and the resulting solution is mixed with the rotary evaporator at 60°C for 30 minutes and again allowed to cool. Water (in a prescribed ratio with Ti,  $R_w$ ) mixed with ethylene glycol is then added to the solution, which is reattached to the rotary

evaporator for a final 30 minutes. Detailed preparation procedures are given for the optimized process elsewhere [75] and in the Appendix.

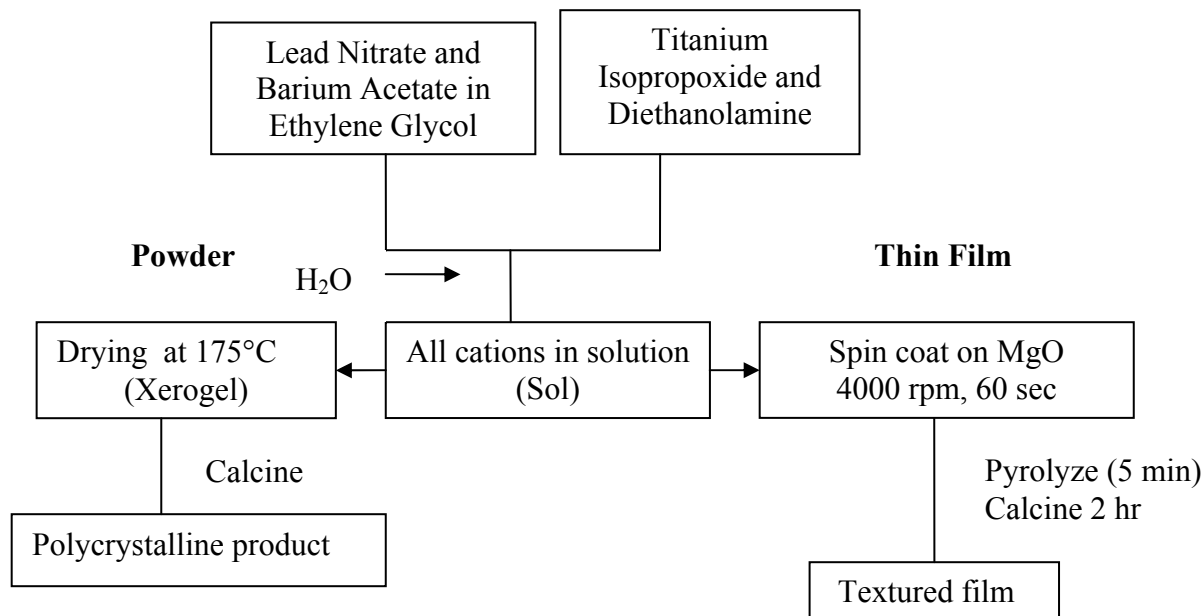


**Figure 5.** Schematic of the TIpDEA sol-gel process for producing powder and thin film PBT.

As discussed earlier, for this system the ratio of diethanolamine to titanium was fixed at  $R_a = 4$ . The ratio of water:titanium was then varied from  $R_w = 2$  to 32. The sols were dried at 175°C and calcined to 500°C. XRD data is shown in Figure 6 for these powders. As shown in the figure, the undesired BaCO<sub>3</sub> phase is detected for high water contents. The reason for this is unclear; however, some researchers have suggested gaseous CO<sub>2</sub> in water can promote carbonate formation [100, 101]. The ideal  $R_w$  was thus chosen to be 4 for subsequent experiments. This optimized sol has a concentration of 0.35M and shows remarkable stability. TIpDEA sol has been used for over a year to produce PBT thin films without any noticeable degradation.

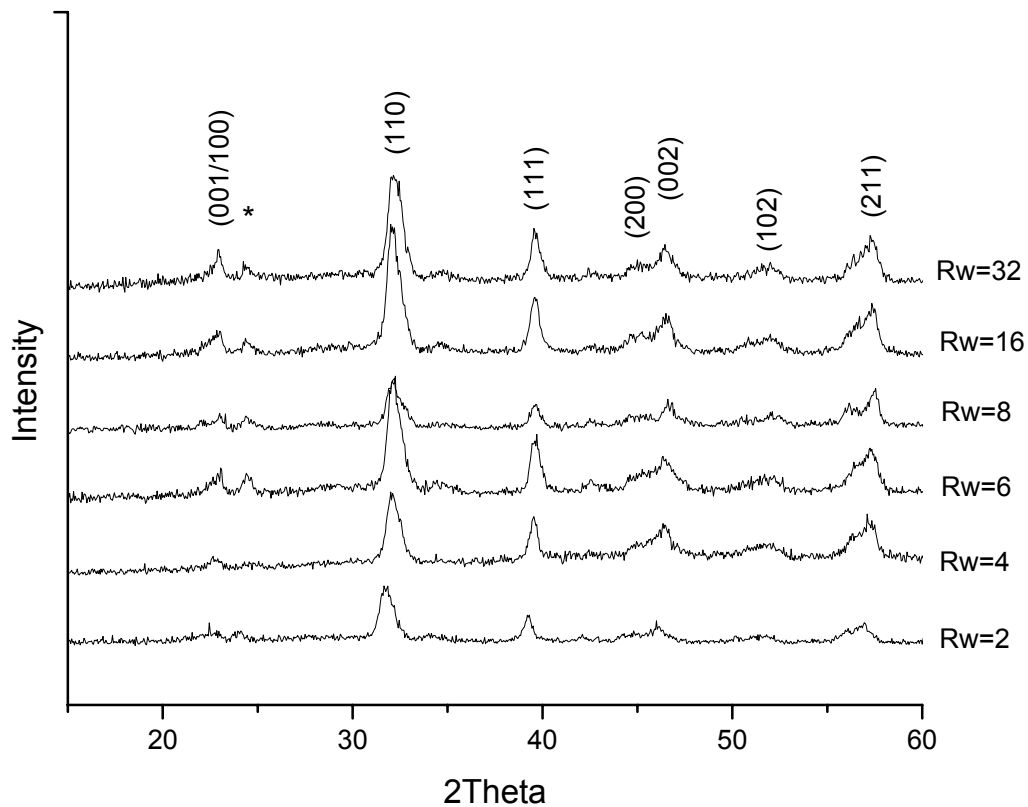


**Figure 6.** XRD of TiPDEA sols prepared with the stated water:titanium (R<sub>w</sub>) ratio and calcined at 500°C (\* indicates BaCO<sub>3</sub> impurity phase).

TiPDEA sol ( $R_a = R_w = 4$ ) was dried at 175°C to form a xerogel. The xerogel was then calcined at a range of temperatures (T<sub>c</sub>) in air using a tube furnace. The resulting powders were examined using FTIR and XRD (Figure 7 and Figure 9).

FTIR of the sol, xerogel, and powders shows that most organics are removed during drying. The sol exhibits peaks due to the presence of the organic moieties of ethylene glycol, isopropoxide, acetate, and diethanolamine, as indicated on the figure. After drying at 175°C to form the xerogel, most of the organics are removed. The OH/NH [3300–3370  $\text{cm}^{-1}$ ], CH [2900  $\text{cm}^{-1}$  doublet], and (CH) [875  $\text{cm}^{-1}$  doublet] peaks are greatly diminished in intensity. The COO stretching band (1350  $\text{cm}^{-1}$  broad doublet for symmetric and asymmetric stretching modes) is retained, suggesting that acetate groups remain bound to barium and/or lead ions. Perhaps more significantly, a new peak appears at 1620  $\text{cm}^{-1}$ , with a comparable intensity to the peak at 1065  $\text{cm}^{-1}$ . The moieties responsible for these absorptions are not readily identifiable, and the peaks are tentatively attributed to strong chelation of titanium by DEA. On heating to 450°C, only a peak at 1425  $\text{cm}^{-1}$  is present, along with a very small peak at 855  $\text{cm}^{-1}$ . The spectrum at 600°C is identical, with the exception of the appearance of the Ti-O band at 540  $\text{cm}^{-1}$ . This pair of peaks (1425 and 855  $\text{cm}^{-1}$ ) is likely due to  $\text{Ba}_2\text{Ti}_2\text{O}_5\text{CO}_3$  [102, 103]. An adsorption band at 3000  $\text{cm}^{-1}$ , in addition to that at 1425  $\text{cm}^{-1}$ , would be expected for simple barium carbonate [104]. By 700°C, all trace of organic components is absent, and even the spectrum obtained after annealing at 450°C shows relatively little organic (i.e., oxycarbonate) content. In comparison to these results, preliminary experiments in which lead acetate rather than lead nitrate was used as the lead source indicated retention of the peaks assigned to oxycarbonate to temperatures of at least 800°C (Figure 8). This reinforces the selection of TIpDEA as the ideal system for production of phase-pure PBT at moderate temperatures.

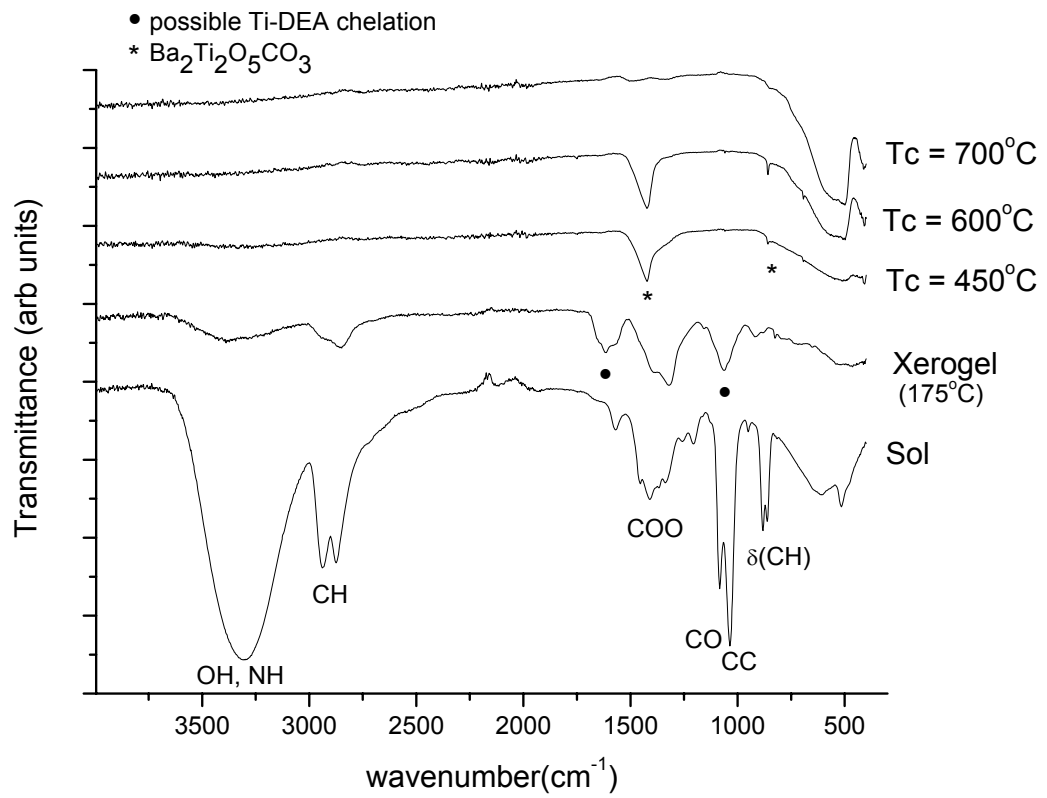
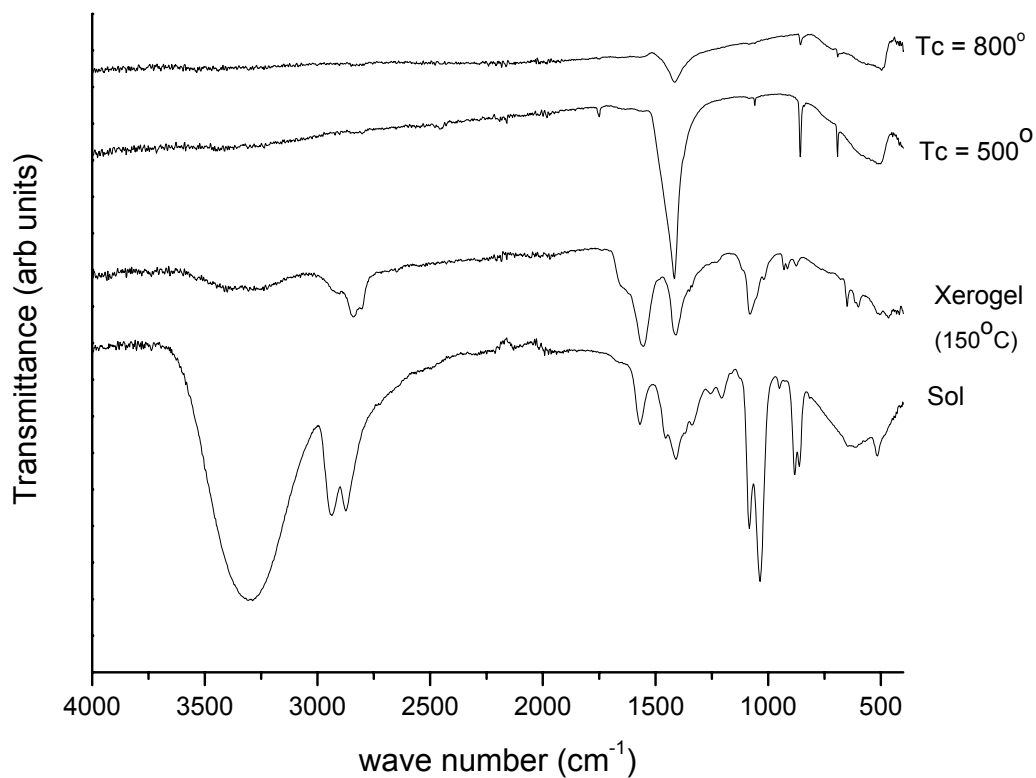


Figure 7. FTIR of TIPDEA sol, xerogel, and calcined powders.



**Figure 8.** FTIR of modified TIPDEA sol, xerogel, and calcined powders made with lead acetate.

XRD shows crystallization of PBT in stagnant air begins by 400°C though in the presence of BaCO<sub>3</sub>, and phase pure PBT is produced by 500°C (Figure 9). Crystallinity continues to increase with higher temperatures. To ensure complete crystallinity, T<sub>c</sub> = 600°C was used in subsequent experiments.

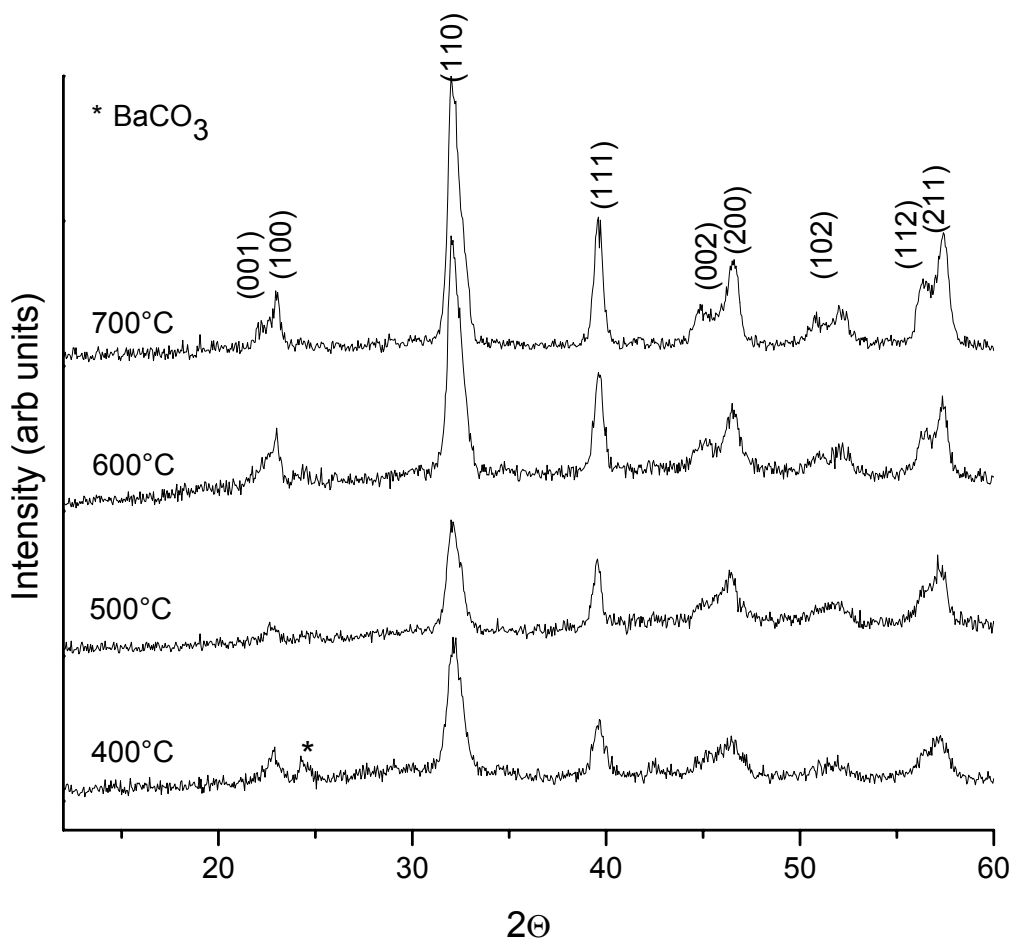


Figure 9. XRD of TIpDEA powders calcined at the given temperatures.

### II.5.2. Effect of Calcination Atmosphere on TIpDEA System

Thermal analysis was performed on TIpDEA xerogel (dried at 175°C) using a Netzsch Model STA-449 simultaneous thermal analysis (STA) system, which provides concurrent

thermogravimetric analysis (TGA), differential scanning calorimetry<sup>5</sup> (DSC), and mass spectrometry (MS). The annealing atmosphere was varied in composition and flow rate, as shown in Table 7 using ultra-high purity argon and oxygen. Error is estimated to be +/-2% due to flow metering methods used. For each STA run, samples were brought from room temperature to 700°C using a heating rate of 5°C/min and data collection rate of 15 points/°C, and then cooled to room temperature at 50°C/min. Results were examined, and the first derivative of the TGA curves (DTG) was plotted using Netzsch's Proteus software suite. Samples were retained and used for subsequent XRD and Raman analysis. To examine the phases present during different stages of thermal treatment, samples were prepared using the same atmosphere and heating rate with various end temperatures to correspond to regions of interest in the DSC to allow for XRD and Raman analysis of intermediate phases. To determine the effects (if any) of gas flow rate, a second run in 50% oxygen was carried out using a higher flow rate, denoted by 50(h).

**Table 7.** Composition of annealing atmosphere and flow rates.

<b>% Oxygen (balance Argon)</b>	<b>O<sub>2</sub> (mL/min)</b>	<b>Ar (mL/min)</b>	<b>Total (mL/min)</b>
<b>0</b>	0	34	34
<b>5*</b>	5	97	102
<b>10</b>	19	170	189
<b>20</b>	19	85	104
<b>50</b>	19	19	38
<b>50(h)</b>	54	54	108

\*Single pre-mixed tank used for 5%O<sub>2</sub> runs.

<sup>5</sup> Technically, this instrument is better described as a 'heat flux DSC,' which uses differential thermal analysis rather than scanning calorimetry [105].

XRD showed that except for the case of pure Ar, PBT is the predominant phase after STA runs to 700°C. TGA and DTGA results as a function of annealing atmosphere and flow rate are shown in Table 8. There is very little difference in total weight loss between 100-600°C for any of the atmospheres containing oxygen.

**Table 8.** Weight loss and endo-/exotherms observed between 100-600°C for the TIPDEA system, with %O<sub>2</sub> atmosphere indicated (exotherms in italics are questionable).

<b>% Oxygen</b>	<b>Weight loss (100-600°C)</b>	<b>Endo-/Exotherms (100-600°C)</b>
<b>0%</b>	32.3%	265,576
<b>5%</b>	42.0%	261, 358, 576
<b>10%</b>	48.7%	260, 440, 470
<b>20%</b>	48.3%	264, 428, 454, 579
<b>50%</b>	50.5%	253, 352, 435, 581
<b>50%(h)</b>	50.1%	258, 359, 441, 582

For convenience, the STA data is broken down into four temperature regimes: 100-285, 285-380, 380-550, and 550-600°C (Figure 10, Figure 11, Figure 12). TGA and DTGA data for all of the atmospheres are shown in Figure 10 and Figure 11, respectively. The curves for samples in 10-50% oxygen appear somewhat similar, while those of 0 and 5%O<sub>2</sub> are significantly different from the others. Complete results, including TGA, DSC, and MS, are given in the Appendix.

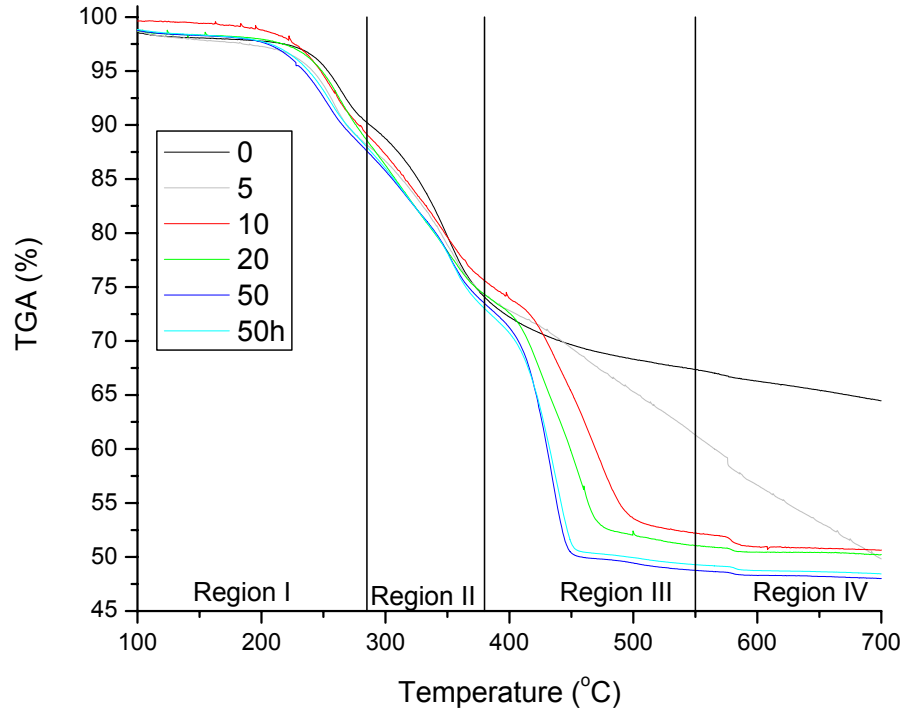


Figure 10. TGA of TIpDEA xerogels in the %O<sub>2</sub> atmosphere indicated.

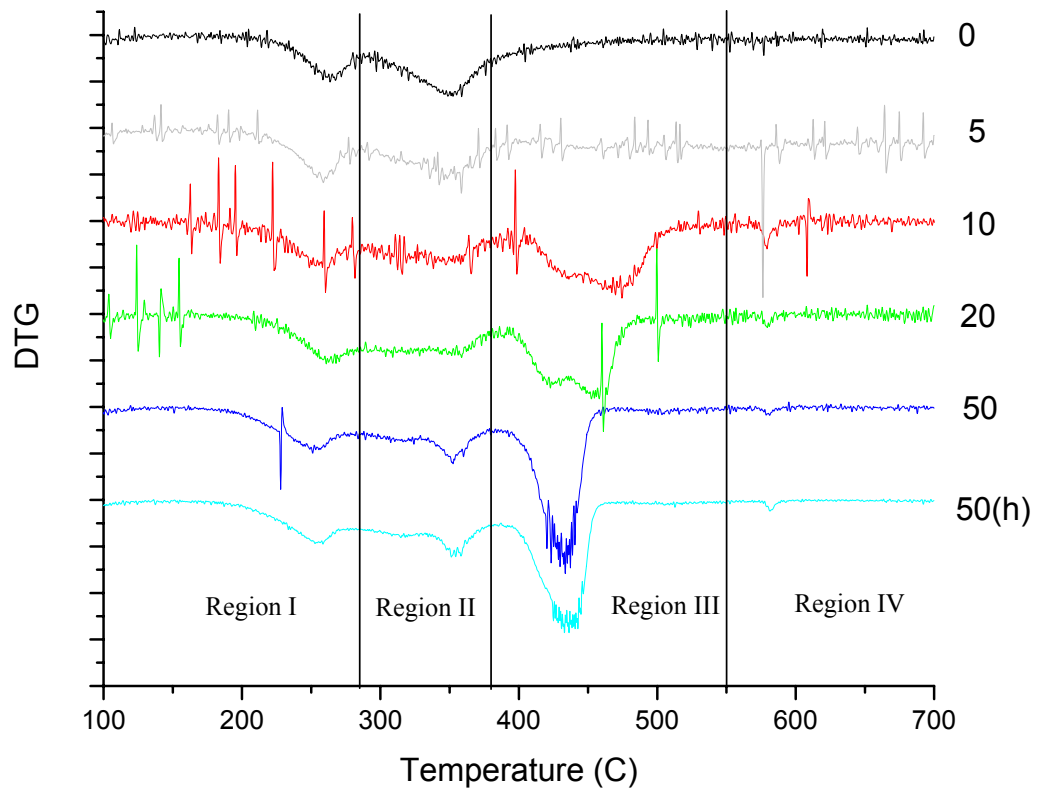
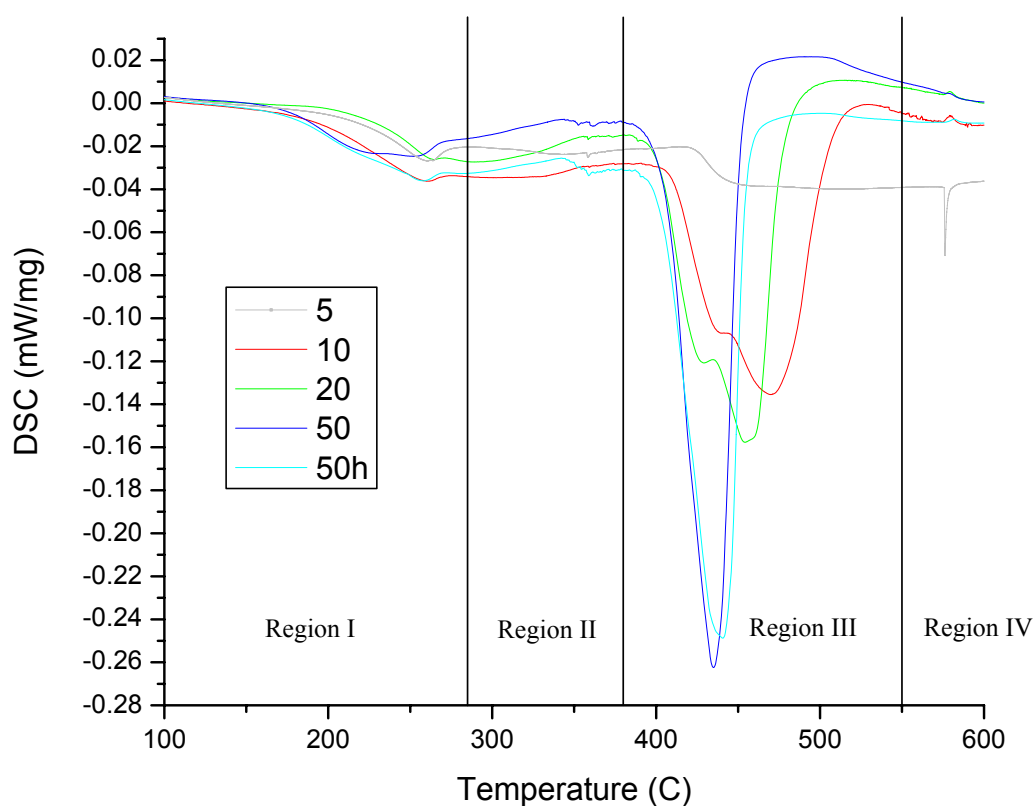


Figure 11. DTGA of TIpDEA xerogels in the %O<sub>2</sub> atmosphere indicated.

DSC data for oxygen-containing atmospheres are shown in Figure 12. The features of the sample heated under pure argon are too small to be shown clearly at the same scale. DTG, when compared with DSC, shows that all weight losses correspond well to DSC peaks.

A brief analysis of the four thermal regimes is given below.



**Figure 12.** DSC of TIPDEA xerogels in the %O<sub>2</sub> atmosphere indicated.

*Region I: 100-285°C*

This regime contains the first DSC peak, an exothermic event near 260°C. The percentage of total weight loss occurring in this regime is given for each of the atmospheres in Table 9. Presumably, volatile species not strongly chelated to any of the metal ions in the gel network are given off in this regime. Increasing the flow rate caused the DSC curve to broaden and deepen for the 50%O<sub>2</sub> case. However, the peak did not shift significantly with changes in %O<sub>2</sub>.

**Table 9.** Percent weight loss in Region I (100-285°C) for the indicated %O<sub>2</sub> atmosphere.

O <sub>2</sub> (%)	% Weight Loss (100-285°C)
0	8.4
5	10.5
10	9.7
20	10.2
50	11.2
50(h)	10.9

*Region II: 285-380°C*

This temperature regime encompasses the temperature range between the first DSC/DTG peak and the main exothermic event in oxygen-containing atmospheres. For the case of pure argon (0%O<sub>2</sub>), most weight loss occurs in this temperature regime, and it is associated with a small exothermic event in the DSC, possibly due to the combustion of

DEA and remaining organics. For oxygen-containing atmospheres, weight loss continues, though without additional exothermic events detected in the DSC. A summary of weight loss in this region II is given in Table 10.

**Table 10.** Percent weight loss in Region II (285-380°C) for the indicated %O<sub>2</sub> atmosphere.

O <sub>2</sub> (%)	% Weight Loss (285-380°C)
0	16.1
5	13.9
10	14.4
20	14.3
50	14.1
50(h)	15.0

*Region III: 380-550°C*

For oxygen-containing atmospheres, region III is the primary weight loss regime, as it includes the large exothermic event seen between ~ 400-450°C in all of the DSC patterns (though it is somewhat weaker for the 5%O<sub>2</sub> case). Increasing oxygen content shifts the main exothermic peak to lower temperatures (Figure 12). There are no sharp weight loss events in the 0 and 5%O<sub>2</sub> DTG curves. A summary of weight loss in region III is given in Table 11.

In all cases, the main exotherm was accompanied by the release of masses 12, 22, 44, 45, which correspond to the release of CO<sub>2</sub> and strongly indicate combustion. Interestingly, in the case of high oxygen content, the large exotherm is preceded by a sharp peak in the MS data indicating mass 17, and broader peaks indicating masses 25, 26, 29, 41, 42, 50,

and 52-59 are released. Thus, in the case of 50%O<sub>2</sub>, decomposition produces a larger number of mass fragments, including many heavy fragments. This might indicate a rapid and ‘dirty’ combustion step. The lack of sharp weight loss for the 0 and 5%O<sub>2</sub> samples is explainable by the low oxygen content, which suppresses combustion.

**Table 11.** Percent weight loss in Region III (380-550°C) for the indicated %O<sub>2</sub> atmosphere.

O <sub>2</sub> (%)	% Weight Loss (380-550°)
0	6.7
5	13.0
10	23.4
20	23.2
50	24.7
50(h)	23.7

*Region IV: 550-600°C*

This small temperature range includes the slight endotherm seen in some DSC curves, and a corresponding peak in DTGA. The peak is likely associated with carbonate or nitrate decomposition and appears to be correlated with flow rate rather than oxygen content. The peak is most prominent for 10%O<sub>2</sub>, which has the highest flow rate, and is progressively weaker in the order 20, 50, 0% which coincides exactly with decreasing flow rate. To verify this, a second run in 50%O<sub>2</sub> was carried out using a flow rate comparable to that of the 20% run (50h in the figures). As can be seen in Figure 11 and Figure 12, the effect of increased flow rate was to broaden and deepen the lower temperature (Region I) endotherm, as seen in DSC, and slightly sharpen the 580° peak

seen in DTGA. Results for the runs were otherwise identical. This supports that the 580°C DTGA peak increases in intensity as flow rate increases.

**Table 12.** Percent weight loss in Region IV (550-600°C) for the indicated %O<sub>2</sub> atmosphere.

O <sub>2</sub> (%)	% Weight Loss (550-600°C)
0	1.1
5	4.6
10	1.3
20	0.6
50	0.47
50(h)	0.54

Excluding the 5% case, weight loss in this region generally decreases with increasing oxygen content, suggesting less carbonate or nitrate decomposes in oxygen-rich atmospheres. Whether it is due to an incomplete conversion of nitrogen-containing precursors into PBT or decreased amount of carbonate formed through the decomposition process remains to be determined.

#### *Post-STA Analysis*

A summary of the weight loss occurring in different temperature regions is given in Figure 13. Regions I and II show relative independence of O<sub>2</sub> content, which is consistent with the removal of volatile species. The positive slope of the curve for Region III indicates increasing weight loss with increasing O<sub>2</sub> content, consistent with combustion.

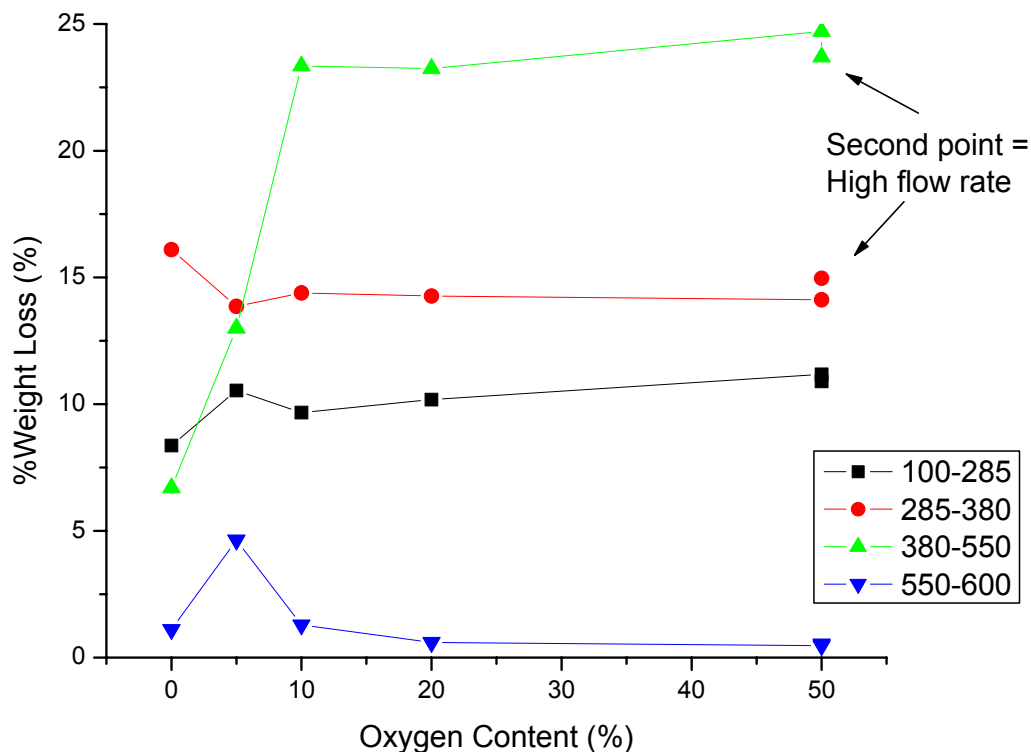


**Figure 13.** Percent weight loss occurring within various temperature ranges as a function of % oxygen atmosphere.

It is apparent that in the absence of oxygen, an entirely different decomposition pathway prevails. Whereas all samples run with oxygen show a series of exothermic peaks with a slight endotherm around 580°C, the sample run in pure Ar shows no significant exothermic events. However, this sample's weight loss is also significantly less, and micro-Raman analysis (Figure 14) shows carbonaceous material remaining behind after heat treatment to 700°C (Raman shifts near 1350 and 1565  $\text{cm}^{-1}$ ). The sample powder appears black under a microscope. Thus, the exotherm for organic decomposition in pure Ar is likely at a higher temperature as organic combustion cannot occur in the absence of oxygen.

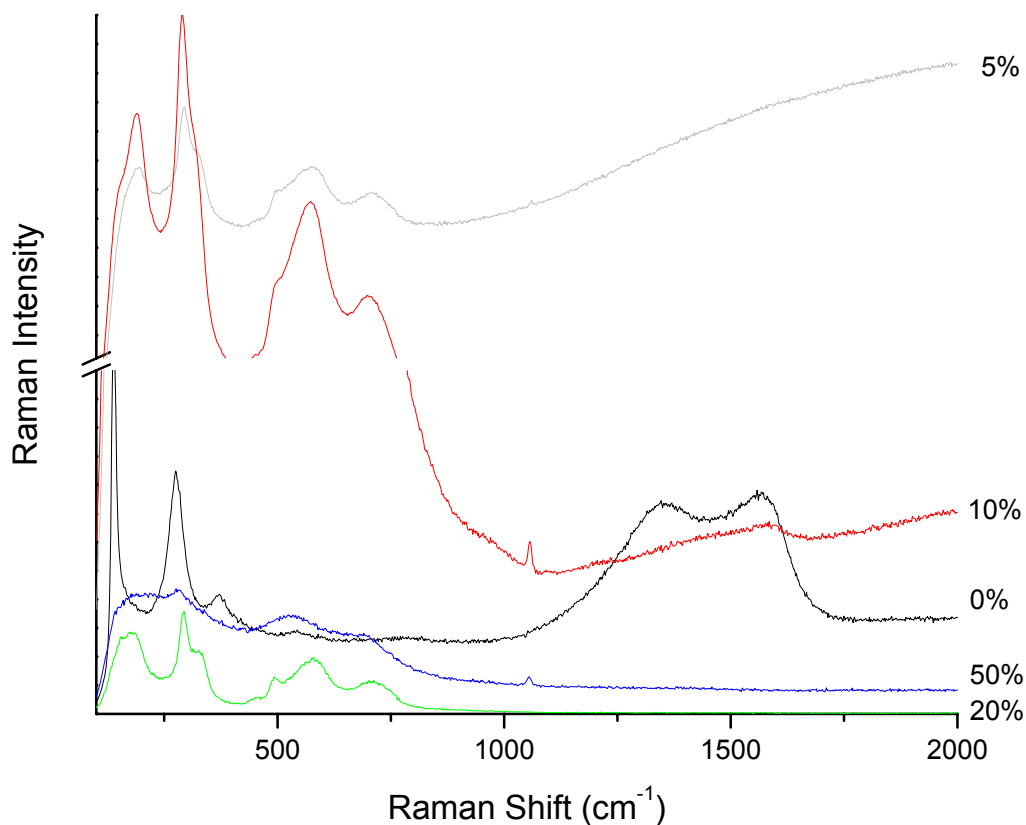


**Figure 14.** Micro-Raman analysis of TIPDEA samples after STA treatment to 700°C.

The case with 5%O<sub>2</sub> shows only a weak exothermic peak above 550°C. This peak might correspond to a right-shifted main exotherm indicating combustion at higher temperatures for this sample. XRD and micro-Raman show PBT is formed by 700°C. The Raman shifts associated with PBT are detailed elsewhere [106] and correlate well with samples prepared in 5-20%O<sub>2</sub>. For the 10% sample, an additional Raman shift at approximately 1060cm<sup>-1</sup> might be attributable to the presence of an intermediate oxy-carbonate phase. Powders prepared in the presence of 5-20% oxygen appeared uniformly white and did not show carbon content in their micro-Raman analysis. Raman signals from samples prepared in 50%O<sub>2</sub>, however, do not correspond well with PBT.

### *Summary*

In summary, annealing atmosphere significantly alters the decomposition pathway of sol-gel derived xerogels for the production of PBT. Low-temperature formation requires at least some oxygen, though a highly-enriched oxygen atmosphere is not desirable for PBT formation, as seen in the Raman spectra. Additional studies are warranted to determine the optimum flow rate and oxygen content for production of phase-pure PBT at the lowest temperature. Further, the influence of atmospheric oxygen content on thin films should be investigated due to the different nucleation mechanisms involved in crystallization.

### **II.5.3. PBT Thin Films**

As described in Chapter I, PBT sols are deposited on lattice-matched MgO(100) single crystal substrates with the goal of achieving heterogeneous nucleation at the substrate interface to produce textured PBT films with (001/100)-orientation. The deposition process is optimized here for the TIpDEA system. Slightly different results would be expected for TBuDEA and, to a greater extent, the TIpAc and TBuAc systems due to differences in viscosity and sol concentration; however, the general optimization procedure is the same.

To determine the thickest attainable single layer oriented film, spin speed was varied between 2-4krpm. Films produced with spin speeds less than 2krpm were visibly

nonuniform, as the spinning was not sufficiently fast to evenly distribute the sol. It is unclear why the thick film produced at 2500rpm shows weak crystallinity, although it is possible insufficient grain growth in heterogeneously nucleated crystallites at the substrate interface resulted in a poor crystallization throughout the thickness of the film. Films prepared with a spin speed of 3krpm showed the best crystallinity and orientation [Figure 15]. Thus, spin speed was held fixed at 3krpm for further studies, as it is the slowest speed (indicating the thickest film) that reliably results in oriented and crystalline PBT.

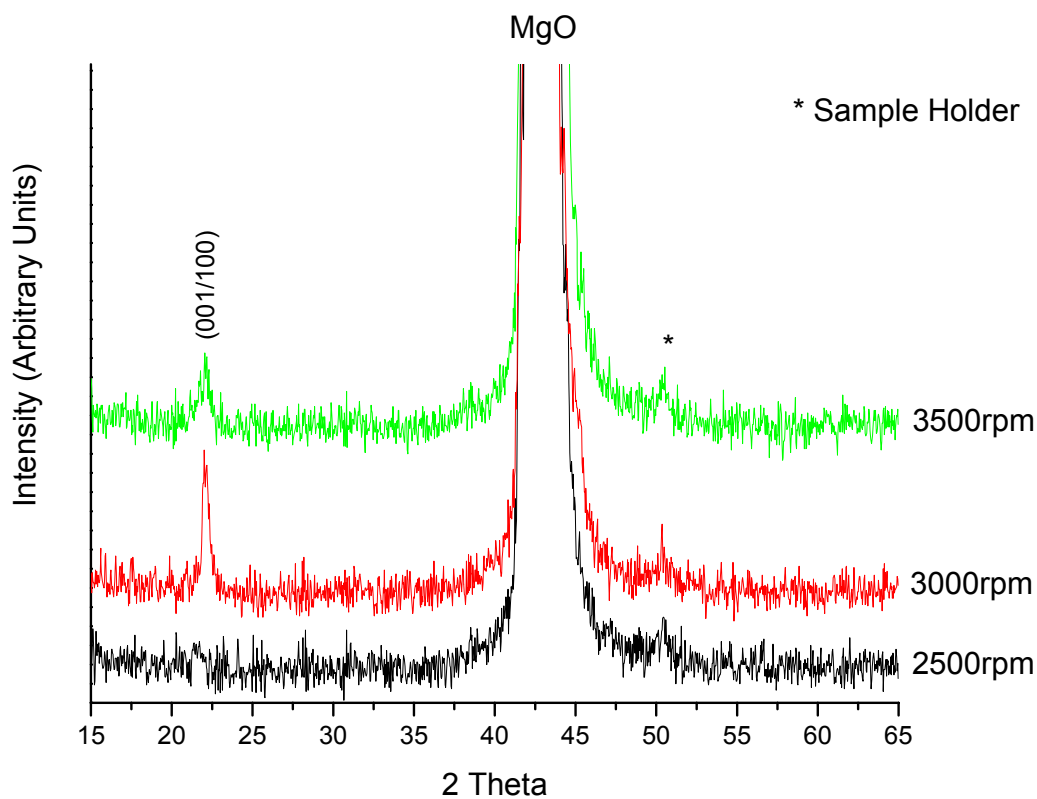


**Figure 15.** XRD of single layer TIPDEA films produced with the spin speeds indicated ( $T_c = 600^\circ\text{C}$ ).

Cross-sectional SEM showed that films prepared by spin coating at 3krpm for 40 seconds were approximately 60nm thick per layer [Figure 16].

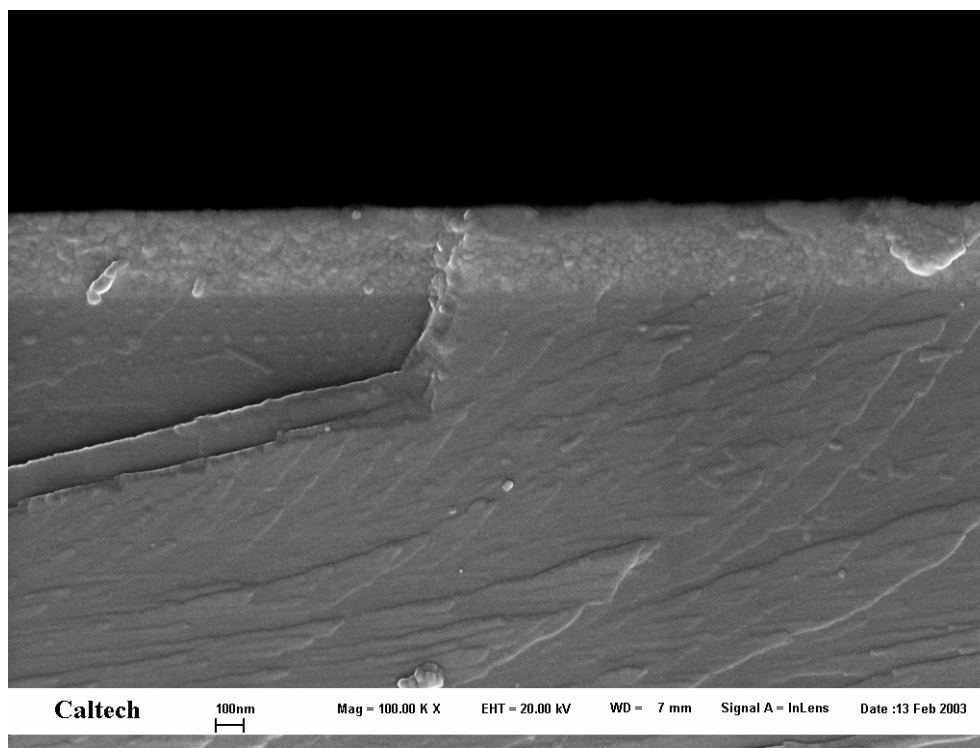


**Figure 16.** Cross-sectional SEM of 3 layer TiPDEA film deposited on MgO showing thickness is approximately 60nm/layer.

To determine the thickest oriented multilayer film attainable, further studies were conducted to investigate the most suitable process for multilayer deposition. A series of two layer films was prepared with either a 5 minute drying (pyrolysis) step or pyrolysis and full calcination between each layer. The pyrolysis step involved placing the wet film on a hot plate at a fixed temperature ( $T_p$ ). Various pyrolysis temperatures were used, and the results for two and three layer films are shown in Figure 17-Figure 19. As can be seen in the figures, the pyrolyzed films showed better orientation retention after multiple layers than those samples calcined to  $600^\circ\text{C}$  between each layer. Since the pyrolysis step is considerably shorter than calcinations (5 minutes vs. 3 hours), this greatly shortened

the time required to make multi-layer films. It is believed that calcination between each layer prevented the layers from coalescing to form a single entity before crystallization. The second layer, then, would crystallize from the imperfect template of the surface of the first layer, rather than the MgO underneath. After two layers, all of the pyrolyzed films except for  $T_p = 300^\circ\text{C}$  remained (001/100)-oriented. Since the  $T_p = 300^\circ\text{C}$  film showed signs of (110)-orientation after two layers, that temperature was not considered further. After three layers, orientation is retained best by the  $T_p = 200^\circ\text{C}$  sample. The loss of orientation by the other samples is attributed to increased surface roughness due to the rapid boiling of DEA in the sol (b.p. =  $217^\circ\text{C}$ ), which provides additional nucleation points for misoriented grains. SEM images of films pyrolyzed at 200 and  $300^\circ\text{C}$  are shown in Figure 20.

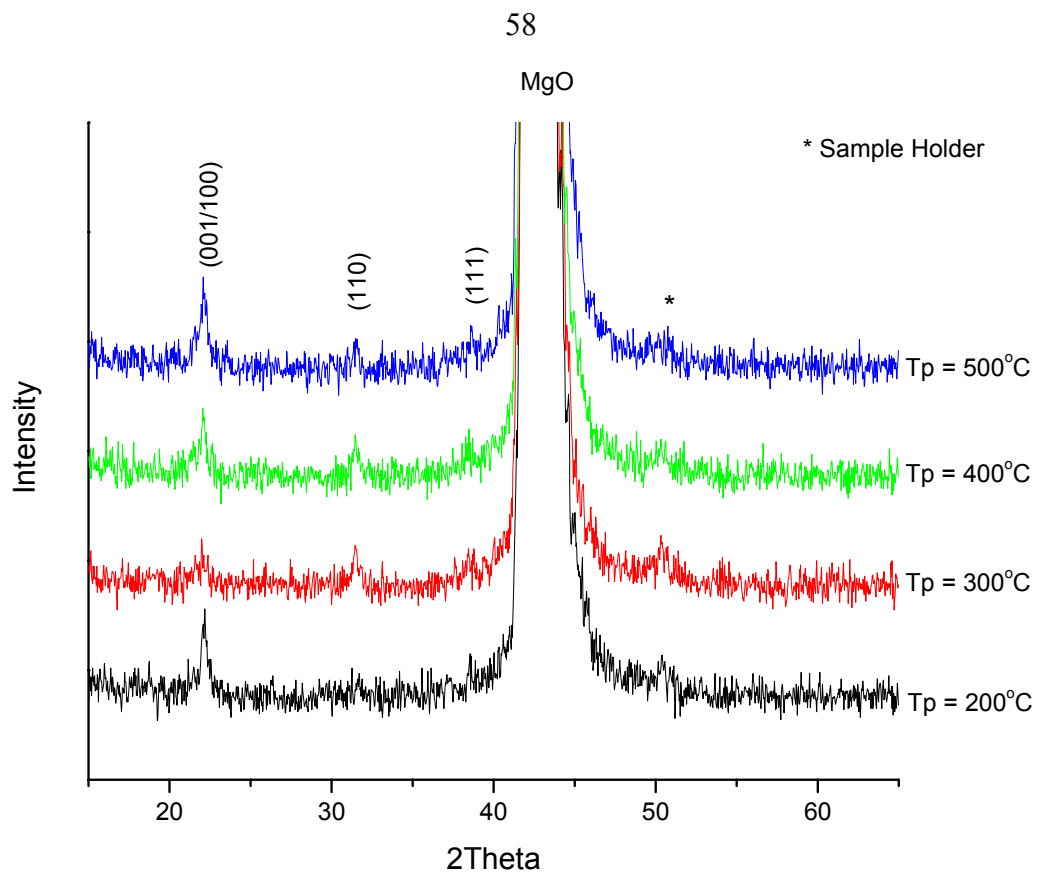


**Figure 17.** XRD of two layer TiPDEA films produced with a five minute pyrolysis at the temperature indicated and full calcination between layers ( $T_c = 600^\circ\text{C}$ ).

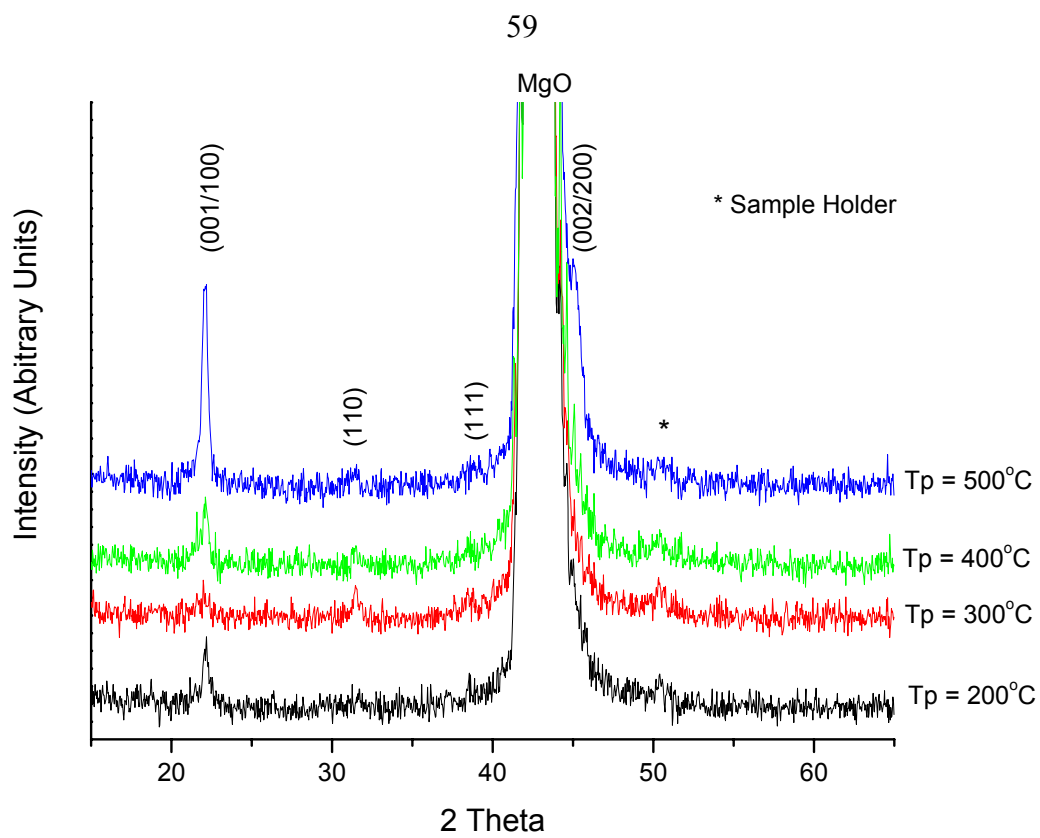


**Figure 18.** XRD of two layer TIPDEA films produced with a five minute pyrolysis at the temperature indicated before calcination ( $T_c = 600^\circ\text{C}$ ).

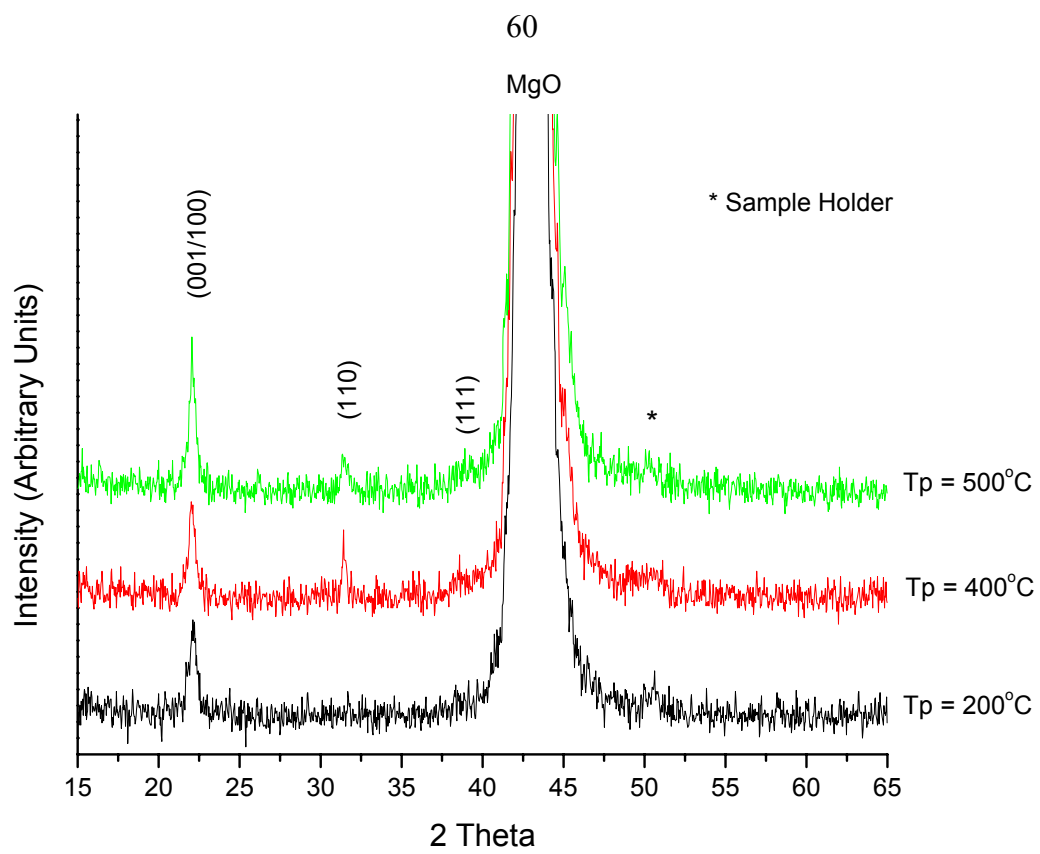


**Figure 19.** XRD of three layer TIPDEA films pyrolyzed at the temperature indicated between layers ( $T_c = 600^\circ\text{C}$ ).

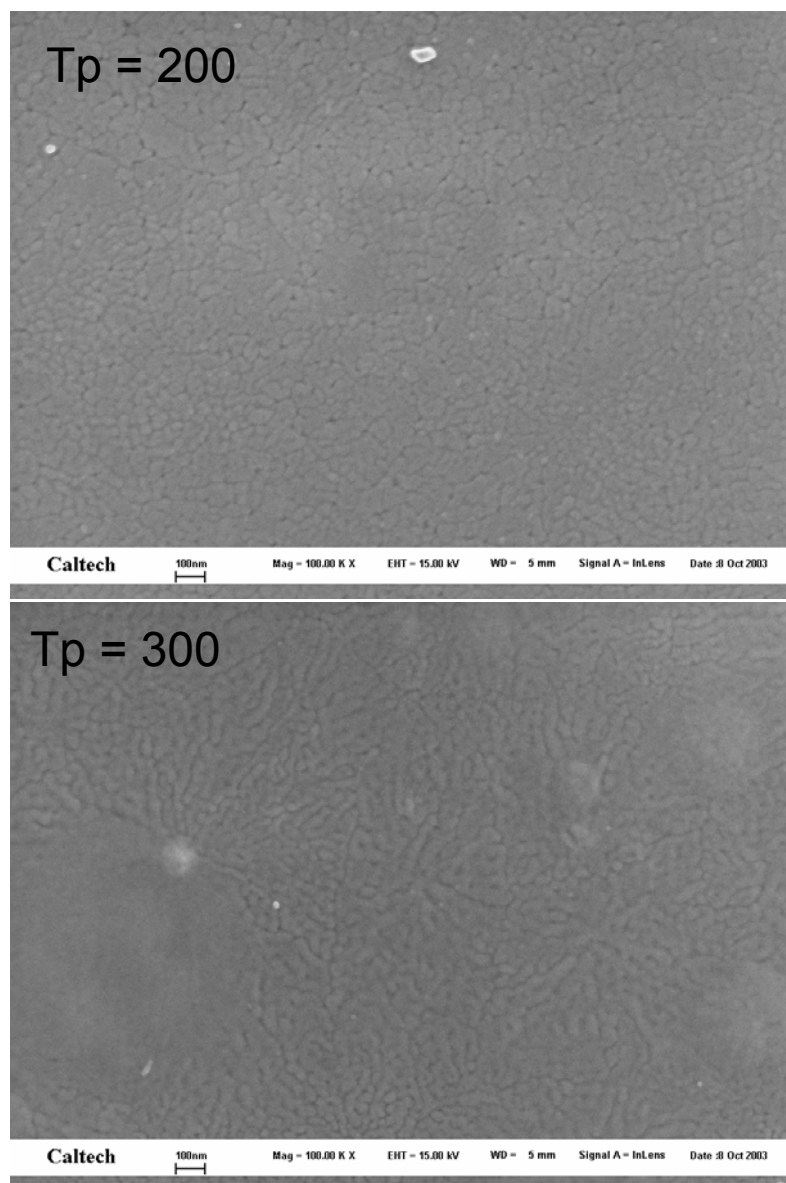


**Figure 20.** SEM images of TipDEA films pyrolyzed at the given temperatures and then calcined to 600°C. Note the increased surface roughness of the film pyrolyzed at 300°C.

Additional layers were deposited, and the film remained oriented for four layers. It was found that an 8 layer oriented film could be prepared by annealing the film after the 4<sup>th</sup> and 8<sup>th</sup> layers (Figure 21).

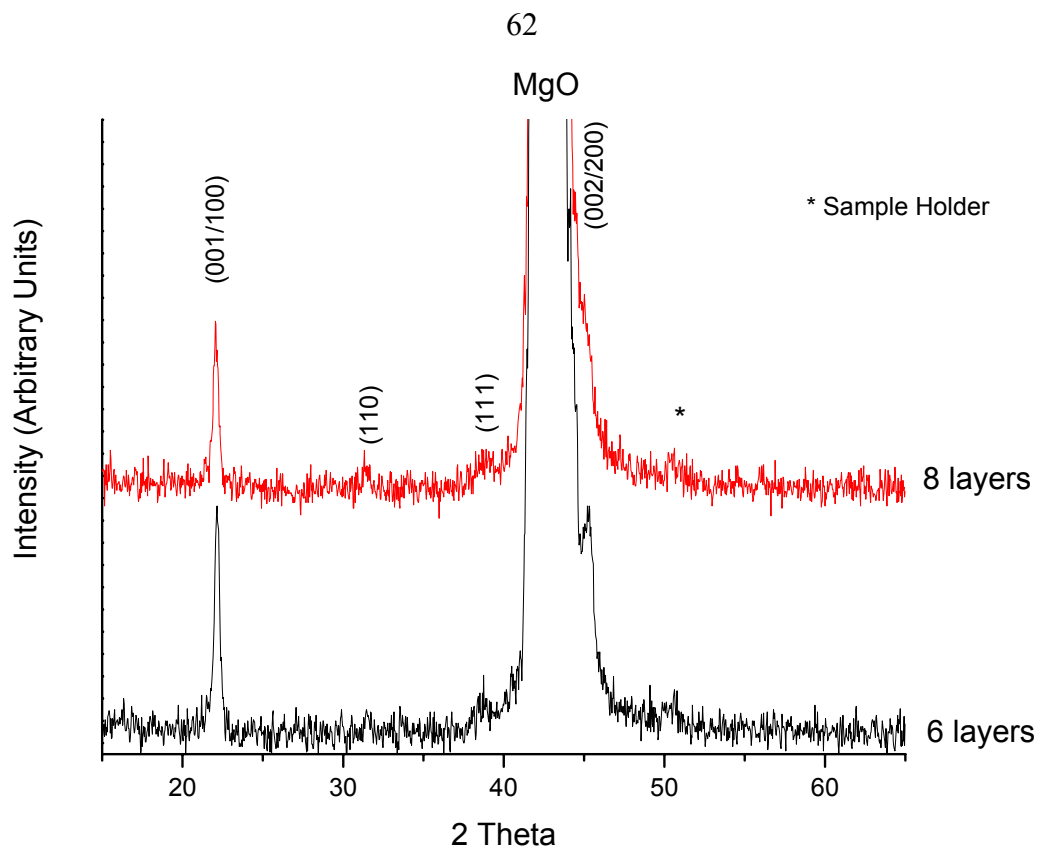


**Figure 21.** XRD of 6 and 8 layer films prepared with  $T_p = 200^\circ\text{C}$  between layers and a full calcination after the 3rd or 4th layer, respectively ( $T_c = 600^\circ\text{C}$ ).

Heating rate was independently varied between  $1\text{-}20^\circ\text{C}/\text{min}$ , respectively. The resulting effect on orientation was determined through XRD (Figure 22). Orientation was not greatly affected by heating rate, although grain size is somewhat smaller and less uniform for faster heating rates. SEM images of films prepared with different heating rates are shown in Figure 23 and Figure 24.

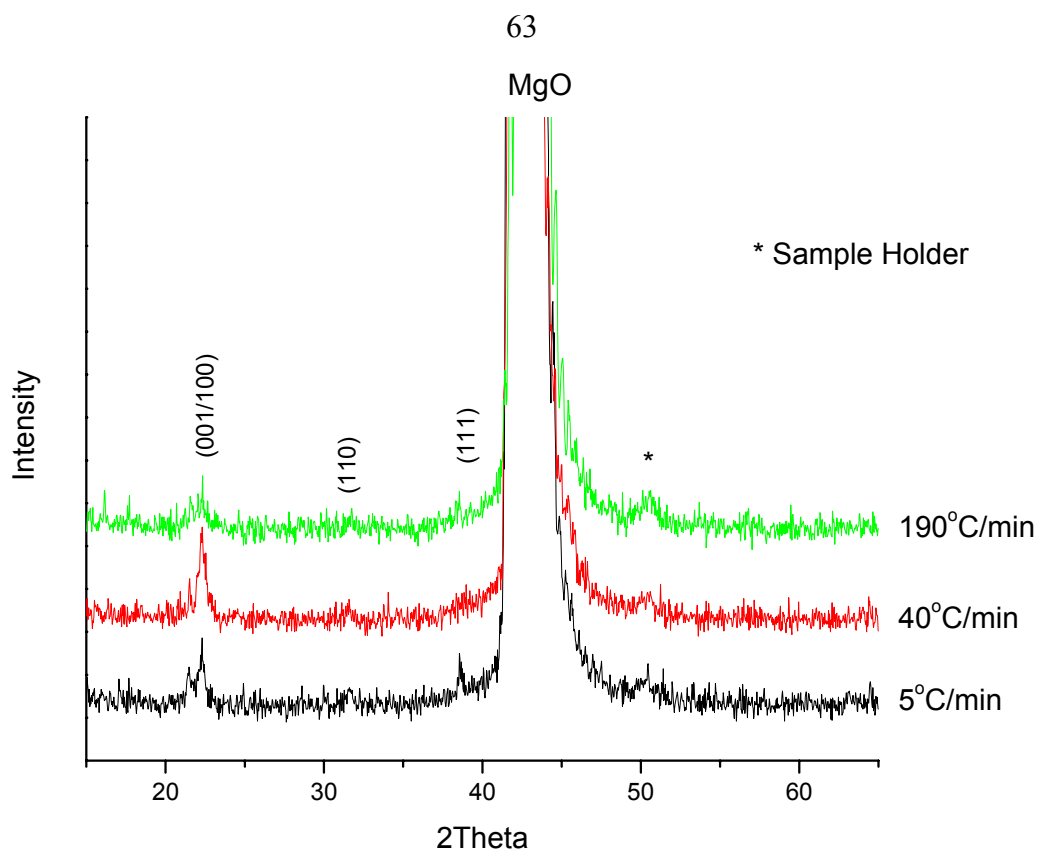


**Figure 22.** XRD of three layer TIPDEA films ( $T_p = 200^\circ\text{C}$ ) calcined with the indicated heating rates ( $T_c = 600^\circ\text{C}$ ).

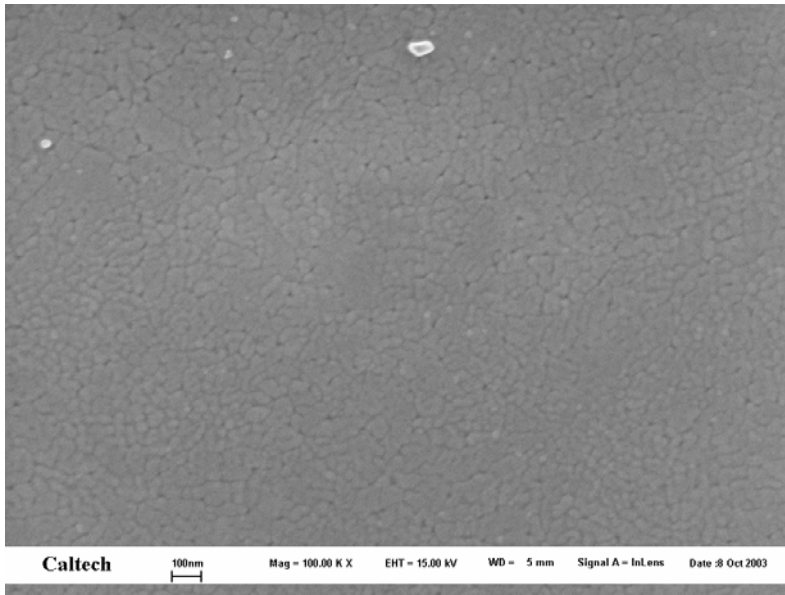


**Figure 23.** SEM image of three layer TIpDEA film prepared with  $T_p = 200^\circ\text{C}$  between layers and a heating rate of  $5^\circ\text{C}/\text{min}$  ( $T_c = 600^\circ\text{C}$ ).

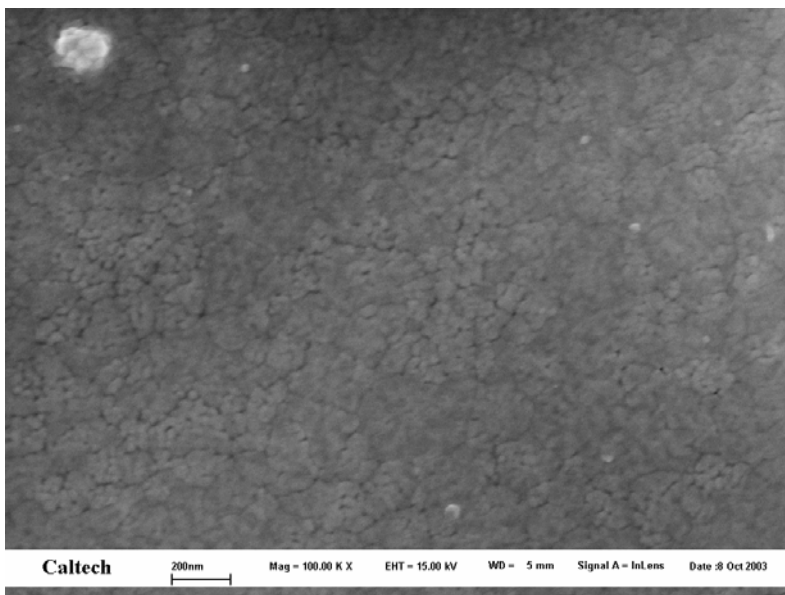


**Figure 24.** SEM image of three layer TIpDEA film prepared with  $T_p = 200^\circ\text{C}$  between layers and a heating rate of  $40^\circ\text{C}/\text{min}$ .

Thin films were prepared for the solid solution  $\text{Pb}_{1-x}\text{Ba}_x\text{TiO}_3$  ( $x = 0.2, 0.4, 0.5, 0.6, 0.8$ ). XRD of these films is shown in Figure 25. Tetragonal splitting of the (001/100) peaks is strongest for higher lead content, as expected due to the larger difference between the  $a$  and  $c$  lattice parameters of  $\text{PbTiO}_3$  compared with  $\text{BaTiO}_3$ . Some excess ethylene glycol was required to dissolve the barium acetate in the case of  $x = 0.8$ . All films show good (001/100)-orientation.

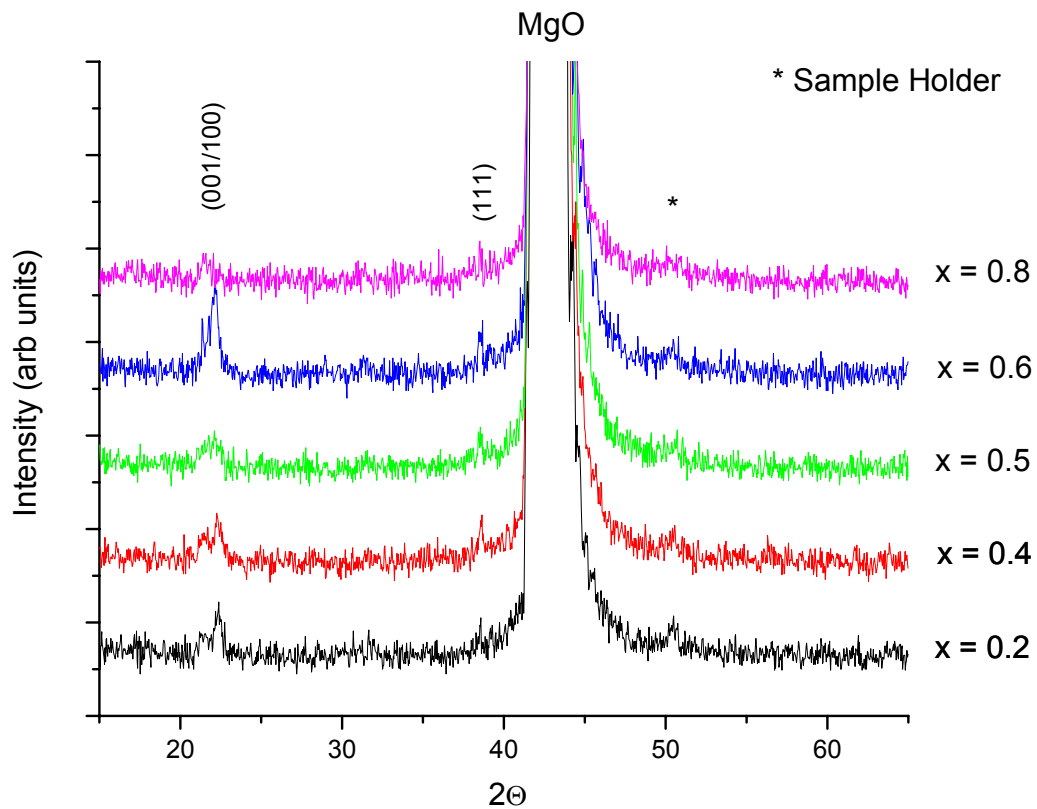


**Figure 25.** XRD of three layer  $\text{Pb}_{1-x}\text{Ba}_x\text{TiO}_3$  films with the compositions indicated (TIpDEA system,  $T_p = 200^\circ\text{C}$ ,  $T_c = 600^\circ\text{C}$ )

## II.6. Summary

Lead barium titanate was produced using a variety of novel sol-gel methods. Four particular systems were studied in detail, and one was found to be remarkably stable against small processing variations. The optimized system involves lead nitrate, barium acetate, and titanium isopropoxide metal precursors with ethylene glycol as a solvent and diethanolamine as a chelating agent. The optimal chelation agent:titanium ratio was found to be 4, and the water:titanium ratio was fixed at 4. Highly (001/100)-oriented  $\text{Pb}_{1-x}\text{Ba}_x\text{TiO}_3$  thin films were deposited onto MgO single crystals using a spin speed of 3000rpm for 40seconds, pyrolysis temperature of 200°C for 5 minutes between layers, and two hour calcination at 600°C with a 5°C/min heating rate. Layer thickness, as determined through cross-sectional SEM, is approximately 60nm.

## III. Electrodes

### III.1. Pt Electrode

Initial testing of ferroelectric properties was completed on a Pt/Si<sub>3</sub>N<sub>4</sub>/Si substrate with a sputtered Pt top electrode. Pt is commonly used as an electrode due to ease of deposition. Films deposited on Pt, however, are randomly oriented due to poor lattice matching between the cubic electrode layer and tetragonal perovskite film. It has been widely shown in literature that Pt electrodes are also associated with high fatigue [40, 87, 107]. Even though Pt is far from ideal for use in devices, it can be used for preliminary testing of the ferroelectric properties of the films.

Piezoresponse force microscopy (PFM) has recently been shown to be a useful technique for measuring the piezoelectric properties of thin films, imaging ferroelectric domain walls, and modifying domain structures [108-110]. The technique is essentially an extension of atomic force microscopy (AFM), involving applying a modulated ac voltage to the film through a conductive tip which is scanned across the film surface serving as a movable top electrode. Tip deflection and torsion from piezoelectric strain upon application of a voltage are used to determine in-plane and out-of-plane polarizations, respectively, thus quantifying the piezoresponse of the film. An excellent review of PFM techniques is given in [108].

PFM results for randomly oriented films deposited on Pt electrodes confirmed the films were indeed ferroelectric (Figure 26 and Figure 27). The figures show the local piezoelectric hysteresis and actuation strain curves for  $\text{Pb}_{0.5}\text{Ba}_{0.5}\text{TiO}_3$  deposited on Pt/ $\text{Si}_3\text{N}_4$ /Si obtained from the out-of-plane PFM signal. The effective piezoelectric coefficient,  $d_{33}^{\text{eff}}$ , obtained by calibrating tip deflection from the force-distance curve is less than 5.3 pm/V [111].

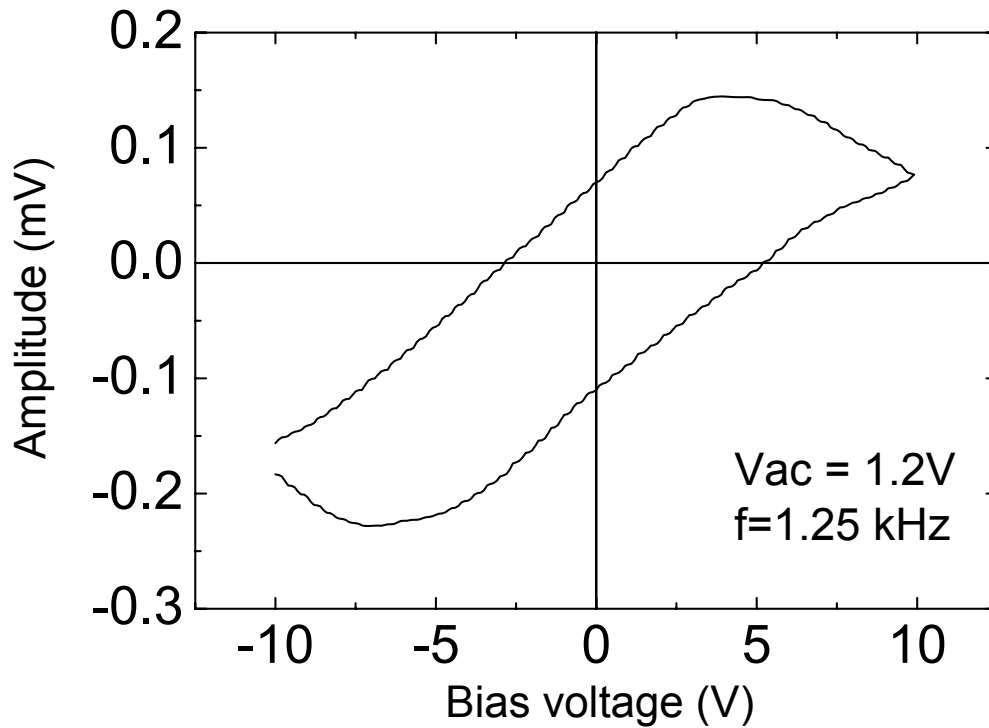


**Figure 26.** Local piezoresponse-electric field hysteresis curve obtained from out-of-plane polarization via PFM for three layer PBT film deposited on Pt/ $\text{Si}_3\text{N}_4$ /Si (TIpDEA system, 3 layers,  $T_p = 200^\circ\text{C}$ ,  $T_c = 600^\circ\text{C}$ ). [Data collected by Y.B. Park].

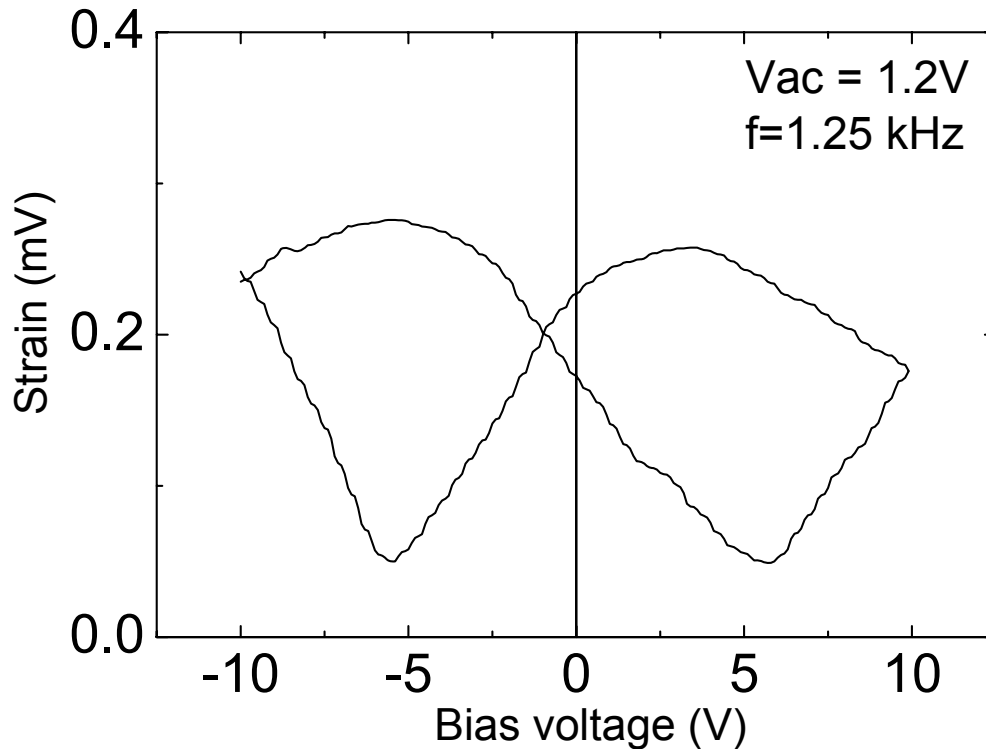


**Figure 27.** PFM results showing actuation strain for PBT film deposited on Pt/Si<sub>3</sub>N<sub>4</sub>/Si (TIpDEA system, 3 layers, T<sub>p</sub> = 200°C, T<sub>c</sub> = 600°C). [Data collected by Y.B. Park]

Traditional atomic force microscopy is achieved by scanning the tip across the film surface without application of an electric field. Vertical deflections of the tip correspond to film topography (Figure 28a). By applying an electric field to selected areas of the film through the conductive tip, domains in discrete areas can be switched by 180° and subsequently imaged using piezoresponse force microscopy [108, 109]. Scanning the tip across areas of the film and selectively applying an electric field, the 180° domain structure can be patterned, as shown in Figure 28b. Light areas and dark areas in the PFM image differ by 180° polarization. Recent work has demonstrated 90° domain

switching in these films through use of combined in-plane polarization and out-of-plane polarization piezoresponse force microscopy [111].

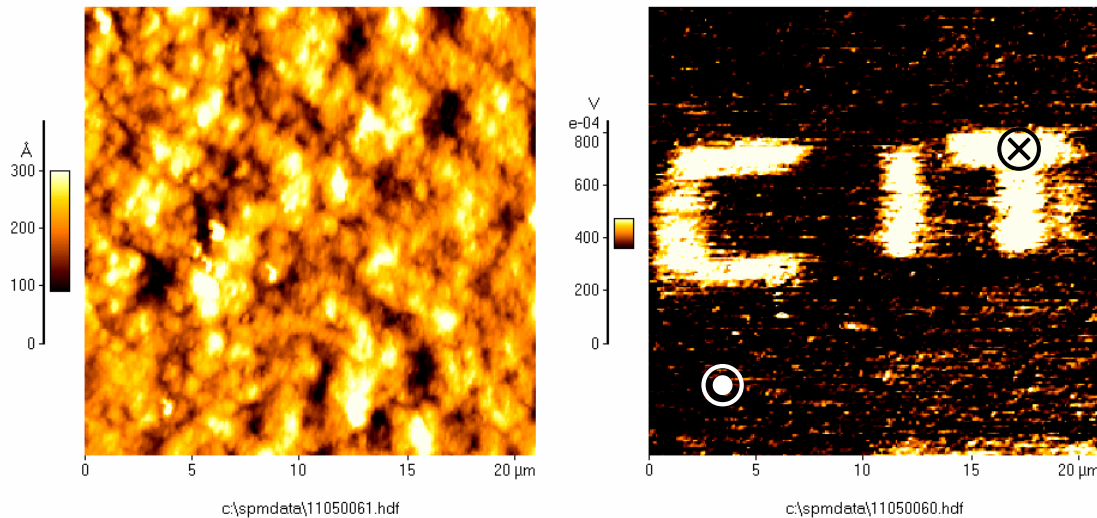


**Figure 28.** Atomic force microscopy of PBT thin film showing surface topography (left) and demonstration of  $180^\circ$  domain patterning using piezoresponse force microscopy (right). Light regions in the PFM image indicate polarization directed into the page, and dark areas show polarization directed out of the page. (TipDEA system, 3 layers,  $T_p = 200^\circ\text{C}$ ,  $T_c = 600^\circ\text{C}$ ) [Data collected by Y.B. Park]

## III.2. Conductive Oxide Electrodes

Conductive oxide electrodes provide an attractive alternative to Pt for use in ferroelectric devices. Though conductivity is slightly less than Pt, conductive oxides with perovskite structures and good lattice matching with PBT might provide better orientated ferroelectrics with improved fatigue compared to Pt electrodes [12]. A summary of the relevant properties of suitable conductive oxides is given in Table 13. The properties of PBT are also given for reference. Literature also provides some examples of doped

conductive oxides, which may be of future interest in tailoring the lattice parameters and TCEs of the chosen electrodes [112].

**Table 13.** Summary of lattice parameters and resistivities of several conductive oxide materials. Lattice parameters of PBT are included for comparison.

	<b>Pseudocubic Lattice Parameters (actual crystal structure)</b>	<b>Resistivity (Ohm*cm)</b>	<b>References</b>
<b>SrRuO<sub>3</sub> (SRO)</b>	$a_c = 3.921$ (orthorhombic)	$4.7-9.1 \cdot 10^{-4}$	[113]
<b>BaRuO<sub>3</sub> (BRO)</b>	$a_c = 4.07$ (rhombohedral)	$1.35 \cdot 10^{-4}$ $10^{-2}-10^{-4}$	[114, 115]
<b>La<sub>x</sub>Sr<sub>1-x</sub>CoO<sub>3</sub> (LSCO, x = 0.5)</b>	$a_c = 3.84$ (orthorhombic)	0.3 $2 \cdot 10^{-3}$	[116, 117]
<b>BaPbO<sub>3</sub> (BPO)</b>	$a_c = 4.27$ (orthorhombic)	$3-8 \cdot 10^{-4}$ $5.4 \cdot 10^{-5}$	[79, 118]
<b>LaNiO<sub>3</sub> (LNO)</b>	$a_c = 3.84$ (rhombohedral)	$5.4 \cdot 10^{-4}$	[119]
<b>Pb<sub>1-x</sub>Ba<sub>x</sub>TiO<sub>3</sub> (x = 0.5)</b>	$a_c = 3.99$ (tetragonal)		

Although most of the above conductive oxide electrodes shown in the table have similar lattice parameters to PBT, limited information is available concerning oriented conductive oxides produced via sol-gel methods [120]. There is even less information

available regarding oriented ferroelectrics deposited on oriented conductive oxide electrodes.

One of the most widely studied conductive oxide electrodes is  $\text{SrRuO}_3$  (strontium ruthenate, SRO). Sol-gel synthesis methods for SRO are generally considered undesirable, as a byproduct of SRO synthesis through annealing is highly toxic volatile  $\text{RuO}_2$ , and preparation of phase pure SRO via sol-gel is difficult [121, 122]. Instead, SRO is typically deposited using molecular beam epitaxy (MBE) or  $90^\circ$  off-axis sputtering [89]. Through MBE, SRO has been successfully grown epitaxially on Si [31, 123]. SRO is thus considered a viable candidate for substrate selection, though inexpensive synthesis via sol-gel is unlikely.

$\text{BaRuO}_3$  has been studied to a much lesser extent; however, its microstructure and conductivity have been shown to strongly depend on deposition temperature [114]. Sol-gel synthesis has not been reported, though  $\text{RuO}_2$  production is expected to remain a concern. Further, only weak orientation has been reported for lattice-matched substrates [115].  $\text{BaRuO}_3$  was not investigated in this study.

LSCO has been shown to have properties that vary substantially depending on particular composition [116, 124, 125]. Further, the tri-metallic nature of this compound greatly complicates sol-gel synthesis compared with the other systems with only two metal cations. Thus, sol-gel synthesis of LSCO was not investigated here.

LaNiO<sub>3</sub> (lanthanum nickelate, LNO) sol-gel methods have been studied to a greater extent, and several researchers have reported the production of preferentially oriented LNO on a limited selection of substrates [120, 126]. Some researchers have noted that diffusion of La and Ni species into PZT thin films has a deleterious effect on their ferroelectricity, possibly due to the high temperatures used in the studies [127]. It is noteworthy that oftentimes La is a desirable dopant for ferroelectrics, especially PZT and (Ba, Sr)TiO<sub>3</sub>. LNO was investigated as an electrode candidate.

BaPbO<sub>3</sub> (barium metaplumbate, BPO) is perhaps the most attractive conductive oxide electrode candidate for use with PBT, since it does not introduce new elements into the system. Liang [128] notes that diffusion of Pb and Ba into a PZT ferroelectric thin film does not negatively affect ferroelectric properties, as can the more commonly used LaNiO<sub>3</sub>. The advantages for modeling a BPO/PBT/BPO system are evident. Additionally, experimental expertise gained investigating PBT can be leveraged in attempts to produce BPO. For CVD production of BPO, for example, one would suspect simply turning off the Ti-source would lead to the desired conductive oxide without the need to move the substrate into a new chamber, or introduce any new processes.<sup>6</sup> Similarly, a sol-gel procedure for producing BPO would obviate the need for sputtering or other high vacuum processes entirely. Thus, using BPO would enable production of thin film stacks using a single deposition method. Such pure-play sol-gel or CVD films

---

<sup>6</sup> This expectation turns out to be incorrect, however, as our colleagues have not been able to produce BPO thin films via MOCVD. Working with the sol-gel version of the material, it appears likely this is caused by poor adhesion to the substrate or BPO having a large surface energy.

would presumably hasten the development cycle for integrating PBT into useful structures and devices, as compatibility issues between electrode and film deposition methods are sidestepped entirely.

### **III.2.1. BaPbO<sub>3</sub>: Literature Survey**

BaPbO<sub>3</sub> has been of sporadic interest to the research community for a variety of uses between its discovery in 1958 and the present [129]. Several papers have addressed the conduction mechanisms of BPO, in which the Pb *6s* and O *2p* orbitals overlap to produce high mobility electrons and lower mobility holes [130-132]. BPO thus has an interesting array of temperature-dependant physical properties. It has variously been suggested for applications in thick film resistors [133, 134], high temperature superconductors [135], thermoelectrics [136], and electrodes. Kuwabara describes thermally bonded BPO and PBT produced via solid state routes for use as a self-controlled heating element [137].

Liang [128] and Luo [107] showed that BPO used as an electrode effectively reduced the crystallization temperature of PZT, and produced a smoother film surface than compared with Pt. Luo also showed that the coercive field of PZT was lower for BPO electrodes than Pt. Skeele reports the single crystal resistivity of BPO is  $3.2 \times 10^{-4}$  Ohm\*cm [138].

In most examples in literature, the solid state synthesis approach is taken, where the precursors are milled together in powder form and then sintered at very high temperatures in controlled atmospheres. Commonly, this leads to Pb-deficient BPO. A few sol-gel

processes for BPO have been reported [13, 79, 129, 139, 140], though most involve high temperature processing. Wang [129] used a particularly simple process involving barium acetate, lead acetate, water, and PVA resulting in BPO phase formation at 600-700°C. Detailed TGA/DTA is provided as well as a discussion of the chemical pathway taken from precursors to final phase. However, the films were found to be unstable when additional layers were deposited, probably due to the redissolution or decomposition of the BPO layer. The authors attribute this to H<sup>+</sup> attacking the Pb-O bond, but note the film can be reclaimed upon re-annealing.

Takahashi [140] reported a 2-methoxyethanol route involving barium metal and lead isopropoxide, which resulted in BPO crystallization at temperatures as low as 500°C with some (110)-preferred orientation on MgO. However, a BaTiO<sub>3</sub> layer deposited on top of the BPO showed phase separation after heat treatment to 600°C, which was not explained.

Kuwabara reported a sol-gel method for depositing randomly oriented PBT on BPO, although it is unclear from the article whether the BPO substrate was oriented [137]. There has been only a single mention of preferentially (100)-oriented PBT on BPO, and the orientation is not perfect [16].<sup>7</sup> Only (100/001)-orientations are permissible for the proposed large-strain domain switching device applications, and thus further experimental study of the BPO system was conducted to determine whether good orientation could be achieved.

---

<sup>7</sup> Note: this study was published while research was ongoing.

### III.2.2. Sol-gel Synthesis of BaPbO<sub>3</sub>

Using the results of the extensive solubility tests performed for the initial synthesis of PBT, a series of compatible lead and barium precursors was selected for consideration. Initial attempts involved simply dissolving the precursors in a common solvent and then drying and calcining. This method, however, is likely to require the highest calcination temperatures, as the lead and barium are not likely to form Pb-O-Ba bonds while in solution, requiring formation of the oxide network through high temperature solid state reactions. The numerous phases present even after calcining at 600°C support this conclusion (Figure 29).

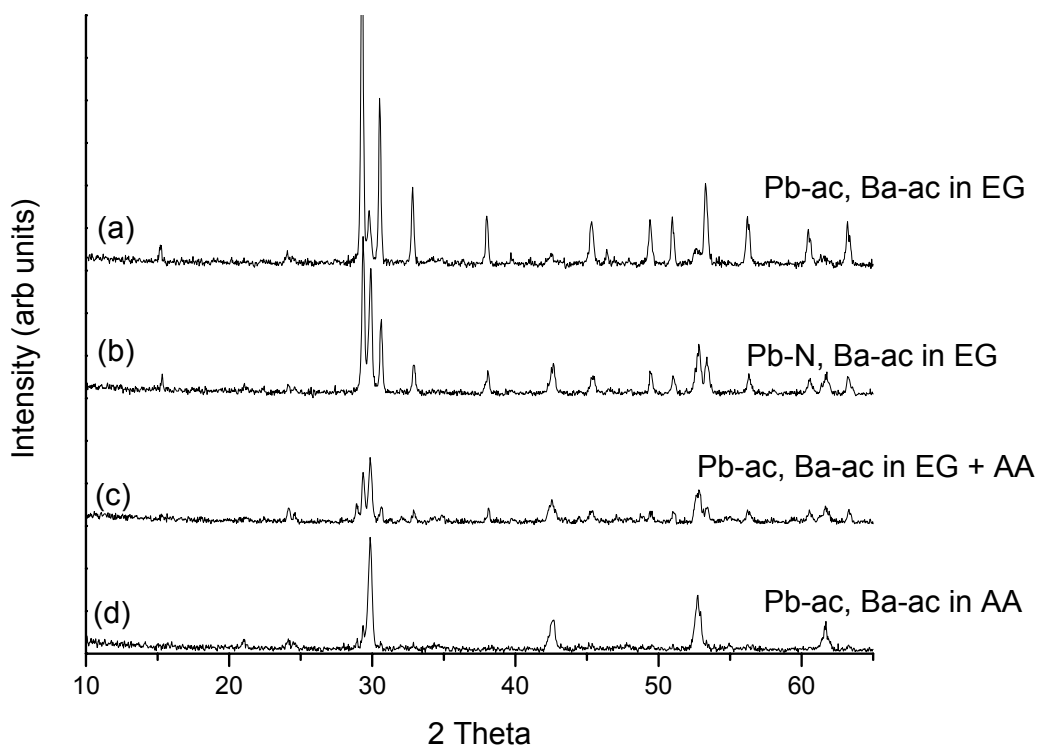


**Figure 29.** XRD of initial attempts to produce BPO powders. (Ba-ac = barium acetate, Pb-ac = lead acetate, Pb-N = lead nitrate, AA = acetic acid, EG = ethylene glycol, Tc = 600°C).

Next, chelating agents were investigated to encourage cross-linking in the sol. Acetic acid, known to encourage bridging bonding, was used to dissolve lead and barium acetate. It has the added benefit of providing a single-ligand system. After calcining at 600°C, this system showed considerably fewer phases (as shown in Figure 29d), and BPO was indeed the most prominent phase present in calcined powders.

The effect of a subsequent hydrolysis step was then considered. Water, in a prescribed ratio with Pb and Ba, was added, and the sol was dried at 175°C. Comparing the XRD results of the xerogels of sols prepared with and without water addition suggests that water addition results in a dramatic reduction in the presence of carbon species in the xerogel (Figure 30). Indeed, the xerogel of the  $R_w = 4$  sol shows primarily a mixture of oxides after drying. This is important because carbonate decomposition typically occurs at a higher temperature than oxide-oxide interaction. However, subsequent experiments showed the hydrolyzed sol became multiphasic by 600°C, and thus  $R_w = 0$  was chosen for further study.

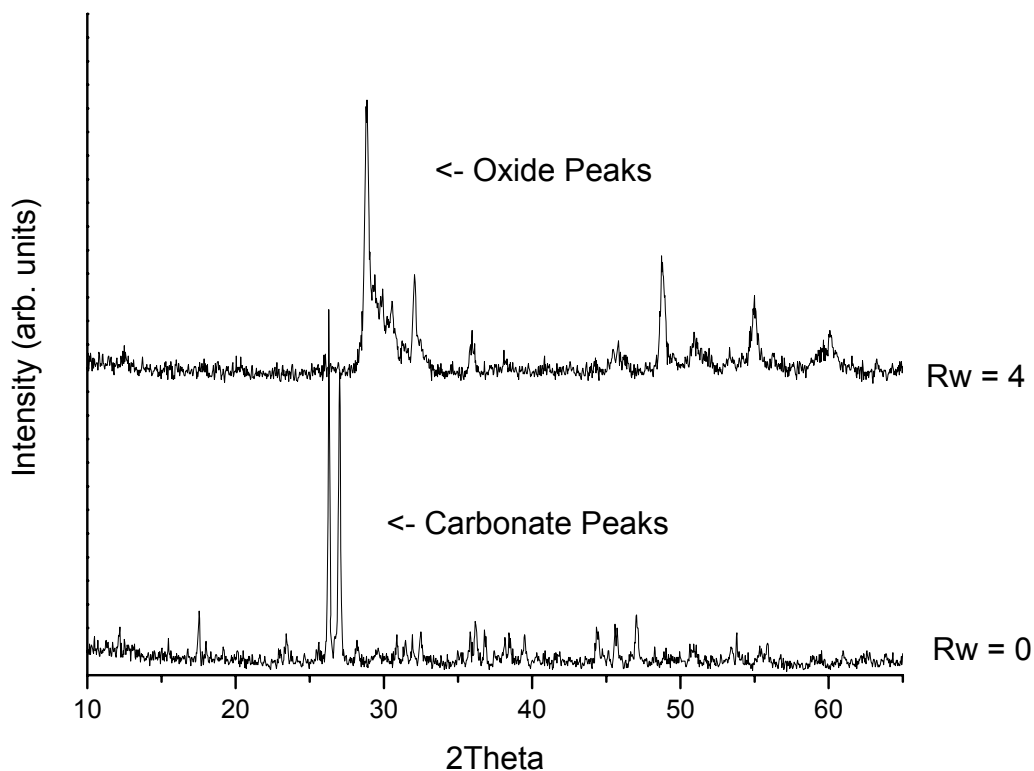


**Figure 30.** Influence of added water on BPO formation. XRD of xerogels with  $R_w = 0$  and 4, as indicated.

TGA/DSC of the dried xerogel ( $R_w = 0$ ,  $T_{\text{dry}} = 175^\circ\text{C}$ ) is shown in Figure 31. The atmosphere was 20% $\text{O}_2$ /80%Ar. A single exothermic event, accompanied by 25% weight loss occurs at  $342.4^\circ\text{C}$ , which is likely due to the release of  $\text{CO}_2$  from the decomposition of  $\text{BaCO}_3$ . ( $\text{BaCO}_3 \rightarrow \text{BaO} + \text{CO}_2$  suggests a weight loss of 22.3%). There is a possible second weight loss event starting at  $600^\circ\text{C}$ , possibly due to lead volatilization, which occurs at high temperatures.

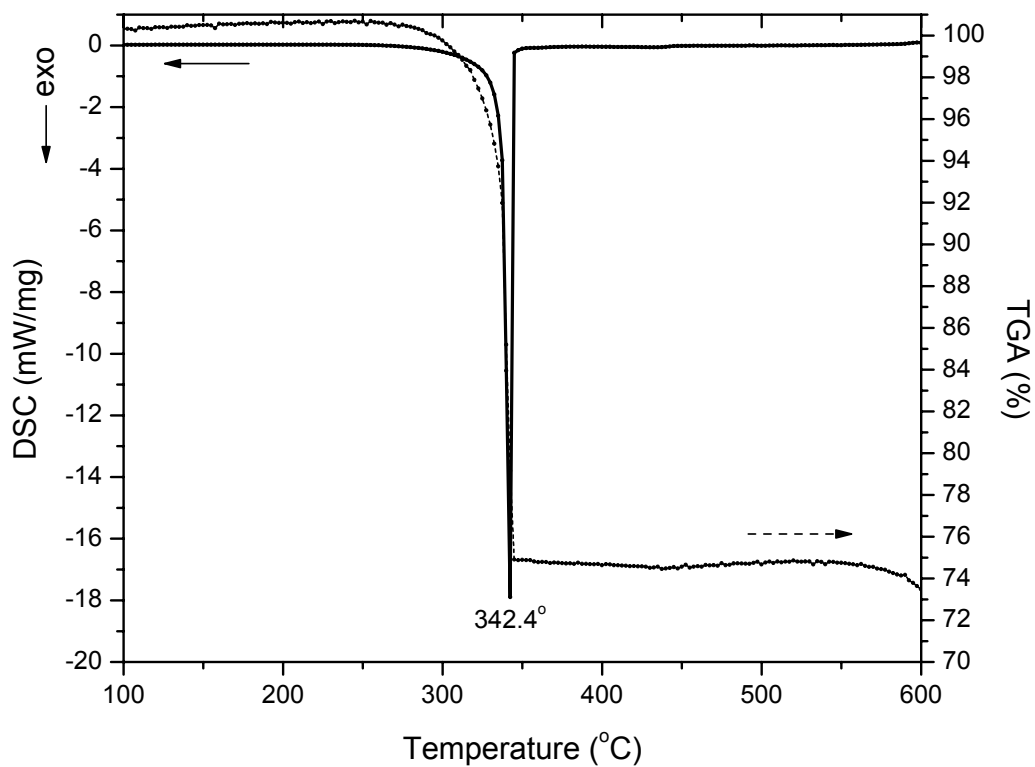


**Figure 31.** TGA/DSC of dried BaPbO<sub>3</sub> xerogel.

As shown in Figure 32, phase pure BaPbO<sub>3</sub> is formed by 600°C. Powders calcined at 600°C were pressed into pellets, and sheet resistance was measured using a four point probe. BaPbO<sub>3</sub> pellets showed surface resistance of 1.05Ωm/□.

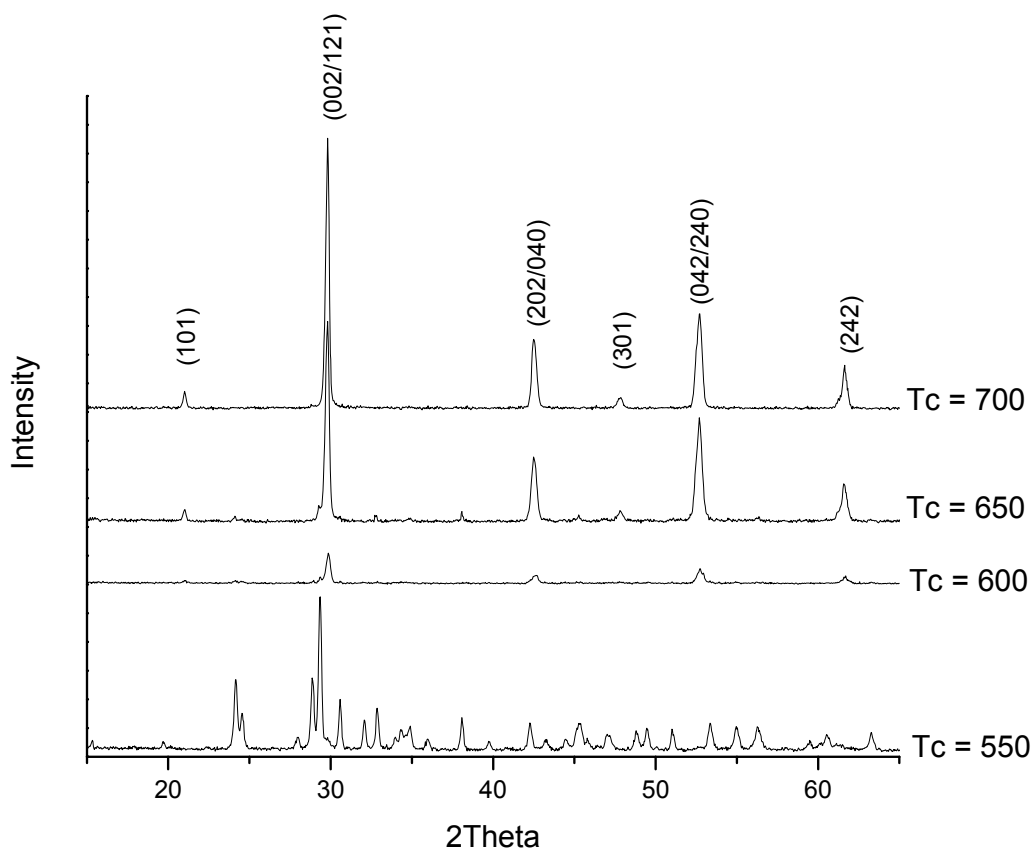


**Figure 32.** XRD of powders calcined in air at the temperatures indicated. The powder calcined at 550°C shows BaCO<sub>3</sub> (ICSD 05-0378) and PbO (05-0570). All others show BaPbO<sub>3</sub>.

Thin films were produced using the BPO sol via spin coating onto MgO single crystals at 2000rpm for 40 seconds. Multilayer films were pyrolyzed for 5 minutes at 200°C between layers. Finally, films were calcined at 600°C for two hours with heating rates of 1-2°C/min. XRD shows slightly oriented, phase pure BPO (Figure 33).

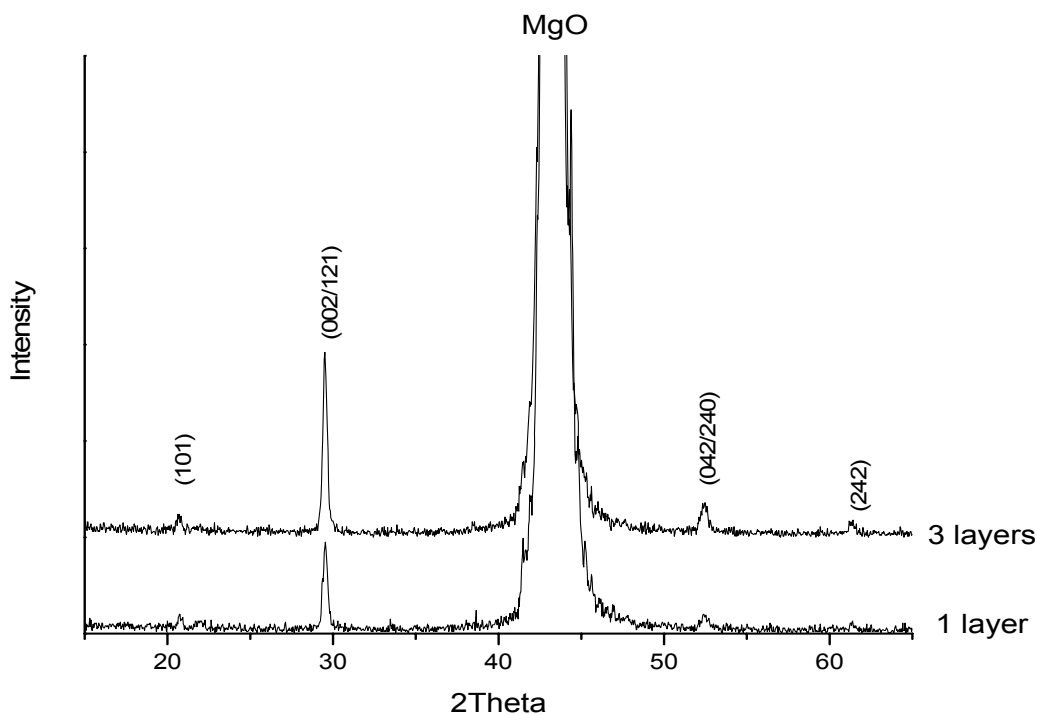


**Figure 33.** XRD of single layer and three layer BaPbO<sub>3</sub> thin films deposited on MgO and calcined to 600°C in air.

Single and multilayer BaPbO<sub>3</sub> thin films, however, showed limited adhesion to the substrate and could easily be rubbed off during handling. Samples were sent to Jandel for four point probe testing (using a tungsten carbide probe with 1mm spacing and 500μm tip radius, with Jandel multi-height probe station and 100g/needle loading). Not surprisingly, as seen in Table 14, thicker films resulted in lower resistances. A thinner film, produced by spin coating at 3000rpm, had a drastically higher resistance. Thus, for electrode applications thicker films are preferred. To determine the effect of calcination atmosphere on surface resistance, two films were calcined in flowing oxygen. As shown

in Table 14, these films showed lower resistance, consistent with p-type conductivity [141].

**Table 14.** Surface resistance of BaPbO<sub>3</sub> thin films calcined at 600°C.

Number of Layers	Atmosphere	Sheet Resistance (Ohm/□)
1*	Air	$1.5 \times 10^5$
3	Air	$5.4 \times 10^3$
1	Oxygen	$2.4 \times 10^3$
3	Oxygen	$1.6 \times 10^3$

(\* spin speed was 3000rpm)

PBT films deposited on the BPO electrodes showed some (001/100)-preferred orientation (Figure 34), with no new phases detected. Although additional studies were performed with varied heating rates, pyrolysis temperatures, and substrates, orientation did not show marked improvement. The lack of strong orientation and poor adhesion to the substrate make BaPbO<sub>3</sub> less than ideal for our research purposes, and other conductive oxide electrodes were subsequently investigated.

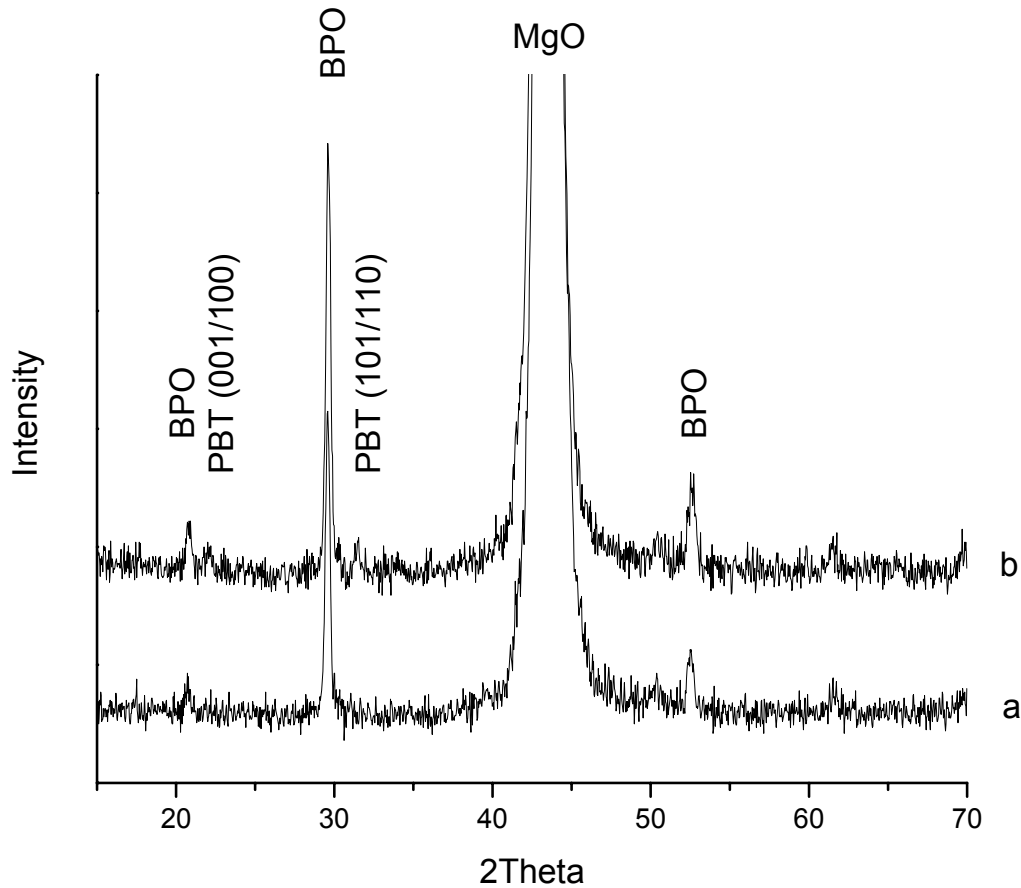


**Figure 34.** XRD of (a) BaPbO<sub>3</sub> thin film on MgO and (b) single layer Pb<sub>0.5</sub>Ba<sub>0.5</sub>TiO<sub>3</sub> film on BaPbO<sub>3</sub>/MgO showing preferred (001/100) orientation.

### III.2.3. Lanthanum Nickelate Literature Survey

LaNiO<sub>3</sub> (LNO) is a conducting oxide with a rhombohedral perovskite structure ( $a = 0.546$  nm). Along its  $\langle 100 \rangle$  pseudocubic direction, the repeat distance is 0.384 nm, which matches well with many ferroelectric materials, including PBT. Several methods have been employed in an attempt to grow oriented LNO thin films suitable for use as an electrode material, including sputtering, metal-organic decomposition, and sol-gel [16,

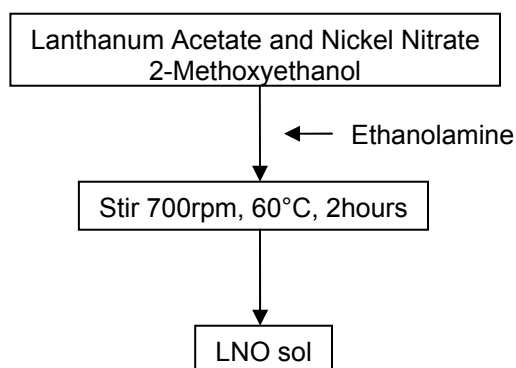
120, 126, 142-144]. Pontes was successful in growing highly, but not completely, (100)-oriented  $\text{Pb}_{0.8}\text{Ba}_{0.2}\text{TiO}_3$  on lanthanum nickelate; however, he used lanthanum aluminate ( $\text{LaAlO}_3$ ) single crystal substrates, which have nearly perfect lattice matching to both LNO and PBT [16]. Pontes also used a very unconventional annealing method involving microwave radiation.  $\text{LaAlO}_3$  is a non-ideal substrate because it is expensive and cannot be as easily integrated into current semiconductor processing methods, in which Si is generally used. Miyake was successful in growing oriented LNO with a 2-methoxyethanol and monoethanolamine system using  $\text{SiO}_2$  glass, Ce/Si, and  $\text{SrTiO}_3$  as substrates; however, few synthetic details were given [120, 126].

#### **III.2.4. Sol-gel Synthesis of $\text{LaNiO}_3$**

Several sol-gel systems were developed to produce  $\text{LaNiO}_3$  (Table 15). In the end, most were found to be unsuitable for producing oriented electrode thin films. One system, however, was found to produce extremely well-oriented films. The  $\text{LaNiO}_3$  sol was prepared by dissolving lanthanum acetate (5 mmol) and nickel nitrate (5 mmol) in 2-methoxyethanol (10.7mL), with the addition of ethanolamine (5 mL) (Figure 35). The resulting sol is stirred at  $60^\circ\text{C}$  for 2 hours. Thin film  $\text{LaNiO}_3$  electrodes were produced via spin-coating the sol onto various cleaned substrates at 3000rpm for 40 seconds. A two-step pyrolysis and short anneal (detailed below) were carried out between layers, as suggested by Miyake. Calcination temperature and film thickness (number of layers) were varied to determine the effect on orientation and conductivity.

**Table 15.** Summary of LaNiO<sub>3</sub> sol-gel systems investigated.

Lanthanum Precursor	Nickel Precursor	Solvent(s)	Oriented Films?
Lanthanum Acetate	Nickel Nitrate	Ethylene Glycol + Water	No
Lanthanum Acetate	Nickel Nitrate	Ethylene Glycol + Ethanolamine	No
Lanthanum Acetate	Nickel Nitrate	Acetic Acid	No
Lanthanum Acetate	Nickel Nitrate	2-Methoxyethanol + Ethanolamine	Yes
Lanthanum Acetate	Nickel Acetate	Acetic Acid	No

**Figure 35.** Sol-gel system for producing LaNiO<sub>3</sub> thin films.

LaNiO<sub>3</sub> sol was dried at 150°C to form a xerogel. Simultaneous thermal analysis data from the xerogel is shown in Figure 36, where a heating rate of 5°C/min was used and the atmosphere was 20%O<sub>2</sub>/80%Ar. As shown in the figure, LaNiO<sub>3</sub> forms through two main exothermic events, and each is associated with a weight loss. Total weight loss between 100-700°C is 58%. Mass spectrometry suggests the first exothermic event,

which peaks at 265°C, is primarily associated with the release of H<sub>2</sub>O. The second exotherm, with a peak at 414°C, is associated with the release of CO<sub>2</sub>, NO, and others, likely corresponding to a combustion process. Weight loss is complete by 700°C, though the DSC curve remains concave-up, suggesting crystallization is continuing.

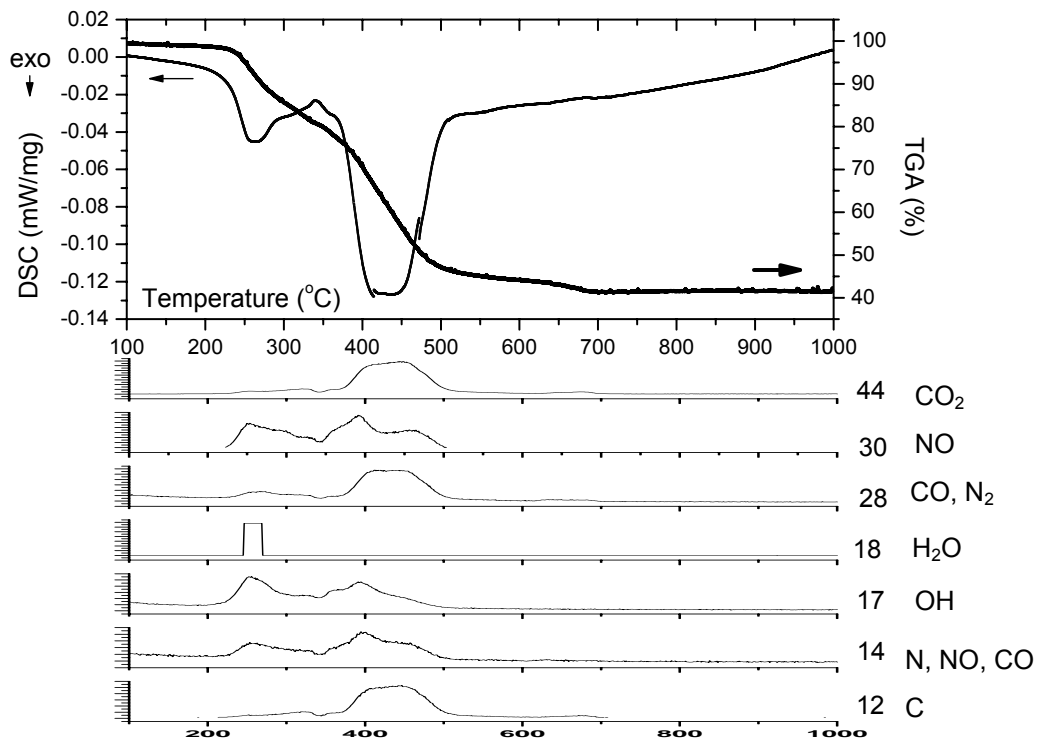


**Figure 36.** Simultaneous thermal analysis (DSC/TGA) of LaNiO<sub>3</sub> xerogel and mass spectrometry data of volatiles released during heating (heating rate = 5°C/min, 20%O<sub>2</sub>/80%Ar).

The conventional film deposition method, involving a five minute pyrolysis at 400°C between layers and then final calcination at 700°C for two hours with a heating rate of 5°C/min, produced unoriented films (Figure 37).

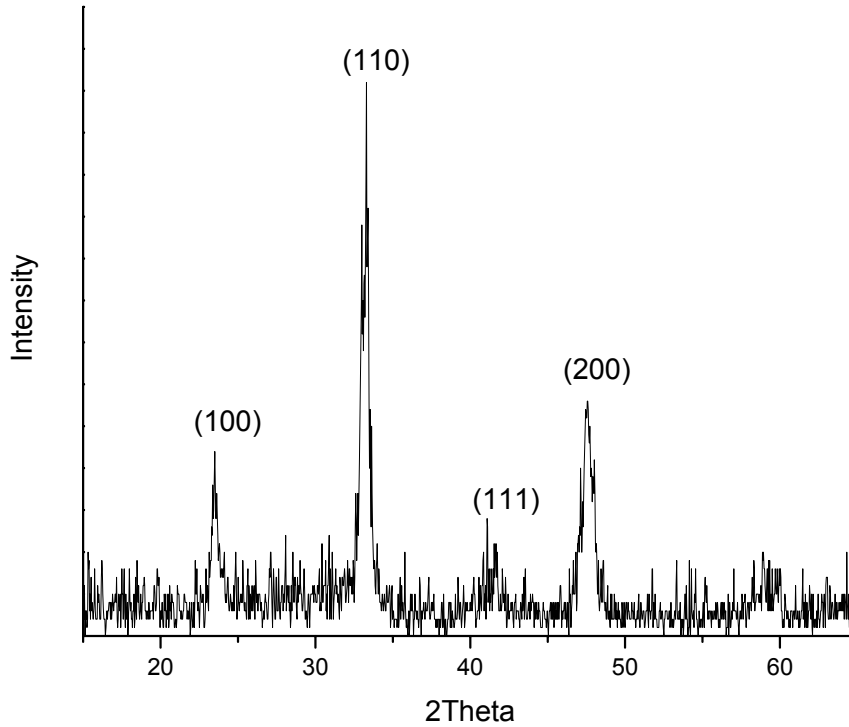


**Figure 37.** XRD of four layer  $\text{LaNiO}_3$  deposited on  $\text{Si}_3\text{N}_4/\text{Si}$  with five minute pyrolysis at  $400^\circ\text{C}$  between layers and final calcination at  $700^\circ\text{C}$  for 2 hours with heating rate of  $5^\circ\text{C}/\text{min}$ .

Better orientation was obtained for films pyrolyzed (at temperature  $T_p$ ) for 5 minutes and then briefly annealed in a preheated furnace at the calcination temperature ( $T_c$ ) for 10 minutes between layers. After the final layer was deposited, the film was calcined at  $T_c$  for 2 hours in stagnant air. XRD of LNO thin films deposited on fused silica (using a pyrolysis temperature of  $300^\circ\text{C}$ ) show that LNO has formed by  $600^\circ\text{C}$ , and crystallization continues to improve to  $700^\circ\text{C}$  (Figure 38). These films are all predominantly (100)-oriented, and orientation increases as crystallization continues.

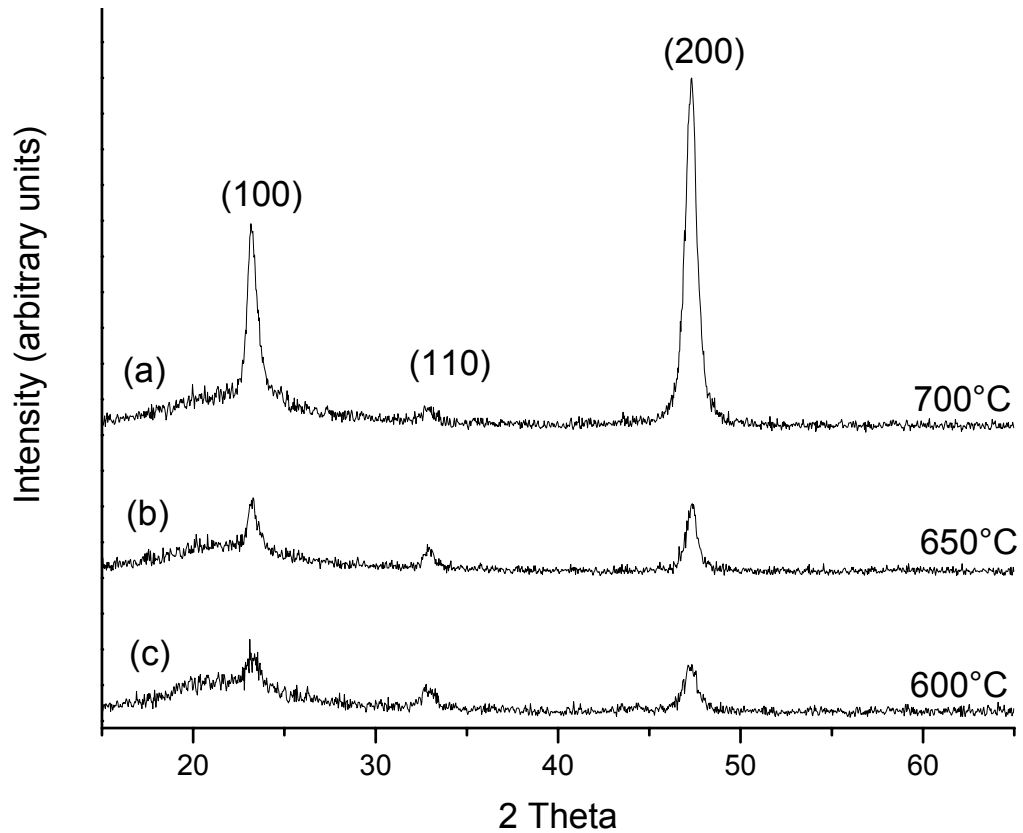


**Figure 38.** XRD of LaNiO<sub>3</sub> deposited on fused silica and calcined at the temperatures indicated. (4 layers,  $T_p = 300^\circ\text{C}$ ) The amorphous hump seen at low 2-theta is due to the amorphous silica substrate.

Pyrolysis temperature was varied, and the resulting effects on orientation and sheet resistance are shown in Table 16. Orientation factors were calculated using XRD patterns from the films. The factor is calculated by adding the intensity of the desired (100) and (200) LNO peaks and dividing by the total intensity of all of the LNO peaks in the scan. For a randomly oriented film, this factor would be 0.362. As shown in the table, a pyrolysis temperature of 400°C produced the most oriented LNO films, though well-oriented films were obtained for all of the pyrolysis temperatures. This suggests the use of a two-stage heating process between layers was more important than the particular

pyrolysis temperature used. Following this optimized procedure, films were produced with 5 minute pyrolysis on a hot plate at 400°C then a 10 minute anneal to 700°C in a preheated furnace between layers.

**Table 16.** Orientation factors (the sum of the intensities of (100) and (200) LaNiO<sub>3</sub> peaks divided by the intensity of all peaks) and sheet resistances of LaNiO<sub>3</sub> films deposited on fused silica prepared using the pyrolysis temperatures (T<sub>p</sub>) indicated. (6 layers, T<sub>c</sub> = 700°C)

Sample	Orientation	Sheet Resistance (Ω/□)
T <sub>p</sub> = 200°C	.980	55.3
T <sub>p</sub> = 300°C	.969	85.5
T <sub>p</sub> = 400°C	.983	78.5
T <sub>p</sub> = 500°C	.977	79.2

LNO was deposited on a variety of amorphous and crystalline substrates using the same procedure. As shown in Figure 39, the LNO is predominantly (100)-oriented in all cases.<sup>8</sup> This is exciting because the ability to obtain oriented LNO electrodes directly on Si enables numerous semiconductor processing techniques that are not typically compatible with specialized single crystal substrates frequently used to obtain oriented ferroelectric thin films via lattice matching (e.g., SrTiO<sub>3</sub>, MgO, LaAlO<sub>3</sub>). The fact that LNO is oriented on a wide variety of materials indicates that the orientation is not inherited from the substrate via templating. Rather, orientation is achieved through a

---

<sup>8</sup> LaNiO<sub>3</sub> was later deposited on sapphire and also found to be (100)-oriented. Sapphire is a commonly used substrate for electronic applications involving UV and microwave radiation. Studies are underway to determine whether LaNiO<sub>3</sub> electrodes on sapphire can provide increased performance of BST for tunable microwave filter applications [collaboration with Melanie Cole at Army Research Lab].

mechanism that involves random heterogeneous nucleation at the film/substrate interface during pyrolysis. During the crystallite growth stage, crystals with slow-growing, low surface energy faces oriented parallel to the substrate eventually overgrow crystals displaying fast-growing, high surface energy faces (Figure 40). This is referred to in literature as the Van der Drift orientation mechanism [145].

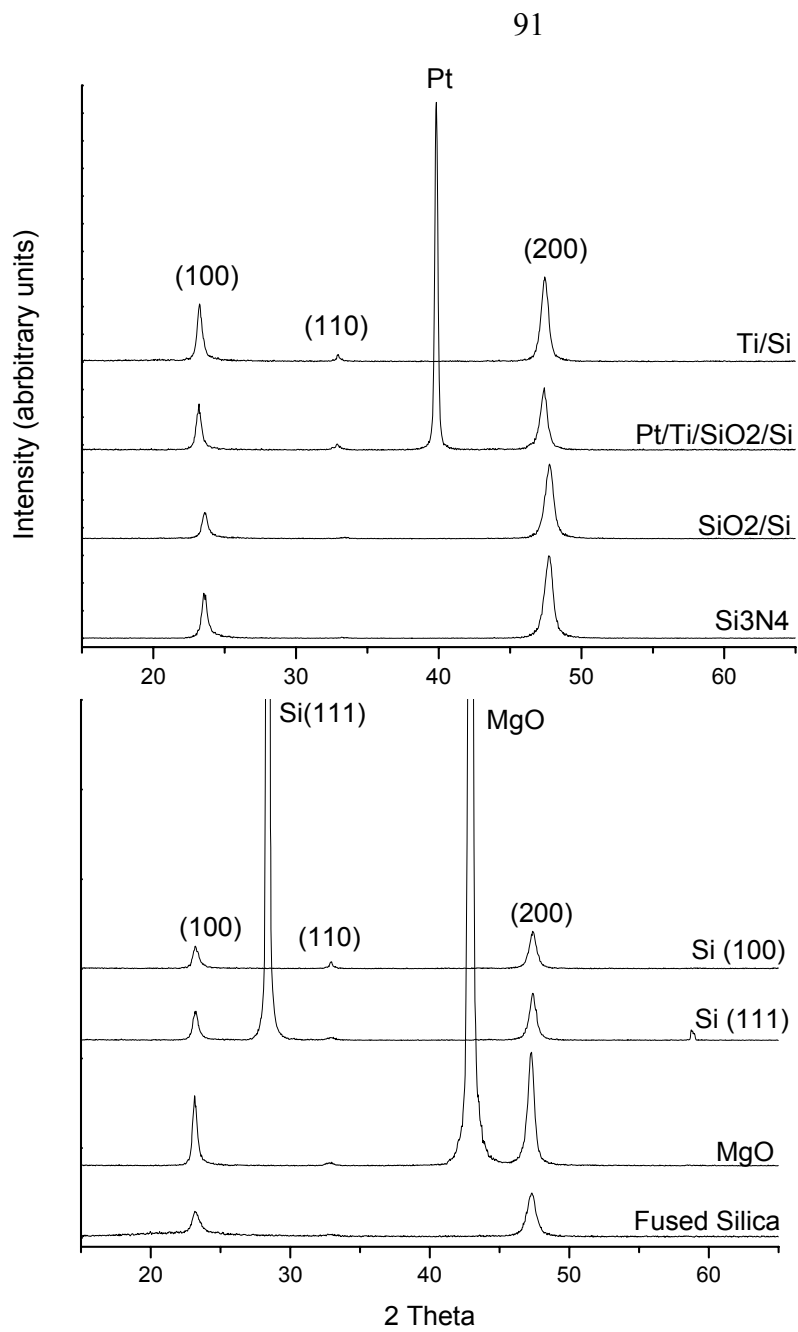


**Figure 39.** XRD of  $\text{LaNiO}_3$  thin films deposited on a variety of substrates. (4 layers,  $T_p = 400^\circ\text{C}$ ,  $T_c = 700^\circ\text{C}$ )

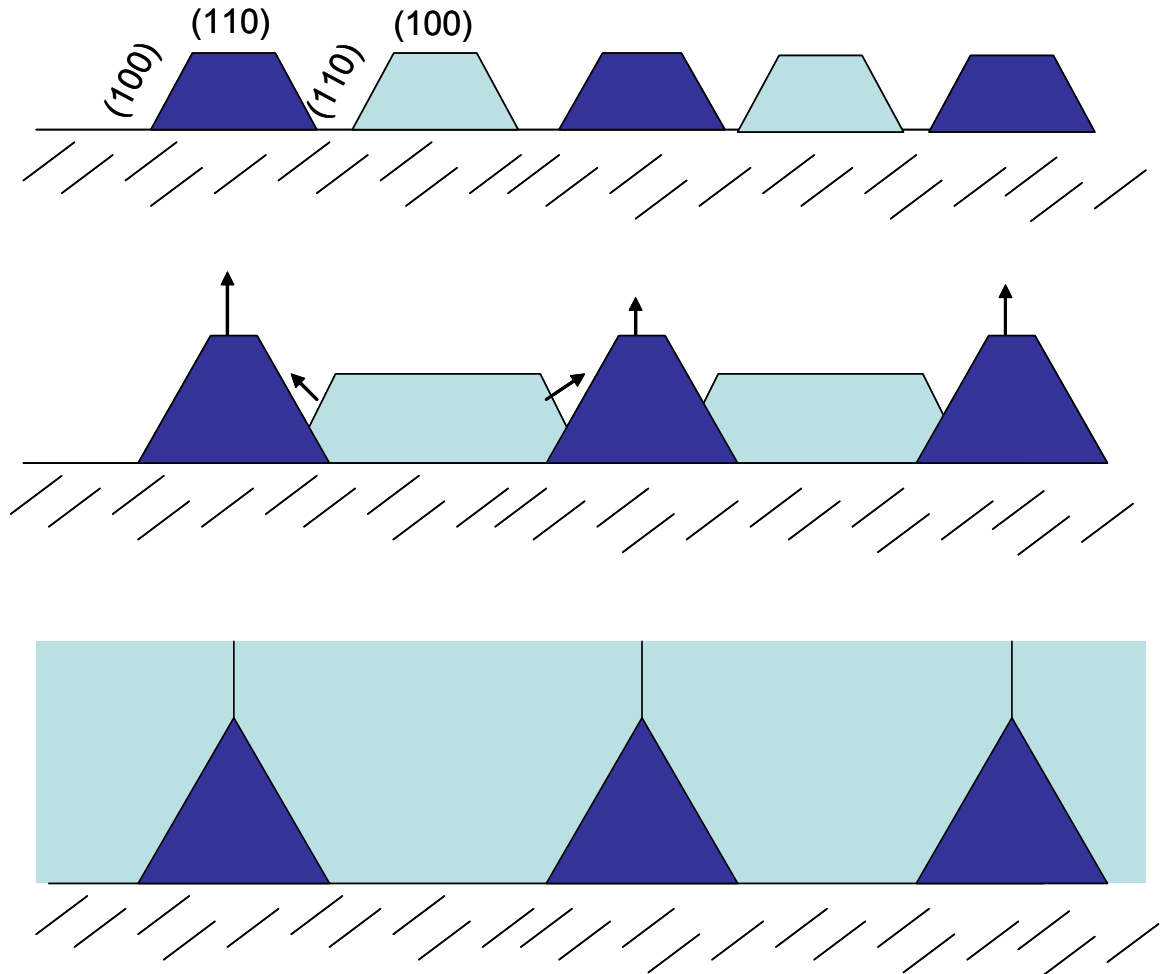


**Figure 40.** Illustration of the orientation mechanism of  $\text{LaNiO}_3$ . (top) Heterogeneous random nucleation occurs at the film-substrate interface. Light nuclei are those with the (100) plane parallel to the substrate and dark nuclei are those with (100) plane at an angle to the substrate. (middle) During growth, the (100) surfaces grow slower than planes with higher surface energy, resulting in unfavorably oriented dark nuclei growing faster vertically and taking on a triangular shape while favorably oriented light nuclei grow outward. (bottom) Outward growth of favorably oriented nuclei overtakes unfavorably oriented grains, leaving a (100)-oriented film.

The sheet resistance of these films is given in Table 17. Cross sectional SEM showed the LNO film thickness was  $48 \pm 5 \text{ nm}$  per layer.

**Table 17.** Orientation and conductivity of the LaNiO<sub>3</sub> films deposited on various substrates.

<b>T<sub>p</sub></b> <b>(°C)</b>	<b># Layers</b>	<b>Substrate</b>	<b>Orientation</b>	<b>Sheet Resistance</b> <b>(Ω/□)</b>
300	8	Fused Silica	.979	85.6
300	6	Fused Silica	.969	85.5
300	4	Fused Silica	.978	146.6
300	4	Pt/Ti/SiO <sub>2</sub> /Si	.949	.92 (see Pt not LNO here)
300	4	MgO	.987	21.3
300	4	Ti/Si	.955	39.4
300	4	Si(111)	.970	44.2
300	4	Si(100)	.901	50.4
400	4	Si(100)	.942	28.4
400	4	Si <sub>3</sub> N <sub>4</sub>	.995	33.5
400	4	SiO <sub>2</sub> (2μm)/Si	.993	39.3

The effect of thickness on orientation and sheet resistance was investigated. XRD shows a single layer LNO film is only slightly oriented, while subsequent layers show improved orientation (Figure 41). This improvement of orientation with thickness further supports the orientation mechanism described above. Similarly, sheet resistance is high for a single layer film and drops rapidly with each additional layers (Table 18 and Figure 42). Thus, for the four layer film deposited on Si(100), sheet resistance is 28.4 Ω /□, corresponding to a resistivity of  $5.45 \times 10^{-4} \Omega \cdot \text{cm}$ . This agrees well with the resistivity of  $5.4 \times 10^{-4} \Omega \cdot \text{cm}$  reported by Bao for LaNiO<sub>3</sub> electrodes used in ferroelectric devices [119], and thus 4 layer films are considered ‘thick enough’ for optimal orientation and conductivity.

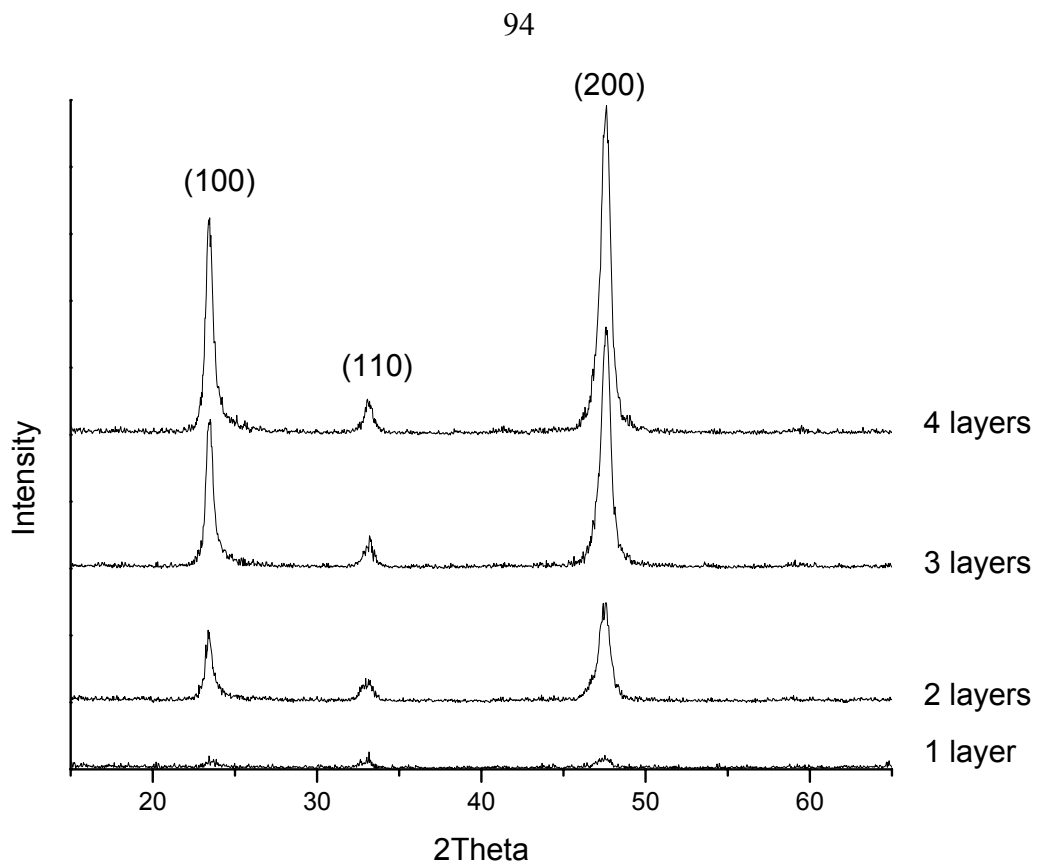


**Figure 41.** XRD of LaNiO<sub>3</sub> thin films deposited on Si(100) with the number of layers indicated ( $T_p = 400$ ,  $T_c = 700^\circ\text{C}$ ).

**Table 18.** Orientation and sheet resistance of LaNiO<sub>3</sub> thin films with the indicated number of layers (on Si,  $T_p = 400^\circ\text{C}$ ,  $T_c = 700^\circ\text{C}$ ).

Number of Layers	Orientation	Sheet Resistance ( $\Omega / \square$ )
1	0.616	536.1
2	0.901	86.6
3	0.929	44.4
4	0.942	28.4

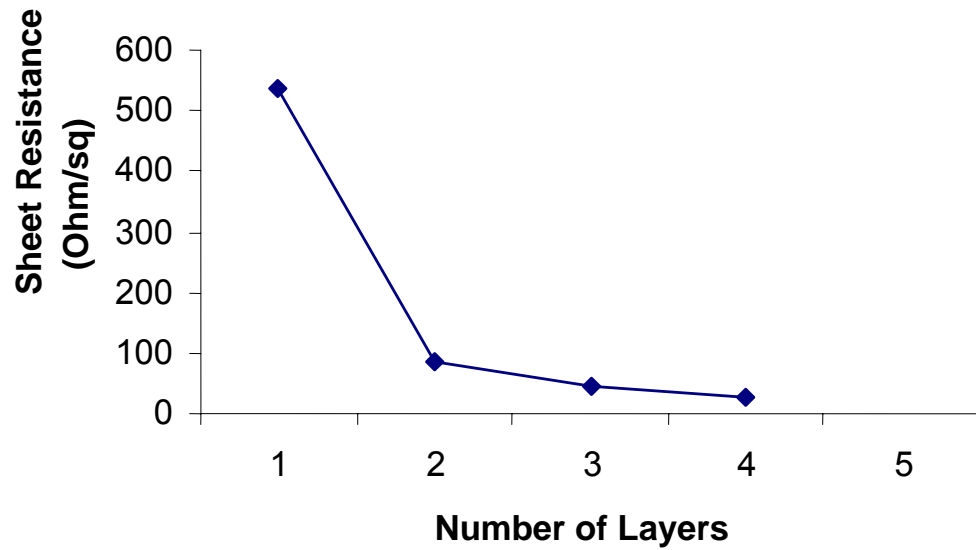


**Figure 42.** Graphical representation of the previous table showing rapid decline in  $\text{LaNiO}_3$  sheet resistance with increasing number of layers.

Surface roughness of four layer films was measured using atomic force microscopy (AFM). Results for various substrates are given in Figure 43. Surface roughness for the sample deposited on MgO is slightly higher than the others, probably due to the degradation of the MgO surface by atmospheric moisture.

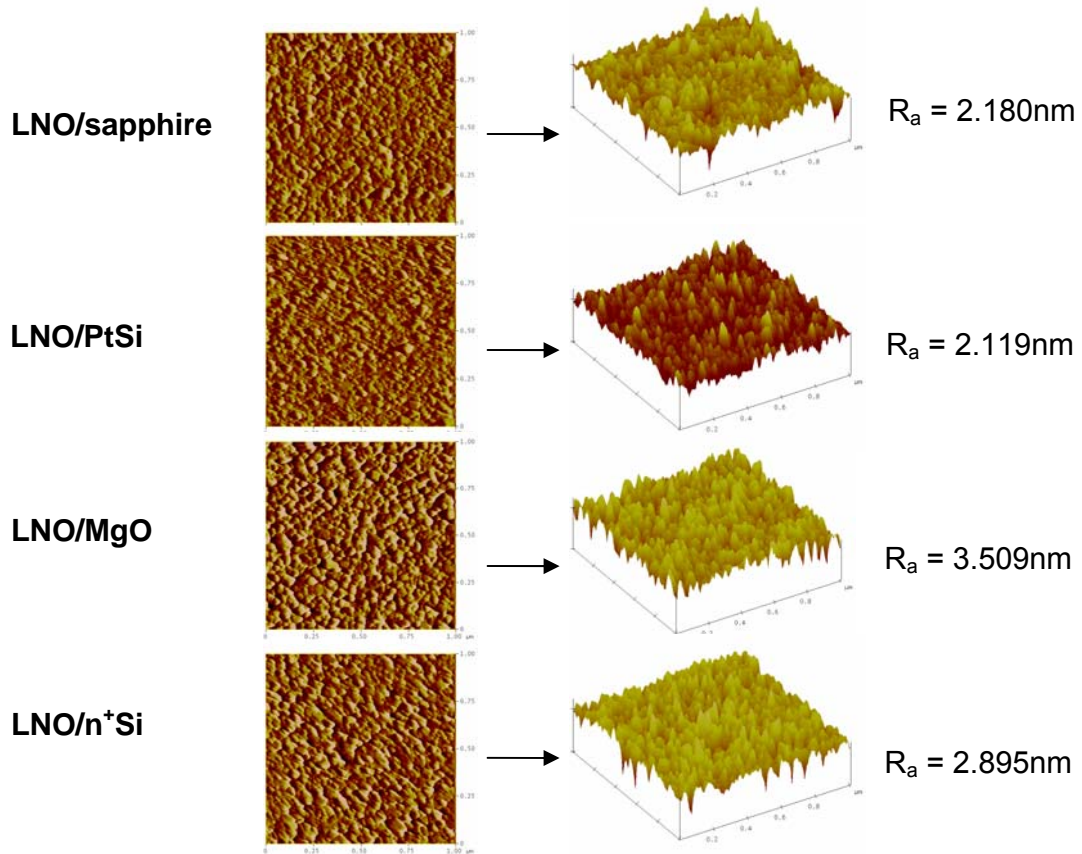


**Figure 43.** Atomic force microscopy (AFM) of 4 layer  $\text{LaNiO}_3$  films deposited on the substrates indicated.

[Data courtesy Melanie Cole, Army Research Laboratory]

SEM was used to image the surface of  $\text{LaNiO}_3$  films. The films were found to be somewhat porous (Figure 44). Preliminary studies show porosity is correlated with processing parameters including concentration, pyrolysis temperature, and calcination temperature.

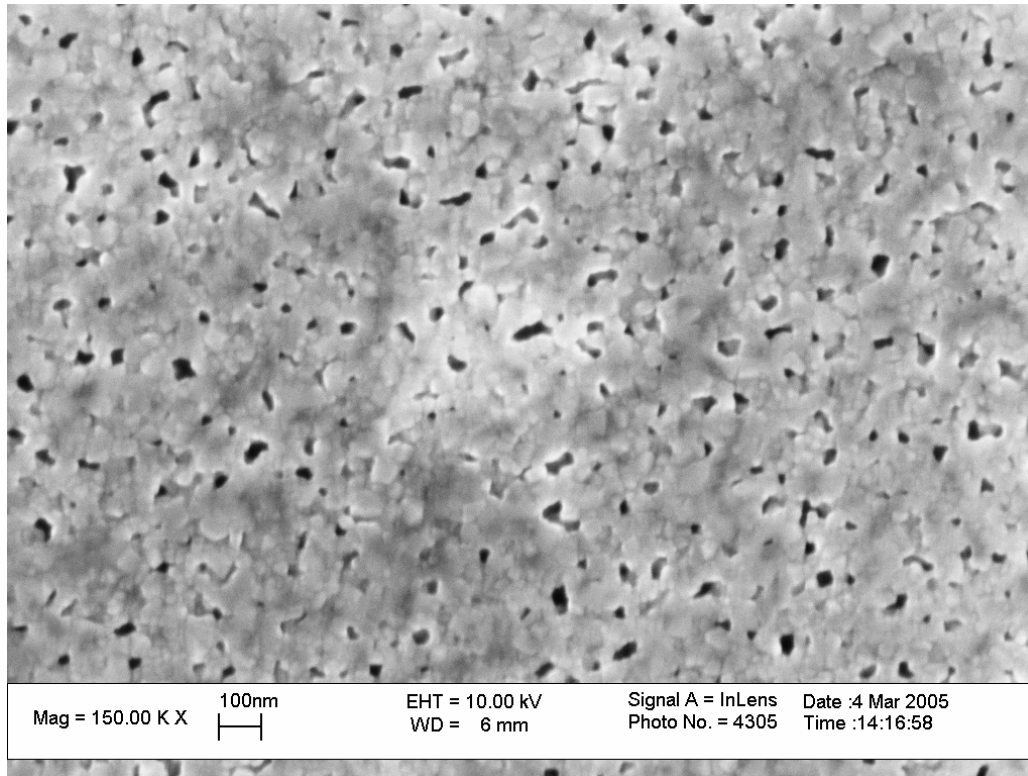


**Figure 44.** SEM image of 4 layer  $\text{LaNiO}_3$  film deposited on Si (sol concentration 0.32M,  $T_p = 400^\circ\text{C}$ ,  $T_c = 700^\circ\text{C}$ ).

The effect of sol concentration on 4 layer LNO films deposited on single crystal MgO substrates is shown in Figure 45 and Figure 46. Higher concentration LNO sols resulted in slightly less porous films; however, they were prone to cracking (Figure 47). Miyazaki presented similar results and attributed the cracking to the large stresses generated as organic components are removed from the thicker films associated with high concentration [146]. Additional studies are necessary to determine the optimal concentration of LNO sols.

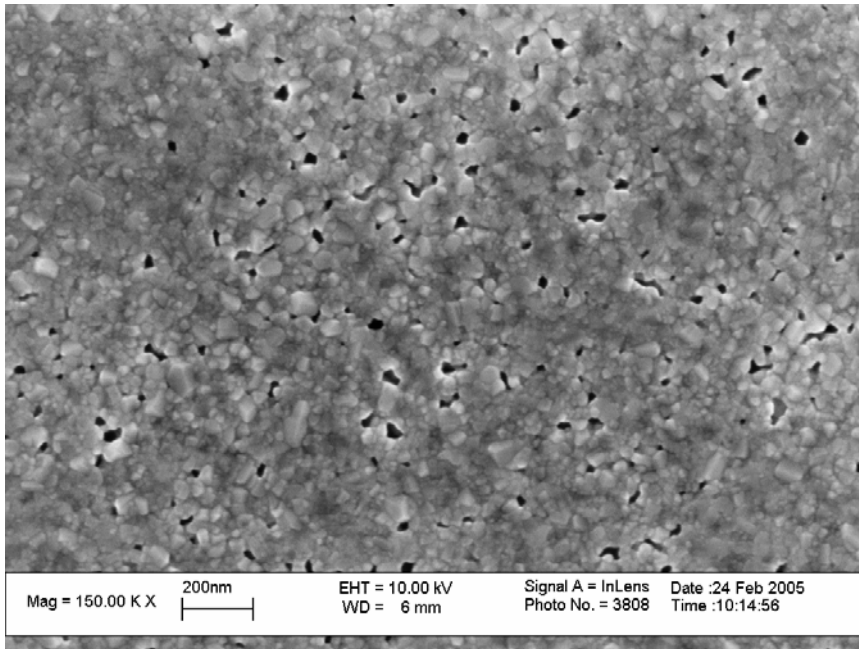


**Figure 45.** SEM image of 4 layer LaNiO<sub>3</sub> film deposited on MgO using sol with 0.22M concentration (T<sub>p</sub> = 400°C, T<sub>c</sub> = 700°C).

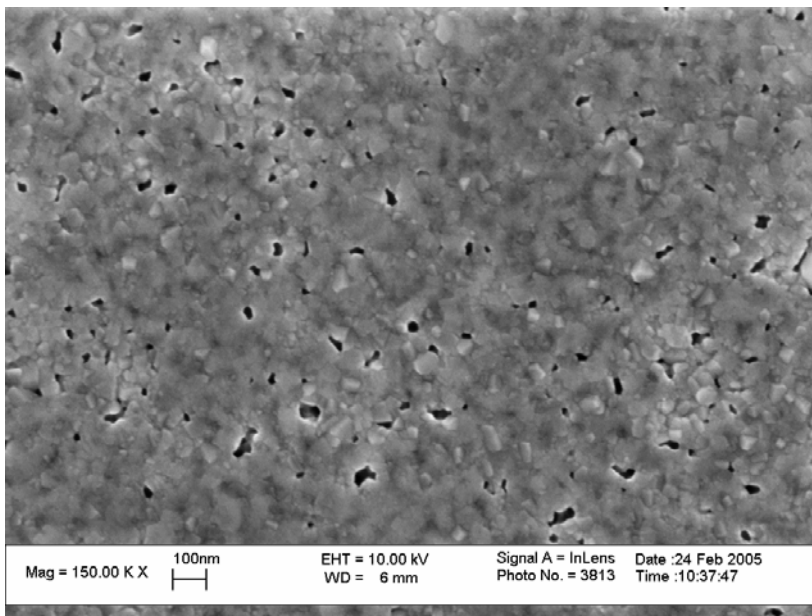


**Figure 46.** SEM image of 4 layer LaNiO<sub>3</sub> film deposited on MgO using sol with 0.42M concentration (T<sub>p</sub> = 400°C, T<sub>c</sub> = 700°C).

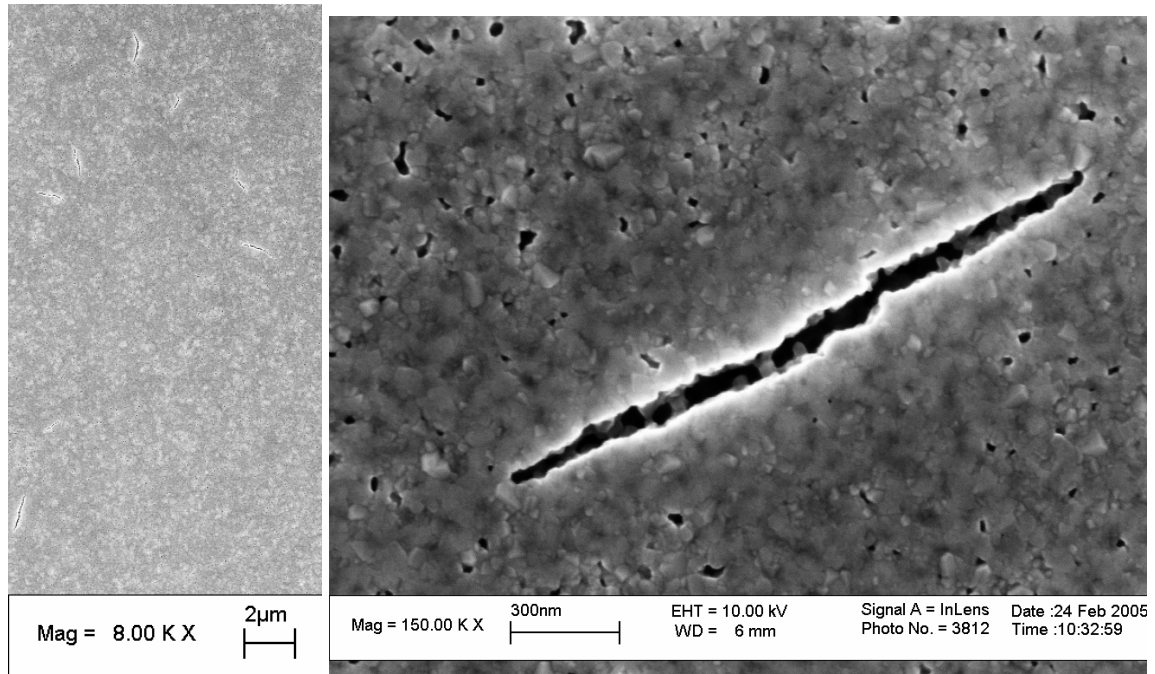


**Figure 47.** SEM images at 8 and 150k magnification of cracking in 4 layer  $\text{LaNiO}_3$  film deposited on MgO using sol with 0.42M concentration ( $T_p = 400^\circ\text{C}$ ,  $T_c = 700^\circ\text{C}$ ).

Additional SEM images showing the effect of pyrolysis temperature, calcination temperature, heating rate, and number of layers on the surface morphology of LNO thin films are provided in the Appendix. Further research is needed to fully optimize processing parameters to produce films with the optimal combination of surface morphology, orientation, and conductivity.

### III.2.5. PBT on $\text{LaNiO}_3$

$\text{Pb}_{0.5}\text{Ba}_{0.5}\text{TiO}_3$  (TIpDEA system) deposited on LNO also showed good orientation regardless of substrate (Figure 48 and Table 19). Thus, oriented  $\text{LaNiO}_3$  thin films provide an excellent template for the growth of (100)-oriented lead barium titanate.

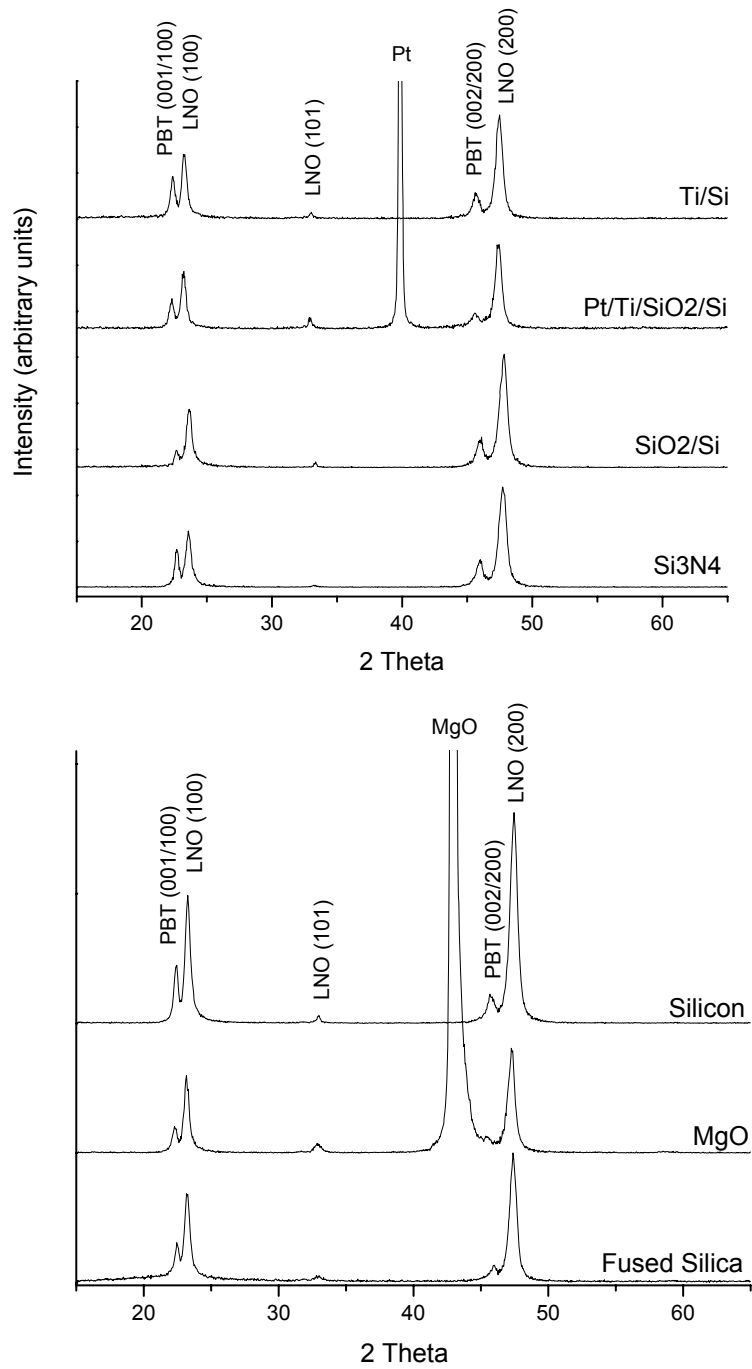


**Figure 48.** PBT on LNO on various substrates (4 layers LNO,  $T_p = 400^\circ\text{C}$ ,  $T_c = 700^\circ\text{C}$ ; 3 layers PBT,  $T_p = 200^\circ\text{C}$ ,  $T_c = 600^\circ\text{C}$ ).

**Table 19.** Orientation of LNO and PBT on various substrates.

<b>Substrate</b>	<b>LNO Orientation</b>	<b>PBT Orientation</b>
Si <sub>3</sub> N <sub>4</sub>	.985	1.0
SiO <sub>2</sub> /Si	.982	1.0
Si (100)	.979	1.0
Ti/Si	.966	1.0
MgO	.955	1.0
Fused Silica	.932	.926
Pt/Ti/SiO <sub>2</sub> /Si	.935	1.0

LaNiO<sub>3</sub> thin film electrodes were also shown to reduce the effects of humidity on the crystallinity of PBT thin films as compared with MgO substrates. As shown in Figure 49 for the TBuDEA system, crystallinity of PBT on single crystal MgO varied significantly with atmospheric humidity, likely due to water adsorption on the single crystal, which has a deleterious affect on heterogeneous nucleation at the interface. Using LaNiO<sub>3</sub>-coated MgO substrates, PBT shows consistently high crystallinity regardless of humidity. Figure 50 shows XRD of the ‘best’ case PBT/MgO compared with a typical result for PBT/LNO/MgO. This result also applies for the TIpDEA system, and a comparison of films deposited on MgO and LNO/MgO prepared under identical conditions is shown in Figure 51. Thus, LaNiO<sub>3</sub> thin film electrodes provide a humidity-insensitive means of depositing oriented PBT, even on moisture-sensitive substrates.

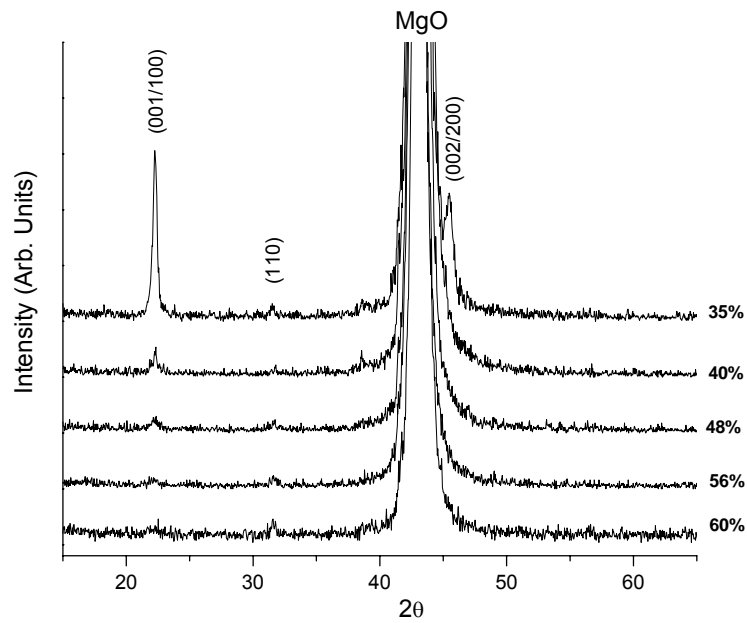


**Figure 49.** Effect of humidity on the crystallization of PBT produced using the TBuDEA system. (3 layer,  $T_p = 200^\circ\text{C}$ ,  $T_c = 600^\circ\text{C}$ ). [Data collected by G. Sukul]

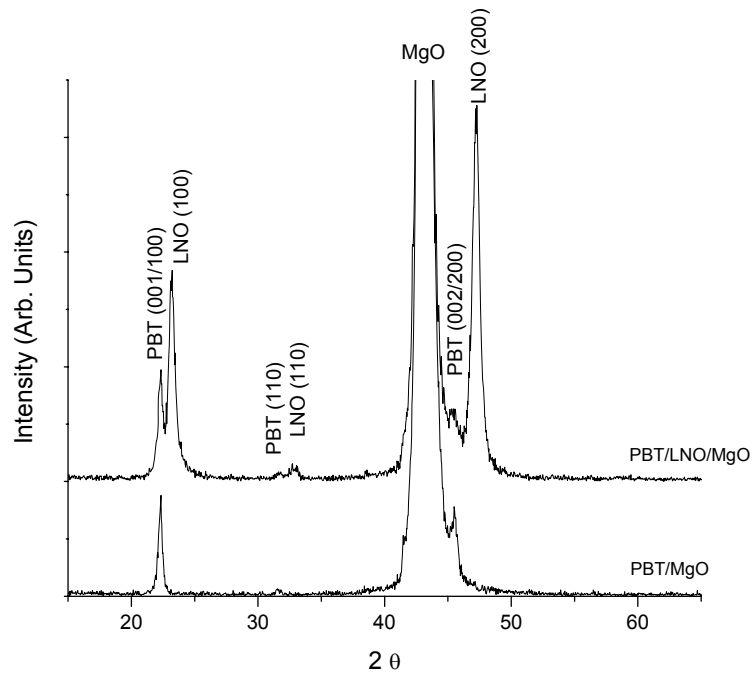


**Figure 50.** XRD of 'best case' PBT thin film deposited on MgO (35% humidity) versus typical PBT film deposited on LNO/MgO using TBuDEA system (PBT: 3 layer,  $T_p = 200^\circ\text{C}$ ,  $T_c = 600^\circ\text{C}$ ; LNO: 4 layer,  $T_p = 400^\circ\text{C}$ ,  $T_c = 700^\circ\text{C}$ ).

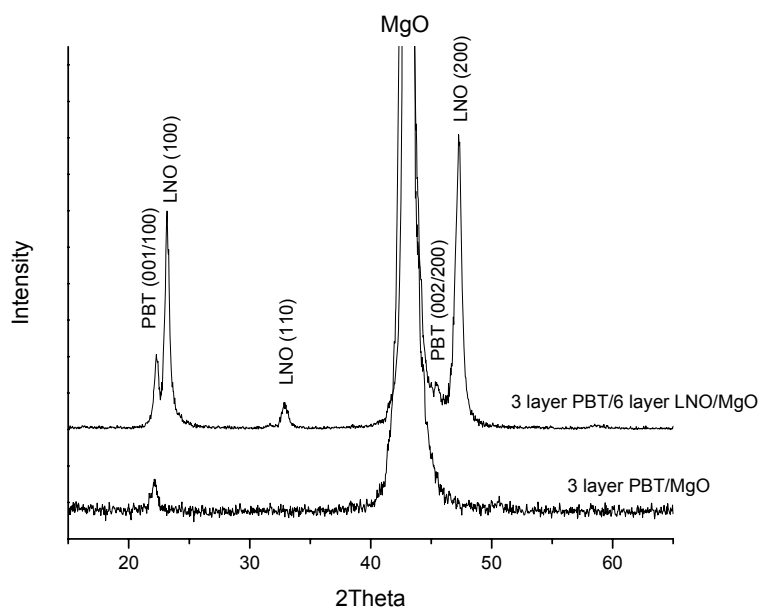


**Figure 51.** XRD of PBT thin films deposited on MgO and LNO/MgO as indicated under the same atmospheric conditions (PBT: TIPDEA system, 3 layer,  $T_p = 200^\circ\text{C}$ ,  $T_c = 600^\circ\text{C}$ ; LNO: 6 layer,  $T_p = 400^\circ\text{C}$ ,  $T_c = 700^\circ\text{C}$ ).

The excellent crystallinity and orientation of PBT on LNO regardless of substrate suggests the  $\text{LaNiO}_3$  provides ample sites for the heterogeneous nucleation of the ferroelectric thin film. Such enhanced nucleation might lower the temperature required for crystallization of PBT. As described in Chapter I, a calcination temperature of  $600^\circ\text{C}$  is required for PBT crystallization on MgO single crystals. As shown in Figure 52, PBT peaks can be discerned on  $\text{LaNiO}_3/\text{Si}$  substrates at a calcination temperature as low as  $450^\circ\text{C}$ —a  $150^\circ\text{C}$  reduction in the required calcination temperature!

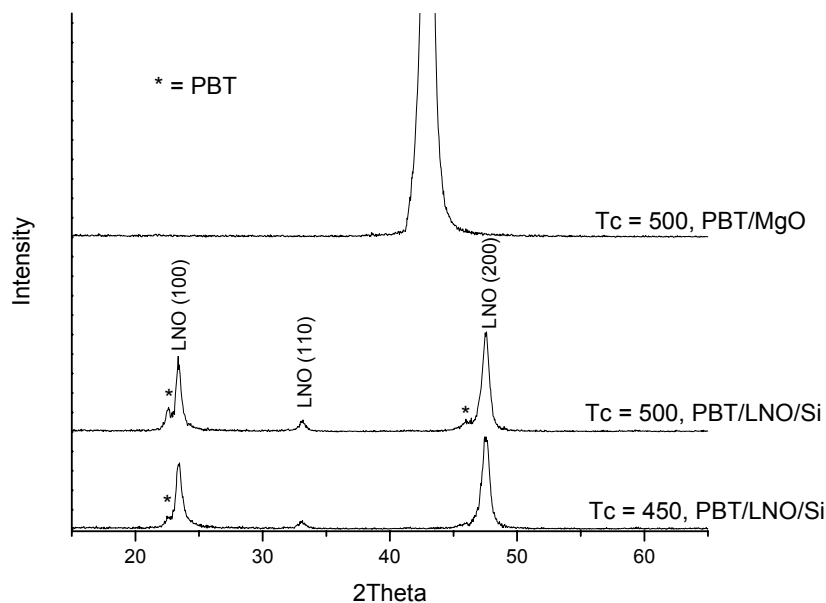


**Figure 52.** XRD of 3 layer PBT films deposited on the substrates indicated and calcined at the stated temperatures. (PBT: TIpDEA system, T<sub>p</sub> = 200°C, LNO: 4 layers, T<sub>p</sub> = 400, T<sub>c</sub> = 700°C).

### III.2.6. Other Ferroelectrics on LaNiO<sub>3</sub>

The pseudocubic lattice parameter of LaNiO<sub>3</sub> matches well with a variety of ferroelectric materials, including BaTiO<sub>3</sub>, PbTiO<sub>3</sub>, Pb(Zr, Ti)O<sub>3</sub>, and (Ba,Sr)TiO<sub>3</sub>. The suitability of LaNiO<sub>3</sub> as a bottom electrode for several of these materials was investigated.

PbZr<sub>0.52</sub>Ti<sub>0.48</sub>O<sub>3</sub> (PZT) polymeric sol was obtained commercially (Item #39758, Alfa Aesar, Ward Hill, MA) and spin coated onto single crystal MgO and LaNiO<sub>3</sub>/Si substrates. XRD shows PZT is crystalline and well-oriented on both substrates (Figure

53). It is noteworthy that PZT cannot be deposited directly on Si because of the formation of lead silicide phases. As no new phases are detected for the PZT/LaNiO<sub>3</sub>/Si film, it can be concluded that in addition to being an electrode, LNO also acts as a sufficient diffusion barrier to Pb, allowing for phase pure and oriented PZT to be deposited on a Si substrate without the use of further buffer layers such as Ta or Ti.

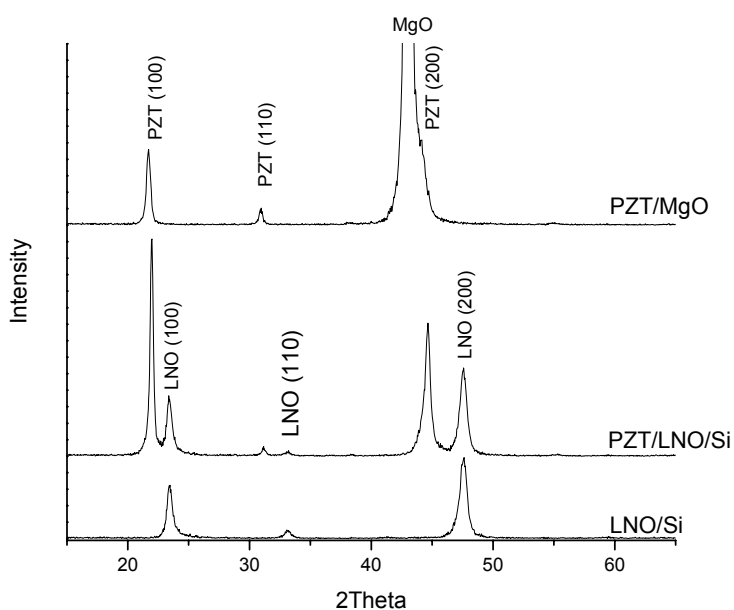


**Figure 53.** XRD of 3 layer PZT thin film deposited on MgO and LNO/Si, as indicated. XRD of the LNO/Si film before PZT deposition is also shown. (PZT: 3 layers,  $T_p = 200^\circ\text{C}$ ,  $T_c = 600^\circ\text{C}$ ; LNO: 4 layers,  $T_p = 400^\circ\text{C}$ ,  $T_c = 700^\circ\text{C}$ )

## **IV. Integration**

### **IV.1. Introduction to Integration Issues**

In order to build complex devices with ferroelectrics, it is desirable to use the wealth of tools and techniques available through semiconductor and, particularly, microelectromechanical systems (MEMS) technology. Typical semiconductor and MEMS devices are based on layer processes. Individual layers are deposited on a substrate, typically silicon, and then patterned, etched, or machined into useful structures and devices. Layers can include metals, nitrides, oxides, or other dielectrics, and they can be deposited or patterned with chemical vapor deposition, oxygen plasmas, reactive ion etching (RIE), deep reactive ion etching (DRIE), wet etching, and others [147]. Dopants are often added to discrete regions in silicon in order to affect its conductivity. As devices have been scaled down to smaller dimensions, individual layers have gotten thinner, and dopant profiles have been carefully controlled.

#### **IV.1.1. Thermal Constraints**

One of the largest hurdles to integrating ferroelectric films into semiconductor processing is the high temperature typically required for calcination of the ferroelectric layer. High temperatures and long dwell times can lead to redistribution of dopant profiles or interdiffusion between discrete layers. Careful attention, therefore, must be paid to the so-called thermal budget, which considers both the temperature and dwell time. The

particular times and temperatures permissible depends on the types of dopants used and the size of structures involved. A detailed discussion of thermal budgets is given in [148]. Alternately, robust device designs can be developed that do not require many layers of carefully controlled composition. Another strategy to side-step the thermal budget constraints is to discretize the ferroelectric part of the device, and integrate it with a conventionally prepared multi-layer stack later. For ferroelectrics to be widely used as a functional layer, however, these strategies only delay the inevitable integration challenges.

Here, the preferred method of addressing thermal constraints is to lower the crystallization temperature of the ferroelectric layer as much as possible. Process flows are also designed with thermal budgets in mind. High temperature processes should be completed as early as possible in the deposition/patterning sequence, so that subsequent layers are not affected at all by high temperatures. This strategy imposes some containment difficulties, because when the ferroelectric layer is incorporated early in the design, the layer must be contained throughout the remainder of processing, as described below.

#### **IV.1.2. Contamination**

In order to produce useful structures and devices using ferroelectric thin films, the films must be either selectively deposited or selectively etched. MEMS techniques are well developed for such purposes. However, due to contamination concerns, most state-of-the-

art MEMS equipment has been unavailable for use with ferroelectric films, especially those containing lead. Thus, early attempts to integrate ferroelectric films as active layers have employed containment strategies to isolate the ferroelectric from the processing equipment. This can mean either encapsulating the ferroelectric film to prevent contamination, or using MEMS techniques only on the front-end of the process before the ferroelectric is deposited. Applying the ferroelectric films as part of a back-end process, however, presents the challenge that processed surfaces are generally not single crystals with good lattice matching suitable for producing oriented ferroelectrics. Rather, the growth surfaces consist of metal layers or dielectric materials that are not generally able to produce texture.

### **IV.1.3. Integration Strategy**

Ultimately, released membrane structures of oriented PBT are desired for electrical and mechanical testing towards implementation of the ferroelectric pump described in Chapter I. In order to take advantage of MEMS process efficiencies and avoid as much contamination concern as is reasonable, processes were designed in which the majority of micromachining was completed before ferroelectric deposition. For membrane design, this meant pre-etching most of the Si before depositing the ferroelectric so that only a small amount of etching needs to be done to release the ferroelectric film. A variety of techniques and strategies developed for addressing these integration concerns is described below, and an excellent review is given in [149].

## **IV.2. Patterning**

The simplest applications of ferroelectric films do not require patterning. To produce a parallel plate capacitor, for example, a conductive substrate can be uniformly coated with a ferroelectric film and then top electrode to finish the device [150]. More interesting devices, however, require patterning of the ferroelectric layer. Patterning in MEMS is generally accomplished either through selective deposition or selective (subtractive) etching. Contamination concerns typically limit the availability of processing equipment, such as RIE or DRIE, suitable for high aspect ratio etching of lead-containing ferroelectrics. Thus, it is generally easier to design devices with patterned substrates rather than patterned ferroelectrics. Wet etching can be used to selectively etch the ferroelectric layer, but such processes are generally isotropic, and etch rates must be carefully calibrated for each ferroelectric material.

### **IV.2.1. Photolithography**

In order to selectively etch films, some sort of masking is generally used. Standard MEMS masking techniques involve photolithography of photoresist. The photoresist polymer is spin coated onto a ferroelectric film and then selectively exposed to UV light. Depending on the particular photoresist used, the UV light either cross-links and hardens the resist, or causes it to breakdown. A series of chemical baths develops the resist, and then strips away the exposed/unexposed areas to reveal the desired pattern. The patterned film can then be subjected to wet or dry etchants to selectively remove the exposed areas of the ferroelectric film. Subsequently, the remaining photoresist is removed, leaving

behind a patterned ferroelectric layer. Preliminary tests indicate the PBT films are at least to first order compatible with photoresist process. Photoresist (AZ4400) was painted onto a PBT film and then the sample was exposed to UV light (365nm, 10 minutes) before developing (AZ351 developer diluted 1:4 with water) and stripping the resist. Optical microscopy and XRD of PBT films before and after photoresist deposition, baking (100°C 10-30 min, 120°C 10 min), and developing show no major changes in the films. However, a cursory test of chemical etchants (KOH, HCl, H<sub>2</sub>SO<sub>4</sub>, Fluoroboric acid) did not find a suitable wet etch capable of etching PBT without also etching photoresist.<sup>9</sup> To achieve good feature scales and photoresist uniformity, a lithography system and clean room setup is needed.

Alternative patterning methods were thus investigated in order to quickly and cheaply produce patterned PBT films without requiring expensive equipment or clean room facilities.

#### **IV.2.2. UV Patterning**

UV radiation has been shown, in some cases, to lower the calcination temperature required for producing ZnO and TiO<sub>2</sub> thin films by facilitating organic decomposition at lower temperatures [71, 151, 152]. Several researchers have also reported use of UV-

---

<sup>9</sup> HCl and H<sub>2</sub>SO<sub>4</sub> appeared to etch PBT faster than photoresist, with HCl etching faster than H<sub>2</sub>SO<sub>4</sub>. Careful etch rate studies might render these chemicals useful for wet etch purposes, but will require more stringent control of photoresist thickness.

sensitive modifiers to facilitate patterning of sol-gel films [153, 154]. Uozumi [154] used a photosensitive modifier known as NBAL to pattern PZT through selective irradiation with 365nm UV and subsequently wash off unexposed areas with solvent. Monoethanolamine and ethylenediamine have a UV sensitive C=N bond, which has also been used to pattern TiO<sub>2</sub> films [151].

Ohya notes that the ideal radiation wavelength corresponds to the ligand-to-metal charge transfer, which weakens metal-chelate bonding [71]. For titanium isopropoxide, the absorption band is found to be ~300nm [151]. Both acetylacetonate (acac) and diethanolamine have been shown to be photoactive in the UV region, with acac absorbing near 300nm and diethanolamine absorbing at ~240nm [152, 153].<sup>10</sup> UV spectrometry was used to determine the UV absorption characteristics of TIpDEA and TBuDEA sols prepared as described in Chapter II. As shown in Figure 54 and Figure 55, both sols absorb UV radiation below 300nm.

---

<sup>10</sup> N-phenyldiethanolamine (PhDEA) was found to be more photosensitive than DEA (it absorbs at 256nm and 303nm) however titanium sols are less stable with PhDEA. Kikuta attributes this to a reduction in the basicity of the N atom by the phenyl group [153].

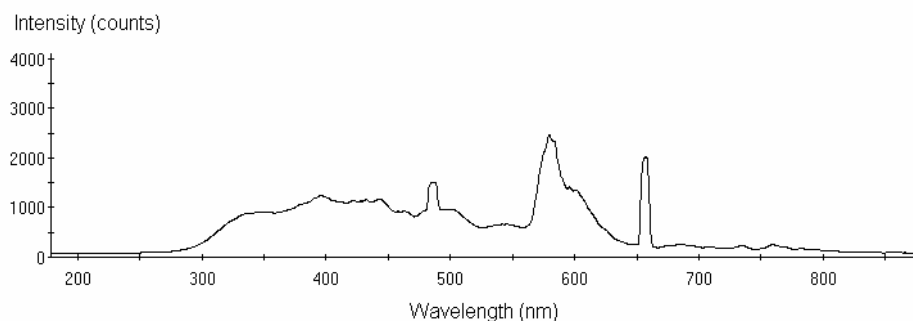


**Figure 54.** UV transmission spectrum for TIPDEA sol.

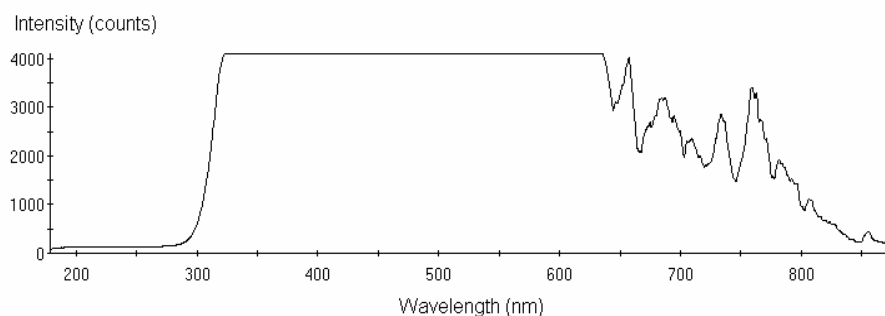


**Figure 55.** UV transmission spectrum for TBuDEA sol.

An inexpensive, low power UV lamp (wavelengths 365nm and 254nm) was used to irradiate PBT thin films during pyrolysis. Preliminary tests were inconclusive, with one film showing enhanced crystallinity at 450°C with exposure to 365nm radiation and others not showing any effect (Figure 56). This experiment was not readily reproducible, as atmospheric conditions were not controlled and varied significantly over the course of film preparation. However, several lessons can be learned from this preliminary effort. An experimental setup should be designed that incorporates a higher power UV source,

perhaps with a wide band emission rather than single discrete wavelength to maximize the effect of absorption. The UV source should be positioned above the film during pyrolysis, however care must be taken to not melt the insulation surrounding the bulb when high temperatures are used. After testing, significant buildup of organics was observed on the lamp, probably due to redeposition of pyrolyzed organics (ruining the lamp). It is reasonable to suspect this significantly reduced the intensity of radiation at the film surface, particularly at the shorter wavelength, which would have been expected to provide the most noticeable effect.

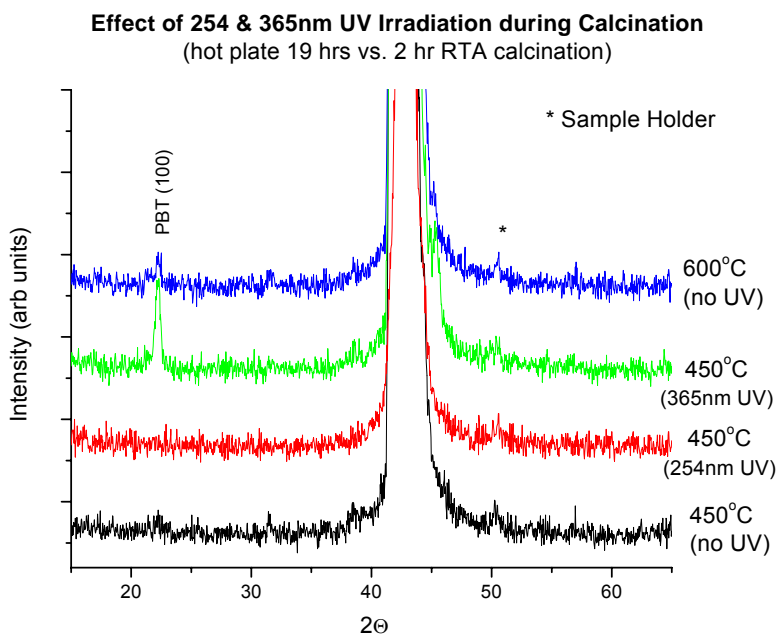


**Figure 56.** XRD of PBT thin films with and without UV treatment, as indicated.

Further study is warranted of the use of UV radiation for both lowering the calcination temperature and patterning PBT thin films, especially in conjunction with LNO electrode substrates. With sufficiently high power, UV irradiation can likely be used to selectively

cure PBT thin films, allowing for the production of films with complex patterns and excellent feature size.

### **IV.2.3. Selective Deposition**

Selective deposition is a more attractive alternative for patterning sol-gel materials. Techniques for selectively depositing sols include simple mask techniques, ink-jet printing [49], screen printing [155] and the “soft lithography” techniques known as microcontact printing [156-158], and micromolding [159, 160], which boast feature sizes down to 30nm [160].

#### Physical Masking

Physical masking provides a quick and cheap alternative to photolithography. Before spin coating, the substrate is selectively covered with a physical mask to prevent deposition in covered areas. Scotch tape was successfully used to provide a physical mask for PBT deposition. After spin coating, the tape is removed before pyrolysis (and reapplied between layers for multi-layer films). Although tedious, this method works quite well for providing access to an electroded substrate for electrical testing. Scotch tape was found to be sufficiently thin so as not to cause the formation of a large edge bead near the tape border; however for thicker tapes or thinner films, this might be of concern. This crude technique is not suitable for very small feature sizes or complex patterns requiring careful alignment.

### Microcontact Printing

Microcontact printing involves surface modification of the substrate using self-assembled monolayers (SAM) to pattern a subsequently deposited film. One method involves using the elastomer polydimethylsiloxane (PDMS) as a stamp to selectively deposit a surfactant, octadecyltrichlorosilane (OTS), which causes a subsequently deposited sol-gel film to crack heavily upon pyrolysis. The cracked areas can then be easily removed through wiping or washing, leaving behind a patterned ferroelectric film. Alternative surfactants can be used to influence the wettability of selected areas of the substrate to achieve similar results. While interesting, this technique is relatively new and not well-studied. If other simpler patterning techniques are found to be unsuitable, microcontact printing should be considered. Feature sizes of  $4\mu\text{m}$  have been reported for microcontact printing of  $(\text{Pb}, \text{La})\text{TiO}_3$  [158].

### Micromolding

Rather than involving the intermediate step of self-assembled monolayers, micromolding techniques (sometimes referred to as micromolding in capillaries, or “MIMIC”) use PDMS as a mold rather than a stamp. PDMS molds can be produced by casting the liquid polymer onto a negatively-machined mold. Alternatively, some PDMS formulations allow for direct UV patterning through photolithography. The cured polymer can then be bonded to a substrate, such as glass. Since PDMS is an elastomer, nonplanar substrates can also be accommodated [159]. Sol is then introduced either through the side of the mold through capillary forces, or through holes drilled into the top of the mold. The sample is dried, and the PDMS mold is peeled off of the substrate to

reveal a patterned xerogel, which can be calcined to produce a patterned ferroelectric. Feature sizes of 500nm have been demonstrated [159], and this technique has recently been proven suitable for producing wonderfully complex patterns in PZT thin films [160].

PDMS has been shown to be compatible with a wide variety of chemicals, including all of the ones used in sol-gel processing of PBT. In order to test proof-of-concept, PBT sol was injected into PDMS (Sylgard 184, Dow Corning, Midland, MI) molds attached to glass slides. Several channel lengths, widths, and geometries were tried (Figure 57 and Figure 58). All channels were 10-12 $\mu$ m in depth. Injection of the sol into the mold using a syringe pump was found to be the most suitable method, as the capillary method required a large (unpatterned) pool of sol adjacent to the mold, which is generally a mess (Figure 59). In order to ensure full channels, a second 'exhaust' hole was drilled at the end of the channels, and the mold was filled through one hole until sol began to spill out of the second hole.

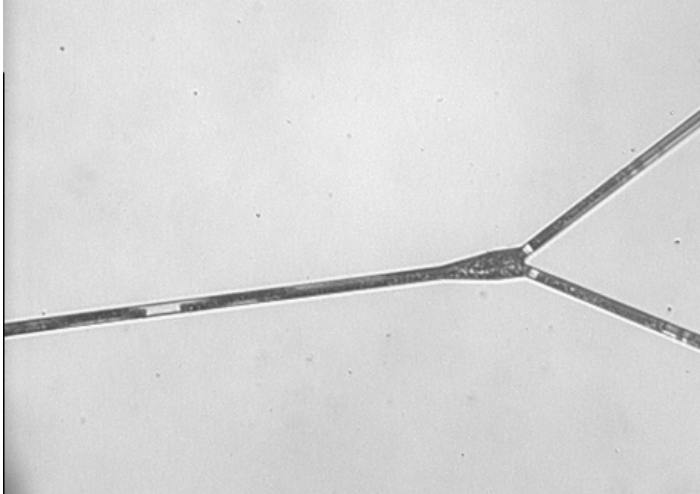


**Figure 57.** PBT sol injected into PDMS mold on glass slide showing ability to fill connecting channels from single injection point. The main channel is 50 $\mu\text{m}$  wide, and the two smaller branches are 40 $\mu\text{m}$  wide.

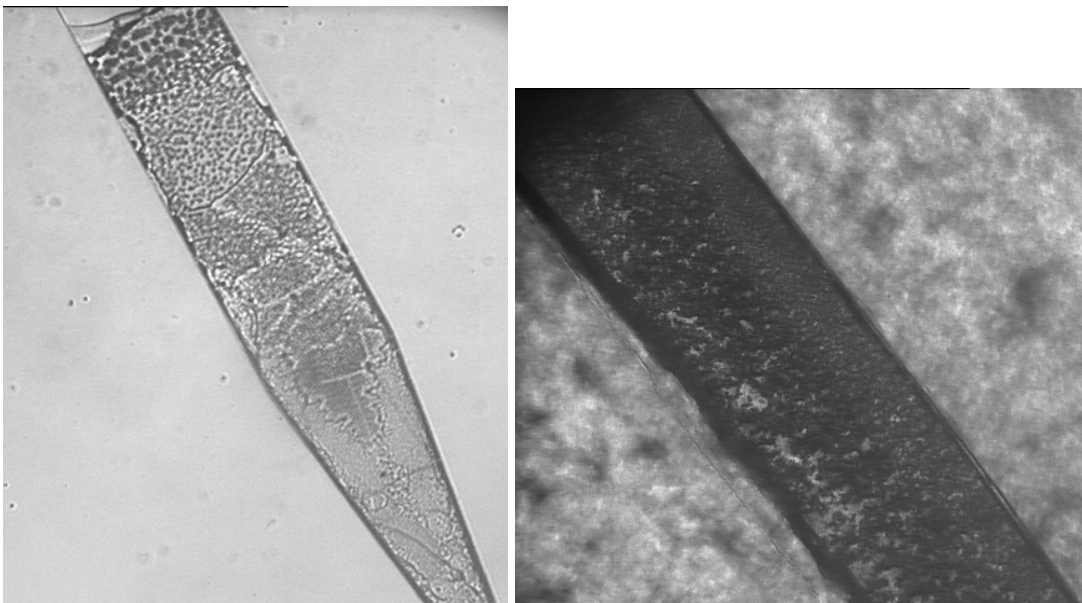


**Figure 58.** Channel filled with xerogel after drying showing cracking as function of channel width. (Dried 100 $^{\circ}\text{C}$ , 20 hours) Widest part is 50 $\mu\text{m}$ .

The patterned ferroelectrics, shown in Figure 59 and Figure 60, are visibly cracked. This is not surprising due to the large shrinkage that occurs during drying and calcination.

More careful study including consideration of the Griffith's criteria should lead to an optimum channel width and depth to suppress cracking [159, 160]; however, more detailed study is required to determine the critical length above which cracking becomes thickness dependant. Repeating the injection-drying step multiple times before removing the mold could also help densify the xerogel, or more concentrated sols can be produced to reduce shrinkage.

Attempts to bond the PDMS to MgO single crystal substrates, however, failed. Upon injection of sol into a mold on MgO, the molds peeled off the substrate, resulting in complete surface wetting. Some limited adhesion was realized by first roughening the MgO with oxygen plasma before bonding with PDMS. Figure 59 shows patterned ferroelectric lines deposited on MgO using the capillary technique. Cracking is most prominent for the thickest line (Figure 60).

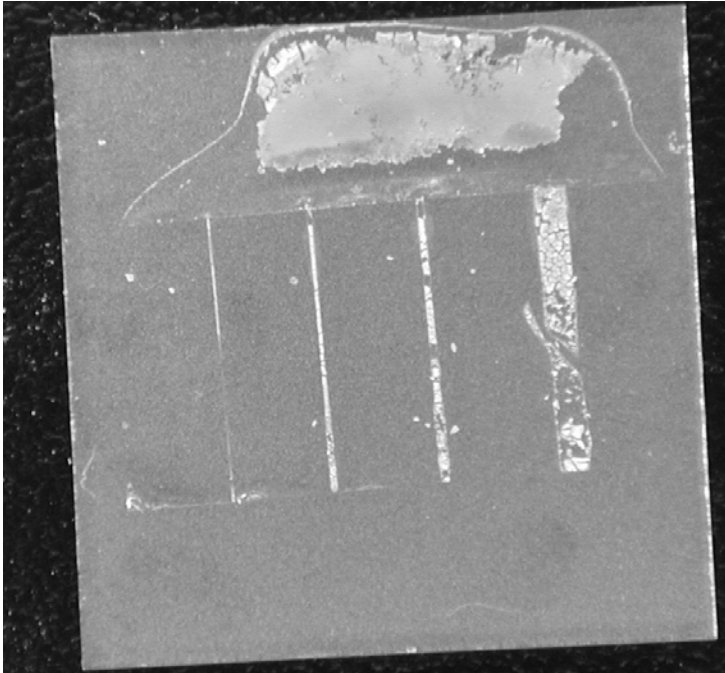


**Figure 59.** PBT deposited using capillary technique on 10mm square MgO substrate showing variety of line widths. Line widths from left to right: 10, 50, 100, and 500 $\mu$ m.

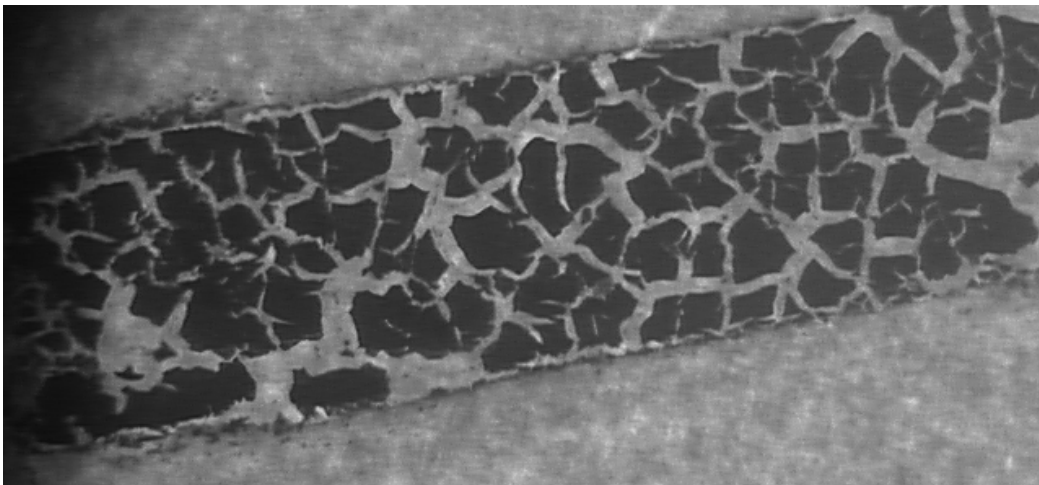


**Figure 60.** Thickest (500 $\mu$ m) line in previous figure, close-up after calcination.

The author strongly recommends revisiting PDMS micromolding in conjunction with  $\text{LaNiO}_3$  electrodes, which should provide better PDMS adhesion and also present the

possibility of oriented patterned structures. Other types of PDMS can also be investigated that allow for higher drying temperatures [161].

### IV.3. Orientation: IBAD MgO

The initial approach taken to address the issue of obtaining oriented ferroelectric films on Si-based substrates involved the use of ion beam assisted deposition (IBAD) MgO. As described more fully elsewhere [162], IBAD involves the use of e-beam evaporated MgO with simultaneous  $\text{Ar}^+$  ion bombardment at a  $45^\circ$  incidence angle to a  $\text{Si}_3\text{N}_4/\text{Si}$  substrate. Biaxial texture can be obtained by varying the ratio of ion/MgO flux during deposition [163, 164]. A 20nm homoepitaxial layer of MgO is then deposited onto the IBAD layer at  $600^\circ\text{C}$ . Subsequently deposited ferroelectrics inherit this biaxial texture, thus providing a route for producing textured PBT on a Si-based substrate. In principle, IBAD can be used to deposit textured MgO on any smooth amorphous substrate.

Both the TIpAc and TIpDEA systems were used to deposit sol-gel lead barium titanate onto IBAD MgO/ $\text{Si}_3\text{N}_4/\text{Si}$  substrates. For both systems, XRD shows the PBT is highly *a*-axis oriented. This is in contrast to MgO single crystal substrates which yield mixed *a*- and *c*-axis orientation. The difference can be easily explained by the large thermal mismatch between the Si substrate and ferroelectric thin film ( $\alpha_{\text{Si}} = 2.6 \times 10^{-6}/\text{K}$  [84],  $\alpha_{\text{PbTiO}_3} = 12.6 \times 10^{-6}/\text{K}$  [165],  $\alpha_{\text{BaTiO}_3} = 9.8 \times 10^{-6}/\text{K}$  [166]), which places the ferroelectric film under tension during cooling, thus favoring *a*-axis orientation (long axis in the plane). On single crystal MgO ( $\alpha_{\text{MgO}} = 14.8 \times 10^{-6}/\text{K}$  [165]), the film is under compression

during cooling, resulting in *c*-axis preferred orientation. However, the compressive stress is comparatively mild compared with the tensile stress of Si, and thus PBT on single crystal MgO results in a mixed *a/c*-orientation (Figure 61).

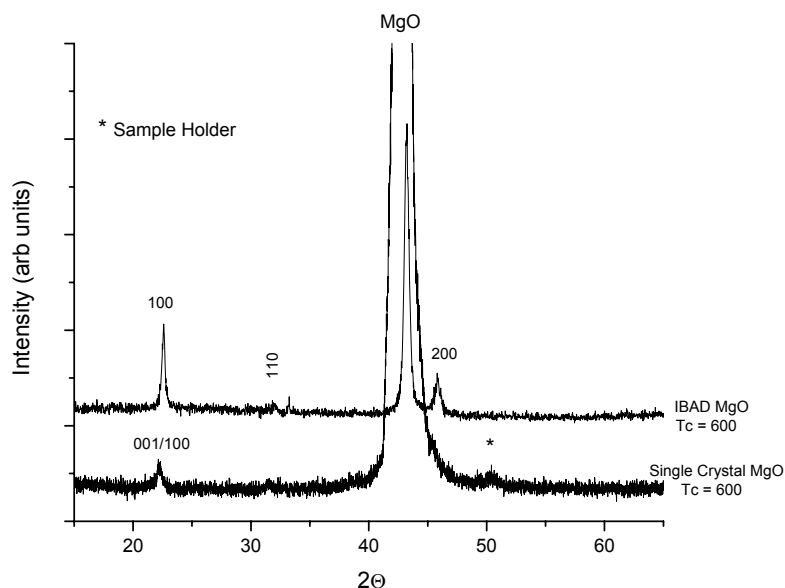


**Figure 61.** XRD of PBT thin film on single crystal MgO and IBAD MgO/Si<sub>3</sub>N<sub>4</sub>/Si. (PBT: 3 layer, TIpDEA, Tp = 200°C, Tc = 600°C)

RHEED analysis of (TIpAc) PBT films deposited on IBAD MgO substrates shows that the out-of-plane orientation distribution (FWHM) is  $\Delta\omega = 4^\circ$ . High resolution transmission electron microscopy (HRTEM) shows the PBT film has grain sizes of 20-30nm. Interestingly, although sol-gel deposition is shown to attack the MgO layer, it results in improved in-plane texture over the template layer itself [162]. This has been explained in the following manner. MgO is susceptible to hydroxylation on its surface in the presence of water, and the damage incurred prevents such surfaces from effectively templating PBT growth. Sol-gel chemistry inherently involves water, and thus the MgO

substrate is attacked, which would otherwise serve as sites for the nucleation of misoriented PBT grains, quickly become hydroxylated retarding PBT nucleation in those regions.

### IV.3.1. Membrane Process Flow

A process flow for using IBAD MgO as a buffer layer to produce oriented ferroelectric films on partially released  $\text{Si}_3\text{N}_4/\text{Si}$  templates is shown in Figure 62.

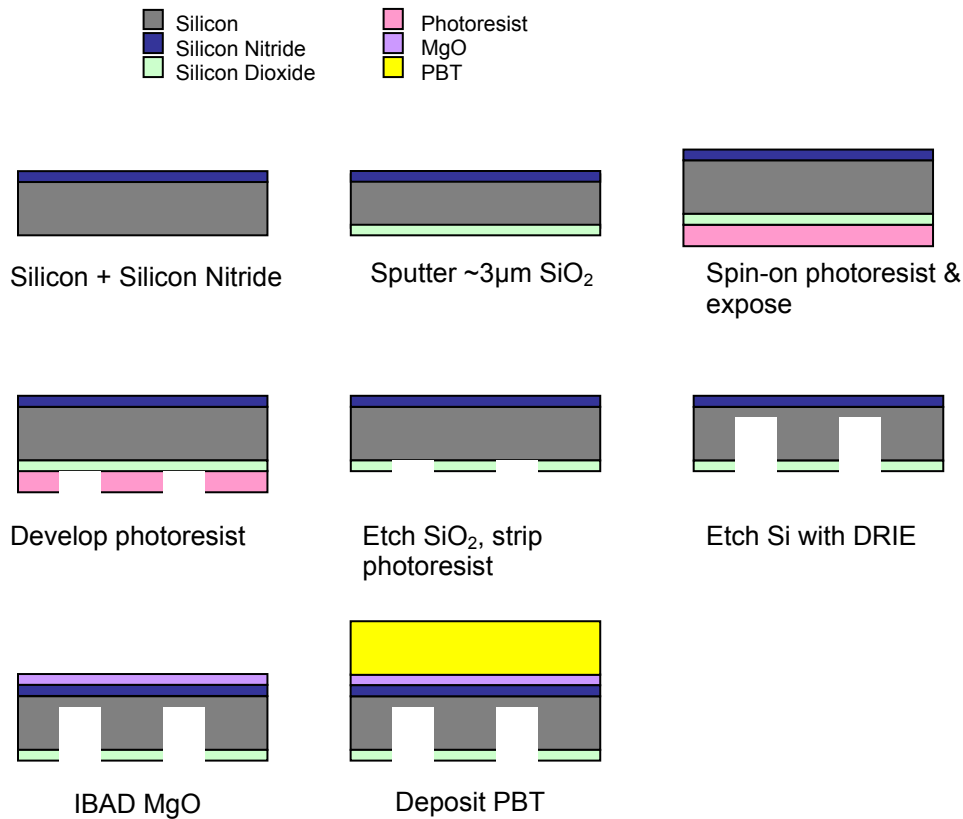


**Figure 62.** Process flow for producing partially released PBT/MgO/ $\text{Si}_3\text{N}_4$  membranes.

The process begins with a  $\text{Si}_3\text{N}_4/\text{Si}$  wafer. First,  $3\mu\text{m}$   $\text{SiO}_2$  is sputtered on the back of the wafer. Photoresist (Clariant AZ4620) is then spun on at 3krpm to produce a  $6\mu\text{m}$  resist layer. The photoresist is patterned with photolithography and developed using Clariant AZ351 developer diluted 1:4 with deionized water to remove the exposed regions of photoresist. The now uncovered regions of  $\text{SiO}_2$  are etched using a buffered hydrofluoric acid etch (BHF). Remaining photoresist is then stripped using acetone, isopropanol, and deionized water. Using the remaining oxide as an etch mask, the wafer undergoes deep reactive ion etching (DRIE), where Si is directionally etched in regions unprotected by  $\text{SiO}_2$ . IBAD MgO is deposited on the wafer, and finally sol-gel PBT is deposited on top to finish the structure.

After PBT deposition, these films can be released to form  $\text{Si}_3\text{N}_4/\text{MgO}/\text{PBT}$  membranes using the additional process steps shown in Figure 63, which uses the same color scheme. As shown in the figure, photoresist is spun on top of the ferroelectric layer to prevent Pb contamination.  $\text{XeF}_2$ , a dry gas that gently and isotropically etches Si, is then used to fully release the film. The protective photoresist cap is then removed either through wet chemical methods or supercritical  $\text{CO}_2$ .

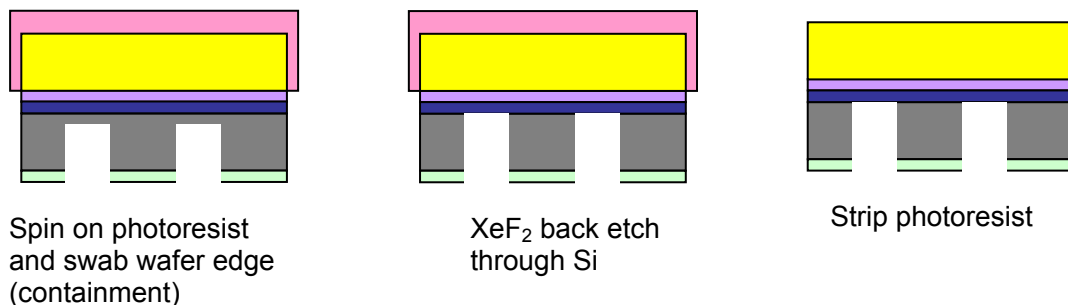


**Figure 63.** Process flow for final release of  $\text{PBT}/\text{MgO}/\text{Si}_3\text{N}_4$  membranes.

### IV.3.2. TEM Windows

IBAD MgO and PBT were also deposited on commercially purchased  $\text{Si}_3\text{N}_4$  TEM windows (Figure 64). These windows consist of 30nm  $\text{Si}_3\text{N}_4$  membranes released from a  $200\mu\text{m}$  Si substrate in a 1mm x 1mm square region. The overall dimensions of the TEM windows are 3mm x 3mm, making them exceedingly difficult to handle. Their small size also precluded spin coating. Their delicacy resulted in a high loss rate, as many would break during handling or calcination. One intact film was produced by dripping sol onto the window while holding it on edge and allowing the excess to drip off before calcining. This method was abandoned as being imprecise as well as cost and time prohibitive.

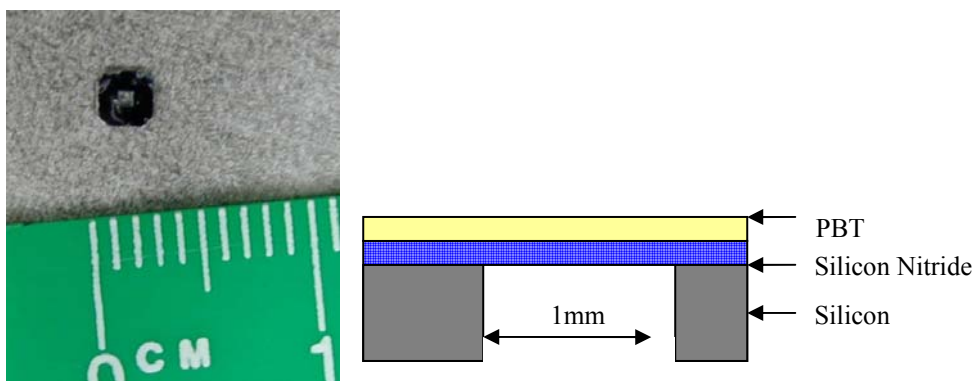


**Figure 64.** PBT-coated TEM window (left) and schematic showing side view of structure (right).

### IV.4. Orientation: Lanthanum Nickelate

The development of conductive oxide electrodes, discussed earlier, mitigates many integration challenges, as it provides a simple way to integrate oriented ferroelectrics

with a wide variety of substrates, while also providing an electrode layer that is stable to sufficiently high temperatures.

#### **IV.4.1. LaNiO<sub>3</sub>/PBT/LaNiO<sub>3</sub>/Si Stacks**

A stack was prepared of LNO/PBT/LNO/Si(111) by depositing 4 layers of LaNiO<sub>3</sub> (as described in Chapter III), then 3 layers of PBT (as described in Chapter II), and finally another four layers of LaNiO<sub>3</sub>. The orientation factor of the LaNiO<sub>3</sub> for this stack structure is 0.967, and the factor for PBT is 1.0, as determined from the XRD (Figure 65). This demonstrates that the PBT layer remains phase pure and oriented after excursions to 700°C. Further, by tape masking the corner of the samples during PBT and top electrode deposition, access to both top and bottom electrodes can be achieved.

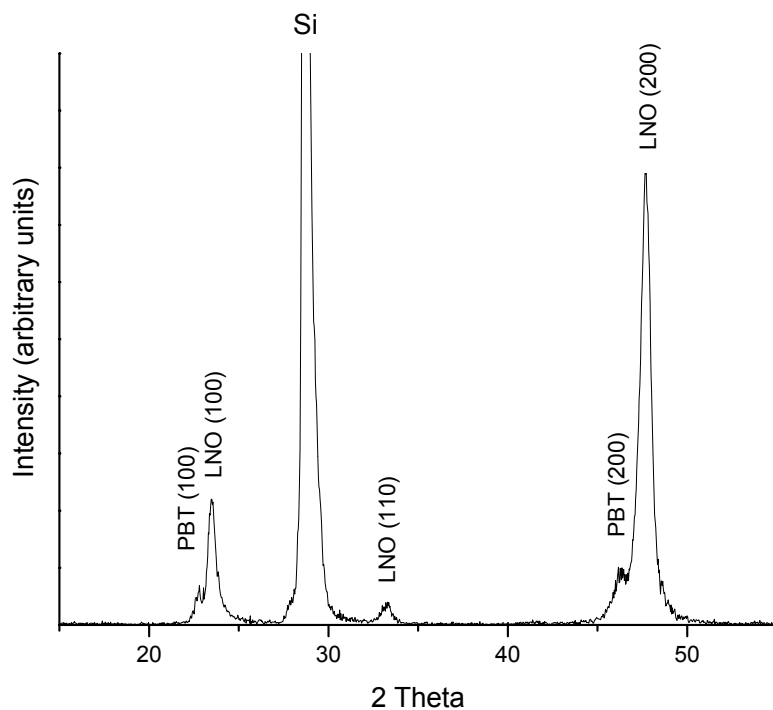


**Figure 65.** XRD of stack structure LNO/PBT/LNO/Si(111).

#### **IV.4.2. Commercial Arrays**

LNO was also deposited on commercially purchased 6 x 6 arrays of 100nm thick membranes of  $\text{Si}_3\text{N}_4$  (Figure 66). The released areas are 0.5mm x 0.5 mm in size. LNO was deposited via spin coating by carefully aligning the vacuum chuck between the windows. As shown by XRD, the two layer LNO film was highly oriented (Figure 67). As part of our collaborators' mechanical testing setup required optical transparency of the films, we were limited to two layers of  $\text{LaNiO}_3$ , as the film became too dark after deposition of subsequent layers. The array was delivered to our collaborators for mechanical and electrical testing.

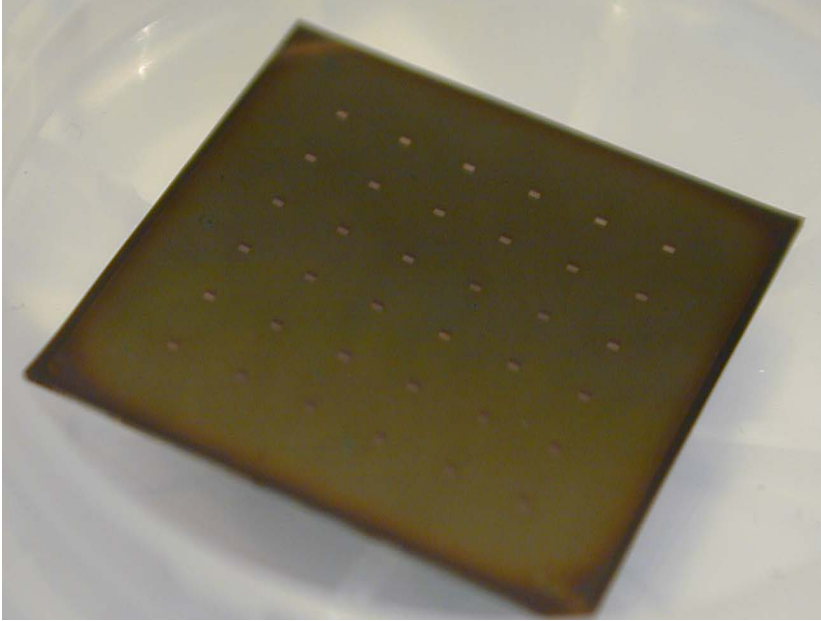


**Figure 66.** LaNiO<sub>3</sub> film (2 layers) deposited on commercially purchased 6 x 6 Si<sub>3</sub>N<sub>4</sub> membrane array.

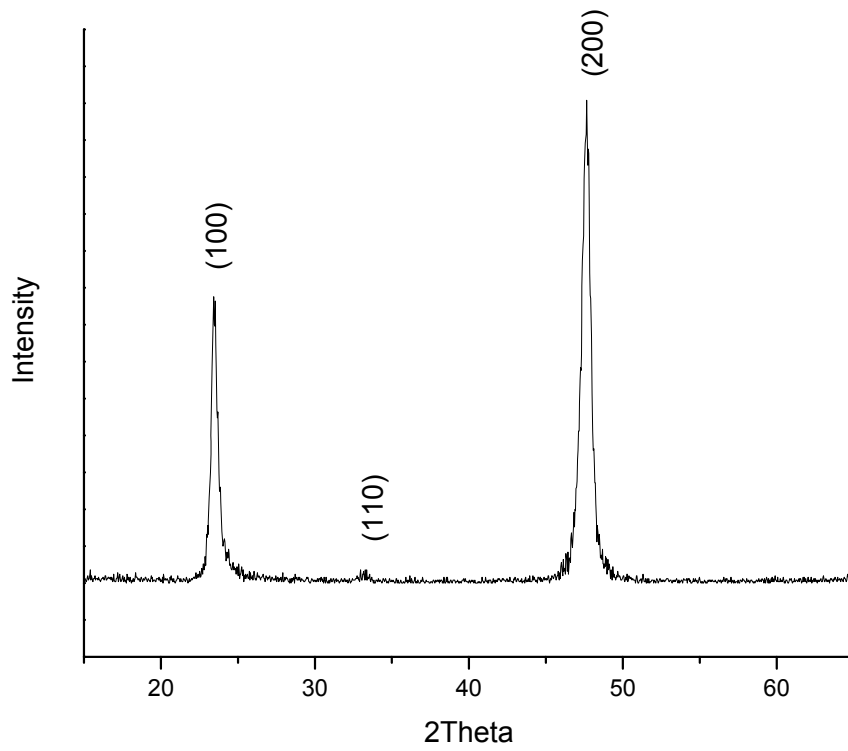


**Figure 67.** XRD of LaNiO<sub>3</sub> film (2 layers) deposited on 6x6 Si<sub>3</sub>N<sub>4</sub> membrane array.

After testing, three layers of PBT were deposited on the array  $\text{LaNiO}_3$  using the TIpDEA process described in Chapter II. One corner was masked with tape to provide access to the bottom electrode for electrical testing. After calcination to  $600^\circ\text{C}$ , XRD shows the PBT film is highly (001/100)-oriented (Figure 68). Twenty membranes remained intact after calcination (Figure 69).

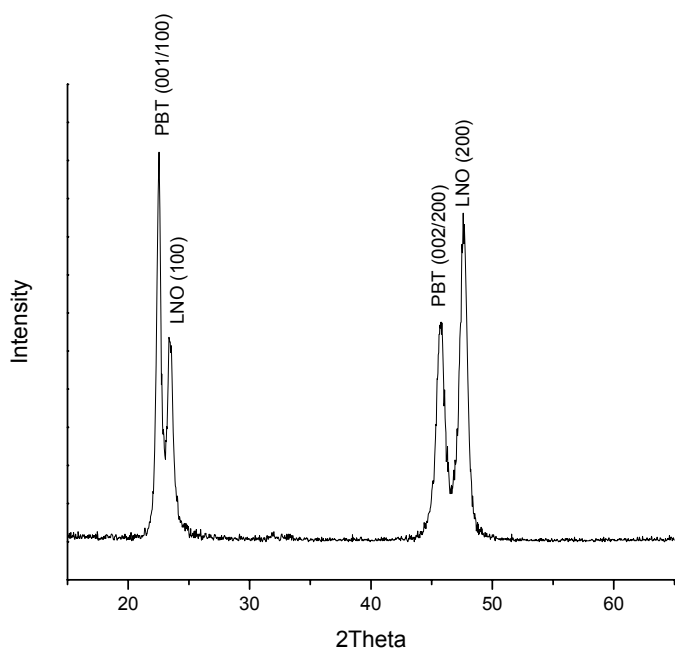
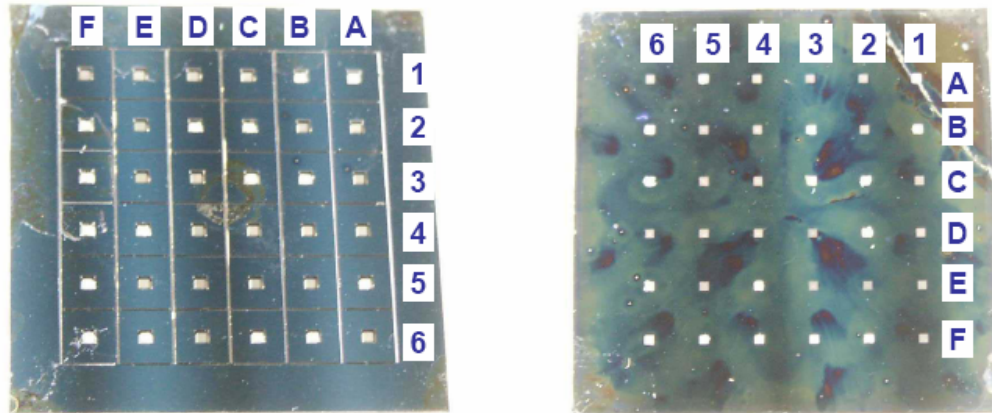


**Figure 68.** XRD of 3 layer PBT films deposited on 2 layer LNO on commercially obtained  $\text{Si}_3\text{N}_4/\text{Si}$  arrays.

### PBT(180nm)/LNO(96nm)/Si<sub>3</sub>N<sub>4</sub>(100nm) Thin Film Structure by Sol-Gel

20 thin films survived

A2,3,4,6    C1,4,5    E1,2,3,5  
 B2,4,5    D1,3,4,5,6    F1



Back view

Front view

**Figure 69.** Photograph of array after PBT deposition showing which membranes remained intact.

#### IV.4.3. Membrane Process Flow

Since the LaNiO<sub>3</sub> electrode is an oxide, it acts as an etch stop for some commonly used silicon etchants, which facilitates bulk micromachining. A process flow for producing released PBT/LNO membranes on a Si substrate is given in Figure 70. The process starts with a thermally oxidized Si wafer. On the backside, photoresist (Clariant AZ4620) is spun on at 3krpm to produce a 6 $\mu$ m photoresist layer. The photoresist is then exposed via photolithography and developed with Clariant AZ351 developer diluted 1:4 with deionized water to remove the exposed regions of resist. Buffered hydrofluoric acid is used to remove the now uncovered regions of SiO<sub>2</sub> on the bottom side of the wafer, as

well as the  $\text{SiO}_2$  on top of the wafer. Remaining photoresist is then stripped using acetone, isopropanol, and water. The wafer is placed in the DRIE machine to directionally etch Si in the regions unprotected by  $\text{SiO}_2$ . After DRIE, only a few microns of Si remain in the etched regions to provide mechanical stability during sol-gel processing. The remaining  $\text{SiO}_2$  is etched with buffered hydrofluoric acid. This substrate is used as a substrate for  $\text{LaNiO}_3$  and PBT deposition as described in Chapters II and III. The sample is then exposed to  $\text{XeF}_2$  to gently and isotropically release the remaining Si to produce free standing PBT/ $\text{LaNiO}_3$  membrane structures.

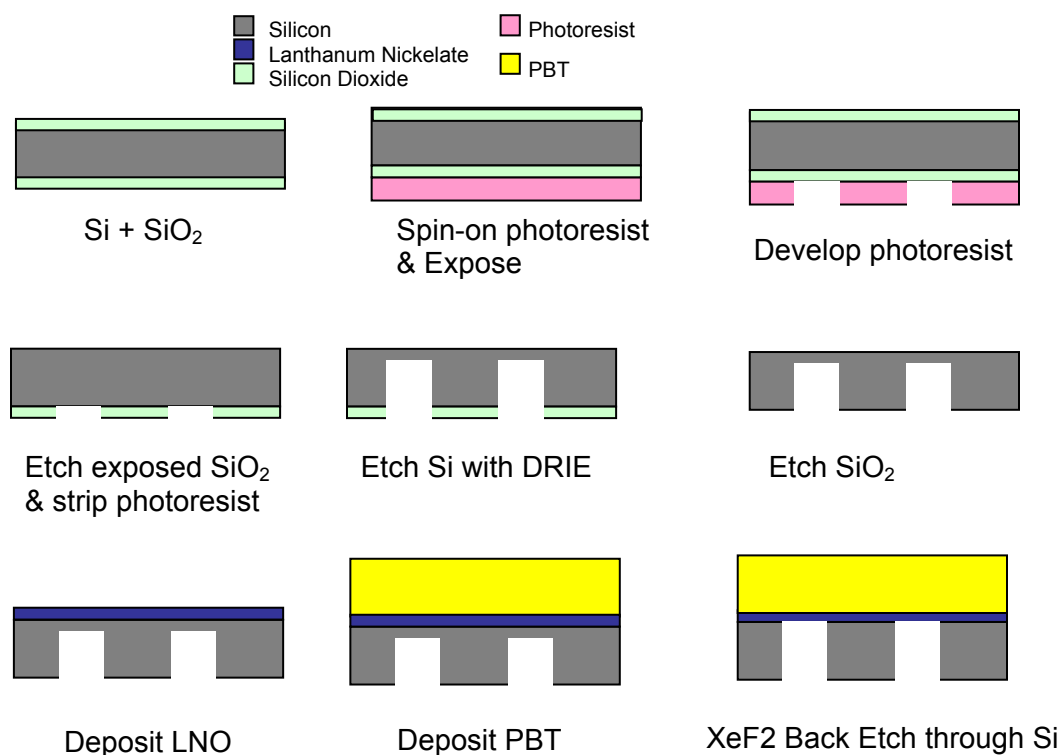


**Figure 70.** Process flow for producing released PBT/LNO membranes on Si.

As an alternate route, the DRIE etch of Si can be replaced by a wet etch if desired. KOH, for example, can be used to provide angled side walls rather than the vertical (high aspect ratio) side walls obtained using DRIE.<sup>11</sup> Further, the Si wafer can be replaced with Si<sub>3</sub>N<sub>4</sub>/Si to provide additional support to the PBT/LNO membrane if necessary. For electrical isolation of the Si substrate, a thin SiO<sub>2</sub> layer may be used between the silicon and LaNiO<sub>3</sub>.

#### **IV.4.4. Mask Design**

The mask design for die used in the process flow shown in Figure 70 is given in Figure 71. It was developed in order to simplify mechanical and electrical testing, considering the experimental setups in use by other groups. Nine square membranes (sized 0.5-1.5mm) are distributed throughout the die, leaving at least 2mm between membranes so they are individually addressable for testing. The center of the die is left intact, to facilitate easy handling during spin coating (the vacuum chuck needs to be placed in the center, which needs to be solid). The mask is designed to allow for 16 individual die per 4" Si wafer processed.

---

<sup>11</sup> Since KOH preferentially attacks the <100> plane of Si, it results in an anisotropic etch with sidewalls inclined 54.7° to the surface.

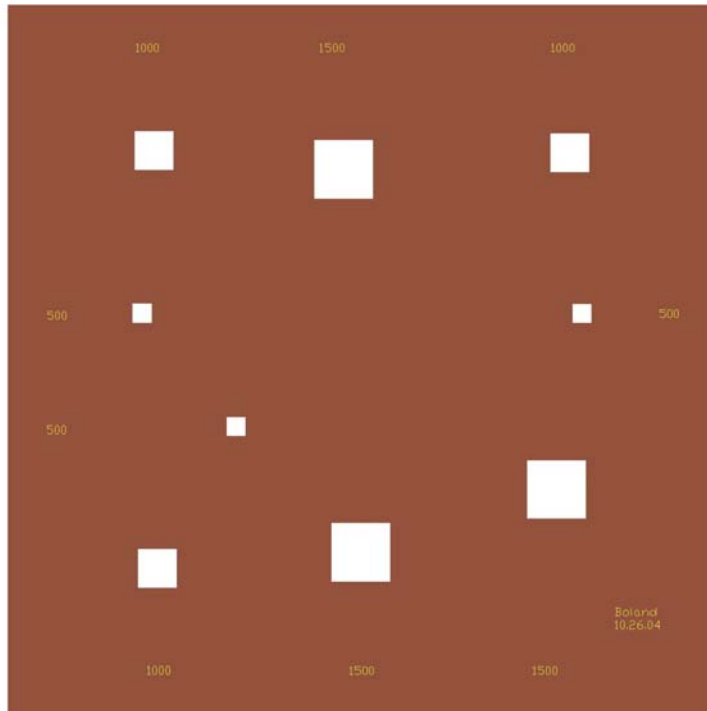


**Figure 71.** Die mask designed for producing released PBT/LNO membranes for electrical and mechanical testing.

#### IV.4.5. XeF<sub>2</sub> Dry Etch

Dry gas etches are useful in releasing delicate membrane structures from Si, as they avoid the stiction and surface tension effects often reported with wet etch techniques. XeF<sub>2</sub> dry gas etching has been used in MEMS processing to isotropically etch Si. It has a high selectivity over SiO<sub>2</sub> (10,000:1), meaning that Si is etched much faster than SiO<sub>2</sub>. Thus, silicon dioxide can be used as an etch mask to produce patterned structures. PZT membranes and cantilevers released using XeF<sub>2</sub> have already been reported [167-169]. LaNiO<sub>3</sub> was subjected to XeF<sub>2</sub> to determine whether the conductive oxide could be used as an etch stop. The etch process involves a series of loops in which XeF<sub>2</sub> is introduced

into a vacuum-purged chamber for 30 seconds and then vented, after a set number of loops the chamber is purged with  $N_2$ . For the die size used, each loop corresponds to approximately  $4\mu\text{m}$  of Si etching. It was determined that  $\text{XeF}_2$  has a high selectivity over  $\text{LaNiO}_3$ , with the  $200\text{nm}$ -thick conductive oxide being unaffected after 4 etch loops (while comparatively Si is etched  $16\mu\text{m}$ ). This presents the possibility of using LNO as both a template for orientation and an etch stop for patterning PBT released structures.

Test arrays were produced with Si substrates prepared using the mask design and process described above. Square membranes with three different sizes ( $0.5\text{-}1.5\text{mm}$ ) were patterned onto a Si wafer using conventional photolithography techniques. The wafer was then partially etched using DRIE to leave only  $12\mu\text{m}$  Si in those regions. The wafer was cleaved into 16 individual die, which were used as substrates for LNO deposition.

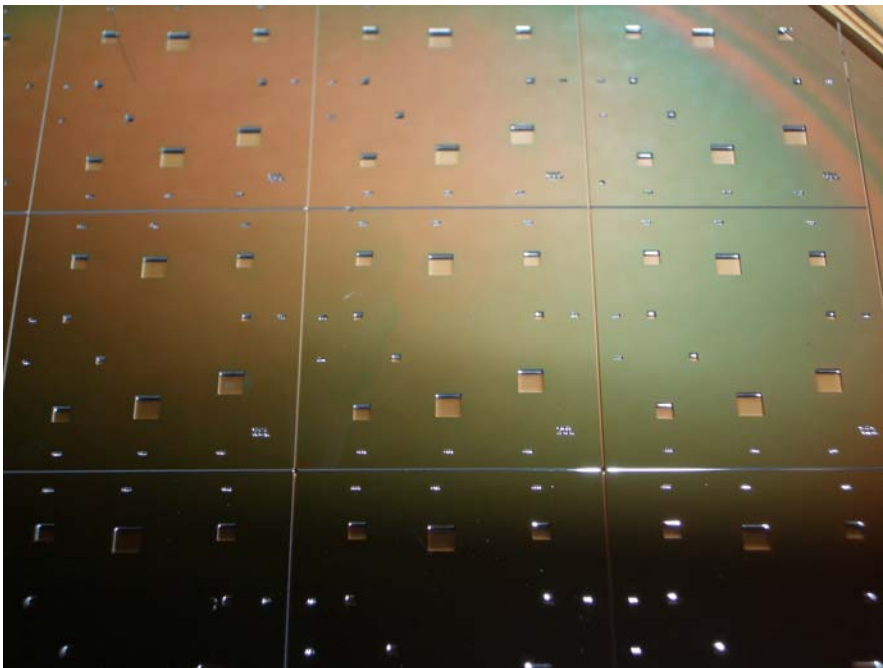


**Figure 72.** Partially released Si membranes produced using DRIE.

After LNO deposition, the die were then subjected to  $\text{XeF}_2$  to isotropically etch away the remaining Si from the membrane regions. Initial attempts to produce fully released LNO membranes via  $\text{XeF}_2$  were encouraging, although not entirely successful. In both DRIE and  $\text{XeF}_2$  etching, large regions of Si are preferentially etched over small regions. This so-called “loading effect” causes a differential etch rate between the membrane sizes, with the largest membranes showing some release after 4 loops, and small membranes only partially released after 11 etch loops. Some areas, particularly for the largest membranes, showed cracking or rupture. These ruptures are likely caused by the large tensile stress in the LNO thin (200nm) film, which is built up during the annealing process. Low stress  $\text{SiO}_2$  or  $\text{Si}_3\text{N}_4$  buffer layers might improve the thermal coefficient of expansion mismatch to reduce the stress in the film, allowing for larger released structures.

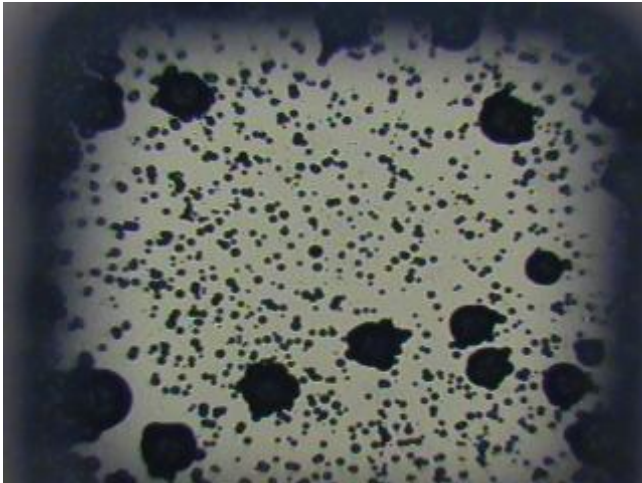


**Figure 73.** Small (0.5mm) square membrane showing partial release from the Si substrate after 11 etch loops (20x magnification).



**Figure 74.** Cracking and rupture of partially released membrane in large square (1.5mm) membrane after 11 etch loops (20x magnification).

## IV.5. Soluble Substrates

Free-standing oriented PBT films are desired to facilitate mechanical and electrical testing, and TEM analysis. Towards this goal, we present here preliminary results of efforts to produce oriented thin films on water soluble substrates.

Both NaCl and LiF are readily integrable into multilayer semiconductor process, as they can be deposited using evaporation or sputtering for use as sacrificial layers. Although LiF is only marginally soluble in water (1.3g/L), it has a cubic lattice constant ( $a = 4.03\text{\AA}$ ) that is comparable to that of PBT ( $a = 3.94\text{\AA}$ ,  $c = 4.07\text{\AA}$ ) [170]. Thus, good orientation of PBT on LiF(100) is expected. In contrast, NaCl is both highly soluble in water (359g/L) and well-matched to PBT. Although its cubic lattice constant is  $5.64\text{\AA}$ ,

the  $\langle 110 \rangle$  directions have a repeat distance of  $\sqrt{2}a/2 = 3.99\text{\AA}$ , which compares favorably with c-axis oriented PBT.

Some success attaining preferentially oriented ferroelectric thin films on LiF and NaCl has already been reported [48, 171-174]. MOCVD has been used to deposit (001)-oriented  $\text{PbTiO}_3$  on  $\text{NaCl}(100)$  [171, 172]. However, sol-gel deposition of  $\text{PbTiO}_3$  on NaCl by Ren et al. resulted in unoriented films [174], while some slight c-axis preference was exhibited in another sol-gel process by Lu et al. [173]. Xiong et al. used pulsed laser deposition to obtain (100)-oriented  $\text{Pb}_{0.72}\text{La}_{0.28}\text{TiO}_3$  on LiF using an MgO buffer layer [48]. No studies have yet examined sol-gel deposited ferroelectrics on LiF. Here, we seek to determine whether sol-gel methods might be used to deposit oriented lead barium titanate on NaCl or LiF.

Lead barium titanate sol was prepared using a sol-gel technique involving lead nitrate, barium acetate, and titanium isopropoxide precursors, with diethanolamine as a chelating agent and ethylene glycol as a solvent (TIpDEA system, described extensively in Chapter II). LiF(100) and NaCl(111) single-side polished substrates were obtained from MTI Crystal and used as received. NaCl(100) substrates were prepared through cleaving single crystals (obtained from Structure Probe, Inc.) in air just prior to deposition. PBT thin films were deposited onto the LiF and NaCl substrates via spin coating at 3krpm for 40 seconds (Chemat KW4-A Spin Coater) and were calcined for 2 hours in air. Heating rate (HR) and calcination temperature ( $T_c$ ) were varied to determine the resulting effects

on film characteristics. X-ray diffraction (XRD) was used to determine the phases present and extent of orientation in the films.

For all the substrates, heating/cooling rates of 20°C/min or higher led to heavy crack formation. This can be explained by the large difference in the coefficients of thermal expansion between the ferroelectric thin film and substrates (Table 20). Lower heating and cooling rates (1-5°C/min) resulted in smooth, crack-free films. The problem of substrate volatility or ‘out-gassing,’ reported by researchers using PLD deposition processes, was not observed here, likely due to the ambient pressures involved in sol-gel processing [17]. By not requiring a low pressure atmosphere, the sol-gel process makes it possible to calcine the films to higher temperatures, even near the melting point of the substrate, without significant out-gassing.

**Table 20.** Properties of LiF, NaCl, and  $\text{Pb}_{0.5}\text{Ba}_{0.5}\text{TiO}_3$ .

	<b>Lattice Parameters</b>	<b>TCE (<math>\times 10^{-6}/\text{K}</math>)</b>	<b>Melting Point (°C)</b>	<b>Solubility in Water (25°C) (g/L)</b>
<b>LiF</b>	<b>a = 4.03</b>	<b>37</b>	<b>870</b>	<b>1.3</b>
<b>NaCl</b>	<b>a = 5.64</b>	<b>44</b>	<b>801</b>	<b>359</b>
<b>PBT</b>	<b>a = 3.944 c = 4.075</b>	<b>9 (for <math>\text{BaTiO}_3</math>) 12 (for <math>\text{PbTiO}_3</math>)</b>	<b>-</b>	<b>-</b>

### IV.5.1. PBT on LiF

PBT thin films deposited on LiF(100) showed good orientation, but lacked phase purity. The XRD peaks indicate the presence of (100/001)-oriented PBT with a secondary impurity phase of BaPbO<sub>3</sub>, suggesting some titanium from the sol diffused into the LiF substrate (Figure 75). This is supported by the observation that a very slow heating rate (HR = 1°C/min) leads to formation of BaPbO<sub>3</sub> exclusively, as diffusion progresses to a greater extent. The amount of BaPbO<sub>3</sub> appears to remain constant as more layers are added to the film, suggesting the loss of titanium is restricted to the interface of the film and substrate. It also suggests that, once formed, BaPbO<sub>3</sub> serves as a diffusion barrier to further Ti loss. Diffusion is also slowed by lowering the calcination temperature, and, as shown in Figure 76, lowering the calcination temperature to 550°C reduced the amount of BaPbO<sub>3</sub> formation and dramatically improved the orientation of the PBT. While formation of BaPbO<sub>3</sub> was not the goal of these synthesis efforts, its presence may, in fact, be beneficial. Because of its good electronic conductivity, BaPbO<sub>3</sub> could be used as an electrode [79, 141]. Thus, sol-gel deposition of PBT on LiF may provide a route for *in situ* electrode incorporation, but would not get the benefit of lattice matching to LiF.

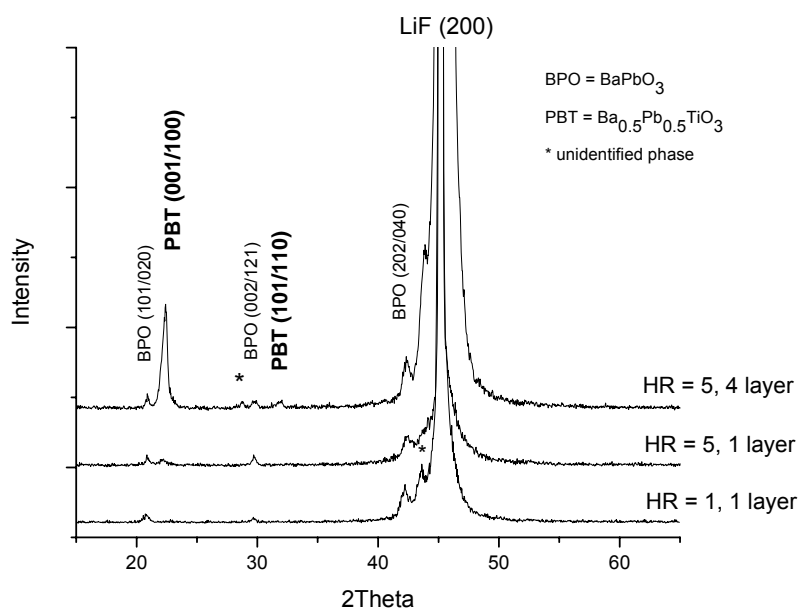


Figure 75. PBT thin films on LiF with the heating rates and number of layers indicated ( $T_c = 600^\circ\text{C}$ ).

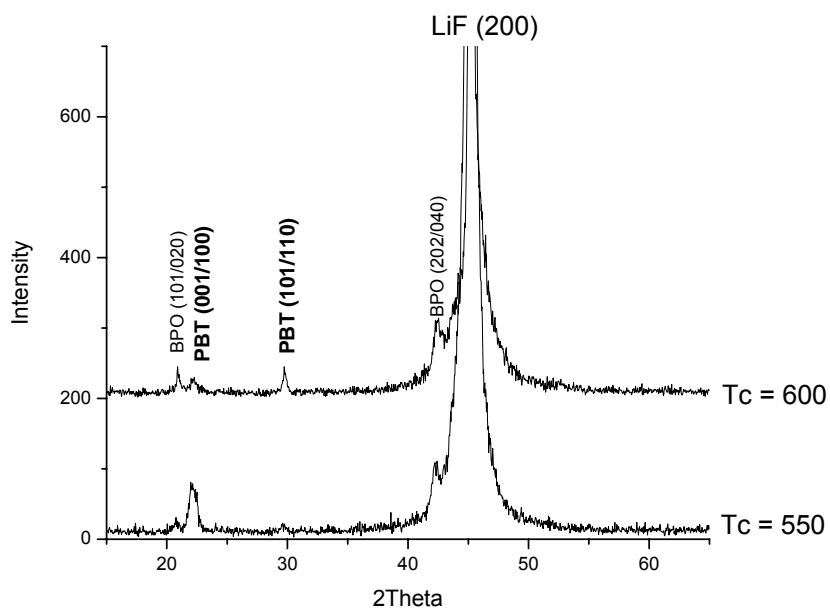
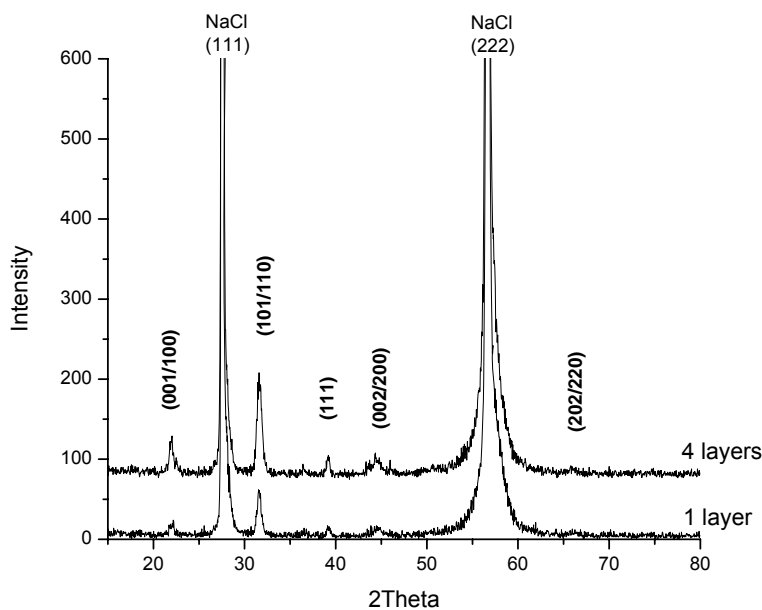


Figure 76. PBT thin films on LiF with the calcination temperatures indicated ( $\text{HR} = 5^\circ\text{C}/\text{min}$ ).

### IV.5.2. PBT on NaCl

In contrast, PBT thin films on NaCl(111) are phase pure, though randomly oriented (Figure 77). As there is no BaPbO<sub>3</sub> formation, titanium diffusion is apparently not a factor for the NaCl(111) substrate. The lack of orientation can be explained by the lack of any lattice match with PBT.



**Figure 77.** PBT thin films deposited on NaCl(111) with the number of layers indicated ( $T_c = 600^\circ\text{C}$  for 120 minutes in air,  $\text{HR} = 5^\circ\text{C}/\text{min}$ ).

As with NaCl(111), NaCl(100) did not suffer from the titanium diffusion observed with LiF, even for very slow heating rates ( $\text{HR} = 1^\circ\text{C}/\text{min}$ ). As shown in Figure 78, PBT thin films deposited on NaCl(100) crystallized by  $500^\circ\text{C}$  and were phase pure by  $550^\circ\text{C}$ . The films show some (001/100) preferred orientation, although other orientations are also present. It is hypothesized that the other orientations occur due to surface imperfections

resulting from the cleaving process. As shown in Figure 79, the surface is quite rough. Further studies are required to determine whether misoriented grains occur preferentially at the surface steps.

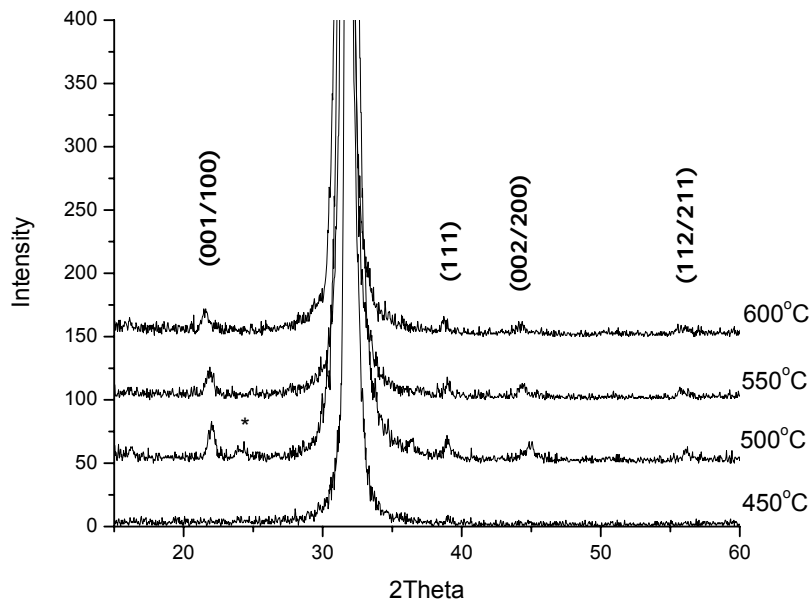


**Figure 78.** PBT thin films deposited on NaCl(100) and calcined at the temperatures indicated (HR = 1°C/min).

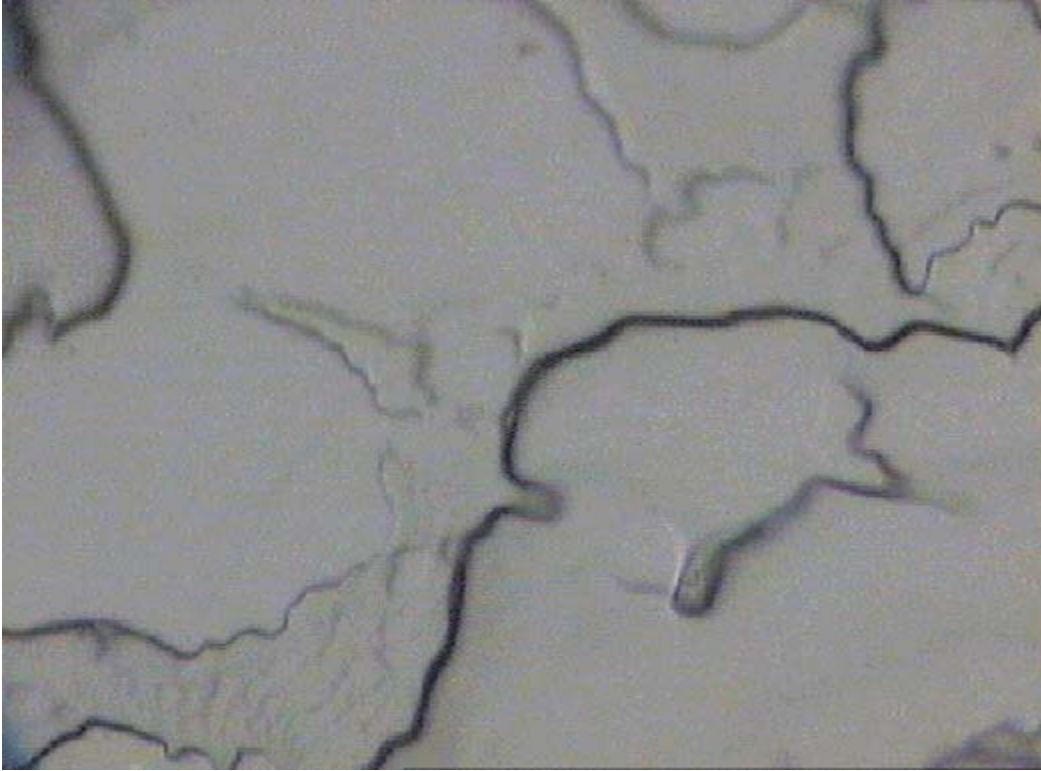


**Figure 79.** Optical microscope image of fresh cleaved NaCl(100) surface, 50x magnification.

## V. Conclusions

Several sol-gel systems were developed to produce powder and thin film lead barium titanate. The importance of several processing parameters was determined and chelating agent selection was found to be critical for reliably producing phase pure powders and films at moderate temperatures. Lead barium titanate thin films were produced using an optimized sol-gel system involving lead nitrate, barium acetate, and titanium isopropoxide metal precursors with ethylene glycol as a solvent and diethanolamine as a chelating agent. Highly (001/100)-oriented thin films were produced on lattice matched substrates at temperatures as low as 600°C.

Conductive oxide electrodes were also investigated to address orientation and fatigue concerns associated with metal electrodes. Sol-gel deposition of  $\text{LaNiO}_3$  thin films resulted in (100)-orientation on a wide variety of amorphous and crystalline substrates. Orientation was achieved through random heterogeneous nucleation at the film/substrate interface followed by the slow growth of (100)-planes which have the lowest surface energy. These highly oriented, lattice matched films were found to be excellent substrates for producing (001/100)-oriented lead barium titanate. Enhanced nucleation at the  $\text{LaNiO}_3$  substrate resulted in a 150° reduction in crystallization temperature of PBT compared to MgO.

Lead barium titanate and lanthanum nickelate were deposited on a variety of patterned substrates to facilitate electrical and mechanical testing. Highly oriented films were

deposited on pre-released 100nm  $\text{Si}_3\text{N}_4$  membranes, and on partially released Si substrates. Further,  $\text{LaNiO}_3$  was found to be an excellent etch stop for  $\text{XeF}_2$  dry gas etchant, allowing for the production of free-standing electrode membranes on Si substrates.

## **V.1. Suggestions for Future Research**

### **V.1.1. Electrical and mechanical testing**

Most parameters investigated here relied on XRD, FTIR, and/or SEM to determine the optimal parameter value on the basis of phase purity, orientation, and/or surface morphology. In some cases, no major difference was seen using these techniques. The influence of these parameters, most notably heating rate, holding time, and titanium alkoxide precursor, should be investigated further using electrical and mechanical testing to determine the relevance of these parameters in terms of future device applications.

### **V.1.2. Solvent selection for $\text{LaNiO}_3$**

Currently, 2-methoxyethanol is used as the solvent in lanthanum nickelate sol-gel preparation. The toxicity of 2-methoxyethanol is well-established, and a more environmentally-friendly chemical should be found if possible. Some studies suggest

using 1,3-propanediol as an alternative, however this substitution was not immediately successful.

### **V.1.3. Application of electric field during calcination**

Below the Curie temperature, all six tetragonal polarization directions are energetically equivalent. For c-axis or a-axis oriented films, two  $180^\circ$  variants possess lower energy and are prevalent. The effect of the application of an electric field during calcination should be investigated to determine whether a single orientation can be obtained, using the applied field to favor one variant over the other. A bias can be applied during calcination using parallel plate electrodes separated by high-temperature insulating ceramic supports and connected to a voltage source using high temperature wire. This should be easily facilitated using  $\text{LaNiO}_3$ -coated substrates, which effectively require only  $T_c = 450^\circ\text{C}$  for PBT calcination.

### **V.1.4. Patterning using broad spectrum UV source**

Both acetylacetone and diethanolamine-based sol-gel processes were found to have broad regions of UV absorption. A broad spectrum UV source should be obtained to determine whether UV exposure can cause organics to breakdown at lower temperatures, resulting in a lower crystallization temperature. If so, this can be used to pattern wet films through selective UV exposure on a hotplate. Exposed regions

would crystallize, while unexposed regions would be easily washed away using the parent solvent (in this case, ethylene glycol).

### **V.1.5. Orientation of LaNiO<sub>3</sub>**

The in-plane orientation of LaNiO<sub>3</sub> should be investigated in detail using pole figure analysis to determine whether there is the possibility of achieving in-plane orientation of the conductive oxide electrode. Bi-axially textured films are required for the micropump application, and a mechanism to produce bi-axially textured LaNiO<sub>3</sub> should be investigated. One possible alternate suggestion is to chemically or mechanically polish LaNiO<sub>3</sub> to produce a smooth surface for IBAD deposition of MgO to provide a template for in-plane orientation of subsequently deposited PBT.

### **V.1.6. Porosity of LaNiO<sub>3</sub>**

SEM studies should be completed to determine the effect of various process parameters on the porosity of LaNiO<sub>3</sub> thin films. The effect of substrate, sol concentration, pyrolysis temperature and time, calcination temperature and time, layer thickness, etc. should be examined.

### **V.1.7. Solid solution range of $\text{Pb}_{1-x}\text{Ba}_x\text{TiO}_3$**

The entire solid solution range of PBT was investigated only in powder form. Thin films should be prepared using varied Pb:Ba on  $\text{LaNiO}_3$ -coated substrates. These films should then be examined using XRD, SEM, and PFM to determine the phase purity, crystallinity, grain size, surface morphology, and ferroelectric properties as a function of Pb:Ba content. Free standing membranes should also be prepared for each composition in order to determine the effect of Pb:Ba on mechanical properties of the thin films.

### **V.1.8. Effect of calcination atmosphere**

The effect of calcination atmosphere should be investigated via measurement of ferroelectric properties of films prepared in atmospheres with varied oxygen content.  $^{13}\text{C}$ -NMR studies might be used to further study the effect of calcination atmosphere on the decomposition pathway in powders, as barium carbonate and oxycarbonate have been reported to have noticeably different NMR spectra [Duran 2001].

## V.2. Final Remarks & Outlook

The ultimate goal of this thesis work, fabricating oriented PBT thin films, was successfully achieved. Moreover, several device fabrication challenges were addressed, most notably the incorporation of conductive oxide electrodes and the preparation of released membrane structures. Although electromechanical testing of the films was not directly a part of this thesis, preliminary experiments carried out by collaborator Rongjing Zhang indicate the films deposited on  $\text{Si}_3\text{N}_4$  have a deflected rest-state (Figure 80), and can withstand mechanical loading and unloading. Calculations are forthcoming which will provide the Young's modulus and ultimate strength for  $\text{LaNiO}_3$  and  $\text{Pb}_{0.5}\text{Ba}_{0.5}\text{TiO}_3$  films. These moduli will aid in the design of future thin film ferroelectric mechanical actuators.

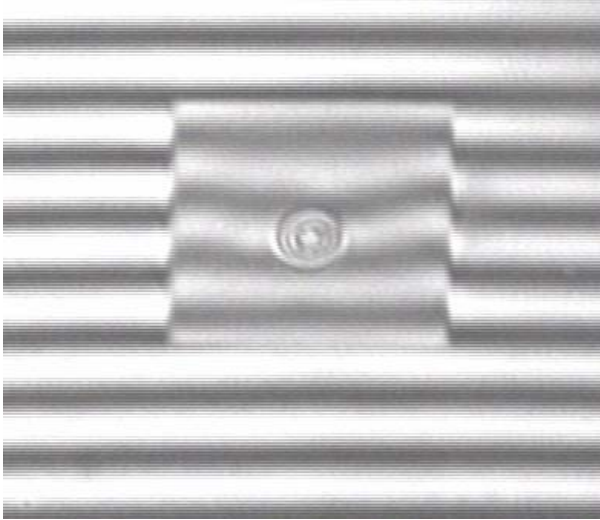


**Figure 80.** Picture at 10x magnification showing micro interferometry of a released membrane of PBT(180nm)/LaNiO<sub>3</sub>(96nm)/Si<sub>3</sub>N<sub>4</sub>(100nm) showing vertical deflection of the film. The substrate is tilted with respect to the camera. Fringe spacing is 0.273 $\mu$ m. [Image courtesy Rongjing Zhang]

The outlook for the integration of ferroelectric films into semiconductor layer process is very promising. The ability to produce oriented, electroded ferroelectric thin films on Si-based substrates will greatly enhance the range of devices and structures achievable using MEMS processing techniques. Fabrication of these films is an essential first step towards demonstration of the concept of microelectromechanical devices controlled via ferroelectric domain boundary reorientation.

## References

1. E. Zakar, M. Dubey, B. Piekarski, J. Conrad, R. Piekarz and R. Widuta, "Process and fabrication of a lead zirconate titanate thin film pressure sensor," *J. Vac. Sci. Technol. A*, 19, [1] 345-348 (2001).
2. R. Thomas and D. C. Dube, "Structural, electrical and optical properties of sol-gel processed lead titanate thin films," *Jpn. J. Appl. Phys.*, 36, [Part 1, No. 12A] 7337-7343 (1997).
3. O. Auciello, C. M. Foster and R. Ramesh, "Processing technologies for ferroelectric thin films and heterostructures," *Annu. Rev. Mater. Sci.*, 28, 501-531 (1998).
4. M. W. Cole, P. C. Joshi and M. H. Ervin, "La doped  $Ba_{1-x}Sr_xTiO_3$  thin films for tunable device applications," *J. Appl. Phys.*, 89, [11] 6336-6340 (2001).
5. D. Xia, M. Liu, Y. Zeng and C. Li, "Fabrication and electrical properties of lead zirconate titanate thick films by the new sol-gel method," *Mater. Sci. Eng.*, B87, 160-163 (2001).
6. E. Burcsu, G. Ravichandran and K. Bhattacharya, "Large strain electrostrictive actuation in barium titanate," *Appl. Phys. Lett.*, 77, 1698-1700 (2000).
7. E. Burcsu, G. Ravichandran and K. Bhattacharya, "Large electrostrictive actuation of barium titanate single crystals," *J. Mech. and Phys. of Solids*, 52, 823-846 (2004).
8. R. Corriu and D. Leclercq, "Recent developments of molecular chemistry for sol-gel processes," *Angewandte Chemie*, 35, [13-14] 1420-1436 (1996).

9. S. H. Kim, C. E. Kim and Y. J. Oh, "Preparation of  $\text{PbTiO}_3$  thin-films using an alkoxide-alkanolamine sol-gel system," *J. Mater. Sci.*, 30, 5639-5643 (1995).
10. U. Selvaraj, A. V. Prasadarao and S. Komarneni, "Sol-gel processing of oriented  $\text{PbTiO}_3$  thin films with lead acetylacetonate as the lead precursor," *Mater. Lett.*, 20, 71-74 (1994).
11. H. Nishizawa and M. Katsube, "Preparation of  $\text{BaTiO}_3$  thin films using glycolate precursor," *J. Sol. State. Chem*, 131, 43-48 (1997).
12. D. Bao, X. Yao, N. Wakiya, K. Shinozaki and N. Mizutani, "Structural, dielectric, and ferroelectric properties of  $\text{PbTiO}_3$  thin films by a simple sol-gel technique," *Mater. Sci. Eng.*, B94, 269-274 (2002).
13. M. Kuwabara, S. Takahashi and T. Kuroda, "Preparation of  $\text{BaTiO}_3$  and  $\text{PbTiO}_3$  thin films on  $\text{BaPbO}_3$  substrates by the sol-gel method and their properties"; pp. 365-370 in Materials Research Society, 271, *Better Ceramics Through Chemistry V* Edited by M. J. Hampden-Smith, W. G. Klemperer and C. Brinker. San Francisco, 1992.
14. N. J. Phillips, M. L. Calzada and S. J. Milne, "Sol-gel derived lead titanate films," *J. Non-Cryst. Solids*, 147 & 148, 285-290 (1992).
15. N. Giridharan and R. Jayavel, "Fabrication of ferroelectric  $(\text{Pb,Ba})\text{TiO}_3$  thin films by sol-gel technique and their characterization," *Mater. Lett.*, 52, [1-2] 57-61 (2002).
16. F. M. Pontes, E. R. Leite, G. P. Mambrini, M. T. Escote, E. Longo and J. A. Varela, "Very large dielectric constant of highly oriented  $\text{Pb}_{1-x}\text{Ba}_x\text{TiO}_3$  thin films prepared by chemical deposition," *Appl. Phys. Lett.*, 84, [2] 248-250 (2004).

17. J. Wu, S. C. Tidrow, M. Z. Tidrow, M. H. Ervin, R. C. Hoffman, C. W. Tipton, D. N. Robertson and W. W. Clark, "Preferentially oriented (La,Sr)CoO<sub>3</sub>/PbLa<sub>0.1</sub>TiO<sub>3</sub>/(La,Sr)CoO<sub>3</sub> tri-layers on lithium-fluoride and sodium-chloride substrates," *Integr. Ferro.*, 28, [1-4] 103-112 (2000).
18. X. Zhu, H. L.-W. Chan, C.-L. Choy and K.-H. Wong, "Epitaxial growth and dielectric properties of functionally Ba<sub>1-x</sub>Sr<sub>x</sub>TiO<sub>3</sub> thin films with stoichiometric variation," *J. Vac. Sci. Technol. A*, 20, [5] 1796-1801 (2002).
19. Z. Huang, X. Meng, Z. Zhang and J. Chu, "Infrared optical properties of PbTiO<sub>3</sub> ferroelectric thin films," *J. Phys. D: Appl. Phys.*, 35, 246-248 (2002).
20. C. H. Ahn, K. M. Rabe and J.-M. Triscone, "Ferroelectricity at the nanoscale: local polarization in thin films and heterostructures," *Science*, 303, [23 January] 488-491 (2004).
21. S. Wada, M. Narahara, T. Hoshina, H. Kakemoto and T. Tsurumi, "Preparation of nm-sized BaTiO<sub>3</sub> particles using a new 2-step thermal decomposition of barium titanyl oxalate," *J. Mater. Sci.*, 38, [12] 2655-2660 (2003).
22. D. L. Polla and L. F. Francis, "Processing and characterization of piezoelectric materials and integration into microelectromechanical systems," *Annu. Rev. Mater. Sci.*, 28, 563-597 (1998).
23. N. Ozer and T. Sands, "Preparation and optical characterization of sol-gel deposited Pb(Zr<sub>0.45</sub>Ti<sub>0.55</sub>)TiO<sub>3</sub> films," *J. Sol-gel Sci. Tech.*, 19, 157-162 (2000).
24. K. T. Kim and C. I. Kim, "Structure and dielectrical properties of (Pb,Sr)TiO<sub>3</sub> thin films for tunable microwave device," *Thin Solid Films*, 420-421, 544-547 (2002).

25. E. Dogheche, B. Jaber and D. Remiens, "Optical waveguiding in epitaxial  $\text{PbTiO}_3$  thin films," *Appl. Optics*, 37, [19] 4245-4248 (1998).
26. L. Beckers, J. Schubert, W. Zander, J. Ziesmann, A. Eckau, P. Leinenbach and C. Buchal, "Structural and optical characterization of epitaxial waveguiding  $\text{BaTiO}_3$  thin films on  $\text{MgO}$ ," *J. Appl. Phys.*, 83, [6] 3305-3310 (1998).
27. G. Yi, Z. Wu and M. Sayer, "Preparation of  $\text{Pb}(\text{Zr}, \text{Ti})\text{O}_3$  thin films by sol gel processing: electrical, optical, and electro-optic properties," *J. Appl. Phys.*, 64, [5] 2717-2724 (1988).
28. K. Torii, Y. Matsui and Y. Fujisaki, "Texture control of  $\text{Pb}(\text{Zr}, \text{Ti})\text{O}_3$  thin films," *Integr. Ferro.*, 25, [1-4] 563-573 (1999).
29. J. Duclere, L. Hamedi, M. Guilloux-Viry and A. Perrin, "Substrate effect on the PLD growth of ferroelectric materials thin films," *Ferroelectrics*, 254, 53-64 (2001).
30. S. Kalpat and K. Uchino, "Highly oriented lead zirconium titanate thin films: growth, control of texture, and its effect on dielectric properties," *J. Appl. Phys.*, 90, [6] 2703-2710 (2001).
31. T. Higuchi, Y. Chen, J. Koike, S. Iwashita, M. Ishida and T. Shimoda, "Fabrication of pseudocubic  $\text{SrRuO}_3$  (100) epitaxial thin films on Si by pulsed laser deposition," *Jpn. J. Appl. Phys.*, 41, [Part 2, No. 4B] L481-L483 (2002).
32. S. R. Gilbert, S. Hunter, D. Ritchey, C. Chi, D. V. Taylor, J. Amano, S. Aggarwal, T. S. Moise, T. Sakoda, S. R. Summerfelt, K. K. Singh, C. Kazemi, D. Carl and B. Bierman, "Preparation of  $\text{Pb}(\text{Zr}, \text{Ti})\text{O}_3$  thin films made by metalorganic chemical vapor deposition for low voltage ferroelectric memory," *J. Appl. Phys.*, 93, [3] 1713-1717 (2003).

33. J. Livage, M. Henry and C. Sanchez, "Sol-gel chemistry of transition-metal oxides," *Progress in Solid State Chemistry*, 18, [4] 259-341 (1988).
34. R. W. Schwartz, "Chemical solution deposition of perovskite thin films," *Chem. Mater.*, 9, 2325-2340 (1997).
35. D. B. Mitzi, "Thin-film deposition of organic-inorganic hybrid materials," *Chem. Mater.*, 13, 3283-3298 (2001).
36. M. Yoshimura, W. L. Suchanek and K. Byrappa, "Soft solution processing: a strategy for one-step processing of advanced inorganic materials," *MRS Bulletin*, [September] 17-25 (2000).
37. M. Yoshimura and J. Livage, "Soft processing for advanced inorganic materials," *MRS Bulletin*, [September] 12-16 (2000).
38. J. Ricote, R. Poyato, M. Alguero, L. Pardo, M. L. Calzada and D. Chateigner, "Texture development in modified lead titanate thin films obtained by chemical solution deposition on silicon-based substrates," *J. Am. Ceram. Soc.*, 86, [9] 1571-1577 (2003).
39. M. Calzada, B. Malic, R. Sirera and M. Kosec, "Thermal-decomposition chemistry of modified Lead-Titanate Aquo-diol gels used for the preparation of thin films," *J. Sol-gel Sci. and Tech.*, 23, 221-230 (2002).
40. G. J. Norga, S. Jin, L. Fe, D. J. Wouters, H. Bender and H. E. Maes, "Growth of (111)-oriented  $\text{Pb}(\text{Zr}, \text{Ti})\text{O}_3$  layers on nanocrystalline  $\text{RuO}_2$  electrodes using the sol-gel technique," *J. Mater. Res.*, 16, [3] 828-833 (2001).

41. W. Gong, J.-F. Li, X. Chu, Z. Gui and L. Li, "Preparation and characterization of sol-gel derived (100)-textured  $\text{Pb}(\text{Zr}, \text{Ti})\text{O}_3$  thin films: PbO seeding role in the formation of preferential orientation," *Acta Materialia*, 52, 2787-2793 (2004).
42. J. Zeng, M. Zhang, L. Wang and C. Lin, "Influence of lead titanate seed layer on orientation behaviour and ferroelectric characteristics of sol-gel derived PZT thin films," *J. Phys.: Cond. Matt.*, 11, [4] 1139-1146 (1999).
43. F. F. Lange, "Chemical solution routes to single-crystal thin films," *Science*, 273, [16 Aug] 903-909 (1996).
44. K. T. Miller and F. F. Lange, "Highly oriented thin films of cubic zirconia on sapphire through grain growth seeding," *J. Mater. Res.*, 6, [11] 2387-2392 (1991).
45. R. W. Schwartz, P. G. Clem, J. A. Voigt, E. R. Byhoff, M. Van Stry, T. J. Headley and N. A. Missert, "Control of microstructure and orientation in solution-deposited  $\text{BaTiO}_3$  and  $\text{SrTiO}_3$  thin films," *J. Am. Ceram. Soc.*, 82, [9] 2359-2367 (1999).
46. F. M. Pontes, D. S. L. Pontes, E. R. Leite and E. Longo, "Synthesis, ferroelectric, and optical properties of  $(\text{Pb}, \text{Ca})\text{TiO}_3$  thin films by soft solution processing," *J. Sol-gel Sci. Tech.*, 27, 137-147 (2003).
47. R. N. Das, R. K. Pati and P. Pramanik, "A novel chemical route for the preparation of nanocrystalline PZT powder," *Mater. Lett.*, 45, [6] 350-355 (2000).
48. S. Xiong, Z. Liu, X. Chen, X. Guo, X. Liu and S. Zhu, "Pulsed laser deposition and characterization of optical waveguiding  $(\text{Pb}, \text{La})(\text{Zr}, \text{Ti})\text{O}_3$  thin films," *Appl. Phys. Lett.*, 67, [18] 2729-2731 (1995).

49. B. E. Yoldas, "Design of sol-gel coating media for ink-jet printing," *J. Sol-gel Sci. Tech.*, 13, 147-152 (1998).
50. Y. Li, B. W. Maynor and J. Liu, "Electromechanical AFM 'dip-pen' nanolithography," *J. Am. Ceram. Soc.*, 123, [9] 2105-2106 (2001).
51. M. Frey and D. Payne, "Synthesis and processing of barium titanate ceramics from alkoxide solutions and monolithic gels," *Chem. Mater.*, 7, 123-129 (1995).
52. H. Matsuda, N. Kobayashi, T. Kobayashi, K. Miyazawa and M. Kuwabara, "Room-temperature synthesis of crystalline barium titanate thin films by high-concentration sol-gel method," *J. Non-Cryst. Solids*, 271, 162-166 (2000).
53. J. F. Meng, R. S. Katiyar and G. T. Zou, "Grain size effect on ferroelectric phase transition in  $\text{Pb}_{1-x}\text{Ba}_x\text{TiO}_3$ ," *J. Phys. Chem. Sol.*, 59, [6-7] 1161-1167 (1998).
54. J. S. Speck, A. Seifert, W. Pompe and R. Ramesh, "Domain configurations due to multiple misfit relaxation mechanisms in epitaxial ferroelectric thin films. II. Experimental verification and implications," *J. Appl. Phys.*, 76, [1] 477-483 (1994).
55. M. Kosec and B. Malic, "Relationship between precursor chemistry and microstructure of CSD derived PZT films," *J. Phys. IV France*, 8, Pr9-17-26 (1998).
56. N. Floquet, J. Hector and P. Gaucher, "Correlation between structure, microstructure, and ferroelectric properties of  $\text{PbZr}_{0.2}\text{Ti}_{0.8}\text{O}_3$  integrated film: Influence of the sol-gel process and substrate," *J. Appl. Phys.*, 84, [7] 3815-3826 (1998).

57. K. Brooks, I. M. Reaney, R. Klissurska, Y. Huang, L. Bursill and N. Setter, "Orientation of rapid thermally annealed lead zirconate titanate thin films on (111)Pt substrates," *J. Mater. Res.*, 9, [10] 2540-2553 (1994).
58. Y. L. Tu and S. J. Milne, "A study of the effects of process variables on the properties of PZT films produced by a single-layer sol-gel technique," *J. Mater. Sci.*, 30, 2507-2516 (1995).
59. C. Brinker and G. Scherer, *Sol-gel Science: The Physics and Chemistry of Sol-gel Processing*, Academic Press, Inc., New York (1990).
60. D. C. Bradley, R. C. Mehrotra and D. P. Gaur, *Metal Alkoxides*, Academic Press Inc., New York (1978).
61. N. V. Golubko, M. I. Yanovskaya, I. P. Romm and A. N. Ozerin, "Hydrolysis of titanium alkoxides: thermochemical, electron microscopy, SAXS studies," *J. Sol-gel Sci. Tech.*, 20, [3] 245-262 (2001).
62. A. Leautic, F. Babonneau and J. Livage, "Structural investigation of the hydrolysis-condensation process of titanium alkoxides  $Ti(OR)_4$  (OR = OPri, OEt) modified by acetylacetone. 2. From the modified precursor to the colloids," *Chem. Mater.*, 1, 248-252 (1989).
63. L. Weng, X. Bao and K. Sagoe-Crentsil, "Effect of acetylacetone on the preparation of PZT materials in sol-gel processing," *Mat. Sci. Eng. B*, 96, 307-312 (2002).
64. F. Ribot, P. Toledano and C. Sanchez, "Hydrolysis-condensation process of B-diketonates-modified cerium (IV) isopropoxide," *Chem. Mater.*, 3, 759-764 (1991).

65. B. Malic, N. Setter, K. Brooks, M. Kosec and G. Drazic, "Acetic acid based sol-gel PLZT thin films: processing and characterization," *J. Sol-gel Sci. Tech.*, 13, 833-836 (1998).
66. L. G. Hubert-Pfalzgraf, "Toward molecular design of oxide precursors for advanced materials," <http://www.solgel.com/articles/jun02/preintro.asp>, (2002).
67. F. X. Perrin, V. Nguyen and J. L. Vernet, "FT-IR spectroscopy of acid-modified titanium alkoxides: investigations on the nature of carboxylate coordination and degree of complexation," *J. Sol-gel Sci. Tech.*, 28, 205-215 (2003).
68. U. Hasenkox, S. Hoffman and R. Waser, "Influence of precursor chemistry on the formation of  $MTiO_3$  (M = Ba, Sr) ceramic thin films," *J. Sol-gel Sci. Tech.*, 12, 67-79 (1998).
69. L. G. Hubert-Pfalzgraf, S. Daniele, S. Boulmaaz and R. Papiernik, "Controlling the properties of bulk metallic oxides at a molecular level: alkoxides vs. carboxylates-alkoxides routes"; pp. 21-27 in Materials Research Society, 346, *Better Ceramics Through Chemistry VI*, 1994.
70. Y. Takahashi, "Dip-coating of  $TiO_2$  films using a sol derived from  $Ti(O-i-Pr)_4$ -diethanolamine- $H_2O-i-PrOH$  system," *J. Mater. Sci.*, 23, 2259-2266 (1988).
71. T. Ohya, A. Nakayama, T. Ban, Y. Ohya and Y. Takahashi, "Synthesis and characterization of halogen-free, transparent, aqueous colloidal titanate solutions from titanium alkoxide," *Chem. Mater.*, 14, 3082-3089 (2002).
72. Y. Djaoued, R. Taj, R. Bruning, S. Badilescu, P. V. Ashrit, G. Bader and T. Vo-Van, "Study of the phase transition and the thermal nitridation of nanocrystalline sol-gel titania films," *J. Non-Cryst. Solids*, 297, 55-66 (2002).

73. T. Ban, Y. Ohya and Y. Takahashi, "Reaction of titanium isopropoxide with alkanolamines and association of the resultant Ti species," *J. Sol-gel Sci. Tech.*, 27, 363-372 (2003).
74. Y. Ohya, J. Mishina, T. Matsuda, T. Ban and Y. Takahashi, "Crystallization and microstructure development of sol-gel-derived titanium dioxide thin films with single and multiple layers," *J. Am. Ceram. Soc.*, 82, [10] 2601-2606 (1999).
75. S. C. Pillai, S. W. Boland and S. M. Haile, "Low temperature crystallization of sol-gel processed  $\text{Pb}_{0.5}\text{Ba}_{0.5}\text{TiO}_3$ ," *J. Am. Ceram. Soc.*, 87, 1388-1391 (2004).
76. H. Tanaka, K. Tadanaga, N. Tohge and T. Minami, "Effect of alkanolamines on the microstructure and dielectric properties of lead zirconium titanium trioxide thin films prepared from modified metal alkoxides," *Jpn. J. Appl. Phys.*, 34 Part 2, [9A] L1155-L1157 (1995).
77. Y. Takahashi, Y. Matsuoka, K. Yamaguchi, M. Matsuki and K. Kobayashi, "Dip coating of PT, PZ, and PZT films using an alkoxide-diethanolamine method," *J. Mater. Sci.*, 25, 3960-3964 (1990).
78. M. L. Calzada and S. J. Milne, "Lead zirconate titanate films from a diol-based sol-gel method," *J. Mater. Sci. Lett.*, 12, 1221-1223 (1993).
79. T. Azuma, S. Takahashi and M. Kuwabara, "Preparation and basic properties of  $\text{BaTiO}_3/\text{BaPbO}_3$  multilayer thin films by metal-alkoxides method," *Jpn. J. Appl. Phys.*, 32, [Part 1, No 9B] 4089-4091 (1993).
80. V. Srikant, E. J. Tarsa, D. R. Clarke and J. S. Speck, "Crystallographic orientation of epitaxial  $\text{BaTiO}_3$  films: the role of thermal-expansion mismatch with the substrate," *J. Appl. Phys.*, 77, [4] 1517-1522 (1994).

81. T. Ogawa, A. Senda and T. Kasanami, "Controlling the crystal orientations of lead titanate thin films," *Jpn. J. Appl. Phys.*, 30, [9B] 2145-2148 (1991).
82. B. H. Moeckley, S. E. Russek, D. K. Lathrop, R. A. Buhrman, J. Li and J. W. Mayer, "Growth of  $\text{YBa}_2\text{Cu}_3\text{O}_7$  thin films on MgO: the effect of substrate preparation," *Appl. Phys. Lett.*, 57, [16] 1687-1689 (1990).
83. M. G. Norton, S. R. Summerfelt and C. B. Carter, "Surface preparation for the heteroepitaxial growth of ceramic thin films," *Appl. Phys. Lett.*, 56, [22] 2246-2248 (1990).
84. R. Hull, *Properties of Crystalline Silicon*; INSPEC, London, 1999.
85. C. Chen, D. F. J. Ryder and W. A. Spurgeon, "Synthesis and microstructure of highly oriented lead titanate thin films prepared by a sol-gel method," *J. Am. Ceram. Soc.*, 72, [8] 1495-1498 (1989).
86. K. Fujito, N. Wakiya, K. Shinozaki and N. Mizutani, "Change of residual stresses and electrical properties of  $\text{Pb}(\text{Zr}, \text{Ti})\text{O}_3$  thin films upon introducing various bottom electrodes," *J. Ceram. Soc. Jpn.*, 110, [5] 421-427 (2002).
87. S. H. Kim, Y. S. Choi, C. E. Kim and D. Y. Yang, "The effects of  $\text{PbTiO}_3$  thin template layer and Pt/ $\text{RuO}_2$  hybrid electrode on the ferroelectric properties of sol-gel derived PZT thin film," *Thin Solid Films*, 325, 72-78 (1998).
88. L. Jiankang and Y. Xi, "Microstructure and electrical properties of  $\text{Pb}(\text{Zr}_{0.52}\text{Ti}_{0.48})\text{O}_3$  ferroelectric films on different bottom electrodes," *Mater. Lett.*, 58, [27-28] 3447-3450 (2004).

89. M. Kondo, K. Maruyama and K. Kurihara, "Epitaxial ferroelectric thin films on silicon substrates for future electronic devices," *Fujitsu Sci. Tech.*, 38, [1] 46-53 (2002).
90. S. Fujii, A. Tomozawa, E. Fujii, H. Torii, R. Takayama and T. Hirao, "Preparation of La-modified PbTiO<sub>3</sub> thin-films on the oxide buffer layers with NaCl-type structure," *Appl. Phys. Lett.*, 65, [11] 1463-1465 (1994).
91. C. Brinker, A. J. Hurd, P. R. Schunk, G. C. Frye and C. S. Ashley, "Review of sol-gel thin film formation," *J. Non-Cryst. Solids*, 147 & 148, 424-436 (1992).
92. G. A. Luurtsema, "Spin Coating for Rectangular Substrates," Thesis, Electrical Engineering and Computer Sciences, University of California, Berkeley, (1997).
93. D. P. Birnie, "Rational solvent selection strategies to combat striation formation during spin coating of thin films," *J. Mater. Res.*, 16, [4] 1145-1154 (2001).
94. D. Meyerhofer, "Characteristics of resist films produced by spinning," *J. Appl. Phys.*, 49, [7] 3993-3997 (1978).
95. H. Gu, W. Cao, R. Song, X. Zhou and J. Wang, "Effects of precursor solution pH value and substrate texture on orientation degree of sol-gel derived bismuth titanate thin films," *Phys. Stat. Sol.*, 198, [2] 282-288 (2003).
96. G. J. Derderian, J. D. Barrie, K. A. Aitchison, P. M. Adams and M. L. McCartney, "Microstructure/process relations in sol-gel prepared KNbO<sub>3</sub> thin films on (100)MgO," *J. Am. Ceram. Soc.*, 77, [3] 820-828 (1994).
97. D. Hoebbel, T. Reinert, H. Schmidt and E. Arpac, "On the hydrolytic stability of organic ligands in Al-, Ti-, and Zr- alkoxide complexes," *J. Sol-gel Sci. Tech.*, 10, 115-126 (1997).

98. S. W. Boland, S. C. Pillai, W.-D. Yang and S. M. Haile, "Preparation of (Pb, Ba)TiO<sub>3</sub> [owders and highly oriented thin films by a sol-gel process," *J. Mater. Res.*, 19, [5] 1492-1498 (2004).
99. S. W. Boland and S. M. Haile, "Comparison of titanium precursors in the sol-gel synthesis of Pb<sub>0.5</sub>Ba<sub>0.5</sub>TiO<sub>3</sub> powders and thin films"; in Materials Research Society Fall Meeting, 784, *Mater. Res. Soc. Symp. Proc.*, Boston, MA, 2003.
100. T. Yogo, "Synthesis of PbTiO<sub>3</sub>/organic hybrid from metalorganic compounds," *J. Mater. Res.*, 14, [8] 3275 (1999).
101. J. Moon, J. A. Kerchner, H. Krarup and J. H. Adair, "Hydrothermal synthesis of ferroelectric perovskites from chemically modified titanium isopropoxide and acetate salts," *J. Mater. Res.*, 14, [2] 425-435 (1999).
102. A. Kareiva, S. Tautkus, R. Rapalaviciute, J.-E. Jorgensen and B. Lundtoft, "Sol-gel synthesis and characterization of barium titanate powders," *J. Mater. Sci.*, 34, 4853-4857 (1999).
103. P. Duran, F. Capel, D. Gutierrez, J. Tartaj, M. A. Banares and C. Moure, "Metal citrate polymerized complex thermal decomposition leading to the synthesis of BaTiO<sub>3</sub>: effects of the precursor structure on the BaTiO<sub>3</sub> formation mechanism," *J. Mater. Chem.*, 11, 1828-1836 (2001).
104. NIST, "NIST Chemistry WebBook," (2003).
105. R. F. Speyer, *Thermal Analysis of Materials*, Marcel Dekker, Inc., New York (1994).
106. G. Burns, "Lattice modes in ferroelectric perovskites II. Pb<sub>1-x</sub>Ba<sub>x</sub>TiO<sub>3</sub> including BaTiO<sub>3</sub>," *Phys. Rev. B*, 10, [5] 1951-1959 (1974).

107. Y.-R. Luo and J.-M. Wu, "BaPbO<sub>3</sub> perovskite electrode for lead zirconate titanate ferroelectric thin films," *Appl. Phys. Lett.*, 79, [22] 3669-3671 (2001).
108. A. Gruverman, O. Auciello and H. Tokumoto, "Imaging and control of domain structures in ferroelectric thin films via scanning force microscopy," *Annu. Rev. Mater. Sci.*, 28, 101-123 (1998).
109. S. Dunn, "Strain behavior of thin film PbZr<sub>0.3</sub>Ti<sub>0.7</sub>O<sub>3</sub> (30/70) examined through piezoforce microscopy," *J. Appl. Phys.*, 94, [9] 5964-5968 (2003).
110. T. Tybell, P. Paruch, T. Giamarchi and J.-M. Triscone, "Domain wall creep in epitaxial ferroelectric Pb(Zr<sub>0.2</sub>Ti<sub>0.8</sub>)O<sub>3</sub> thin films," *Phys. Rev. Lett.*, 89, [9] 097601-1-4 (2002).
111. Y.-B. Park, M. J. Dicken, J. L. Ruglovsy, S. W. Boland, S. M. Haile and H. A. Atwater, "Nanoscale domain switching characteristics in polycrystalline Pb<sub>1-x</sub>Ba<sub>x</sub>TiO<sub>3</sub> thin film by out-of-plane and in-plane polarizations with piezoresponse force microscopy," *Appl. Phys. Lett.*, submitted, (2005).
112. A. Klyndyuk, G. Petrov and L. Bashkirov, "Anomalous high-temperature properties of BaPbO<sub>3</sub>-based solid solutions," *Inorg. Mater.*, 37, [4] 399-404 (2001).
113. H. Lee and D. Tsai, "Metalorganic chemical vapor deposition of SrRuO<sub>3</sub> thin film and its characterization," *J. Mater. Sci.*, 38, [12] 2633-2638 (2003).
114. D. Kaur and K. V. Rao, "Microstructural and conductive properties of BaRuO<sub>3</sub> thin films," *Solid State Comm.*, 128, 391-395 (2003).
115. S.-M. Koo, M.-S. Lee and B. M. Moon, "Nonvolatile current-sensing device in all-oxide Pb(Zr, Ti)O<sub>3</sub>/BaRuO<sub>3</sub> structure," *Electronics Letters*, 40, [17] (2004).

116. J.-H. Kim, K. S. Koh and W. K. Choo, "The effect of stoichiometric  $\text{La}_{1/2}\text{Sr}_{1/2}\text{CoO}_3$  as sputtered bottom electrode on  $\text{SiO}_2/\text{Si}$ ," *J. Korean Phys. Soc.*, 42, [April] S1313-S1316 (2003).
117. N. Wakiya, K. Shinozaki and N. Mizutani, "Electrical properties of epitaxial  $\text{La}_{0.5}\text{Sr}_{0.5}\text{CoO}_3$  (LSCO) thin films prepared in low oxygen pressure," *Nihon Seramikkusu Kykai Gakujutsu Ronbunshi*, 110, [5] 353-357 (2002).
118. A. Mardare, C. Mardare, E. Joanni, J. Fernandes, P. Vilarinho and A. Kholkin, "Barium metaplumbate thin film electrodes for ferroelectric devices," *Ferroelectrics*, 293, 177-188 (2003).
119. D. Bao, X. Yao, N. Wakiya, K. Shinozaki and N. Mizutani, "Preparation of conductive  $\text{LaNiO}_3$  film electrodes by a simple chemical solution deposition technique for integrated ferroelectric thin film devices," *J. Phys. D: Appl. Phys.*, 36, 1217-1221 (2003).
120. S. Miyake, S. Fujihara and T. Kimura, "Characteristics of oriented  $\text{LaNiO}_3$  thin films fabricated by the sol-gel method," *J. Eur. Ceram. Soc.*, 21, 1525-1528 (2001).
121. S. Trolier-McKinstry, Personal Communication (2004).
122. P. Ahonen, A. S. Gurav, E. I. Kauppinen, M. J. Hampden-Smith and T. T. Kodas, "Aerosol dynamics during aerosol decomposition synthesis of metal ruthenate powders," *J. Aerosol Sci.*, 27, [Supplement 1] S373-S374 (1996).
123. T. Higuchi, Y. Chen, J. Koike, S. Iwashita, M. Ishida and T. Shimoda, "Epitaxial growth of  $\text{SrRuO}_3$  thin film electrode on Si by pulsed laser deposition," *Jpn. J. Appl. Phys.*, 41, [Part I, No. 11B] 6867-6872 (2002).

124. K. C. Park and J. H. Cho, "Electric field dependence of ferroelectric phase transition in epitaxial SrTiO<sub>3</sub> films on SrRuO<sub>3</sub> and La<sub>0.5</sub>Sr<sub>0.5</sub>CoO<sub>3</sub>," *Appl. Phys. Lett.*, 77, [3] 435-437 (2000).
125. S.-M. Yoon, E. Tokumitsu and H. Ishiwara, "Electrical properties of La<sub>0.7</sub>Sr<sub>0.3</sub>CoO<sub>3</sub>/Pb(Zr<sub>0.52</sub>Ti<sub>0.48</sub>)O<sub>3</sub>/La<sub>0.7</sub>Sr<sub>0.3</sub>CoO<sub>3</sub> thin film capacitors formed on MgO substrates using the sol-gel method," *Jpn. J. Appl. Phys.*, 37, [Part 2, No. 8A] L936-L938 (1998).
126. S. Miyake, K. Yamamoto, S. Fujihara and T. Kimura, "(100)-Orientation of pseudocubic perovskite-type LaNiO<sub>3</sub> thin films on glass substrates via the sol-gel process," *J. Am. Ceram. Soc.*, 85, [4] 992-994 (2002).
127. M. S. Chen, J.-M. Wu and T. B. Wu, "Effects of (100)-textured LaNiO<sub>3</sub> electrode on crystallization and properties of sol-gel-derived Pb(Zr<sub>0.53</sub>Ti<sub>0.47</sub>)O<sub>3</sub>," *Jpn. J. Appl. Phys.*, 34, [Part 1, No. 9A] (1995).
128. C.-S. Liang, J.-M. Wu and M.-C. Chang, "Ferroelectric BaPbO<sub>3</sub>/PbZr<sub>0.53</sub>Ti<sub>0.47</sub>/BaPbO<sub>3</sub> heterostructures," *Appl. Phys. Lett.*, 81, [19] 3624-3626 (2002).
129. F. Wang, A. Uusimäki, S. Leppavuori and H. Zhang, "Preparation of conducting barium metaplumbate thin film using solution coating method," *Mat. Res. Bull.*, 31, [1] 37-46 (1996).
130. L. F. Mattheiss and D. R. Hamann, "Electronic structure of BaPb<sub>1-x</sub>Bi<sub>x</sub>O<sub>3</sub>," *Phys. Rev. B*, 28, [8] 4227-4241 (1983).

131. T. Hashimoto and R. Hirasawa, "Coexistence of electrons and holes in  $\text{BaBi}_{0.25}\text{Pb}_{0.75}\text{O}_{3-d}$  detected by thermoelectric-power measurements," *Phys. Rev. B*, 51, [1] 576-580 (1995).
132. P. B. Allen and W. W. Schulz, "Bloch-Boltzmann analysis of electrical transport in intermetallic compounds:  $\text{ReO}_3$ ,  $\text{BaPbO}_3$ ,  $\text{CoSi}_2$ , and  $\text{Pd}_2\text{Si}$ ," *Phys. Rev. B*, 47, [21] 14434-14439 (1993).
133. Y.-H. Hsieh and S.-L. Fu, "BaPbO<sub>3</sub>-based thick film resistor," *IEEE Transactions on components, hybrids, and manufacturing technology*, 15, [3] 348-352 (1992).
134. Y.-H. Hsieh and S.-L. Fu, "A conduction model for BaPbO<sub>3</sub>-based thick film resistors," *IEEE Transactions on components, packaging, and manufacturing technology—Part A*, 17, [2] 316-319 (1994).
135. P. Ganguly and M. S. Hegde, "Evidence for double valence fluctuation in metallic oxides of lead," *Phys. Rev. B*, 37, [10] 5107-5111 (1988).
136. Y. Kodama, N. Murayama and Y. Torii, "Chemical preparation and properties of semi-metal BaPbO<sub>3</sub> ceramics," *J. Mater. Sci. Lett.*, 17, 1999-2001 (1998).
137. M. Kuwabara, H. Nagata, K. Nakao, R. Liang and M. Takeo, "Joining of BaPbO<sub>3</sub> ceramics with PTCR-type (BaPb)TiO<sub>3</sub> ceramics and their electrical properties," *J. Mater. Sci. Lett.*, 8, 411-414 (1989).
138. F. P. Skeeel, R. E. Newnham and L. E. Cross, "Barium metaplumbate ceramic electrodes for ceramic capacitors," *J. Am. Ceram. Soc.*, 71, [5] C263-C267 (1988).

139. C. L. Sun, H. W. Wang, M. C. Chang, M. S. Lin and S. Y. Chen, "Characterization of BaPbO<sub>3</sub> and Ba(Pb<sub>1-x</sub>Bi<sub>x</sub>)O<sub>3</sub> thin films," *Mater. Chem. and Phys.*, 78, 507-511 (2002).
140. S. Takahashi, S. Sekine, H. Tsumagari, H. Shimooka and M. Kuwabara, "Preparation and dielectric properties of the ferroelectric materials/BaPbO<sub>3</sub> multilayer thin films by sol-gel method"; pp. 371-375 in 6th Tohwa University International Symposium, 1996.
141. H. Ikushima and S. Hayakawa, "Electrical properties of BaPbO<sub>3</sub> ceramics," *Solid State Electronics*, 9, 921-925 (1966).
142. M.-J. Shyu, T.-J. Hong, T.-J. Yang and T. B. Wu, "Highly (100)-oriented thin films of sol-gel derived Pb[(Mg<sub>1/3</sub>Nb<sub>2/3</sub>)<sub>0.675</sub>Ti<sub>0.325</sub>]O<sub>3</sub> prepared on textured LaNiO<sub>3</sub> electrode," *Jpn. J. Appl. Phys.*, 34, [Part 1, No.7A] 3647-3653 (1995).
143. C.-C. Yang, M.-S. Chen, T.-J. Hong, C.-M. Wu, J.-M. Wu and T.-B. Wu, "Preparation of (100)-oriented metallic LaNiO<sub>3</sub> thin films on Si substrates by radio frequency magnetron sputtering for the growth of textured Pb(Zr<sub>[0.53]</sub>Ti<sub>[0.47]</sub>)O<sub>3</sub>," *Appl. Phys. Lett.*, 66, [20] 2643-2645 (1995).
144. A. Li, C. Ge and P. Lu, "Preparation of perovskite conductive LaNiO<sub>3</sub> films by metalorganic decomposition," *Appl. Phys. Lett.*, 68, [10] 1347-1349 (1996).
145. A. Van der Drift, "Evolutionary selection: A principle governing growth orientation in vapour-deposited layers," *Philips Research Reports*, 22, [3] 267 (1967).
146. H. Miyazaki, T. Goto, Y. Miwa, T. Ohno, H. Suzuki, T. Ota and M. Takahashi, "Preparation and evaluation of LaNiO<sub>3</sub> thin film electrode with chemical solution deposition," *J. Eur. Ceram. Soc.*, 24, 1005-1008 (2004).

147. M. Madou, *Fundamentals of Microfabrication*, CRC Press, Boca Raton (1997).
148. W. R. Runyan and K. E. Bean, *Semiconductor Integrated Circuit Processing Technology*, Addison-Wesley, Reading, MA (1990).
149. J. Baborowski, "Microfabrication of Piezoelectric MEMS," *J. Electroceramics*, 12, [1 - 2] 33-51 (2004).
150. R. A. Delaney and H. D. Kaiser, "Multiple-Curie-point capacitor dielectrics," *IBM Journal*, Sept., 511-519 (1967).
151. Y. Takahashi, A. Ohsugi, T. Arafuka, T. Ohya, T. Ban and Y. Ohya, "Development of new modifiers for titanium alkoxide-based sol-gel process," *J. Sol-gel Sci. Tech.*, 17, 227-238 (2000).
152. E. Sukur, S. Nishiyama and T. Hattori, "Effect of UV-irradiation on crystallization and morphology of zinc oxide films prepared by chemical solution deposition," *J. Ceram. Soc. Jpn.*, 109, [1] 1-3 (2001).
153. K. Kikuta, K. Takagi and S.-I. Hirano, "Photoreaction of titanium-based metal-organic compounds for ceramic fine patterning," *J. Am. Ceram. Soc.*, 82, [6] 1569-1572 (1999).
154. G. Uozumi, K. Kageyama, T. Atsuki, N. Soyama, H. Uchida and K. Ogi, "Evaluation of self-patterned  $\text{PbZr}_x\text{Ti}_{1-x}\text{O}_3$  thin films from photosensitive solution," *Jpn. J. Appl. Phys.*, 38, 5350-5353 (1999).
155. Y. B. Kim, T. S. Kim, K. S. Choi and D. J. Choi, "Densification method of screen printed PZT(52/48) thick films," *Integr. Ferro.*, 35, 199-208 (2001).
156. D. A. Payne and P. G. Clem, "Monolayer-mediated patterning of integrated electroceramics," *J. Electroceramics*, 3, [2] 163-172 (1999).

157. P. G. Clem, N. L. Jeon, R. G. Nuzzo and D. A. Payne, "Monolayer-mediated deposition of tantalum(V) oxide thin film structures from solution precursors," *J. Am. Ceram. Soc.*, 80, [11] 2821-2827 (1997).
158. N. L. Jeon, P. G. Clem, R. G. Nuzzo and D. A. Payne, "Patterning of dielectric oxide thin layers by microcontact printing of self-assembled monolayers," *J. Mater. Res.*, 10, [12] 2996-2999 (1995).
159. W. S. Beh and Y. Xia, "Formation of patterned microstructures of polycrystalline ceramics from precursor polymers using micromolding in capillaries," *J. Mater. Res.*, 14, [10] 3995-4003 (1999).
160. J. S. Vartuli, M. Ozenbas, C.-M. Chun, M. Trau and I. A. Aksay, "Micropatterned lead zirconium titanate thin films," *J. Mater. Res.*, 18, [5] 1259-1265 (2003).
161. D. Corning, <http://www.dowcorning.com> – Silicone encapsulants product information for Sylgard family,
162. R. T. Brewer, D. A. Boyd, M. El-Naggar, S. W. Boland, S. M. Haile, D. G. Goodwin and H. A. Atwater, "Growth of biaxially textured  $Ba_xPb_{1-x}TiO_3$  ferroelectric thin films on amorphous  $Si_3N_4$ "; in 204th Meeting of the Electrochemical Society, Orlando, FL, 2003.
163. C. P. Wang, K. B. Do, M. R. Beasley, T. H. Geballe and R. H. Hammond, "Deposition of in-plane textured MgO on amorphous  $Si_3N_4$  substrates by ion-beam-assisted deposition and comparisons with ion-beam-assisted deposited yttria-stabilized-zirconia," *Appl. Phys. Lett.*, 71, 2955-2957 (1997).

164. R. T. Brewer, J. R. Groves, P. N. Arendt and H. A. Atwater, "Reflection high-energy electron diffraction experimental analysis of polycrystalline MgO films with grain size and orientation distributions," *J. Appl. Phys.*, 93, 205-210 (2003).
165. K. S. Lee, J. H. Choi, J. Y. Lee and S. Baik, "Domain formation in epitaxial Pb(Zr,Ti)O<sub>3</sub> thin films," *J. Appl. Phys.*, 90, [8] 4095-4102 (2001).
166. B. Jaffe, W. R. J. Cook and H. Jaffe, *Piezoelectric Ceramics*, Academic Press, London (1971).
167. Q. Zhang, S. J. Gross, S. Tadigadapa, T. N. Jackson, F. T. Djuth and S. Trolier-McKinstry, "Lead zirconate titanate films for d33 mode cantilever actuators," *Sensors and Actuators A*, 105, [1] 91-97 (2003).
168. R. Sood, Y. B. Jeon, J. H. Jeong and S. G. Kim, "Piezoelectric micro power generator for energy harvesting"; pp. 148-151 in Solid-State Sensor and Actuator Workshop, Hilton Head, South Carolina, 2004.
169. B. Piekarski, M. Dubey, E. Zakar, R. Polcawich, D. DeVoe and D. Wickenden, "Sol-gel PZT for MEMS applications," *Integr. Ferro.*, 42, 25-37 (2002).
170. A. Seidell, *Solubilities of Inorganic and Metal Organic Compounds; A Compilation of Quantitative Solubility Data from the Periodical Literature*, D. Von Nostrand Company, Inc., New York (1940).
171. W. Ma, Q. Li, Y. Chen, T. Yu and N. Ming, "Microstructure and epitaxial characteristics of PbTiO<sub>3</sub> ferroelectric thin film on NaCl by MOCVD," *Integr. Ferro.*, 9, 291-297 (1995).

172. W. Ma, M. Zhang, T. Yu, Y. Chen, Q. Li and N. Ming, "Direct observation of ferroelectric domains in MOCVD-grown  $\text{PbTiO}_3$  thin films by means of transmission electron microscopy," *Ferroelectrics*, 200, [1-4] 109-123 (1997).
173. C. J. Lu, S. B. Ren, H. M. Shen, J. S. Liu and Y. N. Wang, "Microstructure, composition, and optical properties of  $\text{PbTiO}_3$  thin films prepared by the sol-gel method," *J. Vac. Sci. Technol. A*, 15, [4] 2167-2172 (1997).
174. S. B. Ren, C. J. Lu, J. S. Liu, H. M. Shen and Y. N. Wang, "Size-related ferroelectric-domain-structure transition in a polycrystalline  $\text{PbTiO}_3$  thin film," *Phys. Rev. B*, 54, [20] 337-340 (1996).

## **A. Appendix**

### **A.1. TipAc System: Standard Procedure**

1. Barium acetate (8.23mmol, 3.12g, Aldrich, 99%,) was dissolved in 20mL of ethylene glycol, using a hotplate/stirrer at 50°C.
2. Lead acetate trihydrate (8.23mmol, 2.10g, Alpha Aesar, 99%) was added to 10mL ethylene glycol and attached to a condenser/guard tube assembly, placed on a hotplate/stirrer at 260°C and 700rpm for 1 hour, and then allowed to cool to room temperature.
3. The two metal acetate solutions were then mixed together with 15mL ethylene glycol and stirred for 15 minutes (room temperature, 700rpm).
4. Titanium isopropoxide (16.46 mmol, 4.83mL, Alpha Aesar, 99%) and acetylacetone (in a prescribed ratio with titanium, Aldrich, 99%) was added to the mixed acetate solution, and the resulting solution was heated to 260°C while stirring for 1 hour attached to a condenser/guard tube.
5. Water (in a prescribed ratio with titanium) and equal amount of ethylene glycol were added to the solution, which was then heated at 260°C in a hotplate and stirred for 1 hour.

6. This solution was alternately dried in an air oven to produce dried gels, or it was spin-coated onto MgO single crystals to produce thin films.

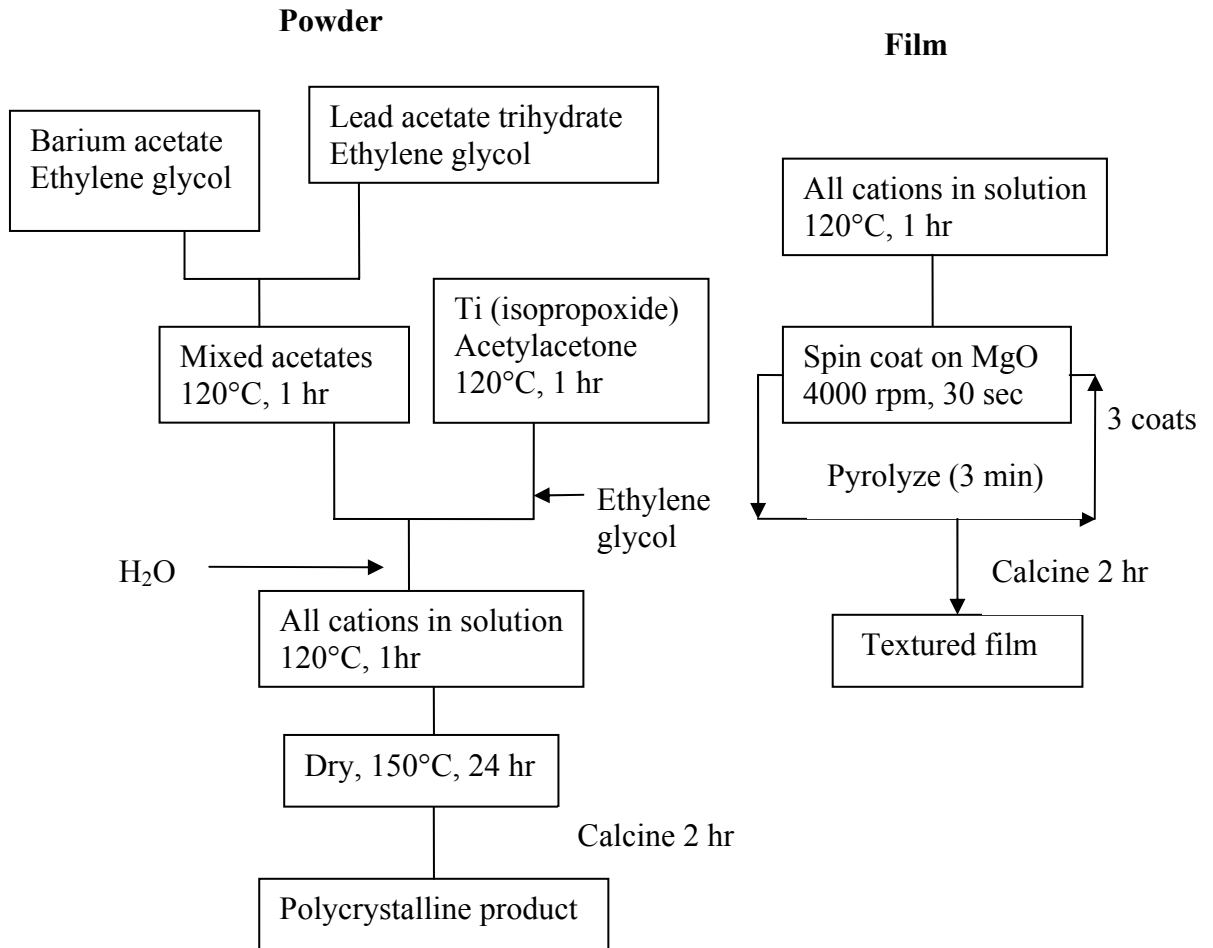


**Figure 81.** Schematic of TIpAc system procedure for producing PBT powders or thin films.

## A.2. TBuAc System: Standard Procedure

1. Lead nitrate (4.14g, 12.5mmol) and barium acetate (3.193g, 12.5mmol) were dissolved in 40mL ethylene glycol in an Erlenmeyer flask on a hotplate/stirrer (700rpm, 120°C, 30min) and then cooled 30 minutes.
2. Titanium butoxide (8.53mL, 25mmol) was added to acetylacetone (15.40mL, 150mmol) in a Erlenmeyer flask and stirred at 700rpm on a hotplate/stirrer at 180°C for 30 minutes. 10mL ethylene glycol was added and the solution stirred at RT, 15 minutes.
3. The Ti/AcAc solution was then added to the Pb/Ba solution and stirred at 700rpm, 120°C, 30min. The solution was allowed to cool for 30min.
4. De-ionized water ( $R_w = 4$ , 1.8mL, 100mmol) was added to the above system together with ethylene glycol in a 1:3 volume ratio (5.4mL). The resulting sol was stirred at room temperature, 700rpm, 15min). The sol was divided into two parts, and one part was used for spin coating and the other part dried at 175°C in an oven to form a xerogel.

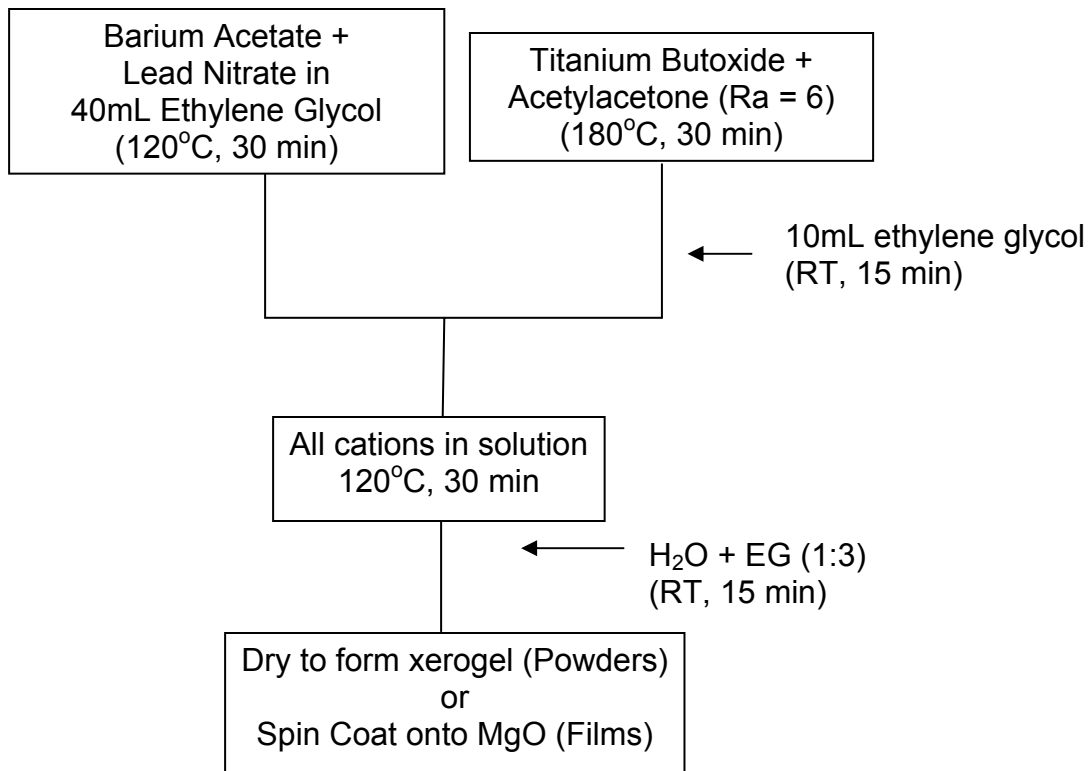


**Figure 82.** Schematic of TBuAc system procedure for producing PBT powders or thin films.

### A.3. TBuDEA System: Standard Procedure

1. Lead nitrate (4.14g, 12.5mmol) and barium acetate (3.193g, 12.5mmol) were dissolved in 40mL ethylene glycol in an Erlenmeyer flask on a hotplate/stirrer (700rpm, 120°C, 30min) and then cooled 30 minutes.
2. Titanium butoxide (8.53mL, 25mmol) was added to diethanolamine (4.79mL, 50mmol) in an Erlenmeyer flask and stirred at 700rpm on a hotplate/stirrer at 180°C for 30 minutes. 10mL ethylene glycol was added and the solution stirred at RT, 15 minutes.
3. The Ti/DEA solution was then added to the Pb/Ba solution and stirred at 700rpm, 120°C, 30min. The solution was allowed to cool for 30 min.
4. De-ionized water ( $R_w = 4$ , 1.8 mL, 100 mmol) is added to the above system together with ethylene glycol in a 1:3 volume ratio (5.4mL). The resulting sol was stirred at room temperature, 700rpm, 15min). The sol was divided into two parts, and one part was used for spin coating and the other part dried at 175°C in an oven to form a xerogel.

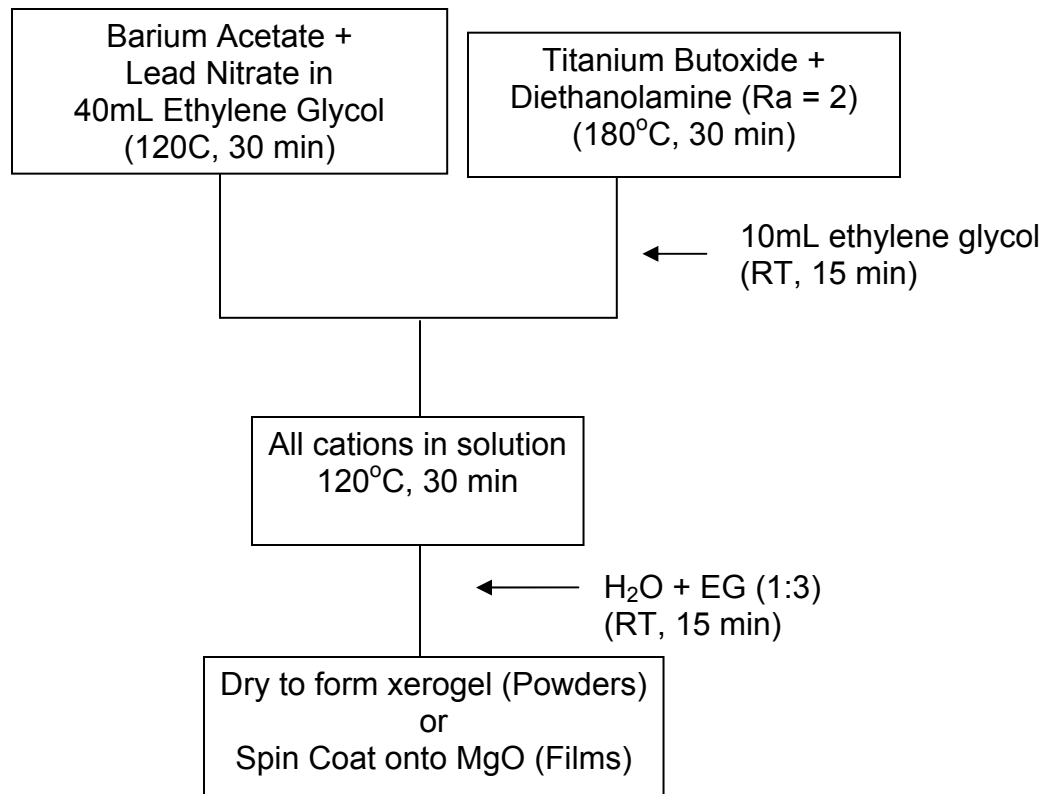


**Figure 83.** Schematic of TBuAc system procedure for producing PBT powders or thin films.

#### **A.4. TBuDEA System: Rotary Evaporator Procedure**

1. Lead nitrate (8.28g, 25mmol) and barium acetate (6.38g, 25mmol) were dissolved in 112.3mL ethylene glycol in a round bottom flask attached to a rotary evaporating system (120rpm, 72mbar, 60°C, 30min) and then cooled 30 minutes.
2. Titanium butoxide (17.052mL, 50mmol) was added to diethanolamine (9.6mL, 100mmol) in an Erlenmeyer flask and stirred at 600rpm on a hotplate/stirrer at room temperature for 30 minutes.
3. The Ti/DEA solution was then added to the Pb/Ba solution and attached to the rotary evaporating system (120rpm, 72 mbar, 60°C, 30min). The solution was allowed to cool for 30min.
4. De-ionized water ( $R_w = 4$ , 3.6mL, 200 mmol) was mixed with ethylene glycol (7.2mL) and then added to the above system. The resulting sol was then attached to the rotary evaporating system (120 pm, 72mbar, 60°C, 30min). The sol was divided into two parts, and one part was used for spin coating and the other part dried at 175°C in an oven to form a xerogel.

### **A.5. TIPDEA System: Standard Procedure**

1. Lead nitrate (8.28g, 25mmol) and barium acetate (6.38g, 25mmol) were dissolved in 112.3mL ethylene glycol in a round bottom flask attached to a rotary evaporating system (120rpm, 72mbar, 60°C, 30min) and then cooled 30 minutes.
2. Titanium isopropoxide (14.6mL, 50mmol) was added to diethanolamine (19.2mL, 200mmol) in a Erlenmeyer flask and stirred at 600rpm on a hotplate/stirrer at room temperature for 30 minutes.
3. The Ti/DEA solution was then added to the Pb/Ba solution and attached to the rotary evaporating system (120rpm, 72 mbar, 60°C, 30min). The solution was allowed to cool for 30min.
4. De-ionized water ( $R_w = 4$ , 3.6mL, 200 mmol) was mixed with ethylene glycol (7.2mL) and then added to the above system. The resulting sol was then attached to the rotary evaporating system (120 pm, 72mbar, 60°C, 30min). The sol was divided into two parts, and one part was used for spin coating and the other part dried at 175°C in an oven to form a xerogel.

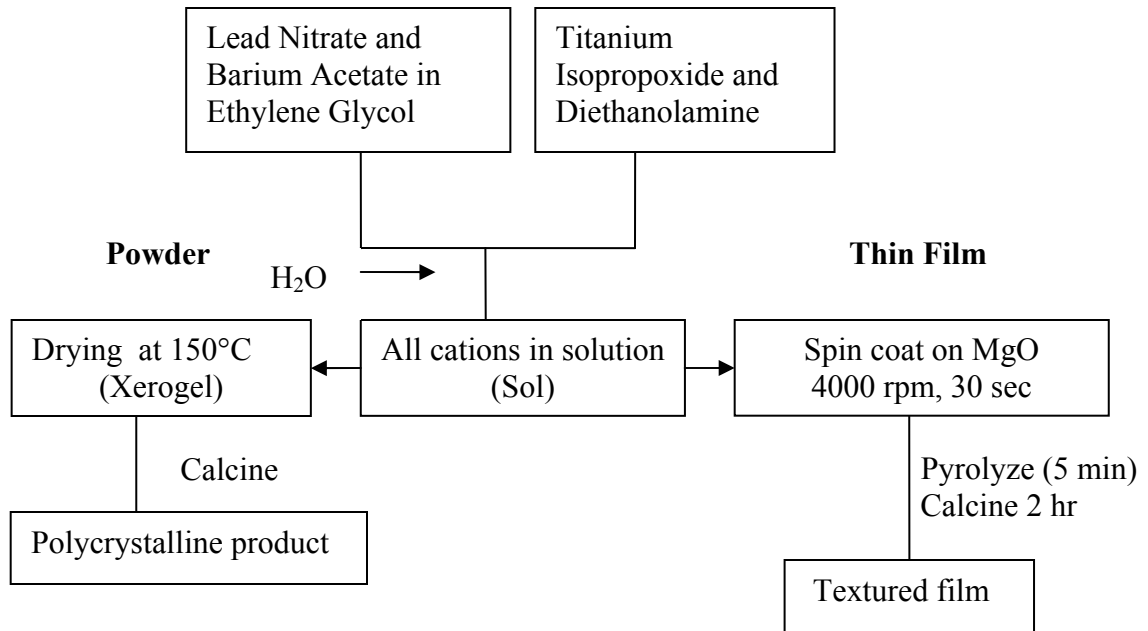


**Figure 84.** Schematic of TIPDEA system procedure for producing PBT powders or thin films.

### A.6. BPO System: Standard Procedure

1. Barium acetate (2.55g, 10mmol) and lead acetate (3.79g, 10mmol) were dissolved in 22.9mL acetic acid in an Erlenmeyer flask on a hotplate stirrer at (60°C, 600rpm, 30 minutes)

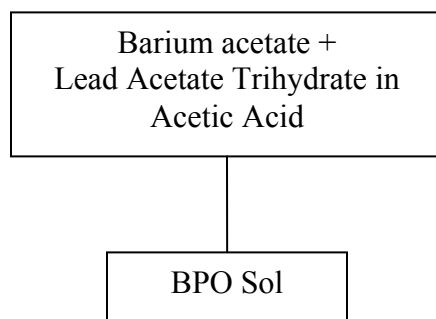


**Figure 85.** Schematic of BPO system procedure for producing BaPbO<sub>3</sub> sol.

### A.7. LNO System: Standard Procedure

1. Lanthanum acetate (1.72g, 5mmol) and nickel nitrate (1.46g, 5mmol) were dissolved in 10.7mL 2-methoxyethanol in an Erlenmeyer flask on a hotplate stirrer at (60°C, 700rpm, 5 minutes).
2. Ethanolamine (5mL) was added, and the solution was stirred for 2 hours (60°C, 700rpm).

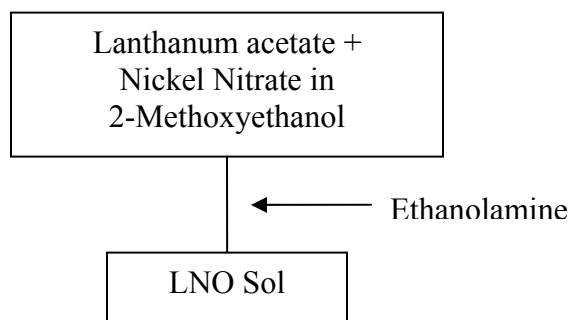


**Figure 86.** Schematic of LNO system procedure for producing  $\text{LaNiO}_3$  sol.

## A.8. Solubility Test Results

Table A-1. Solubility of Barium Precursors

	Barium Acetate	Barium Isopropoxide <sup>12</sup>	Barium Nitrate	Barium Oxalate	Barium Hydroxide	Barium Chloride
Acetic Acid	Yes	-	No	No	No	No
Acetic Anhydride	No	-	No	No	No	No
Acetone	No	No	No	No	No	No
Acetylacetone (2,4-pentanedione)	No	No	No	No	No	No
1-Butanol	No	No <sup>13</sup>	No	No	No	No
N,N-Dimethylacetamide	No	Yes	No	No	No	No
Ethanol	No	No	No	No	No	No
Ethylenediamine	No	-	Yes	Some	No	Some
Ethylene Glycol	Yes	No <sup>14</sup>	Some <sup>15</sup>	No <sup>16</sup>	No <sup>17</sup>	Yes
Hexanes	No	Yes (Highly)	No (crystallized!)	No	No	No
Isopropanol	No	Yes (Highly)	No	No	No	No
Methanol	No	No <sup>18</sup>	No	No	No	No <sup>19</sup>
2-Methoxyethanol	No	Yes (Highly)	No	No	Some <sup>20</sup>	No

<sup>12</sup> Solution quality/concentration suspect—precipitates formed in bottle

<sup>13</sup> Soluble at first, turns cloudy after a few seconds

<sup>14</sup> Gelatinous precipitate, dissolves easily with stirring...maybe try again later?

<sup>15</sup> Some dissolved, try higher temperature and longer time

<sup>16</sup> Also tried refluxing for 1 hour (~5g in 40mL)

<sup>17</sup> Some impurity formed (cottonlike particles) on boiling; on reflux not soluble

<sup>18</sup> Precipitate forms but dissolves upon stirring

<sup>19</sup> Some appeared to dissolve in methanol, anhydrous barium chloride was clearly not soluble

<sup>20</sup> Slightly soluble at 80°C. Some impurity formed (cottonlike particles) on boiling

	<b>Barium Acetate</b>	<b>Barium Isopropoxide</b> <sub>12</sub>	<b>Barium Nitrate</b>	<b>Barium Oxalate</b>	<b>Barium Hydroxide</b>	<b>Barium Chloride</b>
<b>1,3-Propanediol</b>	No	<b>Yes</b> <sup>21</sup>	Some <sup>22</sup>	No	No	No
<b>Propylene Glycol</b>	No	-	No	Some <sup>23</sup>	No	No
<b>Sec-Butanol</b>	No	No <sup>24</sup>	No	No	No	No
<b>Tetrahydrofuran</b>	No	No	No	No	No	No
<b>Diethanolamine</b>	<b>Yes</b>	-	No	No	No	

---

<sup>21</sup> Soluble, highly viscous. Initially 2 layers and small cloudy precipitate—dissolved w/ stirring

<sup>22</sup> Quite a bit dissolved, not enough...higher temps did not help (100°C)

<sup>23</sup> Tried at 100°C also, some dissolved. On refluxing, dark brown solution resulted with some precipitate

<sup>24</sup> Soluble at first, turns cloudy after a few seconds

Table A-2. Solubility of Lead Precursors

	<b>Lead Citrate</b>	<b>Lead Nitrate</b>	<b>Lead Acetate</b>	<b>Lead Acetylacetonate<sup>25</sup></b>
<b>Acetic Acid</b>	No	No	<b>Yes</b> (highly)	
<b>Acetic Anhydride</b>	No	No	No	
<b>Acetone</b>	No	No	No	
<b>Acetylacetone (2,4-pentanedione)</b>	No	No	Some <sup>26</sup>	
<b>1-Butanol</b>	No	No	No	
<b>N,N-Dimethylacetamide</b>	No	<b>Yes</b> (highly)	<b>Yes</b> (highly)	
<b>Ethanol</b>	No	No	No	
<b>Ethylenediamine</b>	Some	<b>Yes</b> (highly)	Yes	
<b>Ethylene Glycol</b>	No	<b>Yes</b> (highly)	<b>Yes</b>	<b>Yes</b>
<b>Hexanes</b>	No	No	No	
<b>Isopropanol</b>	No	No	No	
<b>Methanol</b>	No	No	<b>Yes</b> (highly)	
<b>2-Methoxyethanol</b>	No <sup>27</sup>	No	No	<b>Yes</b>
<b>1,3-Propanediol</b>	No	No	<b>Yes</b> (highly)	
<b>Propylene Glycol</b>	No	No	No	
<b>Sec-Butanol</b>	No	No	No	
<b>Tetrahydrofuran</b>	No	No	No	
<b>Diethanolamine</b>		some	<b>Yes</b>	

<sup>25</sup> Chemical is too expensive and comes in very small quantities—not suitable for study.

<sup>26</sup> Some dissolved at 100°C

<sup>27</sup> Also tried refluxing for 2 hours (~5g in 40mL)

**Table A-3.** Solubility of Lead and Barium Precursors Together

	<b>Solvent</b>	<b>Barium Acetate in Acetic Acid</b>	<b>Barium Acetate in Ethylene Glycol</b>	<b>Barium Chloride in Ethylene Glycol</b>
<b>Lead Acetate</b>	N,N Dimethylacetamide	<b>No</b>	<b>Not repeatable</b>	<b>No</b>
	Ethylene Glycol	<b>Yes</b> <i>(AAS System)</i>	<b>Yes</b> <i>(TIpAc System)</i>	<b>Precip with Ti</b>
	1,3 propanediol	<b>Yes</b>	<b>Yes</b>	<b>No</b>
	Methanol	<b>No</b>	<b>Yes</b>	<b>No</b>
	Acetic Acid	<b>Yes</b>	<b>Yes</b> <i>(AAS System)</i>	<b>No</b>
<b>Lead Nitrate</b>	Ethylene Glycol	<b>Yes</b> <i>(AAC System)</i>	<b>Yes</b>	<b>Yes</b>
	N,N Dimethylacetamide	<b>Yes</b>	<b>Yes</b>	<b>No</b>

## A.9. Sol-gel Systems Investigated

Table A-4. PBT Sol-gel Systems Investigated

	<b>Barium Precursor</b>	<b>Lead Precursor</b>	<b>Solvent</b>	<b>Chelating Agent</b>
<i><b>TIpAc</b></i>	Barium Acetate	Lead Acetate	Ethylene Glycol	Acetylacetone (2,4-Pentanedione)
<i><b>AAS</b></i>	Barium Acetate	Lead Acetate	Ethylene Glycol & Acetic Acid	-
<i><b>AAC</b></i>	Barium Acetate	Lead Nitrate	Ethylene Glycol	Acetic Acid
<i><b>TIpDEA</b></i>	Barium Acetate	Lead Nitrate	Ethylene Glycol	Diethanolamine (DEA)
<i><b>EG2NO3</b></i>	Barium Acetate	Lead Nitrate	Ethylene Glycol	-
<i><b>EG2NO3Ac</b></i>	Barium Acetate	Lead Nitrate	Ethylene Glycol	Acetylacetone (2,4-Pentanedione)
<i><b>F3AC</b></i>	Barium Acetate	Lead Citrate	Trifluoroacetic Acid	-
<i><b>BEtF3AC</b></i>	Barium Ethylhexanoate	Lead Acetate	Trifluoroacetic Acid	-
<i><b>PCBEt</b></i>	Barium Ethylhexanoate	Lead Citrate	Trifluoroacetic Acid	-
<i><b>TBuAc</b></i>	Barium Acetate	Lead Nitrate	Ethylene Glycol	Acetylacetone (2,4 Pentanedione)
<i><b>TBuDEA</b></i>	Barium Acetate	Lead Nitrate	Ethylene Glycol	Diethanolamine

Systems investigated in greatest detail shown in red.

**Table A-5.** Pros and Cons of Various PBT Sol-gel Systems

	<b>Pro</b>	<b>Con</b>	<b>Comments</b>
<i>TIpAc</i>	Stable for long periods after preparation	Process difficult, sometimes doesn't work	Cannot be reproduced using rotary evaporator, metals only slightly soluble in ethylene glycol at reduced pressure
<i>AAS</i>	Simple, all acetate	Impurities	Large number of impurities, even at very high Tc. Best observed for $R_w = 6$ , $T_c = 1000$ , still not pure.
<i>AAC</i>	Low crystallization temp	Impurities	Large number of impurities regardless of water content, Tc
<i>TIpDEA</i>	Stable for long periods, pure phase at 500°C, easily reproducible	Xerogels are messy (DEA)	Pure phase PBT for $R_w = 4$ , Tc between 500-800°C
<i>EG2NO3</i>	Low crystallization temp	Rapid Hydrolysis	Hydrolysis proceeds rapidly on exposure to air
<i>EG2NO3Ac</i>	Similar to EG, more stable than EG2NO3	Impurities	Stable with $R_w = 4$ , though has many impurities
<i>F3AC</i>	Simple system, stable	Impurities	
<i>BEtF3AC</i>	Varies Barium Precursor	Impurities	
<i>TBuDEA</i>	Titanium butoxide more stable than isopropoxide	Impurities difficult to control	Reproducibility not as good as TIpDEA

**Table A-6.** Further Details of Selected PBT Sol-gel Systems

	<b>Optimum R<sub>A</sub></b>	<b>Optimum R<sub>w</sub></b>	<b>Impurity Free (T<sub>c</sub>)</b>	<b>Surface Area (Powder)</b>
<i>TIpAc</i>	4	8	550°C	19.9833 m <sup>2</sup> /g
<i>AAS</i>	-	6	-	15.8631 m <sup>2</sup> /g R <sub>w</sub> = 2
<i>TIpDEA</i>	4	4	500°C	20.0294 m <sup>2</sup> /g
<i>EG2NO3</i>	-	0	500°C	5.1155 m <sup>2</sup> /g
<i>TBuAc</i>	6	4		
<i>TBuDEA</i>	2	4		

### **A.10. AAC System: Additional Results**

A sol-gel system for the synthesis of solid solution lead barium titanate (PBT) was devised using lead nitrate, barium acetate, and titanium isopropoxide as metal precursors, ethylene glycol as a solvent, and acetic acid as a chelating agent. This system differs from the TIpAc system in the lead precursor and chelating agent used.

#### **AAC System Procedure**

Lead nitrate (25mmol, 8.8g) and barium acetate (25mmol, 6.38g) were dissolved in 112.3mL ethylene glycol using a rotary evaporator (120rpm, 80°C, 30 min). Separately, titanium isopropoxide (50mmol, 14.63mL) was added to acetic acid (100mmol, 5.724mL) and stirred for 15 min. The titanium isopropoxide and acetic acid mixture was then added to the above lead/barium precursor solution and attached to a rotary evaporator (120rpm, 80°C, 30 min). The solution was then cooled for 20 minutes. De-ionized water (100mmol, 1.8mL) and ethylene glycol (3.6mL) were then added, and the solution was again attached to a rotary evaporator (120rpm, 80°C, 30 min). The solution was dried at 150°C in an air oven.

#### **AAC System: Stability**

Samples were prepared with  $R_w = 2, 4, 6$ . Immediate gellation occurred for  $R_w = 6$ . For  $R_w = 4$ , gellation occurred within 3 hours of synthesis. The solution with  $R_w = 2$  was stable for 3 days.

### AAC System: XRD Powder Analysis

XRD patterns were obtained for all samples. All samples showed crystallinity by  $T_c = 400^\circ\text{C}$ , though all had significant impurity phases present. Peaks at  $2\theta \approx 24^\circ, 29^\circ, 43^\circ$  are identified as an undesired, non-ferroelectric pyrochlore phase. Peaks at  $2\theta \approx 30^\circ$  and  $34^\circ$  are unidentified. Interestingly the relative intensity of these impurity phases varies as temperature increases. For all values of  $R_w$ , the intensity of peaks at  $24^\circ, 29^\circ,$  and  $34^\circ$  decreases as calcination temperature increases, while the intensity of the  $30^\circ$  peak increases. Results for  $R_w = 4, 6$  are analogous.

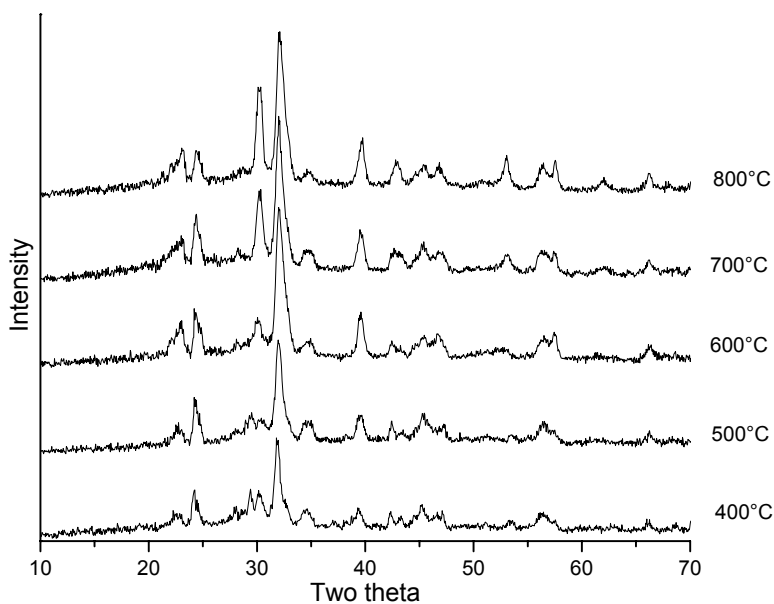


**Figure 87.** AAC System: Powder XRD,  $R_w = 4$ , varied  $T_c$ .

### AAC System: Summary

The AAC System is well-crystallized by  $T_c = 400^\circ\text{C}$ . Though PBT is present, there are a large number of undesired phases present in samples with  $R_w = 2, 4, 6$ . This system was not considered further.

### **A.11. EG2NO3 System: Additional Results**

A sol-gel system for the synthesis of solid solution lead barium titanate (PBT) was devised using lead nitrate, barium acetate, and titanium isopropoxide as metal precursors, and ethylene glycol as a solvent. This system is principally different from previously reported methods in that it does not incorporate a chelating agent.

#### **EG2NO3 System Procedure**

Barium acetate (6.25mmol, 1.596g) and lead nitrate (6.25mmol, 2.07g) were dissolved in ethylene glycol (0.5mol, 28mL) in a round bottom flask attached to a rotary evaporating system (120rpm, 72mbar, 40°C, 15 minutes). Titanium isopropoxide (12.5mmol, 3.66mL) was added, and the solution was stirred in the rotary evaporator, as above, for 1 hour. De-ionized water ( $H_2O:Ti = R_w$ ) was then added, together with an equal part ethylene glycol, and the resulting solution was stirred for 1 hour. The solution was then either stored, used to spin coat thin films, or dried at 150° C to form a powder. Powders were subsequently calcined by holding at furnace temperature ( $T_c$ ) 400, 500, 600, 700, and 800°C for 2 hours.

#### **EG2NO3 System: Stability**

Samples were prepared with  $R_w = 0, 0.5, 1, 1.5, 2, 3$ . Immediate gellation occurred for  $R_w = 3$  and is thus not considered further. Samples with  $R_w = 2$  gelled within 24 hours, while all others were stable for several days when kept in a sealed vial. This system is sensitive to atmospheric moisture, and prolonged exposure to air triggers rapid gellation.

**EG2NO3 System: XRD Powder Analysis**

XRD patterns were obtained for all samples. There is evidence of limited crystallinity at temperatures as low as 150°C, though it appears to be in the form of large crystalline particles rather than a uniformly crystalline powder.

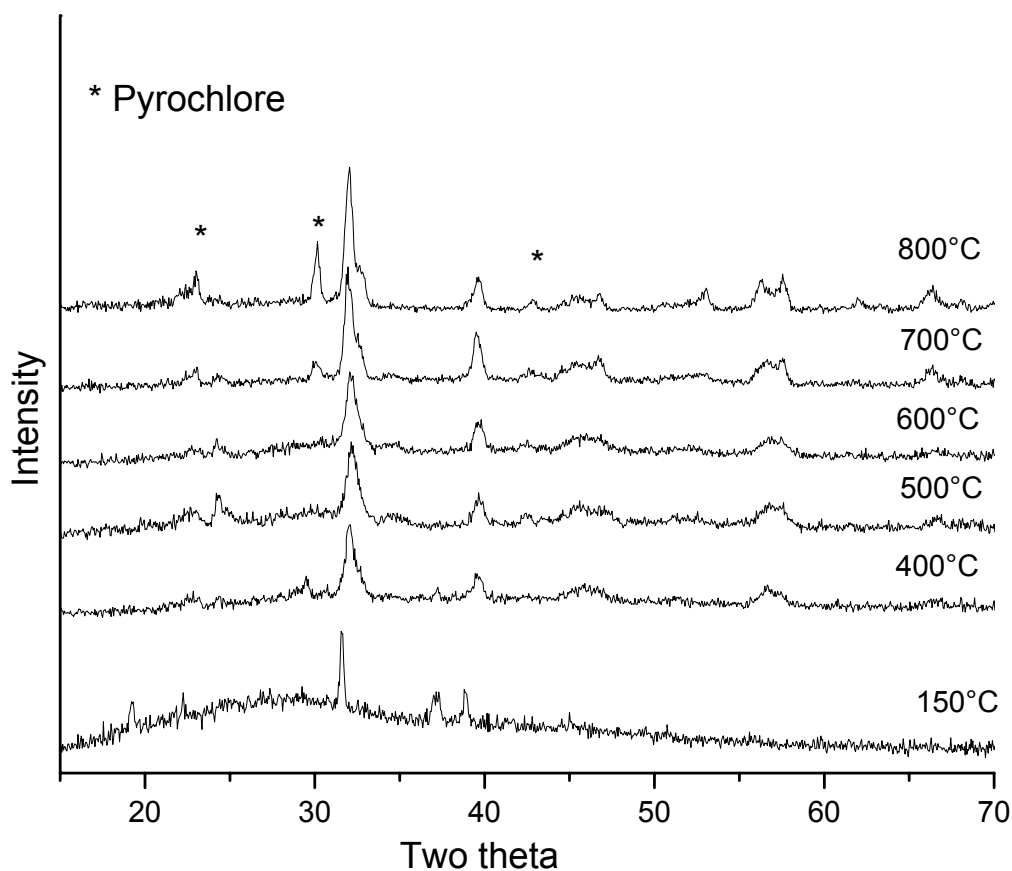


**Figure 88.** EG2NO3 System: Powder XRD,  $R_w = 0$ , varied  $T_c$ .

Peaks at  $2\theta \approx 24^\circ$ ,  $29^\circ$ ,  $43^\circ$  are identified as an undesired, non-ferroelectric pyrochlore phase. As shown in Figure 88, the pyrochlore phase becomes prominent in samples with

$R_w = 0$  at temperatures of 700°C and higher. Interestingly, for  $R_w = 0$ , the PBT phase is most prominent at low temperatures.

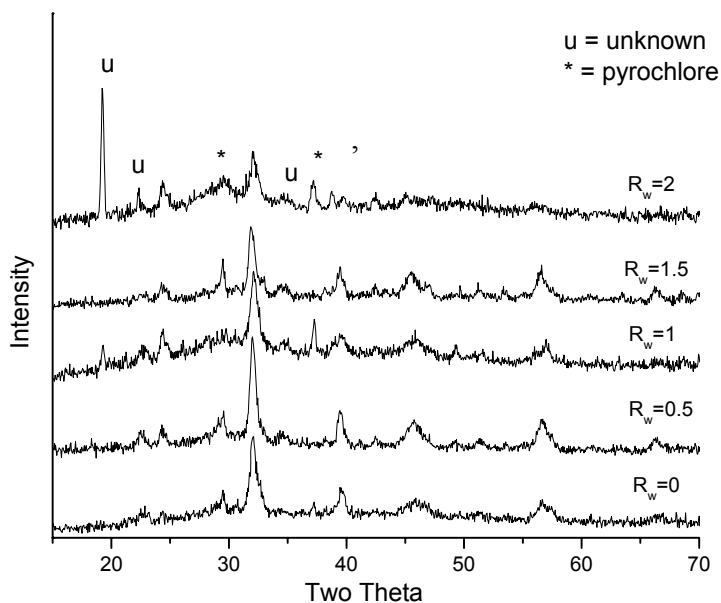


**Figure 89.** EG2NO3 System: Powder XRD,  $T_c = 400^\circ\text{C}$ , varied  $R_w$ .

In Figure 89, it can be seen that at 400°C, the relative amount of pyrochlore:PBT increases with increasing water content. This suggests that lower values of  $R_w$  tend to produce the most phase-pure PBT at low temperatures. Samples with  $R_w > 1$  have multiple undesired phases at all temperatures, and thus are not considered further.

### EG2NO3 System: TGA Analysis

Thermogravimetric analysis was performed between 100-600°C on powder samples dried at 150°C using a Netzsch STA-449 TGA System. The  $R_w = 0$  sample shows considerable weight loss (~14%) between 250-400°C. This corresponds well to the large difference observed between XRD patterns at 150°C and 400°C. Samples were calcined

at 200, 300, and 350°C to further explore the observed change. There is a large shift in XRD patterns between 300 and 350°C, where an unidentified phase with diffraction peaks at  $2\theta = 19^\circ$  and  $37^\circ$  observed at the lower temperature disappears completely in favor of the desired PBT phase.

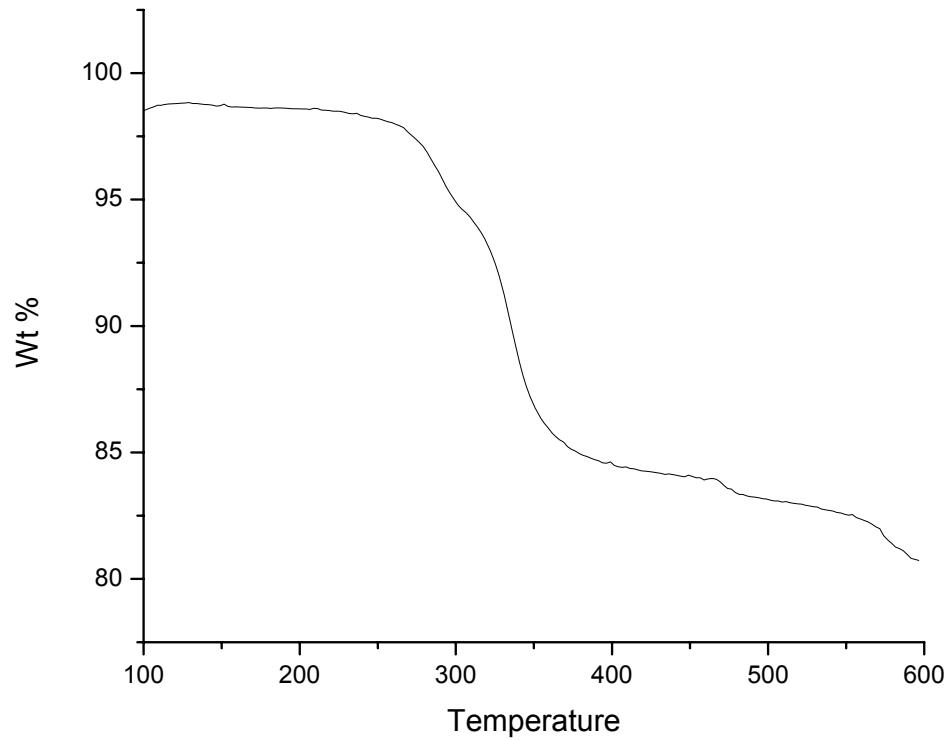


**Figure 90.** EG2NO3 System: TGA,  $R_w = 0$ .

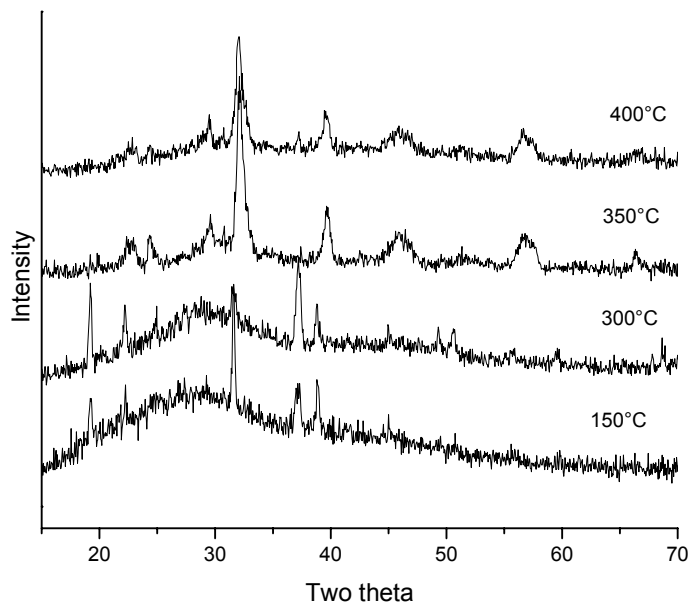


**Figure 91.** EG2NO3 System: Powder XRD,  $R_w = 0$ .

### **EG2NO3 System: Thin Films**

A thin film was prepared with  $R_w = 0$ ,  $T_p = 150$ ,  $T_c = 600^\circ\text{C}$ . XRD shows the film is not highly oriented (Figure 92). Optical microscopy shows the film surface is heavily cracked (Figure 93).

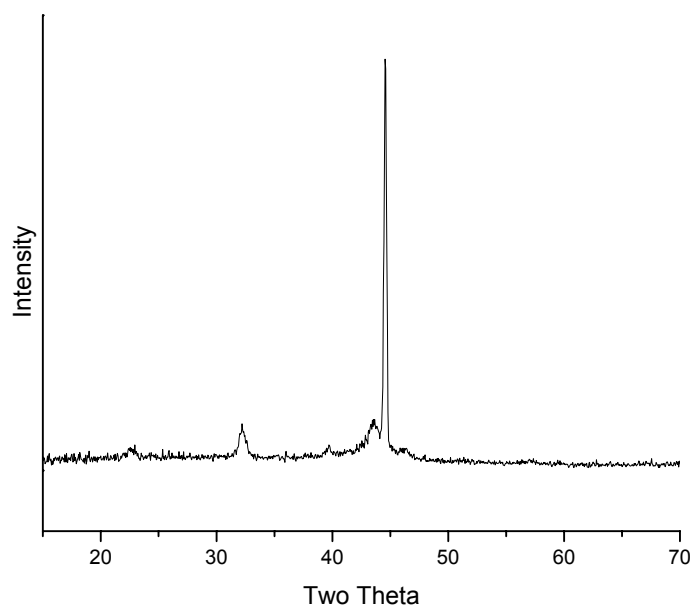


**Figure 92.** XRD of EG2NO3 thin film ( $R_w = 0$ ,  $T_p = 150^\circ\text{C}$ ,  $T_c = 600^\circ\text{C}$ ).



**Figure 93.** Optical microscope image of EG2NO3 film surface.

**EG2NO3 System: Summary**

Powders prepared using the EG2NO3 system begin crystallization at temperatures as low as 150°C, with PBT becoming the predominant phase at 350°C. The perovskite is favored in samples with the lowest  $R_w$  and for moderate  $T_c$ . The pyrochlore phase is favored for higher  $R_w$  and  $T_c$ . Thin films produced with EG2NO3 show large amounts of cracking. This system was not investigated further.

## A.12. F3AC System: Additional Results

A novel sol-gel system for the synthesis of solid solution lead barium titanate (PBT) was devised using lead citrate trihydrate, barium acetate, and titanium isopropoxide as metal precursors and trifluoroacetic acid as a solvent. This system differs from previous systems in the lead precursor and solvent used.

### F3AC System Procedure

Lead citrate trihydrate ( $\text{Pb}_3\text{C}_{12}\text{H}_{16}\text{O}_{17}$ , 8.33mmol, 8.77g) and barium acetate (25mmol, 6.38g) were dissolved in trifluoroacetic acid (1mol, 114mL) and refluxed for 30 minutes in a rotary evaporator (40°C, 90 mbar). The solution was then cooled for 20 min.

Titanium isopropoxide (50mmol, 14.6mL) was added to the above solution and then refluxed (as above) for 30 minutes and cooled for 20 minutes. De-ionized water (200mmol, 3.6mL) was then added and the solution was further refluxed for 30 minutes. The sol was then dried at 150°C for 24 hours.

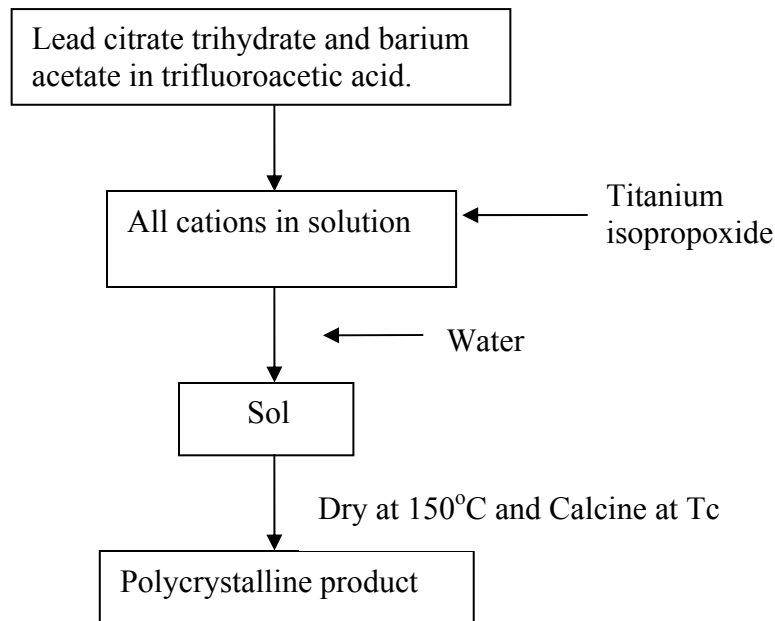


**Figure 94.** F3AC System procedure.

### **F3AC System: Stability**

The F3AC system is stable for at least several weeks without any sign of gellation.

### **F3AC System: XRD Powder Analysis**

Limited XRD analysis has been performed for this system. For  $R_w = 4$ , crystallization is evident in samples calcined at 500° and 600°C. Though some PBT peaks are observed, many significant impurities are also found. Diffraction peaks associated with lead pyrochlore are observed at  $2\theta = 29$  and  $43^\circ$ . Several additional unidentified (and undesired) phases are also present.

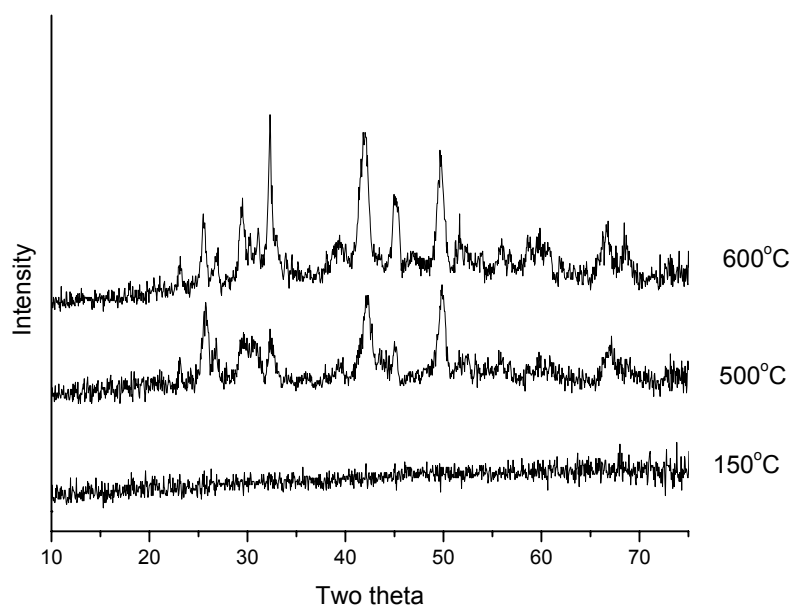


**Figure 95.** F3AC System: Powder XRD,  $R_w = 4$ , varied  $T_c$ .

### **F3AC System: Summary**

The F3AC System is well-crystallized by  $T_c = 500^\circ\text{C}$ . Though PBT is present, there are a large number of undesired phases present in all observed samples. This system was not considered further.

### **A.13. TIpAc System: Additional Results**

A sol-gel process incorporating lead acetate trihydrate, barium acetate, and titanium isopropoxide as precursors, acetylacetone as a chelating agent, and ethylene glycol as a solvent was used to prepare solid solution  $(\text{Pb}_{0.5},\text{Ba}_{0.5})\text{TiO}_3$ . Water content, calcination temperature, and heating rate were varied, and the resulting effects on material properties were studied using TGA/DSC, FTIR, FESEM, and X-ray diffraction.

#### **TIpAc System Procedure**

To prepare  $(\text{Pb}_{0.5},\text{Ba}_{0.5})\text{TiO}_3$ , barium acetate (8.23mmol, 3.12g, Aldrich, 99%) was dissolved in 20mL of ethylene glycol, using a hotplate/stirrer at 50°C. Separately, lead acetate trihydrate (8.23mmol, 2.10g, Alpha Aesar, 99%) was added to 10mL ethylene glycol, attached to a condenser, and stirred at 260°C for 1 hour. After cooling, the two metal acetate solutions were then mixed, 15mL ethylene glycol was added, and the solution is stirred for 15 minutes. Titanium isopropoxide (16.46mmol, 4.83mL, Alpha Aesar, 99%) and acetylacetone (in a prescribed ratio with titanium, Aldrich, 99%) was added to the mixed acetate solution, and the resulting solution was heated to 260°C while stirring for 1 hour attached to a condenser. Water (in a prescribed ratio with titanium) and an equal amount of ethylene glycol were added to the solution, which was then heated at 260°C on a hotplate and stirred for 1 hour. This solution was alternately dried in an air oven to produce dried gels or it was spin-coated onto MgO single crystals to produce thin films. In the spin-coating process, the films were dried on a hotplate at specified temperature ( $T_p$ ) between coats in what was considered a ‘pyrolysis step.’

Using the above procedure as a root, various parameters were modified individually and the resulting effects on material properties observed. For powders, the parameters under consideration were H<sub>2</sub>O:Ti ratio (R<sub>w</sub>) and calcination temperature. For thin films, pyrolysis temperature (T<sub>p</sub>) and calcination temperature were varied. Thermal decomposition characteristics of the oven dried samples were studied by DSC and TGA. The dried gels and thin films were then calcined in a tube furnace and examined by XRD and FESEM.

#### **TiPAc System: Stability**

Samples were prepared with R<sub>w</sub> = 2, 4, 8, 16, 32. All samples were found to be stable for more than two months. During an aging study, one sample (R<sub>w</sub> = 4), held at 120°C for 5 days, remained in liquid form.

#### **TiPAc System: XRD Powder Analysis**

Crystallization behavior as a function of calcination temperature is presented in Figure 96 for (Pb<sub>0.5</sub>,Ba<sub>0.5</sub>)TiO<sub>3</sub> powders processed using the optimized parameters R<sub>A</sub> = 4 and R<sub>w</sub> = 8. At 450°C crystallization of the perovskite phase occurred, along with a secondary phase that is likely pyrochlore. As would be expected, crystallinity increased with increasing temperature. By 500°C, the diffraction data are dominated by the perovskite phase, although peaks due to barium carbonate are evident. Complete crystallization of an impurity-free perovskite phase was obtained at 550°C. Pyrochlore was also evident at 700 and 800°C.

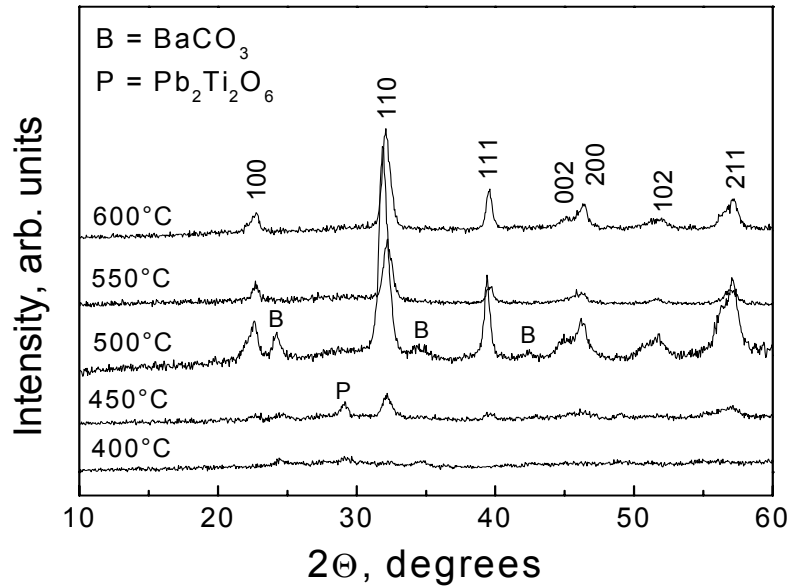


**Figure 96.** TlpAc powder XRD,  $R_w = 8$ ,  $RA = 4$  calcined at the temperatures indicated.

### TlpAc System: Thin films

To understand the effect of pyrolysis temperature ( $T_p$ ) on the crystallinity and orientation of films, the temperature used to heat treat the films between coatings was varied. A series of films was prepared ( $T_p = 150, 300, 450, 500^\circ\text{C}$ ), and the films were calcined at  $500^\circ\text{C}$  for 2 hours with a fixed heating rate of  $5^\circ\text{C}/\text{min}$ . XRD studies showed strong crystallinity and orientation in all samples. FESEM studies showed that all films were crack free. Grain growth was observed in the film heat treated at a pyrolysis temperature  $300^\circ\text{C}$  and  $450^\circ\text{C}$ . The film at  $500^\circ\text{C}$  pyrolysis showed phase separation. The optimal pyrolysis temperature was thus determined to be  $450^\circ\text{C}$ . The heating rate used during calcination ( $H_R$ ) was then varied. Samples were calcined at  $600^\circ\text{C}$  for 2 hours with  $H_R = 1, 2, 5, 10, 20^\circ\text{C}/\text{min}$ . Diffraction data (Figure 97) reveals that both very low ( $1^\circ\text{C}/\text{min}$ ) and very high heating rates ( $\geq 10^\circ\text{C}/\text{min}$ ) lead to undesirable orientations, whereas intermediate values of 2 and  $5^\circ\text{C}/\text{min}$  yield highly a/c-axis oriented films.

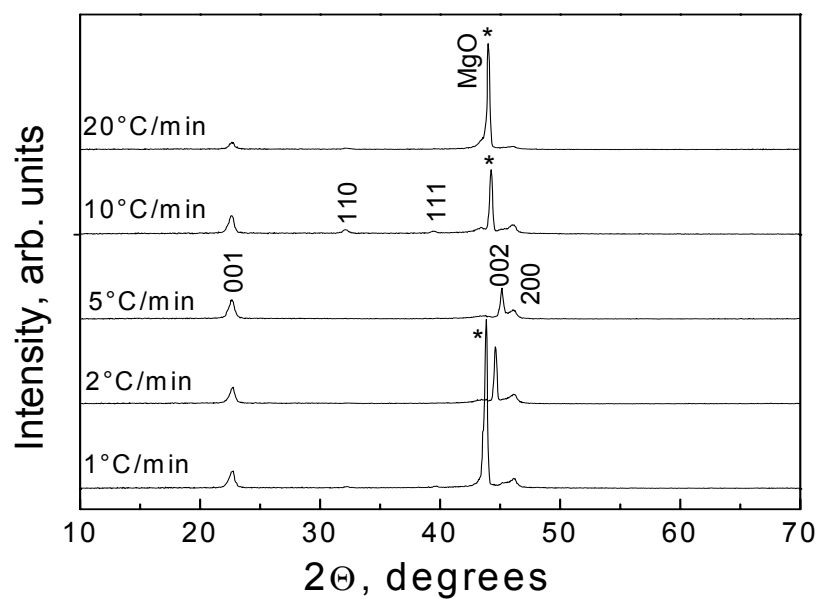


**Figure 97.** TlPac system powder XRD,  $T_c = 600^\circ\text{C}$ ,  $T_p = 450^\circ\text{C}$ , with heating rate indicated.

### **TlPac System: Summary**

Perovskite-phase crystallization occurred at a temperature as low as  $450^\circ\text{C}$ . Single-phase PBT was obtained at  $600^\circ\text{C}$ . Deposition of the optimized sol by spin coating on (100) MgO resulted in highly oriented PBT films, with mixed (001)/(100) orientation.

#### **A.14. TIpDEA System: Additional Results**

A novel sol-gel synthesis procedure for producing PBT was developed using lead nitrate, barium acetate, and titanium isopropoxide as metal sources, ethylene glycol as a solvent, and diethanolamine as a chelating agent.

##### **TIpDEA System Procedure**

Lead nitrate (25mmol, 8.25g) and barium acetate (25mmol, 6.38g) were dissolved in 112.3mL ethylene glycol in a round bottom flask attached to a rotary evaporating system (120 rpm, 72 mbar, 60°C, 30 min). Separately, titanium isopropoxide (50mmol, 14.6mL) was added to diethanolamine (200mmol, 19.2mL) and stirred for 15 minutes. This solution was then added to the lead/barium system and again attached to a rotary evaporating system (120 rpm, 72 mbar, 60°C, 30 min). The solution was then cooled for 20 min. De-ionized water (in a prescribed molar ratio with titanium) and ethylene glycol (7.2 mL) were added to the above system, which was then attached to the rotary evaporating system (120 rpm, 72 mbar, 60°C, 30 min). The solution was divided into two parts and one part was used for spin coating and the other dried at 150°C to form a xerogel. The xerogels were calcined at  $T_c = 400, 500, 600, 700, 800^\circ\text{C}$  for 2 hours.

##### **TIpDEA System: Stability**

Immediate gelation occurred for  $R_w = 32$ . All other samples were stable for at least 3 weeks. Sols with  $R_w = 4$  were stored and used for more than 2 years without noticeable degradation.

**TipDEA System: XRD Powder Analysis**

Diethanolamine:titanium was taken as 4:1 in order to ensure complete chelation. Water for hydrolysis was varied ( $Rw = 2, 4, 6, 8, 16, \text{ and } 32$ ). Powder X-ray diffraction patterns show the presence of impurity phases in all samples except  $Rw = 4$ . Thus,  $Rw = 4$  was chosen as ideal and is fixed in further studies.

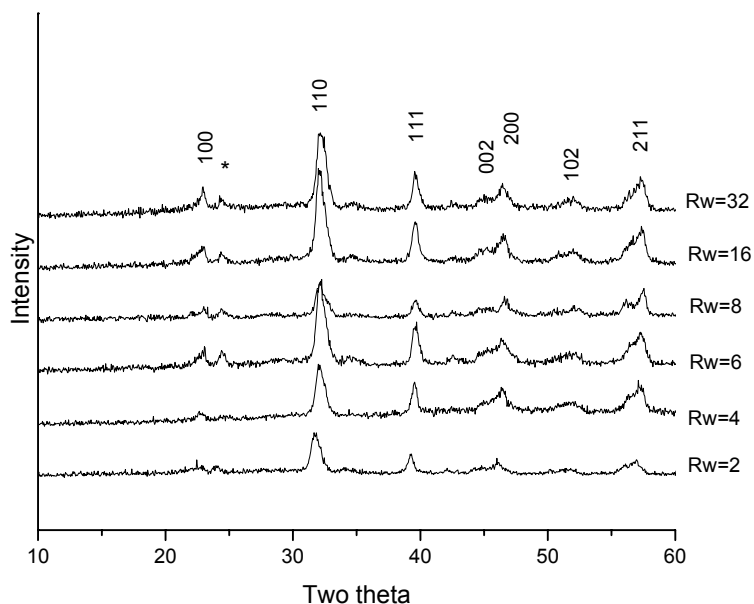


**Figure 98.** TipDEA System: Powder XRD,  $T_c = 500^\circ\text{C}$ , varied  $Rw$ .

Calcination temperature was varied ( $400$  to  $800^\circ\text{C}$ ). PBT phases are observed at a temperature as low as  $400^\circ\text{C}$ , with phase-pure PBT obtained at  $500^\circ\text{C}$ . This method offers a wide range of temperatures with phase-pure PBT.

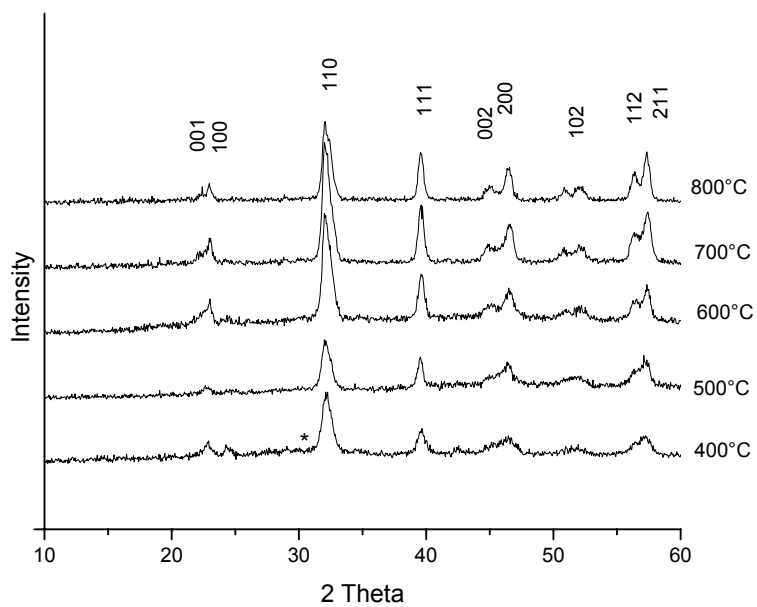


**Figure 99.** TlpDEA system: Powder XRD,  $R_w = 4$ , varied  $T_c$ .

### **TlpDEA System: Summary**

Crystallization of the PBT perovskite phase occurred at a temperature as low as 400°C.

Single-phase PBT was obtained at 500°C.

### TIpDEA System: STA Results for Various Atmospheres

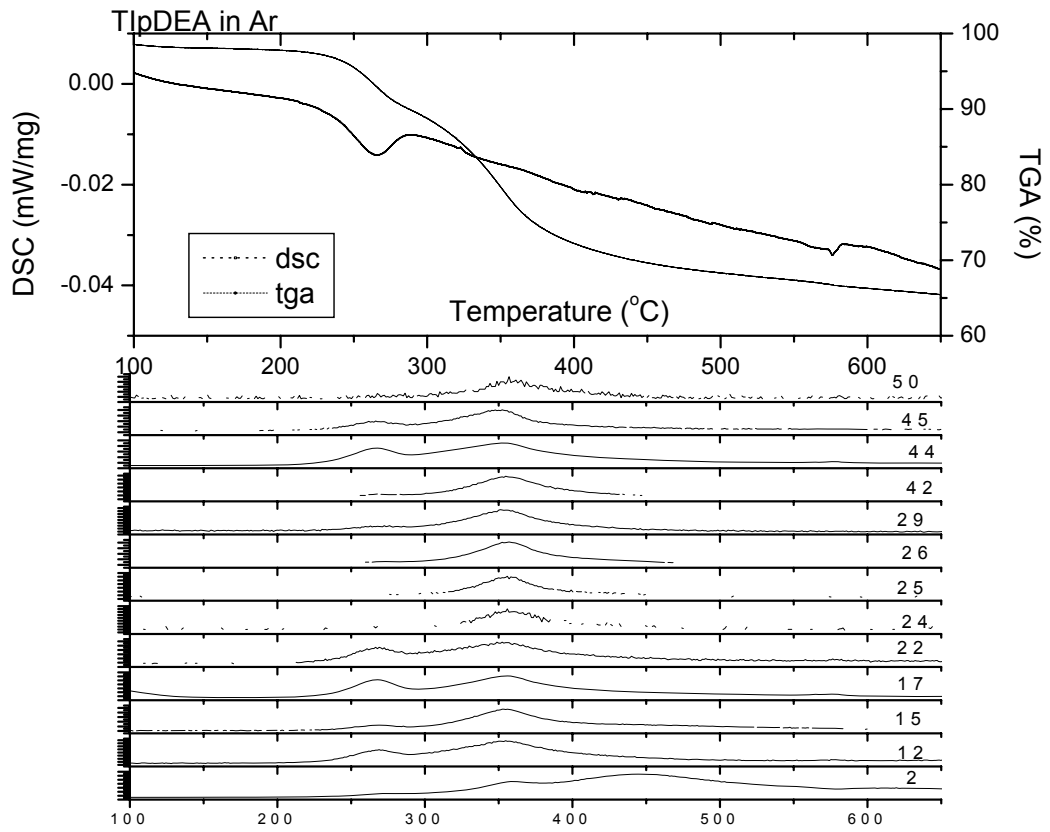


**Figure 100.** STA with mass spectrometry data for TIpDEA (pure Ar atmosphere).

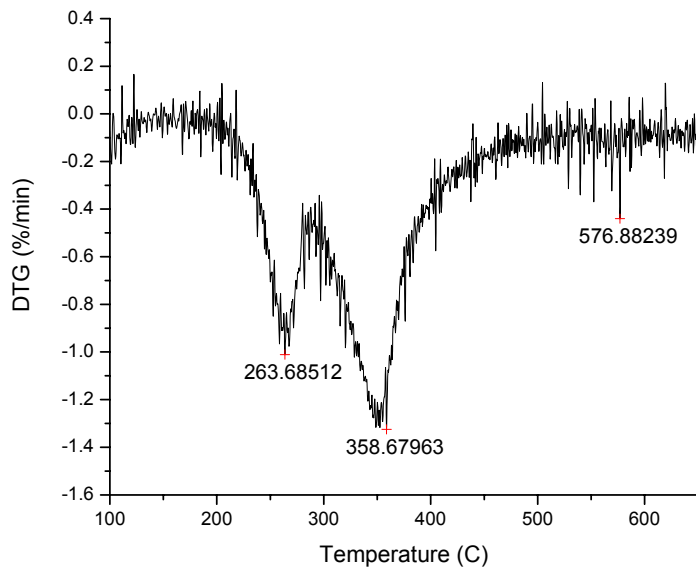


**Figure 101.** DTG of TIpDEA in pure Ar has peaks at 264°C (-2.427 J/g), 359°C, and 576°C (-0.3482 J/g).

The peak at 359°C is not accompanied by a discernible DSC peak.

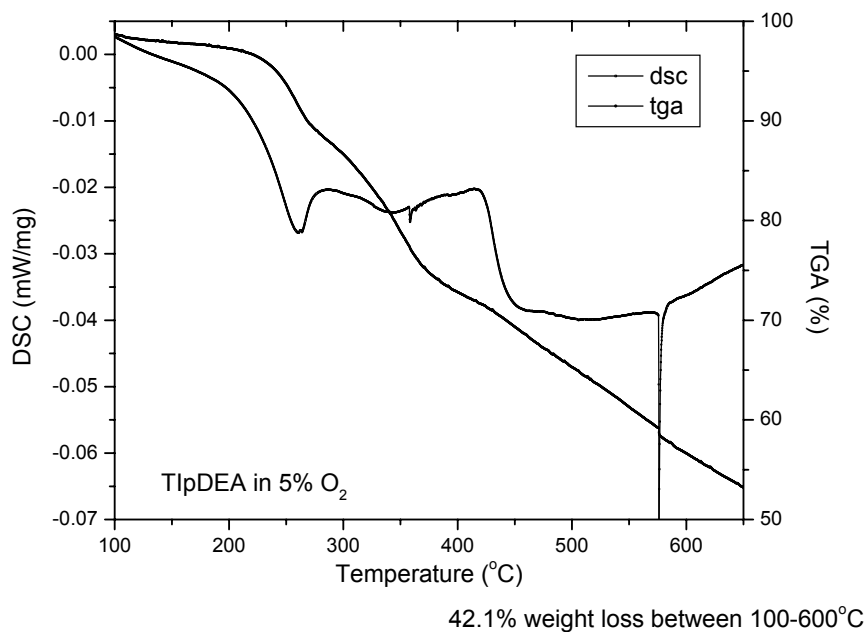


Figure 102. STA of TIpDEA in 5%O<sub>2</sub> atmosphere.

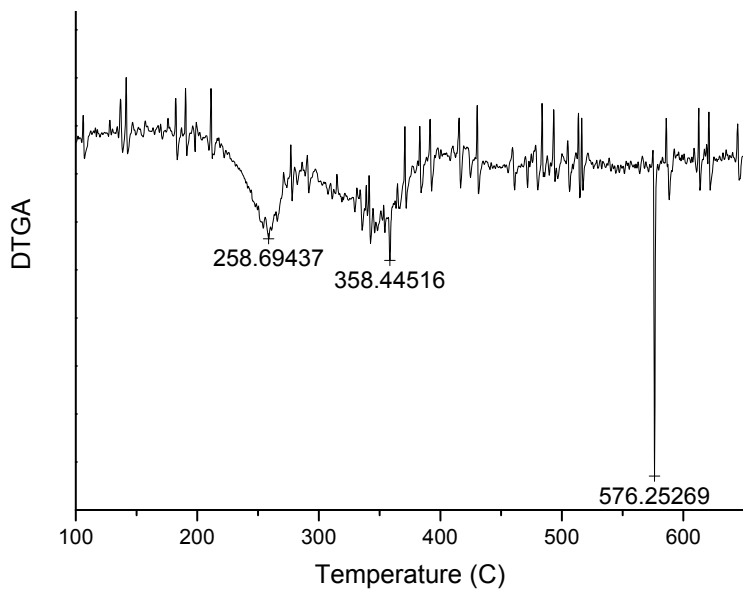
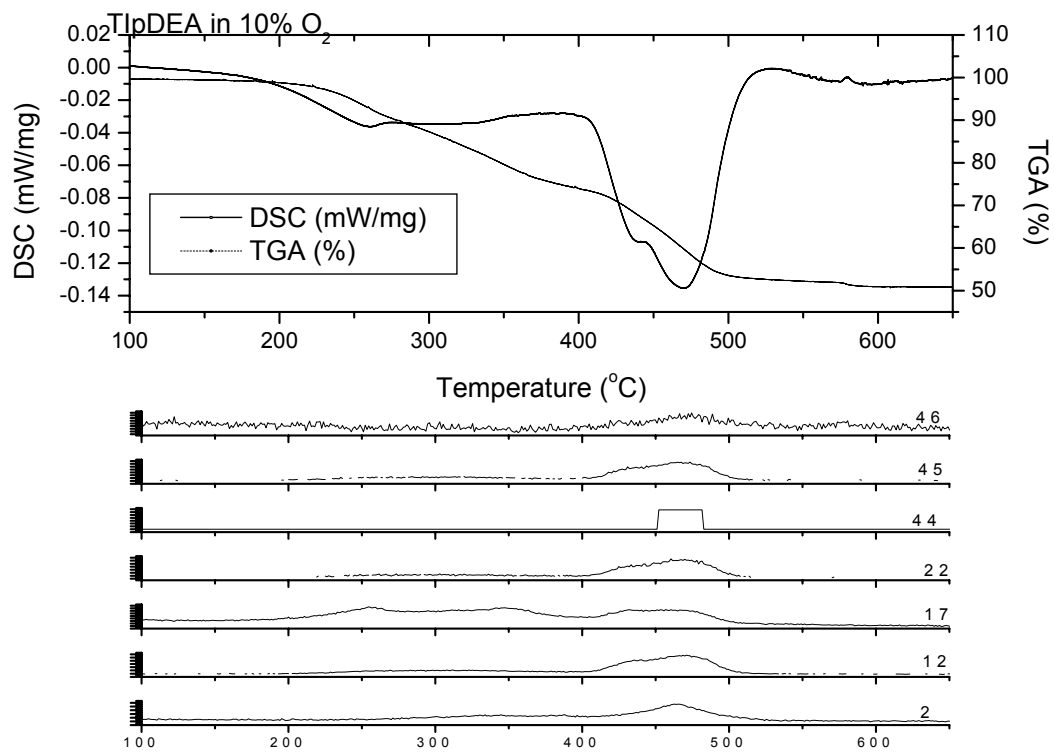
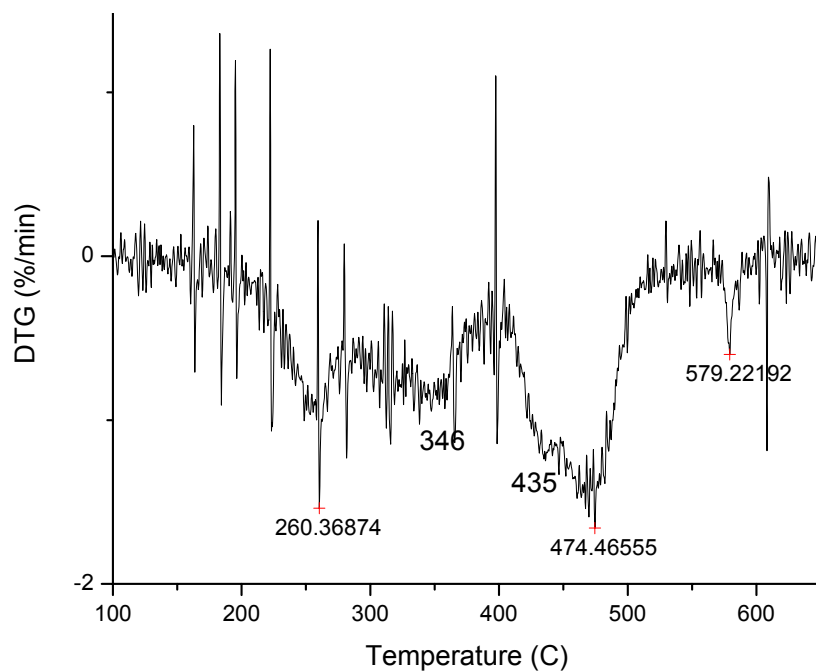


Figure 103. DTGA of TIpDEA (5%O<sub>2</sub>) showing peaks at 258°C (-4.174J/g), 358°C (-0.1601J/g), and 576°C (-1.057 J/g).



**Figure 104.** STA with mass spectrometry data for TIpDEA in 10%O<sub>2</sub> atmosphere.



**Figure 105.** DTGA of TIpDEA in 10%O<sub>2</sub> showing peaks at 260, 474 (-93.14 J/g), and 579°C (+0.2053 J/g). There is also a slight shoulder at 435° and a broader peak at 346° that do not correspond to DSC events.

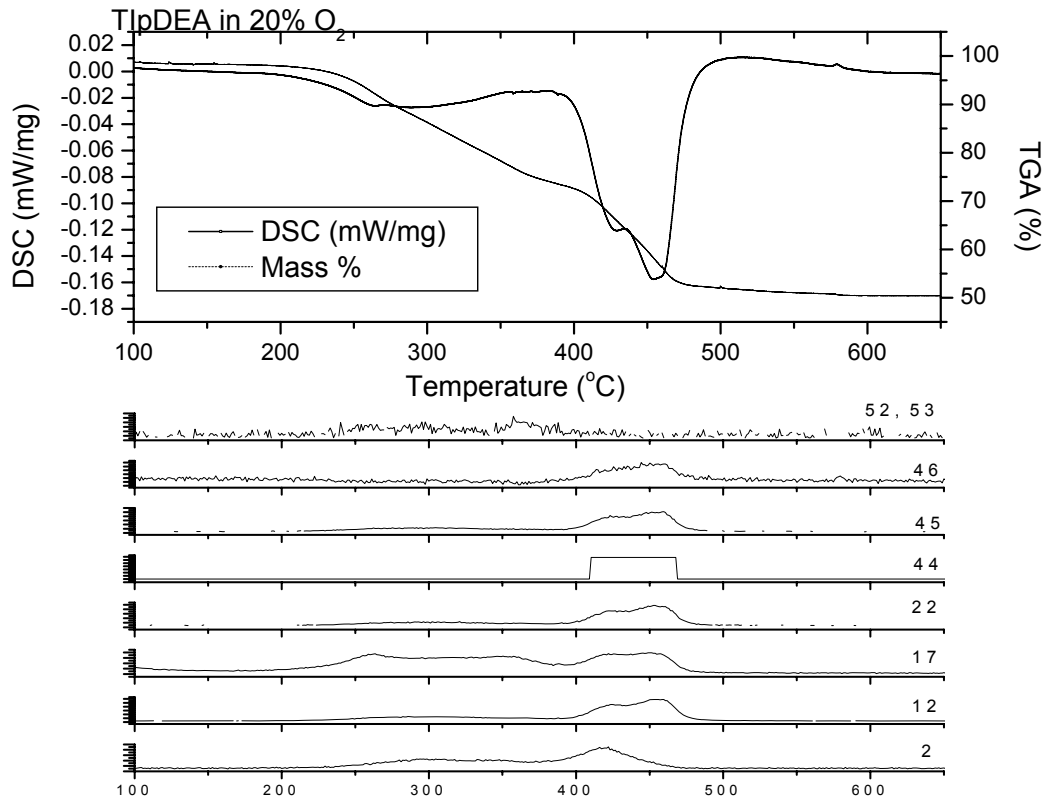


**Figure 106.** STA with mass spectrometry data for TIPDEA in 20%O<sub>2</sub> atmosphere.

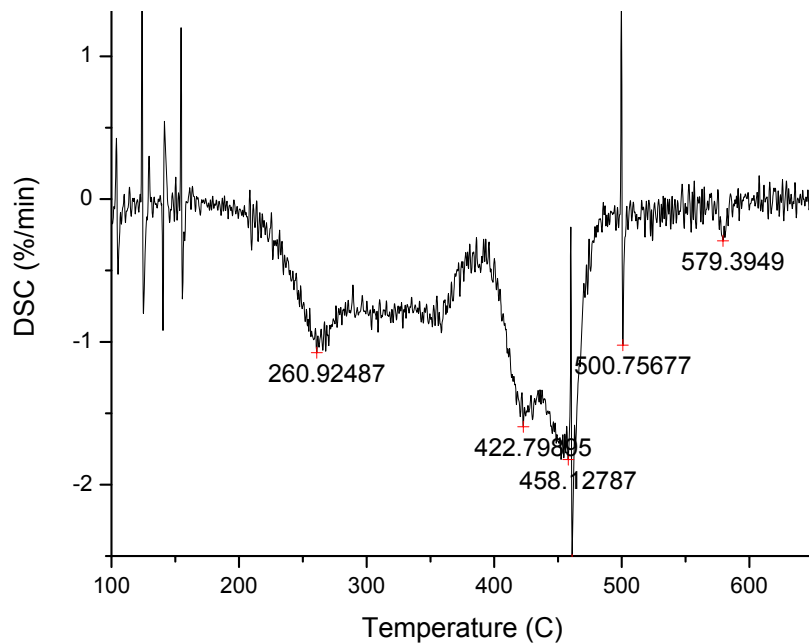


**Figure 107.** DTG of TIPDEA in 20%O<sub>2</sub> shows clear peaks at 261°C (-17.59J/g), 423°C, 458°C (-98.68J/g), and 579°C (0.1431 J/g), which agrees well with DSC. The spike at 501°C is not accounted for.

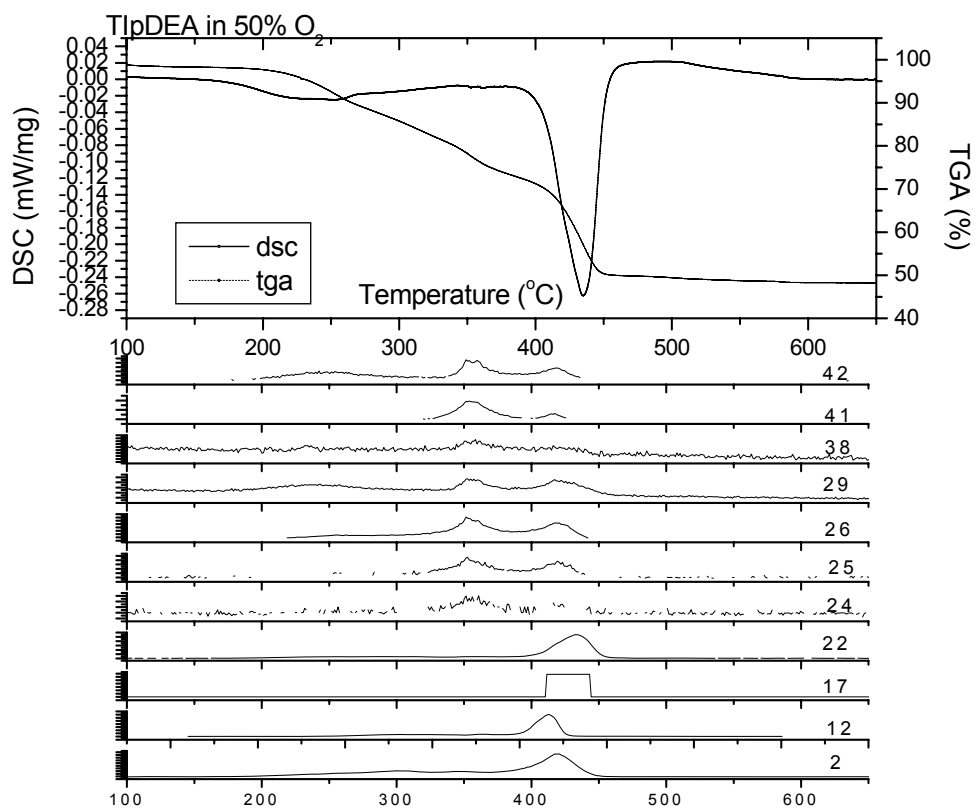


**Figure 108.** STA with mass spectrometry data for TipDEA in 50%O<sub>2</sub> atmosphere showing masses 2-42.

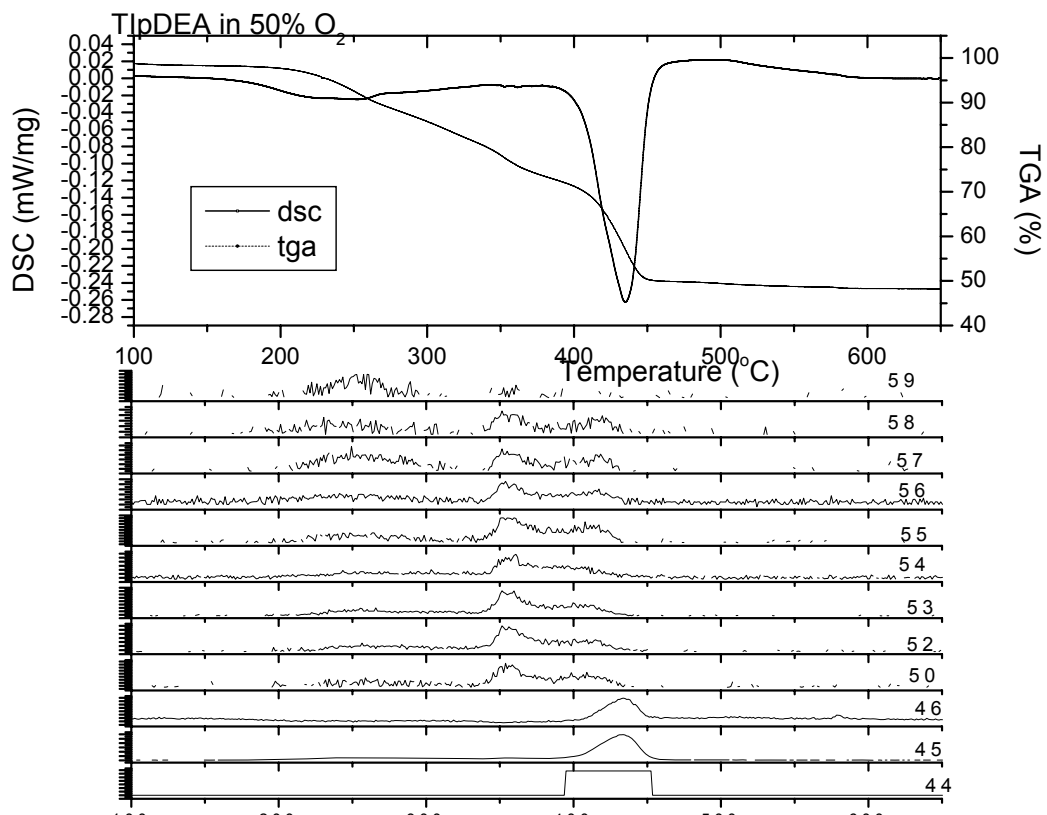
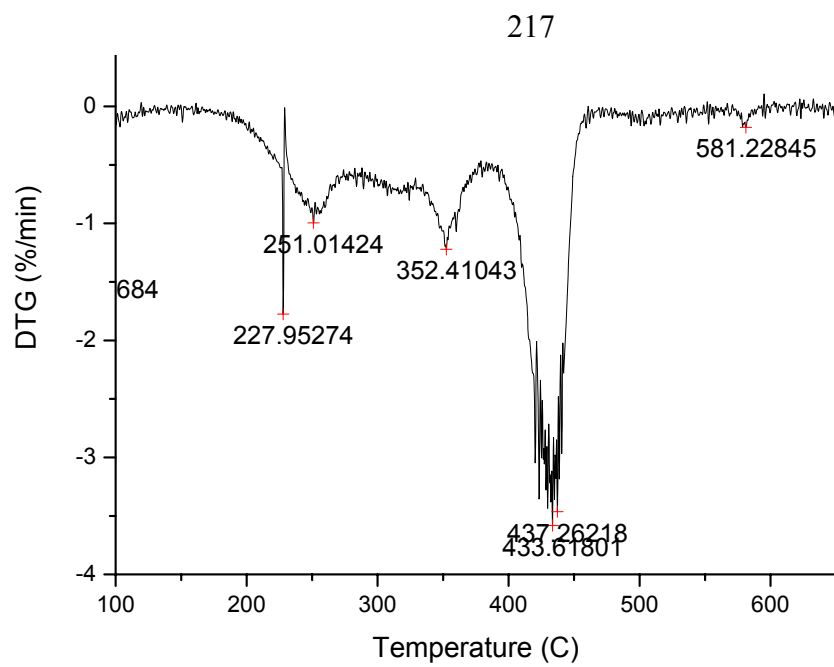


Figure 109. STA with mass spectrometry data for TiPDEA in 20%O<sub>2</sub> atmosphere showing masses 44-59.



**Figure 110.** DTG of TIpDEA in 50%O<sub>2</sub> atmosphere showing clear peaks at 251 (-9.489 J/g), 352, 434 (-99.07 J/g), and 581°C, as well as a spike at 228. The peaks 251 and 434 correspond well with DSC. The peak at 352 is unaccounted for, as is the small peak at 581°C.

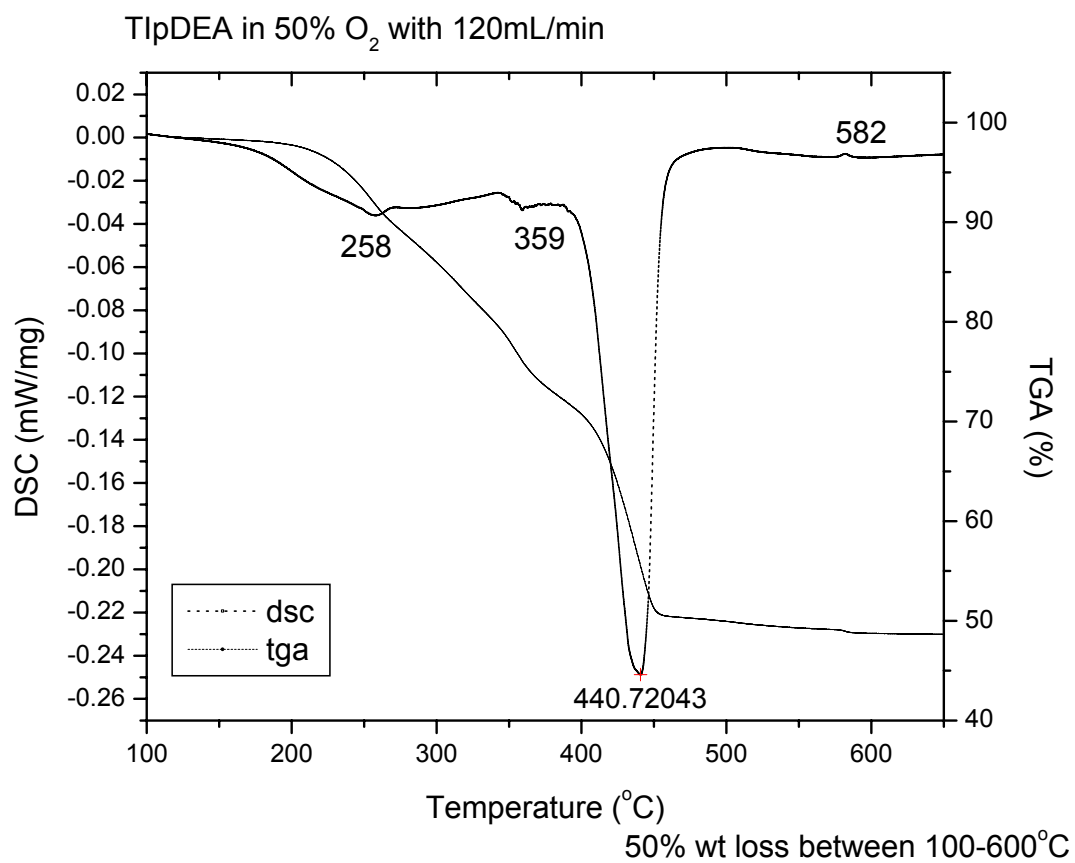
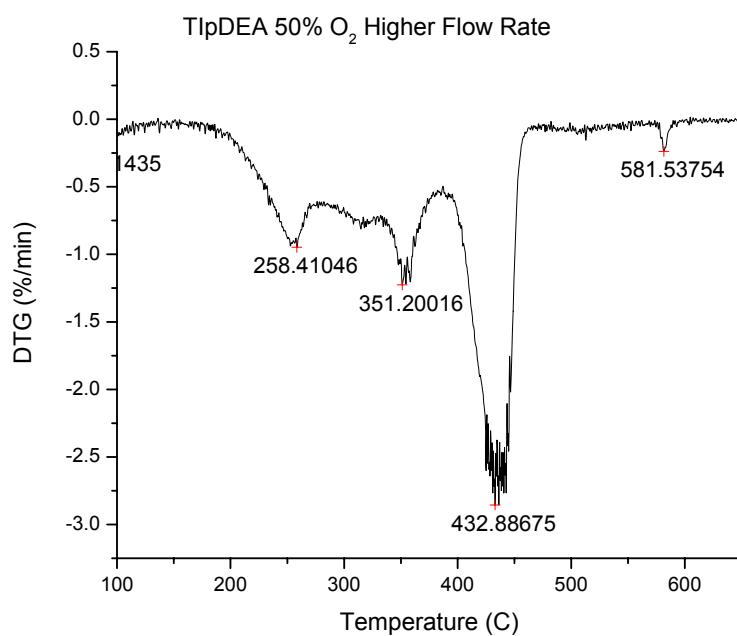


Figure 111. STA of TIpDEA with 50%O<sub>2</sub> atmosphere using high flow rate of 120mL/min.



**Figure 112.** DTG shows clear peaks at 258 (-12.57 J/g), 351, 433 (-130.5 J/g), and 582°C. This corresponds well with DSC.

### A.15. $\text{LaNiO}_3$ : Effect of Pyrolysis Temperature on Surface Morphology

All films were deposited on fused silica substrates. Sol concentration was 0.32M, spin speed was 3krpm, 40 seconds. Pyrolysis was at  $T_p$  indicated for 5 minutes, followed by direct insertion into a preheated furnace at  $700^\circ\text{C}$  for 10 minutes. After deposition of the final (6<sup>th</sup>) layer, the films were calcined at  $700^\circ\text{C}$  for 2 hours.

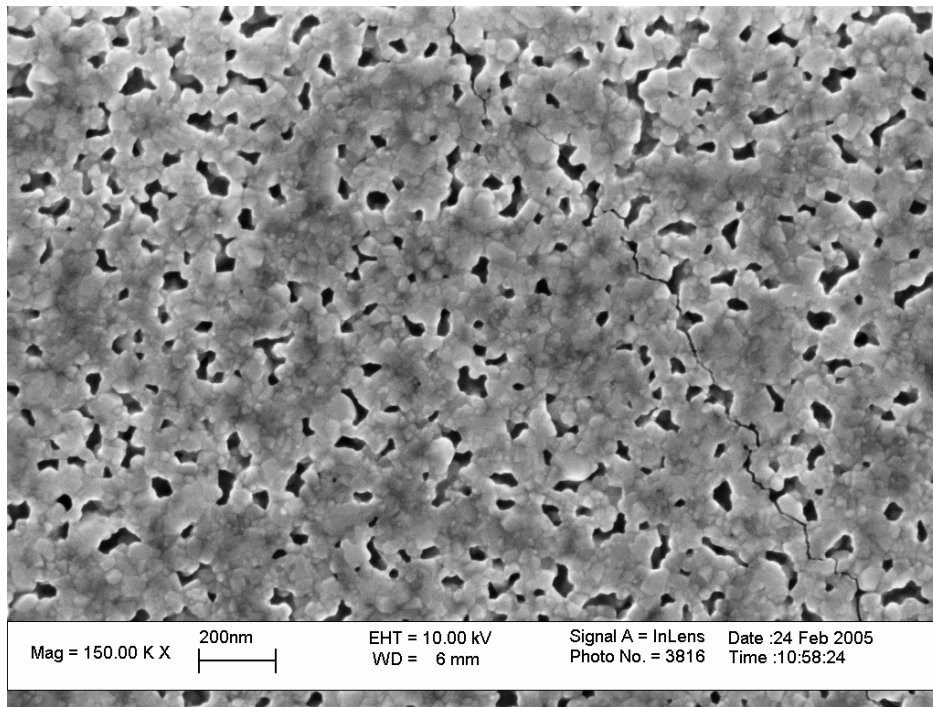


**Figure 113.** SEM image of 6 layer  $\text{LaNiO}_3$  film deposited on fused silica with  $T_p = 200^\circ\text{C}$ .

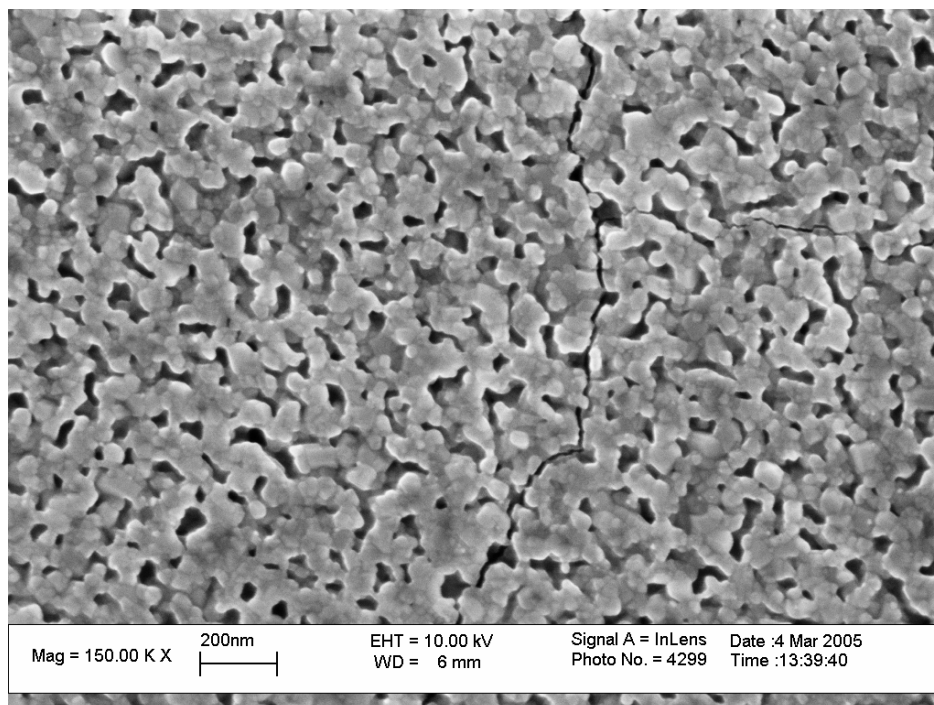


**Figure 114.** SEM image of 6 layer LaNiO<sub>3</sub> film deposited on fused silica with T<sub>p</sub> = 300°C.

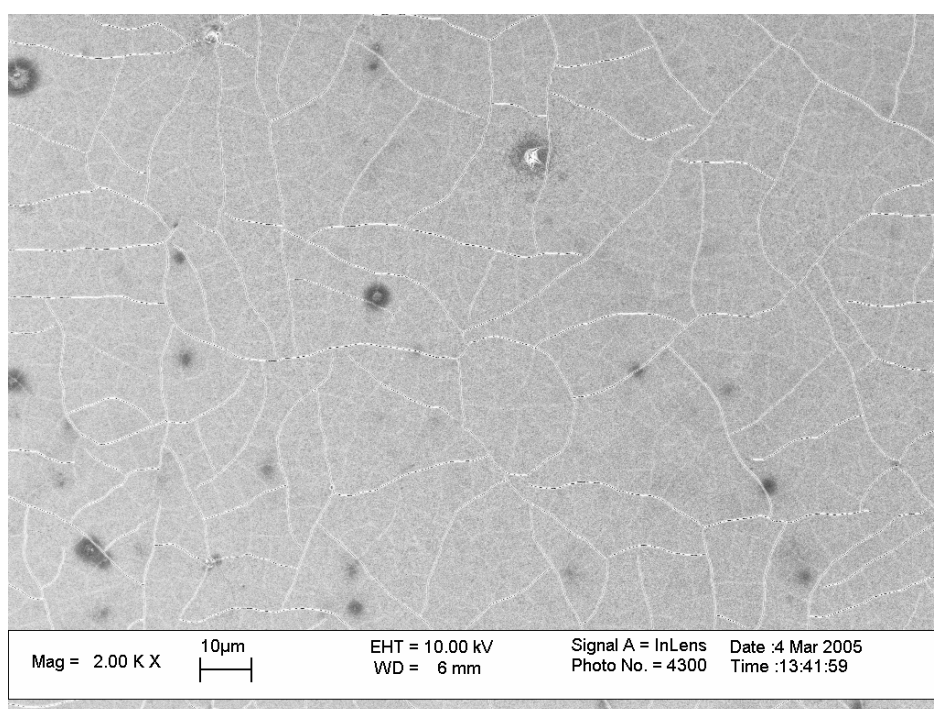


**Figure 115.** SEM image at lower magnification, showing extensive cracking on surface of 6 layer LaNiO<sub>3</sub> film deposited on fused silica with T<sub>p</sub> = 300°C.

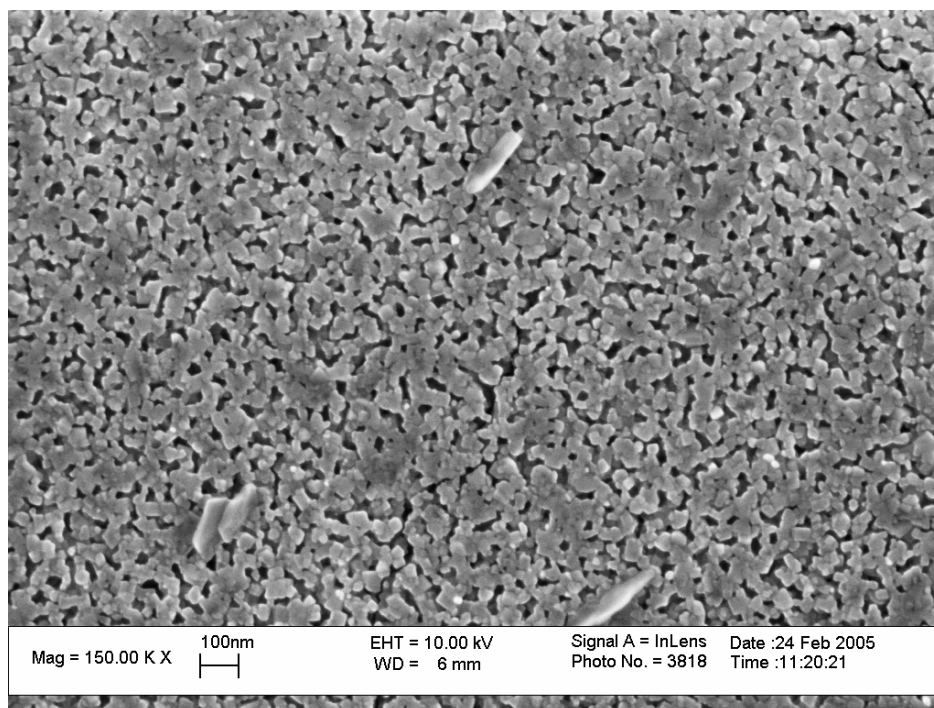


**Figure 116.** SEM image of 6 layer LaNiO<sub>3</sub> film deposited on fused silica with  $T_p = 400^\circ\text{C}$ .

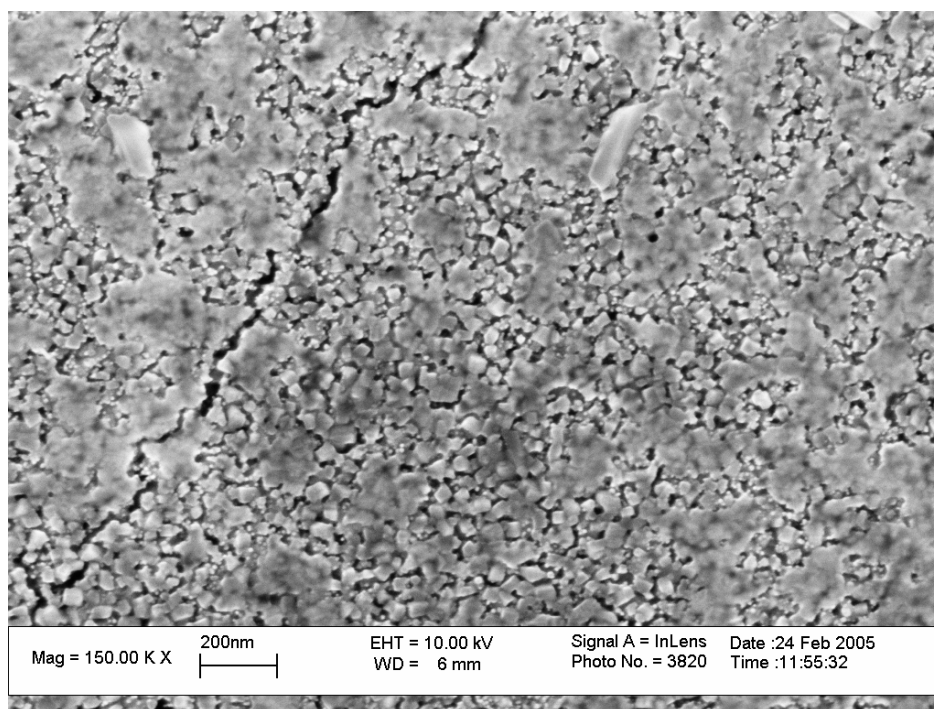


**Figure 117.** SEM image of 6 layer LaNiO<sub>3</sub> film deposited on fused silica with  $T_p = 500^\circ\text{C}$ .

### A.16. $\text{LaNiO}_3$ : Effect of Number of Layers on Surface Morphology

All films were deposited on Si substrates. Sol concentration was 0.32M, spin speed was 3krpm, 40 seconds. Pyrolysis was at 400°C for 5 minutes, followed by direct insertion into a preheated furnace at 700°C for 10 minutes. After deposition of the final layer, the films were calcined at 700°C for 2 hours.

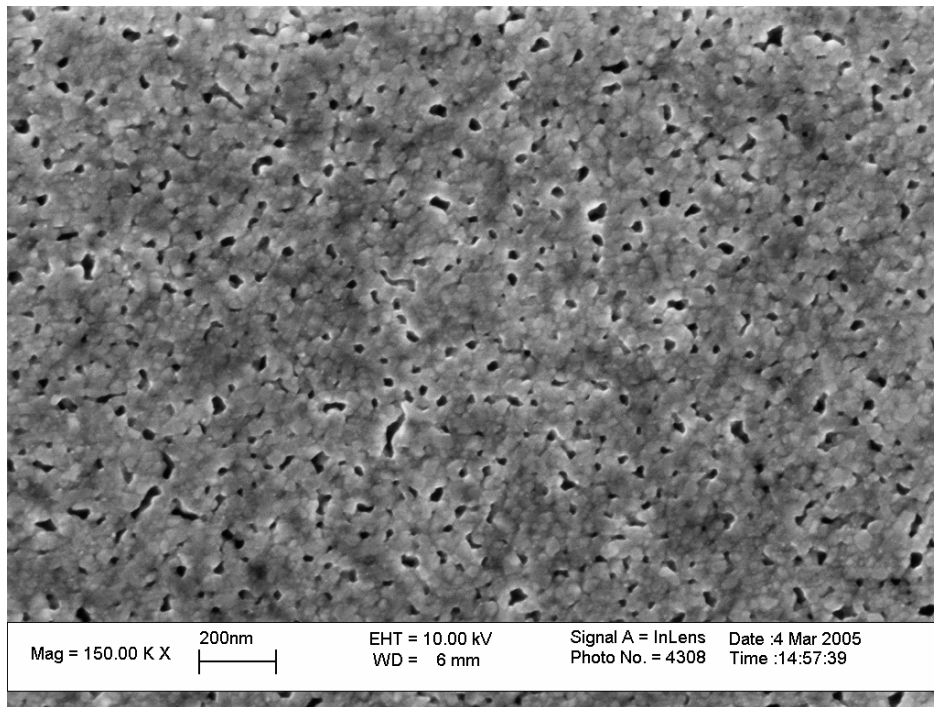


**Figure 118.** SEM image of 1 layer  $\text{LaNiO}_3$  film deposited on Si ( $T_p = 400^\circ\text{C}$ ).

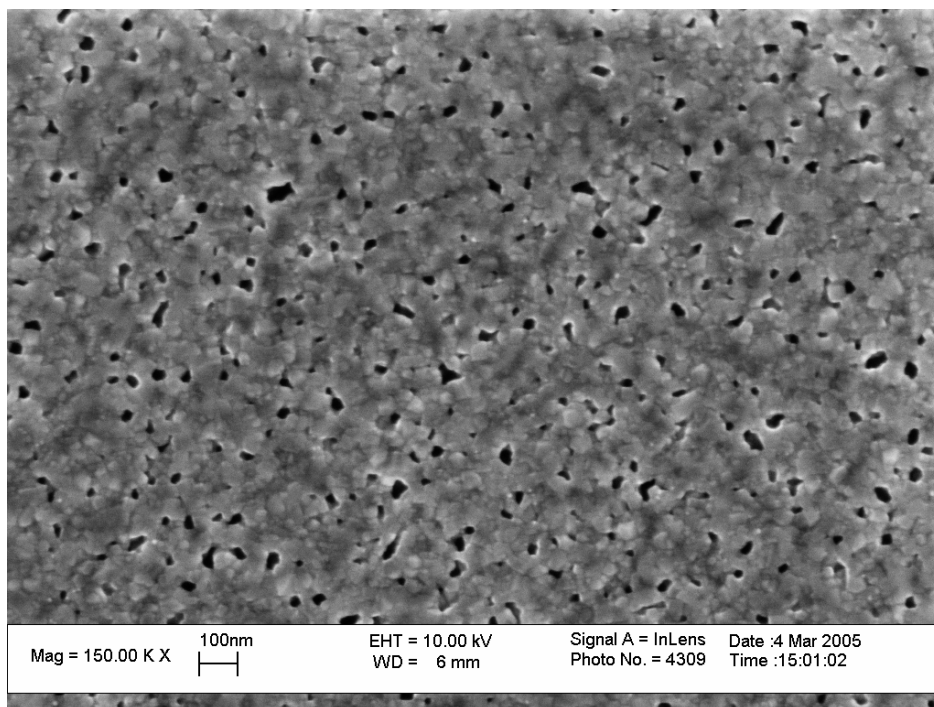


**Figure 119.** SEM image of 2 layer  $\text{LaNiO}_3$  film deposited on Si ( $T_p = 400^\circ\text{C}$ ).

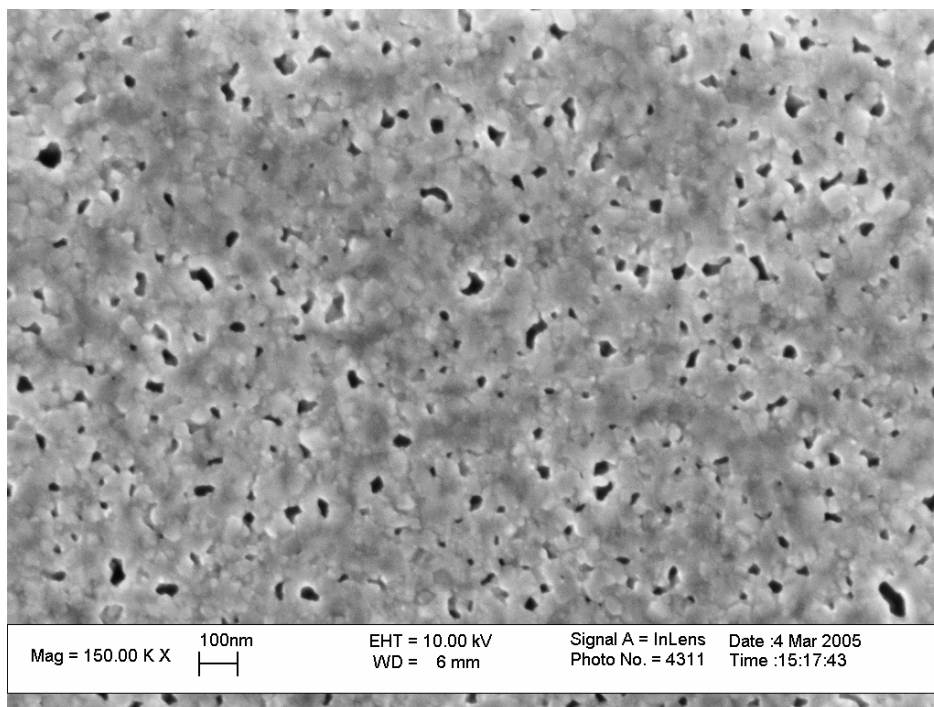


**Figure 120.** SEM image of 3 layer  $\text{LaNiO}_3$  film deposited on Si ( $T_p = 400^\circ\text{C}$ ).

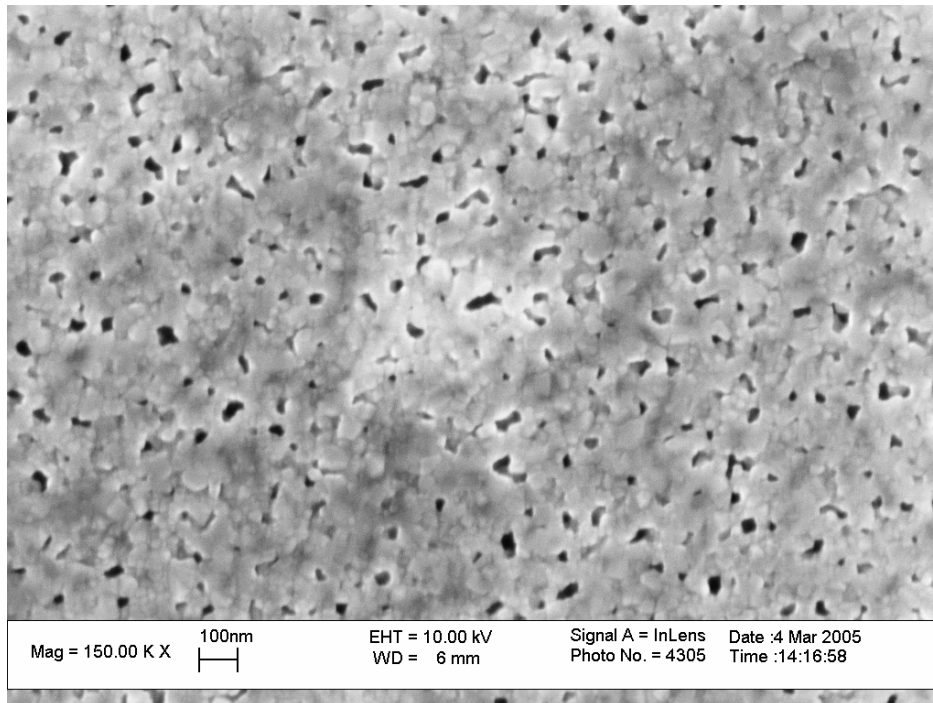


**Figure 121.** SEM image of 4 layer  $\text{LaNiO}_3$  film deposited on Si ( $T_p = 400^\circ\text{C}$ ).

### A.17. $\text{LaNiO}_3$ : Effect of Calcination Temperature and Heating Rate on Surface Morphology

All films were deposited on Si substrates. Sol concentration was 0.32M, spin speed was 3krpm, 40 seconds. Unless otherwise noted, pyrolysis was at 400°C for 5 minutes, followed by direct insertion into a preheated furnace at  $T_c$  for 10 minutes. After deposition of the final layer, the films were calcined at  $T_c$  for 2 hours.

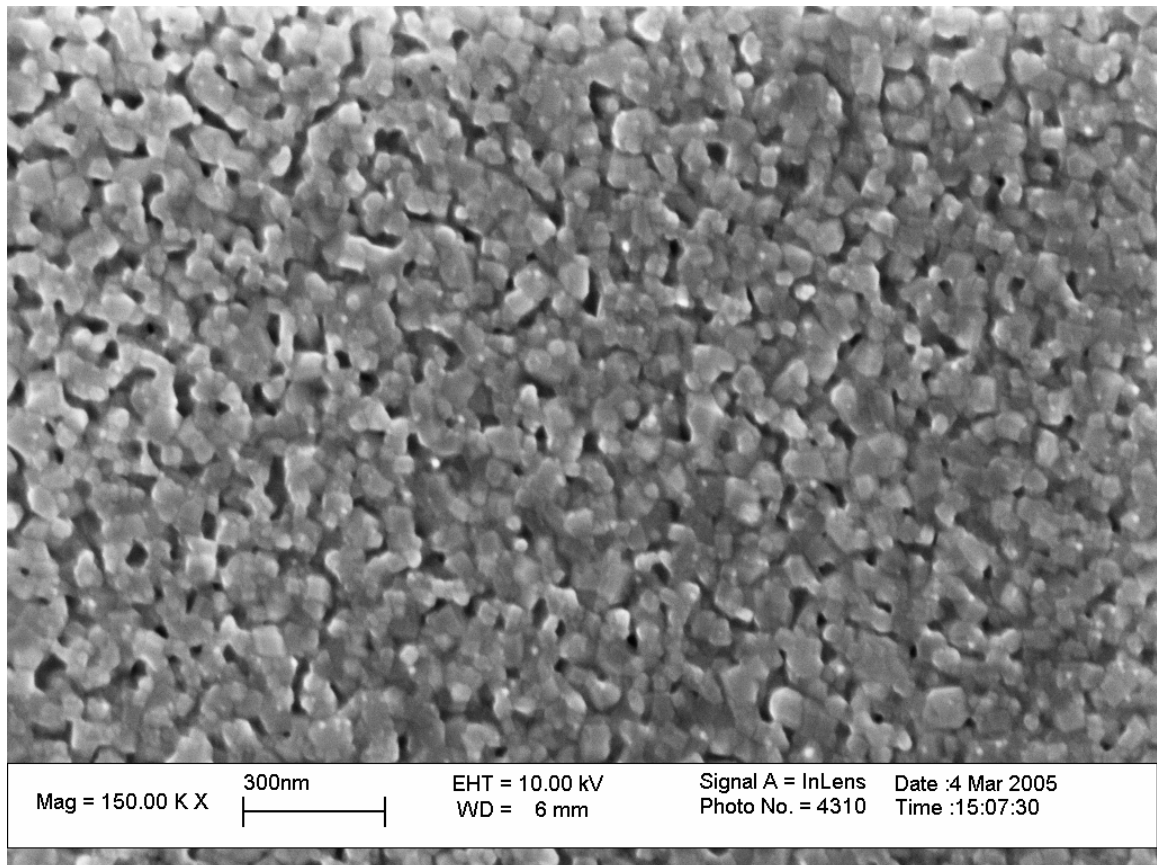


**Figure 122.** SEM image of 4 layer  $\text{LaNiO}_3$  film deposited on Si without pyrolysis step ( $T_c = 700$ ).

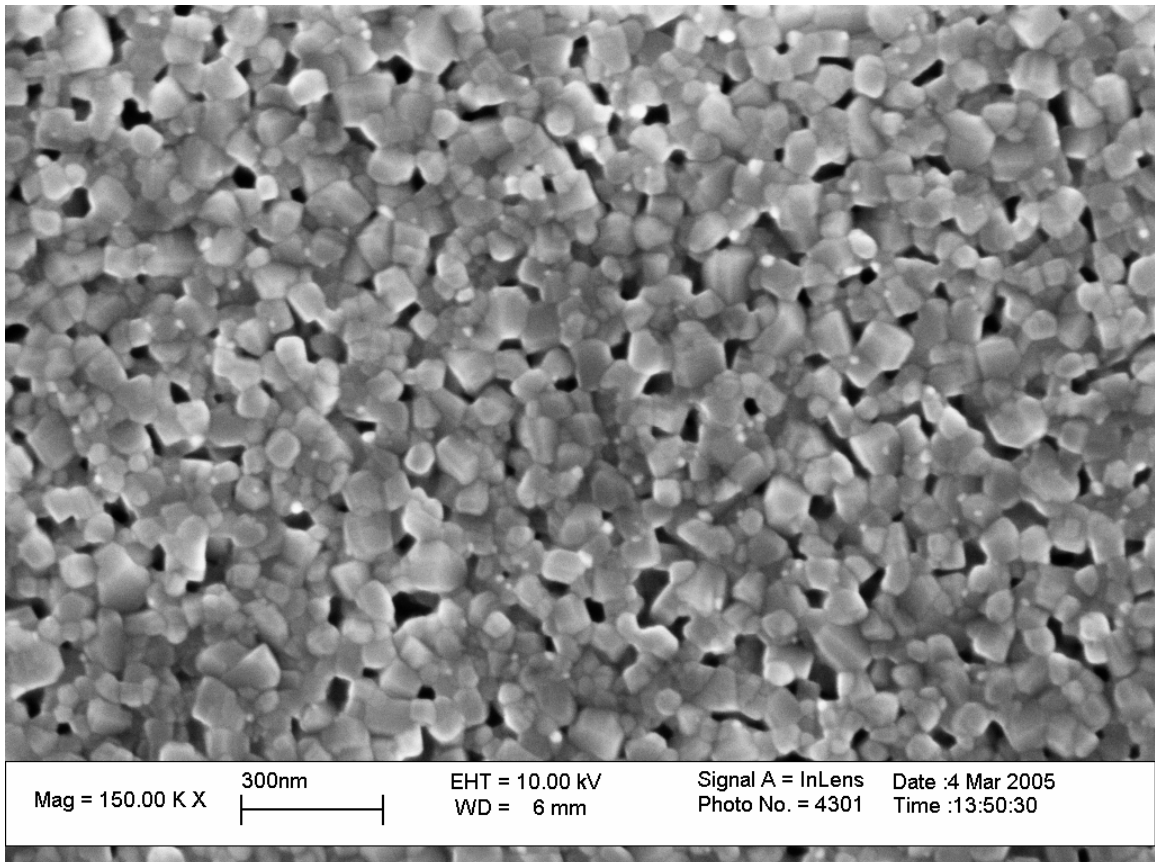


**Figure 123.** SEM image of 4 layer  $\text{LaNiO}_3$  film deposited on Si with  $T_p = 400$ ,  $T_c = 800$ .

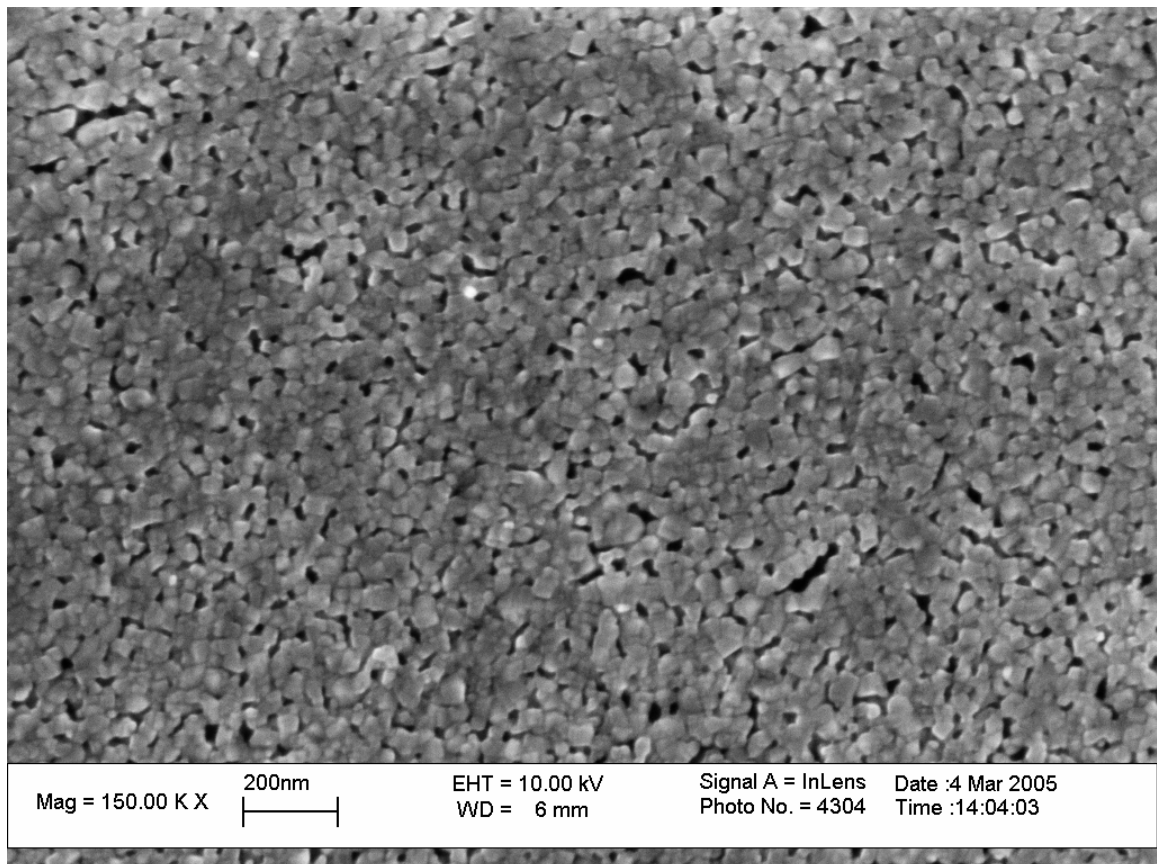


**Figure 124.** SEM image of 4 layer LaNiO<sub>3</sub> film deposited on Si<sub>3</sub>N<sub>4</sub>/Si with only Tp = 400 between layers, and final calcination at Tc = 700 with HR = 5°C/min.